INVESTIGATION OF PHYSICAL PROPERTIES OF NANOCOMPOSITES OF SPINEL FERRITES AND 2D MATERIALS FOR SUPERCAPACITOR APPLICATIONS

Thesis Submitted for the Award of the Degree of

DOCTOR OF PHILOSOPHY

in

Physics

By

Kiranjot Kaur

Registration Number: 12108270

Supervised By

Dr. Deepak Basandrai (11873)

Department of Physics (Professor)

Lovely Professional University, Punjab

Co-Supervised By

Dr. Ajeet Kumar Srivastava (11459)

Department of Physics (Professor)

Lovely Professional University, Punjab

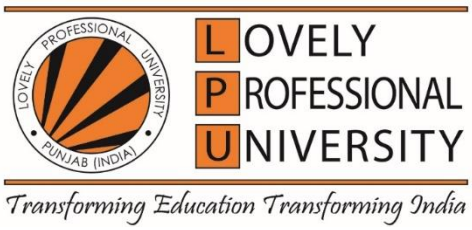

LOVELY PROFESSIONAL UNIVERSITY, PUNJAB

2024

-

Dedicated to my Parents

S. Jaswant Singh and Mrs. Mahinder Kaur

DECLARATION

I, hereby declare that the presented work in the thesis entitled **"Investigation of Physical Properties of Nanocomposites of Spinel Ferrites and 2D Materials for Supercapacitor Applications"** in fulfillment of my degree of **Doctor of Philosophy (Ph. D.)** is the outcome of research work carried out by me under the supervision Dr. Deepak Basandrai, working as Assistant Professor in the Department of Physics of Lovely Professional University, Punjab, India. In keeping with the general practice of reporting scientific observations, due acknowledgments have been made whenever the work described here has been based on the findings of another investigator. This work has not been submitted in part or full to any other University or Institute for the award of any degree.

Kiranjot Kaur

Registration No.: 12108270

Department/School: Physics/ School of Chemical Engineering and Physical Sciences

Lovely Professional University,

Punjab, India

CERTIFICATE

This is to certify that the work reported in the Ph. D. thesis entitled **"Investigation of Physical Properties of Nanocomposites of Spinel Ferrites and 2D Materials for Supercapacitor Applications"** submitted in fulfillment of the requirement for the reward of the degree of **Doctor of Philosophy (Ph.D.)** in the Department of Physics, is a research work carried out by Kiranjot Kaur, Reg.No:12108270, is bonafide record of his/her original work carried out under my supervision and that no part of thesis has been submitted for any other degree, diploma or equivalent course.

(Signature of Supervisor)

Dr. Deepak Basandrai

Professor

Department of Physics
Lovely Professional University

Phagwara, Punjab

(Signature of Co-Supervisor)

Dr. Ajeet Kumar Srivastava

Professor

Department of Physics
Lovely Professional University

Phagwara, Punjab

ACKNOWLEDGEMENT

I thank God for bestowing me with the blessing of being a learner, and for keeping me a knowledge seeker. May this little knowledge lead me and those who are directly or indirectly associated with me on the righteous path, here and hereafter. I cordially express my profound regards and gratitude to my research supervisor Dr. Deepak Basandrai and Dr. A.K. Srivastava, who always paid attention and gave masterly advice to overcome my delusions and hurdles. His expert comments and suggestions made this work meaningful. I would like to express my love and gratitude, especially to my fiance Mehakpreet Singh for his affection and constant motivation. I am very much obliged to all my mentors and would like to express my gratitude, especially to my sisters and brothers, Dr. Gurkirat Kaur, Prabhjot Kaur, and Bikramjeet Singh, who have motivated me in and out in all possible ways and I would take this opportunity to thank them wholeheartedly.

I express my sincere thanks to the Head of the Department (HOS) Dr. Kailash C. Juglan and all other faculty members of the Physics department for their help and support during this period. I would like to show my appreciation and gratitude to the respected panel members, Dr. Jeeban Prasad, Dr. Shankar Dyal Phatak, and Dr. Rajesh Kumar, who helped me to shape my research objectives by providing their insightful and knowledgeable suggestions. My special thanks to all the research holders, members of the technical and non–technical/non-teaching staff especially Nitin Kumar Yadav and Ramesh Kumar of the Department of Physics. I would also like to thank Dr. Sachin Kumar Godara (Department of Chemistry, Guru Nanak Dev University, Amritsar, India) for providing various support in characterization. Moreover, sincere thanks to all my dearest friends, Vijaya Bhaskar, Shruti Bakshi, Kamlash Rani, Shezan, and Anuj Garg who have uplifted and motivated me in and out in all possible ways and I would take this opportunity to thank them wholeheartedly. I consider it an appropriate occasion to record my deep sense of affection for my well-wishers Dr. Anjori Sharma, Dr. Hamnesh Mahajan, and Dr. Ibrahim Mohammed. Finally, and most importantly, I would like to thank my parents who are always there for me and without them this piece of work was impossible. I shall always be indebted to them for their unstinted support, be it financially, morally, or inspirationally. May the almighty God give them a happy life and bless them with good health.

Kiranjot Kaur

(Reg.No.: 12108270)

ABSTRACT

With the severe increase in pollution caused by fossil fuels and the fast depletion of fossil energy sources, there is an increasing demand for the development of new energy storage systems. More efficient electrical storage devices must be developed to address future environmental issues and societal demands. The demand for an efficient and adequate energy storage device has inspired scientific research into designing nanotechnology-based capacitors. Supercapacitors (SCs), which are made of nanostructured electrode materials, serve as a bridge between capacitors and batteries, combining the high-power capabilities of electrostatic capacitors and rechargeable batteries that have a high energy density. To make effective utilization of energy storage devices, state-of-the-art research on novel and advanced electrode materials is needed. The main objective of this thesis was to create a low-cost supercapacitor electrode using a cost-effective technique that is applicable to commercial and industrial usage which is based on 2D material and metal ferrite nanoparticles with high Specific capacitance. The growing interest in the use of nanomaterials for supercapacitors has provided researchers with a new expanded platform for developing suitable electrode materials that are capable of providing excellent specific capacitance. Spinel ferrite, MXene, and Spinel ferrite-MXene nanocomposite are the materials stated herein to produce a synergistic impact for the energy storage supercapacitor application.

In the current research work, three different series of spinel ferrite have been prepared by the facile and cost-effective method by utilizing the sol-gel auto combustion method. Ti_3C_2 MXene was synthesized by using the fluoride etching method and the nanocomposite $Pr_{0.02}Mn_{0.5}Co_{0.5}Fe_{1.98}O_4 – Ti_3C_2$ MXene was synthesized using the physical blending method. The following sample of spinel ferrites has been synthesized and characterized.

(1) $Zn_{0.2}Mg_{0.8}Fe_2O_4$ at 400 ºC, 600 ºC, and 800 ºC for 6h.
(2) $Mn_xCo_{0.5-x}Ni_{0.5}Fe_2O_4$ at 1100 ºC for 6h (x = 0.0, 0.2, 0.4).
(3) $Pr_xMn_{0.5}Co_{0.5}Fe_{2-x}O_4$ at 1100 ºC for 6h (x = 0.00, 0.01,0.02, 0.03, 0.04).
(4) $Pr_{0.02}Mn_{0.5}Co_{0.5}Fe_{1.98}O_4 – Ti_3C_2$ MXene.

The prepared series were initially investigated using various techniques viz. Phase identification by using X-ray Diffraction (XRD), morphologically by Field Emission Scanning Electron Microscopy (FESEM) and High resolution transmission electron microscopy (HR-TEM), elementally by Energy Dispersive X-ray Analysis (EDX) and X-ray photoelectron spectroscopy (XPS), and magnetic properties Vibrating Sample Magnetometer (VSM),

dielectric properties, Cyclic Voltammetry (CV), Galvanic Charge discharge (GCD), and Electrical impedance spectroscopy (EIS) that are required for its use as a supercapacitor electrode material were employed to investigate the above-said characteristics.

$Pr_xMn_{0.5}Co_{0.5}Fe_{2-x}O_4$ (x = 0.00, 0.01,0.02, 0.03, 0.04) have been preferred over the $Zn_{0.2}Mg_{0.8}Fe_2O_4$ and $Mn_xCo_{0.5-x}Ni_{0.5}Fe_2O_4$ ferrite. Because $Pr_xMn_{0.5}Co_{0.5}Fe_{2-x}O_4$ has a large surface area, high porosity, and pore size for the transfer of electrons. out of the five prepared praseodymium doped samples, the sample at x = 0.02 concentration i.e., $Pr_{0.02}Mn_{0.5}Co_{0.5}Fe_{1.98}O_4$ is favored, at 1100 ^oC excellent exhibit porosity, large surface, morphological, elemental, and magnetic characteristics have been exhibited and beneficial for the supercapacitor electrode.

The electrochemical performance of the $Pr_{0.02}Mn_{0.5}Co_{0.5}Fe_{1.98}O_4$ – Ti_3C_2 MXene nanocomposite was investigated using three-electrode cells to determine use as active materials in supercapacitor electrodes. Cyclic voltammetry was used to investigate the redox behavior of electrodes. Galvanic charge-discharge was used to determine the high specific capacitance of $Pr_{0.02}Mn_{0.5}Co_{0.5}Fe_{1.98}O_4$ – Ti_3C_2 nanocomposite 1310.47 F/g at a current density of 2A/g and the retention rate is 75.6%. These findings confirm that the nanostructured composite is a strong candidate material for energy storage devices.

PAPER PUBLISHED AND COMMUNICATED

1. **Kiranjot Kaur,** Hamnesh Mahajan, Anjori Sharma, Ibrahim Mohammaed, Ajeet Kumar Srivastava, Deepak Basandrai, Manganese doped cobalt – nickel spinel ferrite via. sol-gel approach: Insight into structural, morphological, magnetic and dielectric properties, Journal of Material Research 38 (2023) 3837- 3849. https:// doi: 10.1557/s43578-023-01119-1
2. **Kiranjot Kaur,** Tchounak Tekou Carol Trudel, Kamlash Rani, Ajeet Kumar Srivastava, Deepak Basandrai, Crystal structure refinement, morphological, and magnetic properties of ternary nanohybrid $Pr_xMn_{0.5}Co_{0.5}Fe_{2-x}O_4$ ($0.00<x<0.04$) spinel ferrite, Inorganic Chemistry Communications 159 (2024) 111717.
3. PrMnCo-Ti3C2 MXene nanocomposite based supercapacitor for the optimization of electrochemical performance." Journal of Materials Science: Materials in Electronics 35 (2024) 1-21. https://doi.org/10.1007/s10854- 024-11972-3
4. **Kiranjot Kaur,** Hamnesh Mahajan, A.K. Srivastava, Deepak Basandrai. Sintering temperature impact on the structural-magnetic properties of the $Zn_{0.2}Mg_{0.8}Fe_2O_4$ spinel ferrite, AIP Conf. Proc., 2986, 030150, (2024). https://doi.org/10.1063/5.0193013.

5. **Kiranjot Kaur,** Hamnesh Mahajan, A.K. Srivastava, Deepak Basandrai. Role of rare earth Y- doped in $MnCoFe_2O_4$ ($0.00 < x < 0.04$) spinel ferrite electrode for high performance of supercapacitors, Mater. Today: Proc., 2023, (Communicated).

ORAL PRESENTATIONS

1. **Kiranjot Kaur,** Hamnesh Mahajan, A.K. Srivastava, Deepak Basandrai, Sintering temperature impact on the structural-magnetic properties of the $Zn_{0.2}Mn_{0.8}Fe_2O_4$ spinel ferrite, International Conference on Functional Materials, Manufacturing and Performances (ICFMMP-2022), 29-30th July 2022, Lovely Professional University, Punjab.

2. **Kiranjot Kaur,** Hamnesh Mahajan, A.K. Srivastava, Deepak Basandrai, Role of rare earth Y- doped in $MnCoFe_2O_4$ ($0.00 < x < 0.04$) spinel ferrite electrode for high performance of

supercapacitors, International Conference On Energy Materials and Rechargeable Batteries (ICEMRB)-2023, 19-22 December 2023, Manav Rachna University, Haryana.

POSTER PRESENTATION

1. **Kiranjot Kaur,** A.K. Srivastava, Deepak Basandrai, Structural and Magnetic Pr doped MnCo Spinel ferrite. International Conference on Molecules and Materials Technology (MMT-2023), 21st- 22nd April 2023, National Institute of Technology, Kurukshetra.

WORKSHOP

12th User Awareness Workshop on Fabrication Characterization Facility for Nanotechnology, 22-23 February (2024), IIT Delhi, India.

LIST OF SYMBOLS

Symbol	Description
ω	Angular frequency
K_1	Anisotropy constant
i_{pa}	Anodic peak current
E_{pa}	Anodic peak voltage
H	Applied magnetic field
N_A	Avogadro's number
μ_B	Bohr magneton
Θ	Bragg's angle
D_b	Bulk density
C	Capacitance
i_{pc}	Cathodic peak current
E_{pc}	Cathodic peak voltage
ΔE	Charge in energy
R_{ct}	Charge transfer resistance
H_c	Coercivity
A	Cross-sectional area
D	Crystallite size
I	Current
I_m	Current density
I(V)	Current response
I/E	Current to voltage converter
^oC	Degree Celsius
2θ	Diffraction angle
Δt	Discharging time
Δ	Dislocation density
L	Distance between electrodes
$\vec{E}$	Electrostatic field
E	Energy density
R_{ES}	Equivalent series resistance
Y	Frequency

B	Full width at half maximum
J	Imaginary number
Z	Impedance
L	Inductance
d	Interplanar spacing
a_o	Lattice constant
ε	Lattice strain
m	Loaded mass
M-H curve	Magnetic hysteresis curve
n_B	Magnetic moment
μ’	Magnetic permeability
M	Magnetization
M_B	Magnetization of octahedral site
M_A	Magnetization of tetrahedral site
m	Mass of pellets
hkl	Miller indices
MW	Molecular weight
Z	Number of molecules in the unit cell
υ_2	Octahedral band
B-site	Octahedral site
R_s	Ohmic resistance
1-D	One- dimensional
n	Order of the diffraction
%	Percentage
π	pi (3.14)
h	Planck constant
P	Porosity
ΔV	Potential window
P	Power density
r	Radius of pellet
M_r	Remnant magnetization
M_s	Saturation magnetization

υ	Scan rate
C_{sp}	Specific capacitance
S	Specific Surface area
R	Squareness ratio
V_1	Tetrahedral band
A-site	Tetrahedral site
t	Thickness of pellet
3-D	Three-dimensional
2-D	Two- dimensional
V	Voltage
V_{cell}	Volume of the unit cell
W	Warburg impedance
D_x	X-ray density
λ	Wavelength

LIST OF ACRONYMS AND ABBREVIATIONS

List of Acronyms and Abbreviations	Description
AC	Alternative Current
ASTM	American Standards for testing of Materials
AR	Analytical reagent
At.	Atomic
ATR	Attenuated total reflection
Via	By way of
CNT	Carbon nanotube tube
I-V	Current Voltage Characteristics
CV	Cyclic Voltammetry
EDLC	Electric double-layer capacitor
EIS	Electrochemical Impedance Spectroscopy
ESCs	Electrochemical Supercapacitors
EM	Electromagnetic
EDX	Energy dispersive X-ray analysis
Eq.	Equation
ESR	Equivalent series resistance
Etc.	Et cetera
Fcc	Face centered cubic
FESEM	Field emission scanning electron microscopy
Fig.	Figure
Eg.	For example
FTIR	Fourier transform infrared spectroscopy
GCD	Galvanostatic charge-discharge
HRTEM	High-resolution transmission electron microscopy
HC	Hybrid Capacitor
HMF	Hyperfine magnetic field
IR	Infrared
ICDD	International Center for Diffraction Data

IEA	International Energy Agency
JCPDS	Joint Committee Powder Diffraction Standards
LED	Light-emitting Diode
Ltd.	Limited
LSV	Linear Sweep voltammetry
MRI	Magnetic resonance imaging
MOF	Metal-organic framework
Min.	Minute
Mol.	Molecule
Viz.	Namely
NF	Nano ferrite
NSFs	Nano spinel ferrite
NC	Nanocomposite
NCs	Nanocomposites
NP	Nanoparticle
NPs	Nanoparticles
NFR	Natural ferromagnetic resonance
NMP	n-methyl-2-pyrrolidone
PANI	Polyaniline
Ppy	Polypyrrole
PVDF	Polyvinylidene fluoride
pH	Potential of hydrogen
PC	Pseudocapacitor
RE	Rare earth
rGO	Reduced graphene oxide
SEM	Scanning electron microscopy
SAED	Selected area electron diffraction
SS	Stainless steel
SC	Supercapacitor
SCs	Supercapacitors
i.e.	That is

TGA	Thermogravimetric analysis
TG-DSC	Thermogravimetry Differential scanning calorimetry
TG-DTA	Thermogravimetry – Differential thermal analysis
TEM	Transmission electron microscopy
UV-VIS	Ultraviolet-visible
VSM	Vibrating sample magnetometer
Wt.	Weight
XRD	X-ray diffraction
XPS	X-ray photoelectron spectroscopy

LIST OF UNITS

UNITS	Description
A	Ampere
Å	Angstrom
Cm	Centimeter
Cc	Cubic- centimeter
eV	Electron volt
Erg	Ergon
F	Farad
GHz	Giga- Hertz
G	Gram
H	Hour
K	Kelvin
Kg	Kilo-gram
KHz	Kilo- Hertz
Koe	Kilo- Oersted
kW	Kilo- Watt
MHz	Megha- Hertz
M	Meter
µHz	Micro- Hertz
µm	micrometer
mA	Milli-Ampere
mF	Milli- Farad
mL	Milli-liter
mm	Milli- meter
mV	Milli- Volt
mW	Milli- watt
mWh	Milli-Watt-hour
M	Mole
nm	Nano-meter
Oe	Oersted
Ω	Ohm

s	Second
S	Siemens
TWh	Tera- Watt-hour
W	Watt
Wh	Watt-hour

LIST OF FIGURES

LIST OF TABLES

Table of Contents

CHAPTER - 1

Introduction

1.1. Preamble

The world's growing population and modernization have created a global energy crisis, highlighting the need for sustainable and green energy. Fossil fuels are currently the main source used to satisfy humankind's energy needs; however, these resources are limited. Additionally, burning fossil fuels releases greenhouse gases, including nitrous oxide, carbon dioxide, and methane as well as other gases like hydrofluorocarbons and volatile organic compounds, which contribute to global warming [1] . Due to advancing technological innovations and evolving lifestyles, humans are rapidly depleting non-renewable energy resources on the planet, raising concerns about sustainability and life standards [2][3]. The rapid consumption of fossil fuels driven by high energy demand highlights the challenge of relying solely on limited fossil fuel resources to meet future energy needs as in Fig. 1.1. The depletion of fossil fuels and carbon emissions have harmful effects on the climate and ecosystem, which is a danger for future decades [4][5]. To overcome these impeding situations in the environmental and economic sectors, a radical change from the perspective of the energy crisis is required, along with progressive and visionary policy changes. Renewable energy resources have recently received considerable attention as potential solutions to the worldwide energy crisis [6]. Renewable energy does not harm the economic and environmental sectors. Renewable energy resources are typically associated with solar, wind, and hydrothermal energy sources. Over the last few decades, unprecedented energy migration into renewables has occurred. Every year, the demand for renewable energy systems reaches a new high. The rise of large-scale solar and wind plants is a positive step toward more cost-effective and environmentally friendly energy-harvesting initiatives [7]. Renewable energy sources cannot be utilized for commercial or residential purposes, because supply interruptions can result in massive losses. As a result, more efficient, cost-effective, and sustainable energy storage systems can reduce the massive consumption of these non-renewable energy sources. The development of high-end energy storage systems is necessary for efficient and sustainable energy usage. Energy storage systems are essential for maintaining a consistent and dependable energy supply to meet changing demands. Their significance has increased significantly due to their versatility, efficiency, and adaptability,

positioning them as a leading choice among different renewable energy storage technologies. Fig. 1.2 illustrates the current usage of energy storage and conversion devices. Fuel cells, batteries, capacitors, and supercapacitors. Li-ion batteries (LIB) are among the most popular energy storage systems [8][9]. LIBs have influenced the world by finding applications in electronic devices, EVs, and other areas, but their inherent flaws prevent them from being used in large-scale renewable-based power grids and large vehicles. Its hazardous nature and unavoidable deterioration also prevent its integration into large-scale utility systems [10]. In a conventional capacitor, maximum energy storage is not possible because of its small surface area [11]. All these storage systems have benefits and drawbacks depending on the territory in which they are installed. As a result, researchers have focused on identifying devices with high energy storage capacity and the ability to deliver maximum power. When compared with other energy storage systems, supercapacitors can deliver energy quickly and have a long lifespan [12]. Supercapacitors are used in various fields because of their distinctive and inherent benefits, including power grids, public transportation, and energy transportation systems. As a result, SCs are among the best candidates for all of the above energy storage devices.

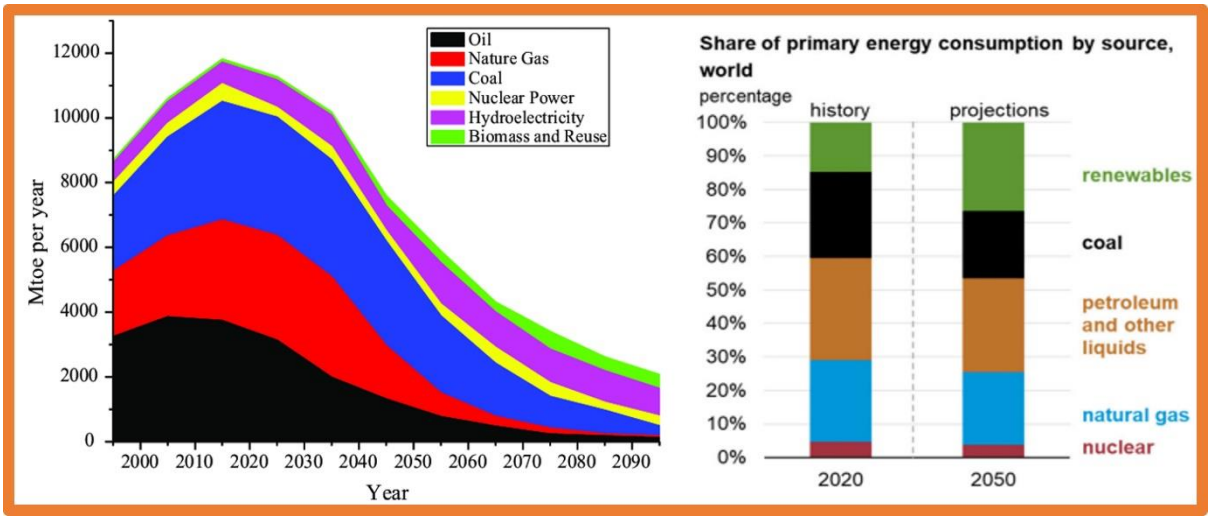

Fig. 1.1. Global energy usage from different resources [3].

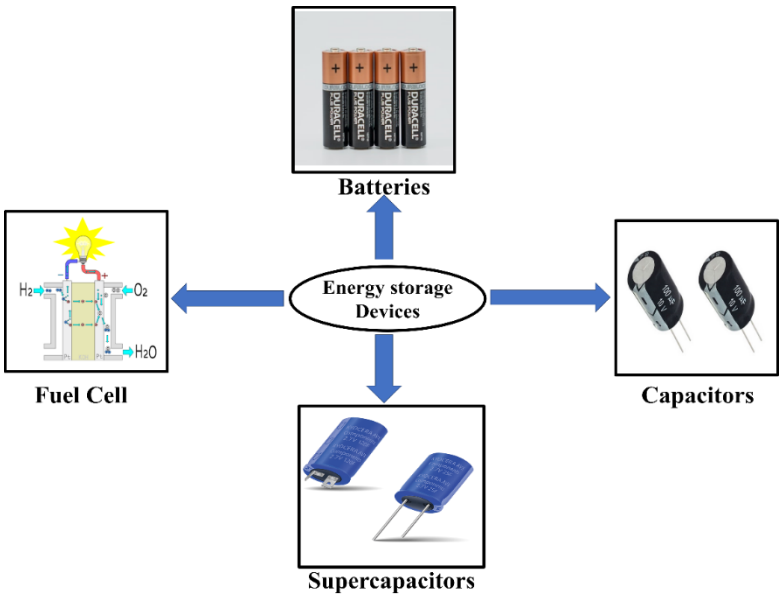

Fig. 1.2. Energy storage and conversion devices.

Fuel cells and batteries are mostly used for high-energy applications because of their low energy density (E). Some of their drawbacks include low power density (P), high cost, limited life cycle, difficulty in designing devices, and lack of safety [13][14][15]. Conventional capacitors have a high power density and long life cycle; however, they have a lower energy density than batteries and fuel cells [16]. As a result, electrochemical supercapacitors (ESCs) are considered to be one of the most intriguing energy storage technologies with the potential to bridge the gap between batteries and conventional capacitors, as seen in the Ragoen plot (energy density vs. power density) of energy storage devices Fig. 1.3. A supercapacitor has a high energy density than a capacitor and high power density than a batteries and fuel cell.

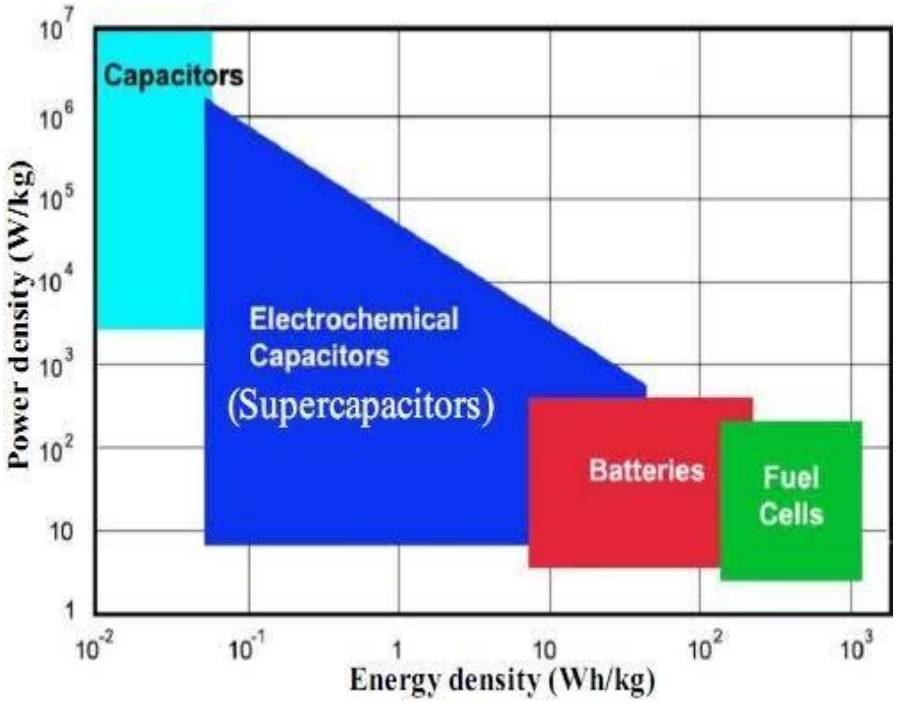

Fig. 1.3. Ragone plot of specific power versus specific energy for supercapacitors [16].

Table 1.1 Basic characteristics of conventional capacitors, batteries, and supercapacitors

Parameters	**Conventional capacitors**	**Batteries**	**Supercapacitors**
Charge time	10^{-6} – 10^{-3} s	0.3 – 3h	1 - 30 s
Discharge time	10^{-6} – 10^{-3} s	1–4 h	1 - 30 s
Energy density (Wh/kg)	<0.12	10 – 100	1-10
Power density (W/kg)	>10,000	50 – 100	1000 – 2000
Cycle life	>500,000	500 – 2000	>100,000
Charge/discharge efficiency	~1.0	0.7 – 0.84	0.90–0.96

As shown in Table 1.1, shows supercapacitors, are associated with higher cyclic life of more than 50,000 cycles than batteries (150-1500 cycles) and enhanced ED (1-10 Wh kg^{-1}) than conventional capacitors (0.01-0.05 Wh kg^{-1}). Electrochemical supercapacitors (ESCs) have superior energy and power density, rapid charge-discharge rate, excellent cyclic life, superb

reversibility, longer life cycle stability, fast dynamic response, minimum equivalent series resistance (ESR), economic feasibility, pliability, high efficiency, and operational safety. Because of the aforementioned characteristics of ESCs, they seem to be used in laptops, mobile phones, smartwatches, memory backups, notebook computers, digital cameras, electric and hybrid electric vehicles, energy power systems, urban rail transit, toys, headphones, calculators, and so on [1][17].

1.2. Supercapacitor

Ultracapacitors, also referred to as supercapacitors or SCs, are capacitors designed with enhanced capacitance and energy density compared to conventional capacitors. They can store capacitance ranging from tens to thousands of farads and demonstrate impressive durability by enduring thousands of charge-discharge cycles without experiencing failure, despite their inability to retain a large charge quantity [18]. SCs operate similarly to an electrochemical device and share similarities with electrolytic capacitors. However, unlike electrolytic capacitors, SCs store electric energy without involving any chemical reactions. They can store significant amounts of charge [19]. The construction of SCs bears resemblance to that of electrolytic capacitors, incorporating porous electrodes (cathode and anode), an electrolyte, and a separator, all of which are illustrated in the diagram Fig. 1.4. SCs rely on solid, liquid, or gel electrolytes that are crucial for their redox processes. A separator, such as a paper membrane, is employed to maintain separation between the electrodes, enabling charge carriers to pass without creating short circuits. The method by which SCs store charge differs significantly from that of conventional capacitors [20]. In conventional capacitors, charge storage is attributed to the polarization of the dielectric material. Unlike in SCs, the electrolyte doesn't function as a dielectric; its main role is to provide charge carriers to the electrodes. However, charge accumulation on the electrodes happens due to the accumulation of opposite charge carriers. The electrolyte's impact is on the internal or equivalent series resistance (ESR) of SCs. As per Eq. (1.1), an increase in the power density (P) of SCs corresponds to a decrease in the electrolyte's resistance (R) [21].

$$P = \frac{V^2}{4R_{ES}} \qquad (1.1)$$

Here, P represents the power density, V signifies the applied voltage, and R denotes the equivalent series resistance [20].

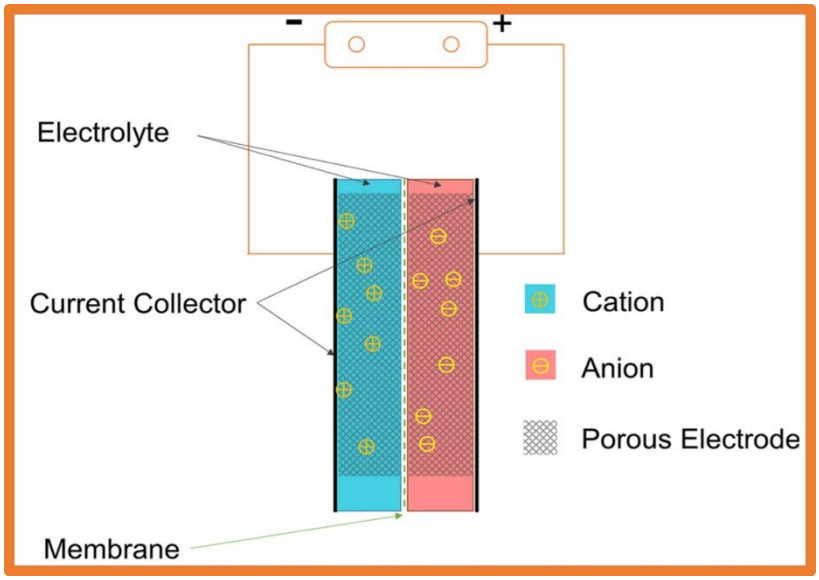

Fig. 1.4. Construction of a Supercapacitor [22].

1.2.1. Principle and Operation of the Supercapacitor

The energy storage mechanism of supercapacitors (SC) can rely on either the electrochemical interaction between the electrode and electrolyte or the transfer of charge to the redox molecule layer located on the electrode's surface. [23]. The setup includes two porous or permeable electrodes divided by a paper membrane, called a separator, that separates the positive and negative plates. Both terminals are linked electrically to an ionic liquid known as the electrolyte. Applying a voltage to the positive electrode attracts negative ions from the electrolyte, while the negative electrode draws positive ions. These ions accumulate on the electrodes' surfaces, reducing the distance (l) between them. [24]. As per Eq. (1.2), the high capacitance (C) of supercapacitors results from the inverse relationship between C and the distance (l) separating the electrodes, with A representing the cross-sectional area between the two electrodes[25].

$$C = \frac{\varepsilon_o A}{l} \qquad (1.2)$$

An electrostatic field ($\vec{E}$) forms between the current collectors due to the accumulation of opposing charges. The supercapacitor (SC) charges until the current collectors achieve balance and counteract the applied voltage. When the supply voltage decreases or switches polarity, the current collectors hold onto charge carriers. As the supplied voltage decreases, the current collectors release a proportional amount of charge carriers back into the electrolyte. This

process involves an equivalent current flowing in the opposite direction through the supercapacitor [26]. The supercapacitor (SC) went through a comparable cycle of charging and discharging after the polarity shifted, as illustrated in Fig. 1.5. The specific capacitance (C_s) and energy density (E) of a supercapacitor (SC) is ten times higher than those of an electrolytic capacitor, and a hundred times higher than those of an electrostatic capacitor [27][28].

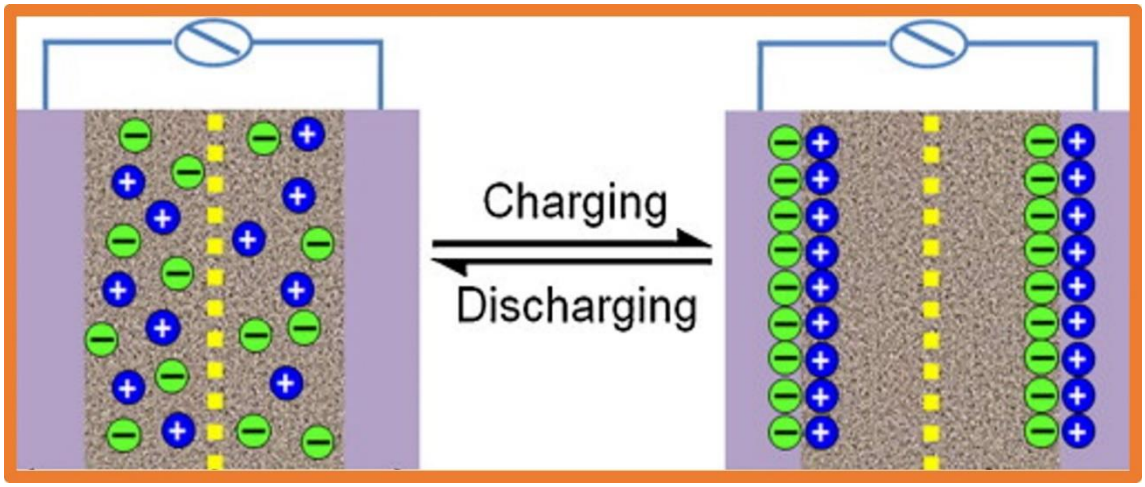

Fig. 1.5. Working of the supercapacitor [29].

1.2.2. Classification of Supercapacitors

Supercapacitors are classified into three types based on their charge-storage mechanism, Electrical double-layer capacitors, Pseudocapacitors, and Hybrid capacitors as shown in Fig. 1.6.

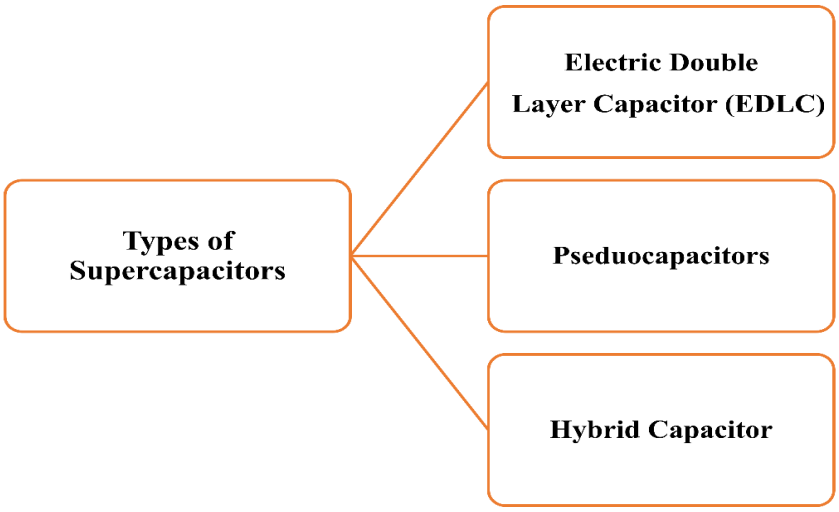

Fig. 1.6. Types of supercapacitors.

1.2.2.1. Electric Double-Layer Capacitor (EDLC)

The electric double layer stores charges at the electrode-electrolyte interface regions. In EDLCs, a large number of charges can be stored because of the large surface area of the electrode. An electrochemical double layer (EDL) is formed at the electrode-electrolyte interface and the atomic range of distance between the electrodes. EDLCs exhibit excellent electrical conductivity, which helps reduce the internal resistance of the electrodes. In addition, the electrolyte provides good wettability, which helps enhance the ion mobility, thereby increasing the capacitive performance [30]. The EDLC stores charges based on the formation of EDL at the interface, which prevents the recombination of ions. In the 19th century, the concept of EDLC formation was first introduced by von Helmholtz. He proposed that when an electrically charged surface is immersed in an electrolyte solution, counterions are attracted to it, while ions with the same charge are repelled. The electrical double layer was composed of a layer formed on the surface of the electrode and a layer formed near the electrode surface with counter ions in the electrolyte [31]. The formation of the EDLC using the Helmholtz model is shown in Fig. 1.7a. The Helmholtz model is similar to that of the conventional capacitor with the distance between the parallel plates as ‘d’, which is approximated to be the radius of the ion. Gouy and Chapman further enhanced the Helmholtz model by considering the continuous distribution of ions in an electrolyte. The Gouy– Chapman model considers the continuous movement of ions in the electrolyte and the combined effects of ion diffusion and electromigration [32]. This is referred to as the ‘diffuse layer, as shown in Fig. 1.7b. However, this model overestimates the EDL capacitance because it considers the ions in the electrolyte as

point charges, resulting in an unrealistic concentration of ions on the electrode. In 1924, Stern proposed a new model by combining the Helmholtz and Gouy–Chapman models. He distinguished two areas: i) the inner region, known as the stern layer, and ii) the diffuse layer, as shown in Fig. 1.7c. Because the electrode has strongly adsorbed ions, the inner region is also known as a compact layer. The stern layer is composed of specifically adsorbed ions and non-specifically adsorbed counter ions. The inner Helmholtz plane (IHP) and outer Helmholtz plane (OHP) were used to distinguish the two types of adsorbed ions. The Gouy– Chapman model is defined by the second region, known as the diffuse region [33].

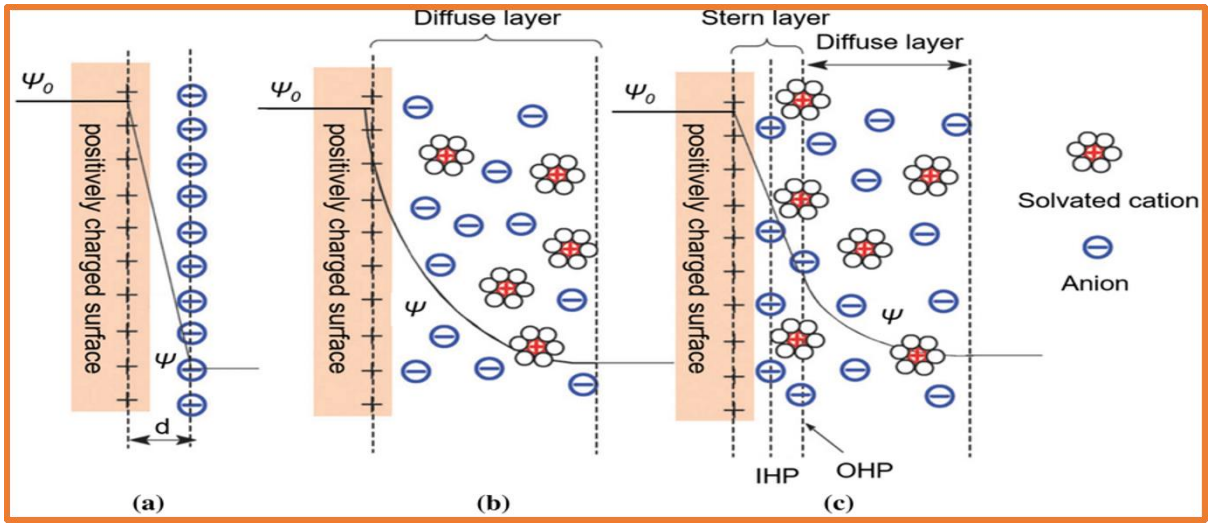

Fig. 1.7. Models of the electrical double layer (a) Helmholtz model, (b) Gouy– Chapman model, and (c) Stern model [34].

Electric double-layer capacitors (EDLC) use carbon-based materials, such as carbon fiber cloth, carbon aerogel, carbon nanotubes, graphene, and activated carbon, as active materials for electrodes, separators, and electrolytes. In EDLCs, charge storage occurs electrostatically in which charge is stored on the surface of the electrode. When a voltage is applied to an electrode, charge accumulates on its surface, and ions in the electrolyte solution begin to diffuse across the separator into the pores of the electrode with the opposite charge [35]. The design of the electrode prevents ion recombination, resulting in a double charge layer at each electrode. The development of a double layer, together with an increase in surface area and a reduction in the distance (d) between the two electrodes, culminates in an EDLC with a higher energy density (E) than a conventional capacitor [36].

1.2.2.2. Pseudocapacitor

Pseudocapacitors store charges based on the exchange of charges between the electrolyte and the electrode. The transfer of charges is done through electron absorption, reduction-oxidation process, and through intercalation of ions [37]. Applied with a potential, a current is produced in the cell through Faradaic reactions wherein charge transfer takes place at the double layer. The Faradaic reactions allow the pseudocapacitor to achieve higher capacitance and energy density than that of EDLCs. Since pseudocapacitors involve Faradaic reactions in charge storage similar to that of batteries, they lack cyclic stability and possess lower power density than that of EDLC. Conducting polymers and Metal oxides constitute the electrode materials used in pseudocapacitors [38].

1.2.2.3. Hybrid Capacitors

Hybrid capacitors combine the advantages of both EDLC and pseudocapacitors, thereby providing an improved performance. They combine faradaic and non-faradaic processes to provide better performance than other types of supercapacitors. Thus, hybrid capacitors exhibit greater energy density than EDLCs while overcoming the cyclic stability and affordability issues of pseudocapacitors [39].

1.3. Supercapacitor Construction

There are various methods for fabricating and constructing supercapacitors. The cell components of the supercapacitors were similar to those of the batteries. The fabrication of the supercapacitor consisted of three major parts, as described below.

1.3.1. Electrode
1.3.2. Electrolyte
1.3.3. Current Collector
1.3.4. Separator

1.3.1. Electrode Materials for Supercapacitors

The electrode materials have a major impact on the supercapacitors' (SCs) electrochemical performance. Electrochemical performance depends upon various factors such as Specific surface area, surface functionality, pore size distribution, and pore shape to achieve these factors different electrode materials are used such as carbon-based materials, metal oxides, transition metal dichalcogenides, and conducting polymers [40].

1.3.1.1. Carbon-Based Materials

In the charge storage mechanism, carbon materials are utilized to produce an electrochemical double layer at the electrode-electrolyte interface. For the fabrication of the carbon-based electrode material was broadly used viz. carbon nanotubes, carbon aerogel, activated carbon, carbon fiber cloth, graphene, etc. These materials have a large specific surface area, pore size, minimal cost ratio, well-established electrode fabrication technology, and easy availability. As a result, the capacitance of carbon-based materials is primarily determined by the surface area available to electrolyte ions. The large specific surface area of carbon materials leads to a high capacity for charge accumulation at the electrode-electrolyte interface. Surface functionalization must be addressed when enhancing the specific capacitance (C_{sp}) of carbon materials, in addition to pore size and high specific surface area [41]. Carbon-based SC electrodes with high conductivity and stability typically offer high cyclic stability and power density (P). However, for energy storage, carbon electrodes for SCs have drawbacks, such as low energy density (E) [42].

1.3.1.2. Metal Oxides

Electrodes made of metal oxides also store energy based on redox reactions and thus exhibit improved capacitance to that of EDLCs. Metal oxides are abundant in nature, easy to synthesize on a large scale, and are of low cost. The morphology, size, and orientation of these nanostructures can be easily tuned. Ruthenium oxide (RuO_2) is the most widely explored material for supercapacitors due to its high capacitive nature with a specific capacitance of over 700 F/g. The capacitance exhibited by hydrous RuO_2 is higher when compared to the carbonaceous electrodes and conducting polymers. Also, its ESR is very less compared to other electrodes. However, the success of RuO_2 is affected due to its high cost. Thus, research went on to focus on other metal oxides such as MnO_2, V_2O_5, Fe_3O_4, Co_3O_4, CuO, SnO, TiO_2, NiO_x, ZnO, and many more [43]. However, most of the metal oxides other than RuO_2 usually experienced a breakdown in acidic electrolytes like H_2SO_4 and thus were used in other milder electrolytes like potassium chloride. An immediate alternative to RuO_2 was MnO_2 which garnered attention due to its low cost, non-toxicity, and natural abundance [28]. Though many metal oxide nanostructures were explored as supercapacitor electrodes, they faced issues of low energy density and poor conductivity when compared to RuO_2. Most of the oxides belong to the class of wide bandgap semiconductors or insulators and hence exhibited poor conductivity. This poor conductivity exhibited by various transition metal oxides, severely limits their

practical applicability, especially at fast scan rates. Thus, research progressed in finding cheaper and more efficient materials with good conductivity and capacitance. These problems can be eliminated using aluminate (MAl_2O_4), and spinel ferrite (MFe_2O_4) [44]. These mixed metal oxides have been considered the best contenders for SCs because they have excellent electrochemical performance owing to the synergetic impact of different metal cations. Metal oxides are spinel ferrite (MFe_2O_4), and have astonishing properties, such as electrochemical stability, exhibiting different oxidation states, and electronic, magnetic, and optical properties. Furthermore, these spinel ferrites are easily available, have massive productivity, low cost, and are convenient to synthesize on an industrial scale [45].

1.3.1.3. Conducting Polymers

Conducting polymers (CPs) are widely used as supercapacitor electrodes as they have low ESR and cost, easy synthesis methods, and higher capacitance and conductivity than carbonaceous electrode materials. CPs possess large surface area and store charges based on redox reactions due to which they exhibit higher capacitance than EDLCs. During oxidation (doping), ions get transferred from the solution to the polymer support and during reduction (de-doping), the ions are released back to the solution. In conducting polymers, the charging occurs throughout the volume of the material and not just only onto the surface, unlike carbon materials. CPs lack an efficient n-doped material which has greatly hindered them from reaching their potential. Also, the oxidation and reduction reactions that happen in CPs, cause mechanical stress in them leading to poor cyclic stability. Polyaniline (PANI), polypyrrole, and poly-(3,4-ethylene dioxythiophene) or PEDOT are the commonly used conducting polymers in pseudocapacitors [46][47].

1.3.1.4. 2D material

Supercapacitors with conventional pseudocapacitive electrode materials can achieve a significant energy density compared to EDLC. The commercial realization of these material-based supercapacitors is hampered by their poor electrochemical stability during long cycles, volume expansion due to slow ionic transfer, and low inherent electrical conductivity. The emergence of 2D materials has created a new horizon of energy storage applications. 2D materials are materials with atomic (or few atoms) thicknesses that exhibit enthralling properties compared to their bulk form. Emerging 2D materials have gained a lot of attention as supercapacitor electrodes due to the large surface area in which all atoms are exposed for electrochemical reactions. The confinement of electron motion in one direction provides ultra-

high electronic conductivity to 2D materials [48]. The high mechanical stability, high surface area, good electron transfer, and flexibility of 2D materials allow them to be used in new-generation flexible and wearable energy storage systems, as depicted in Fig. 1.8. The open van der Waals (vdW) structure in 2D materials enables the intercalation/deintercalation of electrolyte ions. Since the discovery of graphene, numerous two-dimensional (2D) materials with intuitive properties have been reported. Transition metal dichalcogenides (TMDs) are emerging post-graphene 2D materials. TMDs are a few atoms thick 2D materials with unique electronic and mechanical properties and variable oxidation states suitable for supercapacitor electrodes. 2D transition metals show excellent energy storage capability compared to their bulk counterparts. MXene is a relatively recent discovery in the 2D material pantheon. MXene has excellent electronic conductivity, a large surface-to-volume ratio, superior electron mobility, ultra-high mechanical flexibility, and more electrochemical active sites, making it an interesting 2D material showing both surface-bound redox pseudocapacitance and intercalation pseudocapacitance [49]. Close packing of MXene sheets tends to hinder the movement and diffusion of electrolyte ions, particularly organic electrolyte ions, that influence the energy storage performance of MXenes in supercapacitors and hinder their excellent electrochemical performance [50]. This could be overcome by making them composite with other materials, such as metal oxide–carbon, conducting polymer–carbon, metal oxide–conducting polymer, and metal oxide–2D materials, spinel ferrite - 2D material (Ti_3C_2) NC was chosen for PC electrodes [51].

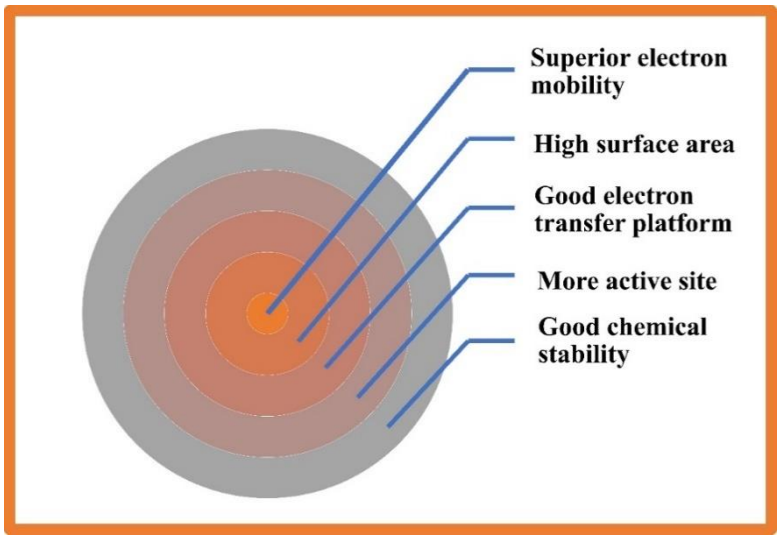

Fig. 1.8. Advantages of 2D materials.

1.3.2. Electrolyte

Electrolytes are the major key components of supercapacitors, which are responsible for the ionic conductivity in the cell. The nature of the electrolyte concerning the type and size of the ion, concentration of ions, interactions between the solvent and ion, interactions between the electrode and the electrolyte, and potential window play key roles in determining the capacitance, cycle life as well as energy and power densities of the supercapacitor. Broadly, the electrolytes can be grouped as liquid and solid/quasi-solid electrolytes. While liquid electrolytes are widely explored for supercapacitors, it is the solid-state electrolytes that are being used commercially in flexible devices, portable electronics, wearable and printable electronics [52]. Liquid electrolytes can be further grouped into aqueous and non-aqueous electrolytes. Examples of aqueous electrolytes include H_2SO_4, KOH, and Na_2SO_4. These electrolytes are extremely safe, as compared to organic electrolytes. However, in terms of the potential window range of organic electrolytes 2.5 to 2.8 V are the more dominating one in comparison to aqueous electrolytes having a potential range of 1.23 V. But with high operating potential, they face issues of high cost, highly flammable, and toxicity, [53].

1.3.3. Current Collector

Supercapacitors need current collectors to enhance the overall performance as the active materials lack adequate conductivity. The main aim of the current collector is to help in the transfer of current from the electrodes to the external load. Thus, they have to be highly conductive and must be able to withstand the chemical effects of the electrolytes. Usually, aluminum, nickel, stainless steel, and copper foils are used as current collectors. Recently, nickel foams and graphite foams have been highly useful as current collectors in energy storage devices. The active electrode materials will be coated onto the current collector to create a firm contact between the two thereby minimizing the interfacial resistance [54].

1.3.4. Separators

A barrier between the two electrodes is created through a separator which helps in preventing an electrical contact between them. The separator allows the permeation of ions through them thereby allowing charge transfer of ions. Careful engineering of separators is necessary as they can create a negative influence on the performance of the supercapacitor. Improper separators can create additional resistances and cause a short circuit in the cell. Initially, glass, paper, glass fiber, and ceramics were used as separators but with the evolution in polymer materials, polymer-based separators are being used widely. The separator should be

nonconductive, and chemically inert to electrolytes and electrodes. The separator should be mechanically stable, and thin for better performance of the supercapacitor [55].

1.4. Ferrite

William Gilbert presented the first magnetic substance for use as a compass as an iron needle in CE 1600 [56]. Ferrites are a kind of ferrimagnetic oxide in which iron, denoted by the chemical symbol 'Fe,' is the primary component. Ferrites are polycrystalline, nonconductive, and occur naturally in shades of grey and dark brown. Several essential criteria, including crystallite, grain and particle size, dopant distribution, manufacturing procedures, calcination and sintering temperatures, and many more, contribute to ferrites' exceptional electrical and magnetic properties in both the bulk and nanoscale ranges. It is important to note that ferrite-based nanomaterials are both scientifically and technologically significant because they have a wide range of applications in various fields of research, including MRI (Magnetic Resonance Imaging), telecommunication industries, cancer treatment, rod antennas, sensors, choke coils, and other similar applications [57]. As a result of all of these many uses, ferrites have been dominating the market of material scientists for a long length of time. Ferrites may be manufactured using a variety of processes, including coprecipitation, sol-gel, auto-combustion, hydrothermal, and the citrate-precursor approach. In terms of nanomaterials synthesis techniques, the sol-gel auto-combustion approach is one of the most successful since it allows for precise control over the particle size of nanoparticles while being cost-efficient [58].

1.4.1. Classification of Ferrites based on Coercivity

In general, ferrites are categorized into two types based on their coercivity:

1.4.1.1. Soft Ferrites

Soft ferrites are generally known as spinel ferrites. These ferrites are easily magnetized and demagnetized. The general formula for spinel ferrites is $MeIIFe_2(III)O_4$ where MeII represents divalent metal ions like Ni, Mn, Cd & Mg, etc. and FeIII is a trivalent iron cation. The soft ferrite unit cell has a cubic structure and comprises $MeOFe_2O_3$ molecules in which oxygen anions form an FCC packing with 64 tetrahedral (A) and 32 octahedral (B) vacant spaces that are partially filled by Fe^{3+} and Me^{2+} cations. Magnetic recording media, computer memory chips, microwave devices, radio frequency, and electronic engineering are only a few of the applications for such materials. Among all of these applications, antenna shrinking has recently piqued the interest of numerous academics. Because soft ferrites have low coercivity,

their magnetization can reverse easily without wasting a lot of energy. Soft ferrites are prominently used in inductors and transformers [59].

1.4.1.2. Hard Ferrites

Hard ferrites have a high coercive field, i.e. the coercive field (H_c) from 10 Oe to 100 Oe, and are used for permanent magnet applications. They have high density and achieve fine grain size. These ferrites are also known as hexagonal ferrites. Hexagonal barium ferrite is mostly used in permanent magnets, microwave devices, and magnetic recording media due to its high coercivity, high saturation magnetization, good chemical stability, and corrosion resistance. Hard magnetic materials have magnetic properties like high coercivity, large magnetization, and broad hysteresis loop which shows that hexaferrite is ferrimagnetic in nature [60].

1.4.2. Classification of Ferrites

The crystal structure of the ferrites can be used to categorize them, as per most investigations conducted on ferrites by the researcher's group. Subsequently, ferrites are categorized into four main types: spinel, hexagonal, garnet, and ortho, as illustrated in Fig. 1.9.

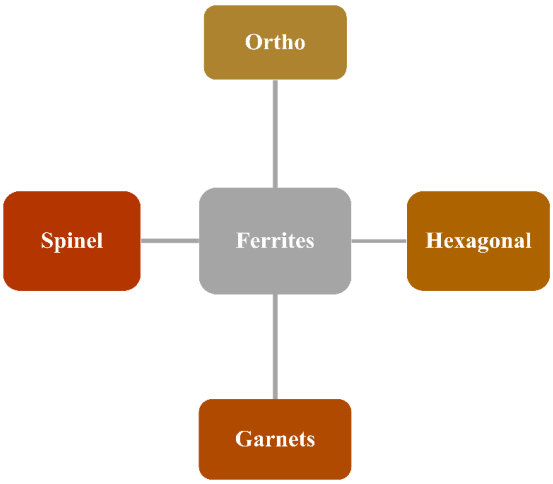

Fig. 1.9. Classification of ferrites.

1.4.2.1. Spinel Ferrite

The structure of SFs as possessed by $MgAl_2O_4$ was first determined by Bragg and Nishikawa in 1915 [61]. The spinel structure is derived from the mineral spinel ($MgAl_2O_4$ or $MgO{\cdot}Al_2O_3$), Analogous to the mineral spinel, the general formula MFe_2O_4, where M is the divalent metal cation (Mn, Mg, Co, Ni, Zn) [62][63]. The smallest cell of the spinel lattice with cubic symmetry contains eight "molecules" of MFe_2O_4. The crystal structure of spinel ferrite is face-centered cubic (fcc) with space group Fd-3m.[64].

1.4.2.2. Hexagonal Ferrite

Hexaferrites were first discovered in 1930. Hexaferrites exist in the natural state of lead ferrite. It is also known as a magnetoplumbite. The molecular representation of hexagonal ferrite molecular representation is $MFe_{12}O_{19}$ where M = Ba, Sr, and Pb. Fig.1.10 represents the structure of hexagonal ferrite. Several isomorphous compounds have been suggested, including $BaFe_{12}O_{19}$, and $SrFe_{12}O_{19}$. $BaFe_{12}O_{19}$ and $SrFe_{12}O_{19}$ were found to have a hexagonal crystal structure with two lattice parameters: a and c, where a is the width of the hexagonal plane and c is the height of the crystal. These ferrites are permanent magnet materials [65].

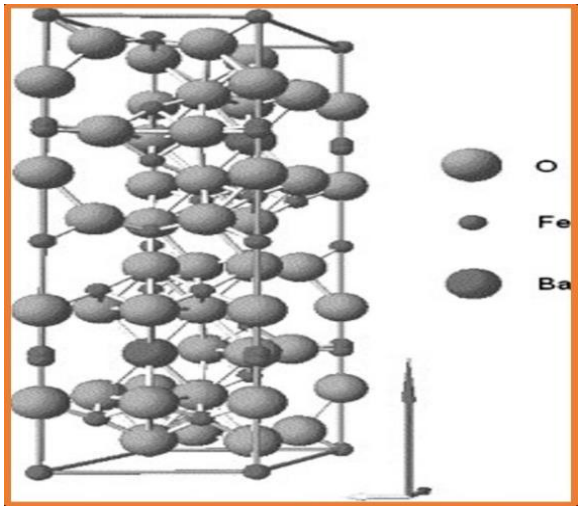

Fig. 1.10. Structure of Hexagonal Ferrite [66].

1.4.2.3. Garnets Ferrite

Garnet ferrite's chemical composition is $M_3(Fe_5O_{12})$ in which M is rare earth metal ions such as Y, Sm, Tb, Eu, and so forth as in Fig. 1.11. with a structure that is comparable to the structure of the silicate mineral $Ca_3Fe_2(SiO_4)_3$. As a result, only metal ions with an oxidation

state of +3 are found in this form of ferrites. The crystalline structure of garnet ferrite is very complicated and consists of eight formula units of $M_3(Fe_5O_{12})$, as well as an edge length that is about equivalent to 12.5Å, which makes it a good candidate for use in the research field of memory storage [67].

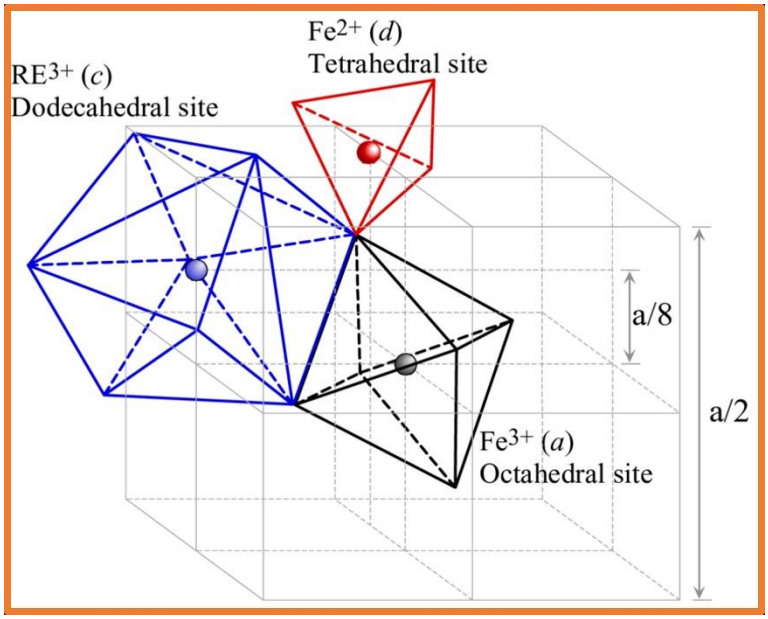

Fig. 1.11. represents the Garnets Ferrite [68].

1.4.2.4. Ortho Ferrite

Ortho ferrites are ferrites with the chemical composition $MFeO_3$ where M is a rare earth metal ion (Gadolinium and many others) that exhibits multiferroic properties. It has been concluded that these types of materials exhibit more than ferroic characteristics, such as ferroelectricity, ferroelasticity, and so on, and are therefore referred to as such. Bertaut and Forrat, two well-known scientists, were the first to explain the structure of ortho ferrites in their original work. Bismuth ferrite with a perovskite structure is a typical example of ortho ferrites, which are composed of a variety of ferroic characteristics that vary from one another [69]. Fig. 1.12 represents the Ortho Ferrite Structure.

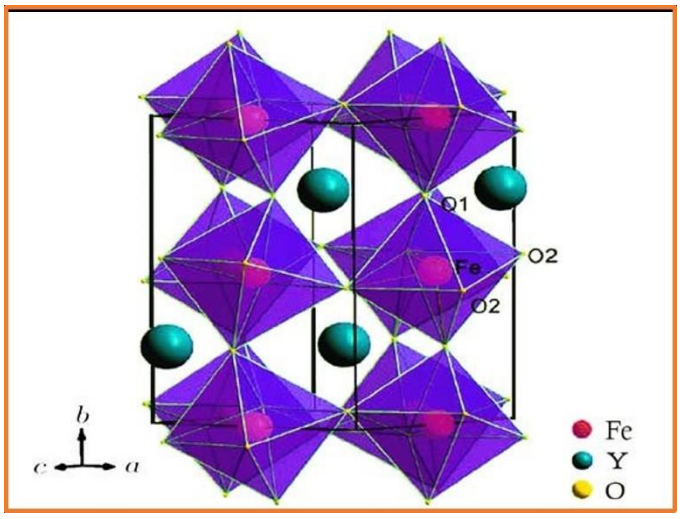

Fig.1.12. represents the Ortho Ferrite [70].

1.4.3. Superiority of the Spinel Ferrites

However, the above ferrites scientist shows immense interest in the spinel ferrite due to the immense scope of utilization in high-performance energy storage supercapacitors (SCs). Spinel ferrites are desirable because of their multiple redox sites, electrical and optical properties, and stability during electrochemical conversion. It is believed that the spinel ferrites will demonstrate a richer redox chemistry due to the contribution from the M and Fe ions than the single metallic oxides in electrochemical reactions. Many ferrites show their superior electrochemical properties due to the multiple vacancies of the divalent transition metal ions. This contribution of the metallic cations makes them catalytically active on the electrode surface, which improves the electrochemical properties. So, the addition of more divalent ions in the spinel ferrites will significantly enhance the electrochemical properties of these spinel ferrites and can uplift the capacitance of energy storage devices [71][72].

1.4.4. Crystal Structure of Spinel Ferrite

Bragg and Nishikawa first discovered spinel ferrite. Spinel ferrite contains eight small unit cells of MFe_2O_4, where M is divalent cation Mn, Zn, Mg, Ni) [73]. The structure of the spinel ferrite unit cell contains 32 closely packed oxygen anions. The arrangement of oxygen anions in a face-centered cubic structure, with two types of voids present between them:

Tetrahedral site or A site, which is surrounded by 4 oxygen anions, and B or octahedral site, which is surrounded by 6 oxygen anions. The spinel ferrite unit cell contains 64 tetrahedral sites, 8 of which are occupied, and 32 octahedral sites, 16 of which are occupied. The two neighboring octants are depicted in the ionic circumstance, the left side octant showing A or tetrahedral site and the octant on the right showing B or octahedral site. Each octant in spinel ferrite has 4 oxygen anions on the body diagonals and at the tetrahedron's corners [74]. Fig. 1.13 shows the crystal structure of spinel ferrite.

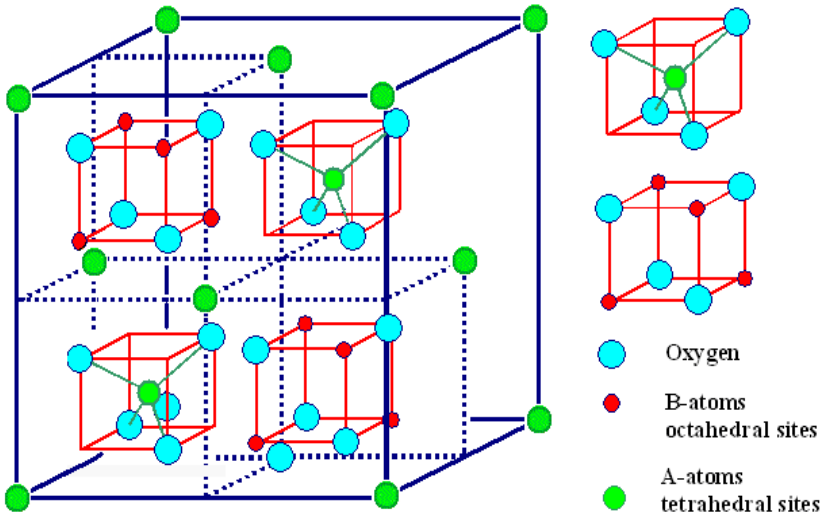

Fig. 1.13. Structure of spinel ferrite [74].

1.4.5. Classification of spinel ferrite

The general formula for spinel ferrite is $M_x^{2+}Fe_{1-x}^{3+}[M_{1-x}^{2+}Fe_{1+x}^{3+}]O_4^{2-}$. The cations that are outside the square bracket are represented by A or tetrahedral sites, and the cations that are inside the square brackets are represented by B or octahedral sites. According to the arrangement of the cations A- site, and B- site, the vacant space and filling space of the spinel ferrite are categorized into three different types [75]. Here, x is the inversion factor that determines the classification of spinel ferrites, as shown in Fig. 1.14.

1.4.5.1. Normal Spinel Ferrites

1.4.5.2. Inverse Spinel Ferrites

1.4.5.3. Mixed Spinel Ferrites

Table 1.2 Classification of the Spinel Ferrite

Type of Spinel Ferrite	Cation Distribution	Example	References
Normal Ferrite	$M^{2+}{}_A\,[Fe^{3+}]_BO^{2-}$	$CdFe_2O_4$ and $ZnFe_2O_4$	[76][77]
Inverse Ferrite	$Fe^{3+}{}_A\,[M^{2+}Fe^{3+}]_B\,O^{2-}$	$CoFe_2O_4$ and $NiFe_2O_4$	[78]
Mixed Ferrite	$M1\text{-}x^{2+}\,Fe_x{}^{3+}{}_A[M_x{}^{2+}\,Fe2\text{-}\,x^{3+}]BO4^{2-}$	$CuFe_2O_4$, $MgFe_2O_4$	[79]

1.4.5.1.Normal Spinel Ferrite

In normal spinel ferrites, A-sites and B-sites are distributed by divalent and trivalent ions, respectively, where M is the divalent metal ion such as $CdFe_2O_4$ and $ZnFe_2O_4$ [76].

1.4.5.2. Inverse Spinel Ferrite

In inverse spinel ferrites, divalent ions go to B-sites, whereas trivalent ions are evenly distributed across A and B-sites, where M is the divalent metal ion. Examples of such ferrites are $CoFe_2O_4$ and $NiFe_2O_4$ [78].

1.4.5.3. Mixed Spinel Ferrite

In mixed spinel ferrites, A-site and B-site cations are randomly distributed depending on the physicochemical circumstances of preparation and sintering. $M_{1-x}{}^{2+}\,Fe_x{}^{3+}{}_A[M_x{}^{2+}\,Fe_{2-x}{}^{3+}]_BO_4{}^{2-}$, is the cation distribution for random spinel ferrite, where M is the divalent metal ion and x is the degree of inversion. $0 < x < 1$ represents random spinel ferrite, 1 represents normal spinel ferrite, and 0 represents inverse spinel ferrite. $CuFe_2O4$, $MgFe_2O_4$, and other oxides are examples of mixed spinel ferrites [79].

1.5. MXenes

Two-dimensional materials are only a few atomic layers thick and have extremely high aspect ratios, they have piqued the researchers' intense attention. Since the discovery of all 2D materials graphene has been comprised of atomically connected plane bonds of sp^2 carbon atom, in a single layer. MXenes, relatively new members of 2D materials, have posed several fascinating concerns to scientists because of their unique properties. Because of their ceramic composition, they are chemically and mechanically stable. Structurally, MXenes exist in monolayer and multilayer forms with a significantly larger interlayer spacer than graphite, and the thickness of the MXene layer is controllable. Ions of different sizes can be injected into the space between the layers because it is capable of ion intercalation. Because the layered structure is partially delaminated, intercalation and electric double layers (EDL) formation, contribute to charge storage in supercapacitors [80]. MXene layer interactions are mainly determined by hydrogen bonding and van der Waals interactions. The presence of functional groups as surface terminations provides a plethora of options for designing surfaces with desirable electrochemical, thermoelectric, and dielectric properties [81].

In 2011, MXenes was discovered at Drexel University by Barsoum and Gogotsi. The $M_{n+1}AX_n$ formula for ternary carbides and nitrides is well known with the presence of early transition metal (Sc - Ta) represented as M, A stands for an alkali metal (Al), a silicon metal (Si), a lead metal (Pb), X stands for a carbon or nitrogen atom, where, n can be 1, 2, or 3 to create layered structures with anisotropic characteristics. Fig. 1.15 shows A-group element layers are interweaved in the m6X octahedrons as layers of edge. The thickness of $M_{n+1}X_n$ changes depending on the value of n; n=1 results in 211 phases with consists of a single block of octahedral (3 atoms thick), and N+2 results in 413 phases with 3 blocks of octahedral. More than sixty pure different MAX phases are known so far. Conversely, various combinations of M atoms viz., ($Ti_{0.5}$, $Nb_{0.5}$) AlC, A atoms viz., $Ti_3(Al_{0.5}, Si_{0.5})$ C_2 and X Sites and viz., Ti_2Al ($C_{0.5}$, $N_{0.5}$) which has a quite large potential number may be adopted for the synthesis of MAX phases [82].

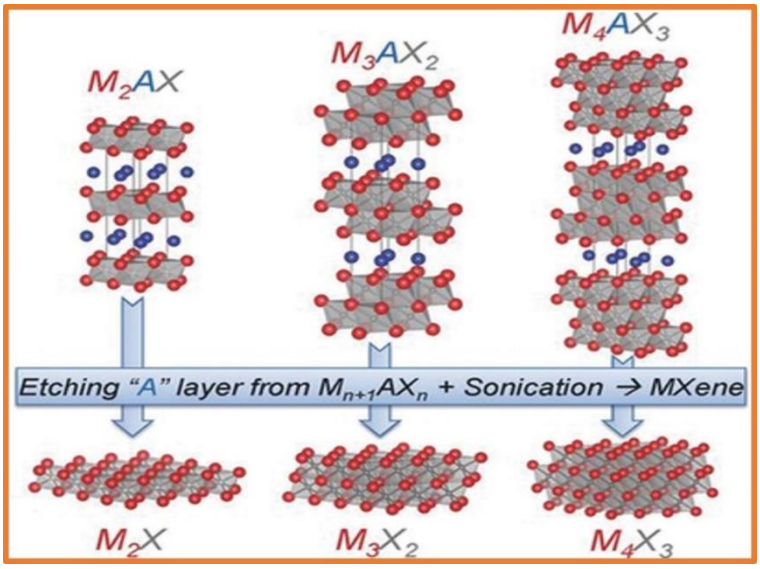

Fig. 1.15. Structure of MAX phase [83].

To achieve the thickness of the lamellas from tens to hundreds of nanometers partial delamination was done reconciled by basal dislocations which are anisotropic [81]. This leads to the automated deformation of the MAX Phases being exfoliated to a few nanometers thick of graphene as they possess slightly strong M-A bonds. Yury Gogotsi et al. were the first to exfoliate the A – A-group layers from the MAX phases at room/ moderate temperature by liquid or gas phase extraction [84]. MAX phases are exfoliated by the selective etching of A layers to produce 2D transition metal carbides and nitrides. MXenes represent the absence of the A group from the MAX phases. Similar to the properties of graphene the suffix "ene" in "MXene" represents their 2D nature. The A layers are exfoliated from the MAX phases by selective etching. More than sixty MAX phases exist to date. Among these, more than twenty pure $M_{n+1}X_n$ phases were obtained by the effect of removing the A layers from the MAX structures. Also, several MXenes are synthesized on M and X sites from MAX solid solutions. In this study, the exfoliated MAX phases are utilized for electrochemical supercapacitors [85][86].

MXenes, a new class of 2D transition metal carbides has engrossed recent research owing to their specific properties like hydrophilic surfaces which enhance the stability of aqueous environment and high metallic conductivity. These properties lead the 2D MXenes for a variety of applications as in Fig. 1.16. The MAX phase has an M - X bond with a predominant

covalent/metallic character. As the M-A bond is metallic the MAX phase bond cannot be broken easily. However, MA bonds are weaker as they can be etched with aqueous solutions containing fluoride by selective etching to yield MXenes. After the removal of Al layers functionalized MXenes are produced with the terminal O, OH, and F atoms, which are abbreviated as T in the general formula $M_{n+1}X_nT_x$ [87][88].

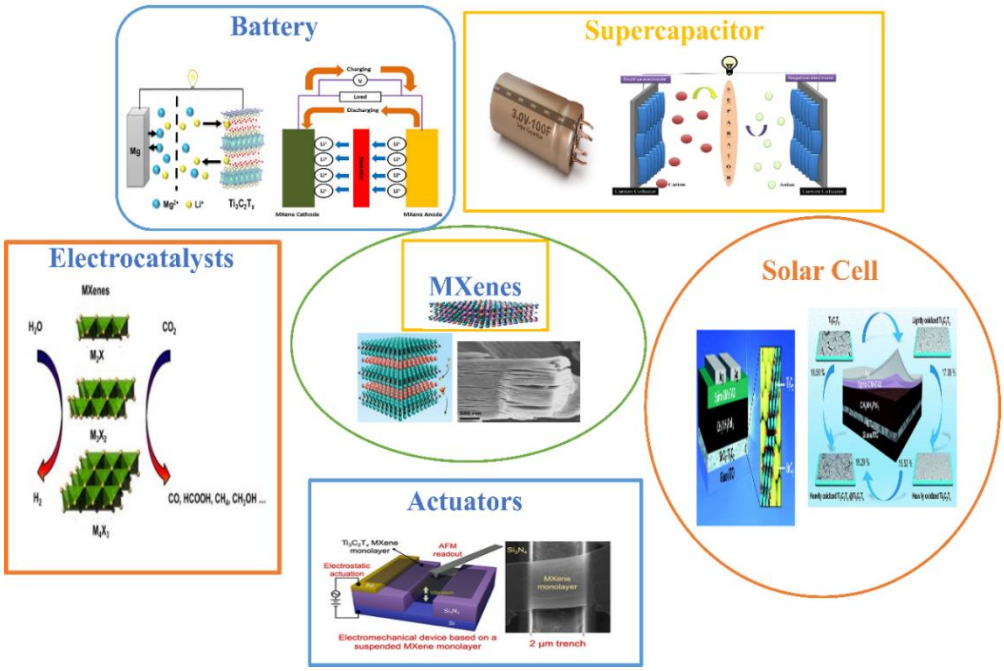

Fig. 1.16. Application of the MXenes.

1.5.1. Structure of MXene

MXenes exhibit distinctive properties like huge electrical conductivity, high surface area, and adequate surface terminal groups for layered structures. The conducting behavior of MXene differs in metallic, semi-metallic, and semi-conducting phases of MXene. Similar to the symmetry of MAX phases, the resultant MXenes possess a symmetrical hexagonal structure. The X layers are sandwiched between the M layers in which the particles are arranged into a lamellar arrangement [89]. Fig. 1.17 illustrates the presence of carbon or nitrogen atoms sandwiched between the M and X layers. Predominantly, the generalized gradient approximation (GGA) methodology was used to calculate the electronic properties and nanostructured properties of the MXenes. Still, a detailed assessment of the electronic bandgap was likely to be achieved by hybrid functional. It is expected that the pristine MXenes exhibit metallic characteristics. Compared to the MAX phase the conventional MXenes are predicted to have superior charge carrier density of states (DOS) which are nearer to the fermi level. After

functionalization, the electrical properties of MXenes are enhanced by suppressing the metallic behavior to achieve the semiconducting properties that correspond to the configuration of M, X, and T atoms [90].

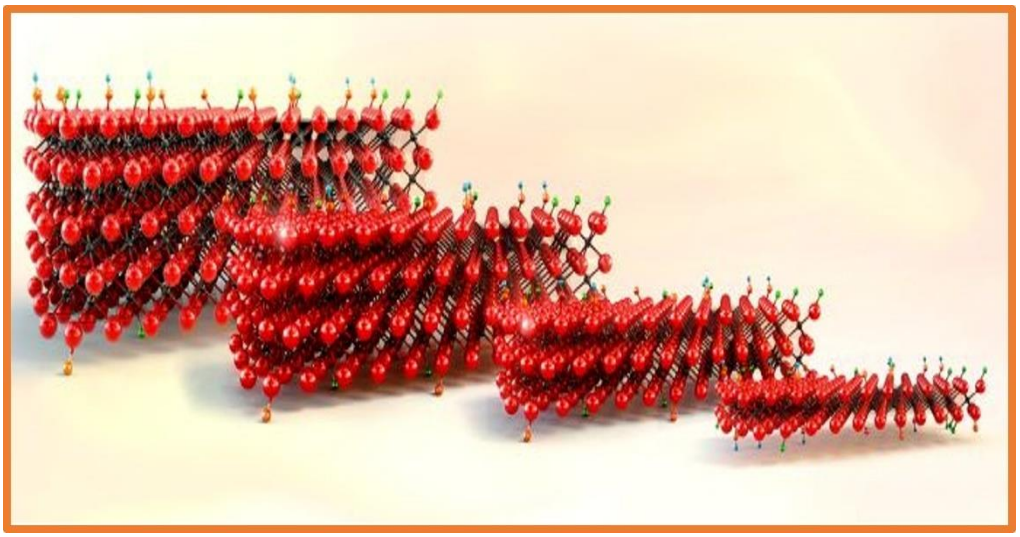

Fig. 1.17. Structure of MXene [91].

1.5.2. Properties of MXene

When it comes to the inimitable properties of MXenes, it could be ascribed that each type of MXene reported exhibits a distinct set of properties and surface chemistries that are tunable based on the compositions and fraction of the elements present. These unique combinations of properties common in different MXenes such as high electrical conductivity, hydrophilicity, mechanical strength, high electrochemically active surface, polar surface, etc. make them a potential candidate for creating an advanced material composite with MXene for high energy and power density supercapacitors [92].

The electronic properties such as the electronic conductivity of MXene including $Ti_3C_2T_x$ are ideal supercapacitor requirement that governs power density and energy density. The conductivity largely tends to depend on the amalgam of M, X, and surface groups ranging from metallic conductivity, and semiconductivity to insulating properties. MXenes with any functionalization exhibit metallic behaviour which possess more transition metals in the arrangement. Correspondingly, a very high conductivity of ~20000 Scm^{-1} was achieved for $Ti_3C_2T_x$ MXene prepared by blade-coating technique owing to large flake size and orderly arrangement which is higher compared to 2D materials such as --graphene and MoS_2.

Noteworthily, Nb_2CT_x MXene even exhibited superconductivity at low temperatures <10K possessing surface terminations including –Cl, –S, –NH, and –Se. This higher electronic conductivity helps faster electronic, ionic transport, and rate capability and also excludes the need for a separate conducting agent or a current collecting substrate for supercapacitor electrodes that augments the device energy density to a higher value [93].

Considering the future demands of wearable and miniaturized electronic systems coupled with flexible/micro-supercapacitors, 2D MXene possessing outstanding mechanical properties could address the requirement comfortably. Here, assembled MXene films are effectively fabricated and used as electrodes for supercapacitors which withstand mechanical deformations including twisting, folding, bending, and rolling. Based on theoretical calculations, bare MXenes (M_2XT_x; M = Ti, Mo, Sc, Hf, Zr) were found to possess breaking strength in the range of 92- 161 N m^{-1} displaying its superior mechanical stability. The excellent properties of tensile strength, flexibility, and bending resistance render MXene a promising electrode material for flexible and micro-supercapacitors [94].

1.6. Spinel Ferrite – MXene Nanocomposite

Researchers have conducted intensive investigations on MXenes as a supercapacitor electrode material because of its ease of synthesis, high specific capacitance, and good electrical conductivity. It alone may be used to prepare SC electrodes for excellent C_s. For energy storage SCs, MXenes are considered to be a candidate material, which requires additional research and product development [95]. Despite the excellent properties of MXene as a supercapacitor material, some constraints must be explored to determine its maximum potential. The exfoliation of MXene layers is a significant issue because of the possibility of layer restacking, which causes charge carrier immobility and thus hinders the redox reaction. To solve this problem, it is necessary to combine MXene with other active materials possessing good chemical stability and multiple redox states that are abundant in nature and inexpensive. Therefore, a type of complex metal oxide called spinel ferrite and MXene, as a new class of electroactive materials has attracted attention. To the best of our knowledge, the mixed metal oxide viz. spinel ferrite has been envisioned as a possible candidate for SC applications, as discussed earlier in section 1.3.3 [50]. This is an intriguing process of combining the remarkable features of spinel ferrite and MXenes into a single electrode. This process enables the spinel ferrite–MXene (NC) materials to have synergistic effects that are not possible with individual constituents. The NPs of spinel ferrite can be merged and deeply embedded with the MXene

matrix in the NC electrode, resulting in improved electrical conductivity, porous structure, and structural stabilization, thereby giving rise to superfluous charge storage by kinetic operations and enhanced charge transportation [96].

1.7. Scope of the Study

In this work, we attempt to identify potential solutions to the issue of energy storage devices by synthesizing materials with considerable magnetic, dielectric, and conductive properties. For, this spinel ferrite, a magnetic material with a high saturation magnetization, and Ti_3C_2MXene with good conductivity. In the present work (i) $Zn_{0.2}Mg_{0.8}Fe_2O_4$ at the temperature of 400 °C, 600 °C, 800 °C. (ii) $Mn_xCo_{0.5-x}Ni_{0.5}Fe_2O_4$ ($0.0<x<0.4$), (iii) $Pr_xMn_{0.5}Co_{0.5}Fe_{2-x}O_4$ ($0.00< x< 0.04$) different concentration ferrite nanoparticles are synthesized by simple, quick, and inexpensive sol-gel autocombustion strategy for pH 7 and strengthen by annealing at the temperatures of 1100 °C. Among all the three series of synthesized ferromagnetic material, the samples annealed at 1100 °C are experimented with for practical applications in applicable fields such as charge storage (SC) application. By synthesizing a large number of ferrites, by varying annealing temperature, and dopant, it becomes more focused in choosing the best samples for the application purposes. This is done to improve the efficiency of these samples and hence make them useful for futuristic applications. Electrochemical capacitors are promising energy storage gadgets for meeting the powerful electric market. Corresponding to batteries, electrochemical capacitors can give predominant power density and cyclability and can be viewed as intermediate devices between conventional ceramic capacitors and batteries. $Pr_{0.02}Mn_{0.5}Co_{0.5}Fe_{1.98}O_4$ - Ti_3C_2 MXene nanocomposite is best-suitable for energy storage devices.

CHAPTER 2

Review Of Literature

2. Review of Literature

Anwar et al. (2024) prepared the Co-doped Ni-Zn ferrites {$Ni_{0.6}Zn_{0.4-x}Co_xFe_2O_4$ (for x = 0.00, 0.05, 0.10, 0.15, 0.20)} utilized the sintering method. XRD and FTIR reveal that $Ni_{0.6}Zn_{0.4-x}Co_xFe_2O_4$ exhibits a single cubic crystal structure. The average crystallite grain size is 644 nm – 677 nm by utilizing the SEM micrographs. As increases the Co concentration the AC conductivity decreases. The saturation magnetization (87.39 emu/g) and magnetic moment (3.69 μ_B) have a significant increment of 15% Co–doped Ni - Zn ferrites. With increasing Co concentration, the value of initial permeability decreases significantly. The TanM vs. frequency plot depicts the start of relaxation peaks for all NZCFO composites at higher (> 10^7 Hz) frequencies [97].

Chai et al. (2024) reported that $MnFe_2O_4$/rGO nanocomposite was prepared by hydrothermal method. At 1 A g^{-1} current density, $MnFe_2O_4$/rGO nanocomposite exhibits the C_{sp} 195 F g^{-1} as compared to individual $MnFe_2O_4$ ferrite (77 F g^{-1}) and rGO (67 F g^{-1}). $MnFe_2O_4$ ferrites are homogeneously spread on the rGO sheets. However, an asymmetric supercapacitor device exhibits an energy density of 16 W h kg^{-1} and a power density of 1280 W kg^{-1} [98].

Ghaemi et al. (2024) reported the synthesis of a $Ni_{0.5}Zn_{0.5}Fe_2O_4$/MXene nanocomposite using a combustion method. The $Ti_3C_2T_x$ MXene exhibited a sheetlike morphology. The $Ni_{0.5}Zn_{0.5}Fe_2O_4$/MXene nanocomposite achieved a specific capacity of 1614 C g^{-1} at a current density of 1 A g^{-1}. When used in a hybrid capacitor with the $Ni_{0.5}Zn_{0.5}Fe_2O_4$/MXene composite powder as the positive electrode and activated carbon as the negative electrode, the device demonstrated an energy density of 53 Wh kg^{-1} at a power density of 1335 W kg^{-1} and a current density of 1 A g^{-1} [99].

Agale et al. (2023) utilize the sol-gel auto-combustion method to synthesize Nickel $Cu_{1-x}Ni_xMn_{1.0}Fe_{1.0}O_4$ ferrite. Rietveld refinement confirms the material exhibits the single phase and cubic spinel structure. FESEM study reveals that the spherical and multi-faced shapes morphology observed. The crystalline nature of the synthesized samples is revealed by TEM images, also in good agreement with FESEM images. VSM was used to investigate the magnetic properties of all ferrites. With increasing concentration, Ni^{2+} the $Cu_{1-x}Ni_xMn_{1.0}Fe_{1.0}O_4$ ferrite changes from a ferrimagnetic to a superparamagnetic state. The electrochemical analysis

revealed that $Cu_{1-x}Ni_xMn_{1.0}Fe_{1.0}O_4$ (x = 0.75) is superior to the other samples in electrochemical performance. At a scan rate of 5 mVs^{-1}, $Cu_{1-x}Ni_xMn_{1.0}Fe_{1.0}O_4$ (x = 0.75) had a C_{sp} 975 F g^{-1}, energy density of 20.8 Wh kg^{-1}, and 94.4% capacity retention over 5000th cycles [100].

Mayakkannan et al. (2023) utilize the microwave combustion method to prepare the $NiZnFe_2O_4$ ferrite. XRD revealed the material exhibits the single phase and Fd-3m space group. The supercapacitor material exhibits the C_{sp} 73.28 F g^{-1} at 5 mVs^{-1} scan rate energy density 3.56 Wh kg^{-1} and power density 2051.28 W kg^{-1}. SEM micrographs reveal irregular in shape and size [101].

Amani et al. (2023) reported the main goal of this research work is to develop and investigate a cost-effective nanomaterial for utilization in supercapacitors. $CoMnFeO_4$/rGo nanocomposite was synthesized. At a 1A g^{-1} current density, the specific capacity and the energy density of rGO/$CoMnFeO_4$ are 380 F g^{-1} and 58.18 Wh kg^{-1}. The findings of the present investigation show that $CoMnFeO_4$ nanoparticles behave appropriately as active materials for supercapacitors, and the addition of reduced graphene oxide (rGO) improved their electrochemical behavior [54].

Jeevanatham et al. (2023) utilized the sol-gel auto-combustion technique to prepare the Sr-doped $CoFe_2O_4$ ferrite nanoparticles at different 200 °C, 300 °C, and 500 °C temperatures. XRD identifies the phase and crystallinity of the synthesized sample. The crystallite sizes vary from 33nm - 35 nm at increased temperatures of 200 °C, 300 °C, and 500 °C. FESEM micrograph reveals the homogeneous size and shape of the sample. Tauc's plot as the direct bandgap energy values are 1.24, 1.21, and 1.20 eV using UV-Vis-NIR spectroscopy. At 300 °C, the $Co_{0.8}Sr_{0.2}Fe_2O_4$ has a supercapacitance value of 637 F g^{-1} at 0.5 A g^{-1} and retains 85.5% after 1000 cycles at 5 A g^{-1}, with an efficiency of 98.79% after 5000 cycles at 15 A g^{-1} [102].

Mahajan et al. (2022) study reports the preparation of the composite $Mn_{0.3}Co_{0.2}Zn_{0.5}Fe_{1.97}O_4$ – PANI by mechanical blending method, $Mn_{0.3}Co_{0.}2Zn_{0.5}Fe_{1.97}O_4$ by sol-gel auto combustion method and PANI can be prepared by the chemical oxidative method. X-ray diffraction indicates the synthesis of the nanocomposite $Mn_{0.3}Co_{0.2}Zn_{0.5}Fe_{1.97}O_4$ – PANI due to the presence of two distinct kinds of peaks: sharp $Mn_{0.3}Co_{0.2}Zn_{0.5}Fe_{1.97}O_4$ and broader PANI peaks. FTIR affirms the presence of the vibrational bond in the nanocomposite which is also determined in the individual $Mn_{0.3}Co_{0.2}Zn_{0.5}Fe_{1.97}O_4$ and PANI. Field emission scanning electron microscopy (FESEM) micrograph reveals the encapsulation of the spinel ferrite with the PANI matrix and confirms the formation of the nanocomposite of $Mn_{0.3}Co_{0.2}Zn_{0.5}Fe_{1.97}O_4$ – PANI. The

electrochemical properties of the nanocomposite $Mn_{0.3}Co_{0.2}Zn_{0.5}Fe_{1.97}O_4$ - PANI show the C_{sp} 286. 91 F g^{-1} at the 10 mVs^{-1}. Electrochemical impedance spectroscopy (EIS) shows the ion transfer resistance is 1.25, 1.12, and 0.57 Ω. Nanocomposite $Mn_{0.3}Co_{0.2}Zn_{0.5}Fe_{1.97}O_4$ – PANI shows better performance than the individual $Mn_{0.3}Co_{0.2}Zn_{0.5}Fe_{1.97}O_4$ and PANI [62].

Manohar et al. (2022) study reports preparing the nanoparticle Mg substituted $MnFe_2O_4$ (x= 0.1, 0.2, 0.3, 0.4, and 0.5) by solvothermal reflux method. X-ray diffraction (XRD) revealed that all the samples exhibit a single phase without the presence of impurity. FESEM micrograph reveals the homogeneous spherical morphology of all the samples. $Mg_{0.1}Mn_{0.9}Fe_2O_4$ had the highest specific capacitance 226.4 Fg^{-1} as compared to the other $Mg_{0.3}Mn_{0.7}Fe_2O_4$, $Mg_{0.4}Mn_{0.6}Fe_2O_4$, and $Mg_{0.5}Mn_{0.5}Fe_2O_4$ electrodes. The cyclic stability at the 3000^{th} cycle $Mg_{0.1}Mn_{0.9}Fe_2O_4$ is 94.95 %, and $Mg_{0.5}Mn_{0.5}Fe_2O_4$ is 92.47 % [103].

Kiey et al. (2022) report preparing $Co/CuFe_2O_4$ by auto combustion method using citric acid as a fuel agent. XRD reveals the sample exhibits a single-phase cubic structure. The synthesized nanomaterial exhibited a spherical shape with a particle size range that varies from 30 to 50 nm using TEM images. The electrochemical performance using a three-electrode configuration, ferrite nanoparticles C_{sp} 893 Fg^{-1} at a scan rate of 5 mV s^{-1}. At a current density of 1 A g^{-1}, Co–Cu ferrite exhibited 90% capacity retention for 3000 cycles [104].

Dippong et al. (2022) prepared Ni^{2+} doped in manganese spinel ferrite by sol-gel technique and studied the effect of structural, morphological, and magnetic characteristics of $Mn_{1-x}Ni_xFe_2O_4@SiO_2$ (x = 0, 0.25, 0.50, 0.75, 1.00) nanocomposites (NCs). The formation of a SiO_2 matrix and ferrite is confirmed by Fourier transform infrared spectra, and the XRD study reveals the poor crystalline ferrite at low temperatures and high temperatures highly crystalline mixed cubic spinel ferrite with the presence of secondary phases. With increasing Ni content and by Vegard's rule, the lattice parameters decrease as the crystallite size, volume, and X-ray density of $Mn_{1-x}Ni_xFe_2O_4@SiO_2$ NCs increase. The coercivity falls as the Ni concentration rises, while the M_s, magnetic moment per formula unit, and anisotropy constant K_1 all increase. For samples that were annealed at greater temperatures and had the same chemical formula, these parameters were bigger. The materials exhibit a paramagnetic nature but with the addition of Ni content in Mn – ferrite the material exhibits the supermagnetic behavior [105].

Akhtar et al. (2021) have investigated the rare-earth (RE) elements Yb, and Gd in Ni–Zn spinel ferrite to determine the magnetic, optical, and electrical conductivity analysis of the synthesized samples. By using the sol-gel auto combustion method to synthesize the $Ni_{0.5}Zn_{0.5}Yb_xGd_xFe_{2-}$

$_xO_4$ (where x = 0.00, 0.20, 0.40, 0. 60, 0.80 and 1.00). XRD study reveals the material exhibits a single-phase cubic structure. With increasing the RE element concentration, grain size is varied. FTIR affirms the vibrational at the 400 – 600 cm^{-1} of the RE-doped spinel ferrite. The saturation magnetization (M_s) is decreased with the addition of RE - elements. The temperature-dependent electrical conductivity was also investigated to better understand the conduction mechanism over a temperature range of 323 K-563 K. Yb and Gd doped NiZn ferrite exhibits excellent magnetic and electrical properties and also a potential candidate for nanoantennas, sensing, data storage applications, and energy storage devices [106].

Yaqoob et al. (2021) prepared MXene/Ag_2CrO_4 nanocomposite by co-precipitation technique. Ag_2CrO_4 spinel was synthesized by sol-gel method and MXene was etched from MAX powder. X-ray diffraction (XRD) demonstrated an increase in inter-planar spacing from 4.7 Å to 6.2 Å. SEM micrograph reveals Ag_2CrO_4 nanoparticles dispersed as clusters over MXene layers. EDX study determines the elemental present in the sample. Raman spectroscopy studies the presence of bonding in the prepared nanocomposite. Furthermore, the current study will be an evaluation of the capacitive behavior of electrodes in different electrolytes, such as acidic 0.1 M H_2SO_4 has a specific capacitance C_{sp} = 525 F/g at 10 mV/s and basic 1 M KOH electrolyte has a much lower value [107].

Safari et al. (2021) used a two-step approach for Fe_2Co-MOF production viz. solvothermal procedure and then calcination. The occurrence of the cubic structure of $CoFe_2O_4$ and MIL-88A (Fe) structure of Fe_2Co-MOF has been validated by XRD patterns. As per FE-SEM micrographs, the calcination method transforms the morphology from spindle (Fe_2Co-MOF) into yolk-shell ($CoFe_2O_4$). As per BET analysis, the specific surface areas of Fe_2Co-MOF and $CoFe_2O_4$ are 36.0 and 29.2 m^2 g^{-1} respectively. VSM study found that $CoFe_2O_4$ had a high value of coercivity of 2500 Oe owing to the surface anisotropy. During morphological change, the optical band gap is decreased from 1.92 to 1.77 eV. GCD curves at 1 A g^{-1} yield Cs of 489.9 F g^{-1} (Fe_2Co-MOF/NF) and 192.6 F g^{-1} ($CoFe_2O_4$/NF). The Fe_2Co-MOF/NF exhibits more magnificent cyclic stability than their counterparts beyond 3000 cycles [108].

Balideh et al. (2021) prepared $Ni_{0.3}Co_{0.7}Dy_xFe_{2-x}O_4$ (x = 0:0, 0.02, 0.04, 0.06, 0.08, and 0.1) samples by utilizing the hydrothermal process, an annealing treatment, and NaOH as a solvent. The prepared samples underwent a 7-hour annealing process at 150. On structural, morphological, electrical, and magnetic characteristics, the effect of Dy doping was investigated. The structure, size, morphology, and magnetic characteristics of synthesized

compounds were examined using X-ray diffraction, Fourier transform infrared spectroscopy, field emission scanning electron microscopy, an energy dispersive spectrometer, and a vibrating sample magnetometer (VSM). X-ray diffraction proved the presence of a ferrite phase. An increase in Dy doping has been seen to result in larger average crystallite and grain sizes. Two distinct, significant absorption bands at 500-600 cm^{-1} were visible in the Fourier transform infrared spectra. Particles with an average size ranging from 45 to 60 nm were seen by field emission scanning electron microscopy to have a consistent spherical form. The presence of the component elements Co, Ni, Fe, and Dy, with proportions that are extremely near to the stoichiometry of the chemical formula, was confirmed by examining the energy dispersive spectrometer analysis patterns. The characteristic magnetic behavior of spinel ferrite nanoparticles was validated by magnetic measurements, and the magnetic hysteresis behavior was enhanced over that described in other studies [109].

Nawaz et al. (2021) developed $Ni_{0.5}Zn_{0.5}Fe_2O_4$ as electrodes with and without binders. Simple hydrothermal procedures are used to directly produce the binder-free electrode on nickel foam. X-ray diffraction is used to investigate the crystalline phase of both of these electrodes. Through the use of high-resolution transmission electron microscopy (TEM) and scanning electron microscopy (SEM), their morphology has been studied. These techniques have shown a well-defined nanostructure that resembles tiny hexagonal platelets. Using energy dispersive spectroscopy (EDX), the chemical composition is confirmed. Due to the nickel foam's 3-D linked structure, the NZF@NF electrode has surpassed the NZF electrode based on a binder. The NZF@NF electrode produced a specific capacity (C_{sp}) of 504 F g^{-1} at a current density of 1 A g^{-1}, whereas its counterpart produced a specific capacity of 151 F g^{-1} at 1 Ag^{-1} [110].

Raza et al. (2021) $LaCeFe_2O_4$ ferrite was successfully synthesized using both the co-precipitation and hydrothermal methods. X-ray diffraction (XRD) analysis confirmed that the prepared material exhibited a single-phase structure. Scanning electron microscopy (SEM) revealed a porous morphology, while energy-dispersive X-ray spectroscopy (EDX) confirmed the absence of impurities and the presence of all required elements in the prepared sample. When tested at a scan rate of 10 mV/s, the specific capacitance (C_{sp}) was found to be 1197 F g^{-1}, with a retention rate of 92.3% after 2000 cycles, indicating good cycle life. At a current density of 5 A/g, the electrode demonstrated an energy density of 59 Wh/g and a power density of 9234 W/kg [111].

Sathiyamurthy et al. (2021) had been synthesizing the $ZnFe_2O_4$, $CoFe_2O_4$, and Co-doped $ZnFe_2O_4$ via. Co-precipitation method. XRD studies confirm the cubic spinel structure of the Co-doped $ZnFe_2O_4$ nanoparticles. In the FTIR characteristic two types of vibrational modes are present: tetrahedral (A) and octahedral (B). TEM and FE-SEM corroborated the shape, exhibiting a spherical structure with an aggregation of the nanocomposite. EDX study indicates the elemental characteristics of the Co-doped $ZnFe_2O_4$ nanocomposite. A VSM was used to investigate the produced NC, which revealed the transition from paramagnetic to ferromagnetic activity. The C_s of the prepared ferrites were estimated scan rate of 10 mV s^{-1}, and $Co_{0.5}Zn_{0.5}Fe_2O_4$ had significantly enhanced C_{sp} of 218 F g^{-1}. The NC that has been prepared can be utilized in energy storage systems [58].

Raza et al. (2021) employed hydrothermal and co-precipitation methods to synthesize the lanthanum cerium ferrite nanoparticles. The structural along morphological characteristics of NPs were investigated employing XRD, SEM, TEM, and EDX. For CV, GCD, and EIS of J1 and J2 electrodes, a 3-electrode configuration in 6 M KOH electrolyte has been used. The excellent C_{sp} of 1195 F g^{-1} was attained for J2 at 10 mV s^{-1} and had 92.3 % capacitive retention beyond 2000 cycles. The E and P densities for the J2 electrode at 5 A g^{-1} were noticed to be 59 Wh kg^{-1} and 9234 W kg^{-1}. As a consequence, the developed J2 electrode is a potential contender for supercapacitor [111].

Baig et al. (2021) prepared the $NiFe_2O_4$ by the sol-gel method and SiO_2 by the Stober method. XRD study reveals the crystal size of the nanocomposite 20 nm ± 1 nm. The electrochemical process is measured using CV, GCD, and EIS which represent the electrode materials' comparable efficiency and reversibility. After 5000 cycles at 20 mA/cm^2, the prepared electrode has a capacitance of 925 F g^{-1} at 1 A g^{-1} and a capacitance retention of 95.5%. Because of the high surface area, the enhanced electrochemical performance of the $NiFe_2O_4/SiO_2$ electrode can be subjected to the prompt diffusion process provided by $NiFe_2O_4/SiO_2$ and enhanced redox reactions. According to electrochemical impedance spectroscopy (EIS), the aforementioned characteristics reduce the total impedance of the electrodes [112].

Anwar et al. (2020) employed a coprecipitation method to prepare the $NiDy_xFe_{2-x}O_4$ ferrites ($0.0 \leq x \leq 0.1$). XRD study reveals the prepared samples exhibit the single-phase FCC cubic spinel structure. FTIR spectra demonstrate the two vibrational frequency bands (v_1 and v_2). The magnetic properties demonstrated a M_s is reduced and Bohr magneton (n_B) is decreased. With the Dy substitution anisotropy constant first increased and then decreased, H_c showed a non–

linear behavior. Increased resistivity of nickel ferrite along with the reduction in M – H loss makes it beneficial for high-frequency devices [113].

Tanbir et al. (2020) studied the effects of Eu^{3+}, Sm^{3+}, and Gd^{3+} doping on the magnetic, optical, and structural characteristics of Ni-Co ferrite NPs produced via the facile co-precipitation route. XRD confirmed the development of single-phase (spinel) for all the samples. Owing to the larger radius of the dopant, a decrement in the crystallite size was exhibited. The HR-TEM micrograph-derived mean particle size closely matched the X-ray diffraction data. At ambient temperature, the paramagnetic character of rare-earth ions decreases the superexchange interactions between sublattices. In contrast with the dopant, the Curie temperature, M_s, and coercivity were noticed to be lower than the pristine samples. The nano-size effect of the produced NPs is responsible for the enhancement in the bandgap (optical) [114].

Mazen et al. (2020) prepared $Li_{0.25}Mn_{0.5-x}M_xFe_{2.25}O_4$ by the conventional ceramic method. The metal cations (M) viz. Co^{2+}, Ni^{2+}, and Cu^{2+} were doped at different concentrations (x = 0.0, 0.1, 0.3, and 0.5) to enhance the magnetic characteristics. The structural along magnetic characteristics of the prepared samples were examined by employing the XRD, SEM, and VSM. For all prepared samples the single-phase (spinel) was affirmed by the XRD. With increasing doping concentrations, the lattice parameter fell linearly. The crystallite sizes range from 60 to 101 nanometers. VSM tests demonstrated that different metal ion replacements had a significant impact on the M_s of $Li_{0.25}Mn_{0.5-x}M_xFe_{2.25}O_4$, which is attributable to the distribution of metal cations in the A and B sites. Owing to the enhanced magnetic characteristics of the $Li_{0.25}Mn_{0.5-x}M_xFe_{2.25}O_4$ as compared to their counterparts, it can be eventually implemented in the magnetic recorders and microwave appliances. It was noticed that the prepared $Li_{0.25}Mn_{0.5-x}M_xFe_{2.25}O_4$, structural and magnetic characteristics can be tuned by the substitution of various divalent transition metal ions [115].

Garg et al. (2020) studied MXene as a member of the 2D carbide and nitride family. The layered structure of MXene is successfully obtained by modifying the process parameters, as evidenced by the presence of an XRD peak (110). FESEM images reveal the MXene has an accordion-like structure. After the etching process, the peak (002) is slightly shifted towards the lower angle, confirming the increase in spacing of MXene layers to 12.92 A˚. Furthermore, the etching time is reduced, as a result, the d-spacing of MXene layers is decreased because the aluminum content is not removed successfully. The presence of AlF_3 in the MXene is confirmed by characteristic peaks (106), (108), and (109). The occurrence of (106), (108), and (109) peaks

which correspond to the growth of AlF_3 is highly dependent on any variation in process parameters. To obtain the best MXene layers regarding structural and electrical properties, the process factors must be tuned so that aluminum etching can be done completely without increasing the fluorine content in the MXene. In this paper, we reveal for the very first time the fabrication of the best-optimized MXene film on the flexible polypropylene (PP) substrate employing the best-optimized factors for supercapacitor applications and compare the results to those obtained on the polyethylene terephthalate (PET) and glass substrates. The PP-supported MXene device exhibits an areal capacitance of 82.6mF/cm^2 at 5 mV/s, and a capacitive retention of 73.3%. The research opens the door to new high-performance device designs based on different flake sizes, morphologies of MXene, and their combinations [85].

Nabi et al. (2020) employed the $Ce_xCoFe_{2-x}O_4$ (x = 0, 0.3, 0.5) electrode have been prepared successfully by the coprecipitation method. Scanning electron microscopy (SEM) micrograph analysis revealed the non-uniform shape and size and presence of agglomeration. The electrochemical investigation of $Ce_xCoFe_{2-x}O_4$ (x = 0, 0.3, 0.5) electrodes in 1 M KOH electrolyte solution was carried out using CV, GCD, and EIS. With a long cycling life of 82.3% retention after 4000 cycles, the highest specific capacitance (937.50 Fg^{-1}) was achieved. As a result, the $Ce_xCoFe_{2-x}O_4$ electrode is a promising candidate for supercapacitor applications [28].

Singh et al. (2020) study reveals the PANI prepared by in situ chemical oxidative method and Mn ferrite ($MnFe_2O_4$) by hydrothermal method. Mn infused in polyaniline (PANI) shows the synergetic effect for the transfer of the ions. The fluffy nature of PANI provided charge transport channels, and manganese ferrites assisted in electron storage via changes in the valence state of the active sites. At a current density of 1 A g^{-1}, we obtained a high specific capacitance of 623 F g^{-1}. After 10,000 cycles, a prototype of the developed supercapacitor demonstrated excellent device performance with a high energy density of 179 Wh kg^{-1} and a maximum power density of 982 W/kg with 95% retention of specific capacitance [116].

Cheng et al. (2020) investigated the high activity and electrical conductivity of $NiCo_2O_4$ which has been regarded as an effective electrode material. $NiCo_2O_4$ (core-shell) structural composites have been produced, and the composites seem to have superior Cs than pure $NiCo_2O_4$. This research is aimed at the present state of composites (core-shell) that use $NiCo_2O_4$ as a scaffolding. In core-shell structures conductive polymers, sulfides, hydroxides, and metal oxides are explored in detail as shell materials. The structure (core-shell) produced on conductive substrates can prevent material agglomeration and allow electrolytes to penetrate

more easily. The cores of $NiCo_2O_4$ act as conducting conduits to the shell materials, ensuring synergic impact, while the shell materials protect and stabilize the $NiCo_2O_4$ cores. The electrodes of the $NiCo_2O_4$ core were examined in terms of potential development paths and prospects [117].

Barakzehi et al. (2020) prepared at room temperature, a commonly utilized PET that is modified utilizing MIL-53(Al), via a layer-by-layer fabrication process. The rGO is then dipped into a GO solution and deposited on the surface of PET-MOF following chemical reduction. Finally, an in situ chemical polymerization method polymerizes pyrrole on the PET-MOF-rGO surface. The produced composite has been used as electrode material in an H_2SO_4 solution, yielding a C_{sp} of 510 mF cm^{-2} at 1 mV s^{-1}. The improved electrode is used in symmetrical SCs that have a 3.5 F cm^{-3} (volumetric C_s), 64 mWh cm^{-3} (E), and 0.6 mW cm^{-3} (P). The fabricated SC maintains 85 % of its initial C_{sp} beyond 1000 cycles after twelve months of storage under ambient temperature [118].

Uke et al. (2020) synthesized Zn-doped $MgFe_2O_4$ by sol-gel technique, as an electrode material for SC at varied Zn concentrations. The concentration of Zn in $MgFe_2O_4$ improves the SC's performance and raises the value of electric conductivity. The 2 wt. % Zn concentration in $MgFe_2O_4$ has been reported to be a high mesopores content with a modest surface area for ions to be accommodated. In 1 mol L^{-1} of Na_2SO_4 electrolyte, Zn doping in $MgFe_2O_4$ exhibited excellent C_s. The enhanced C_{sp} of 484.6 F g^{-1} for 2 wt. % Zn in $MgFe_2O_4$ at 1 mA cm^{-2} was observed in the GCD investigation. P and E are determined to be 2 kW kg^{-1} and, 9 Wh kg^{-1} respectively. Furthermore, EIS demonstrates that 2 wt. % Zn-doped $MgFe_2O_4$ has a lower resistance for intercalation and de-intercalation. The larger value of resistance is 1.2, and R_{ct} is 3.2, which is quite low, thus it's a great choice for SCs [119].

Slimani et al. (2020) utilized an ultrasonic irradiation procedure for the preparation of $Ni_{0.4}Cu_{0.2}Zn_{0.4}Fe_{2-x}Eu_xO_4$ (x = 0.00-0.10) ferrite NPs and thoroughly researched as a green and simple approach. Various properties viz. dielectric, electrical, magnetic, optical, morphology, and structure were examined on doping Eu^{3+} in NiCuZn ferrite NPs. The band gap in the range of 1.86-1.90 eV was evaluated utilizing the tauc plots. At ambient temperature, magnetization tests revealed superparamagnetic activity. A transition from superparamagnetic to ferromagnetic might be observed below the blocking temperature (TB). The decrement in the M_s was noticed with the doping of Eu^{3+}. The greatest fluctuation in DC conductivity was exhibited at the

concentration of x = 0.02. The activation energy is shown to be significantly dependent on both the substitution ratios of Eu ions and the temperature regions [120].

Almessiere et al. (2020) used the sol-gel technique to prepare Eu-doped Ni-Cu-Zn ferrite NPs. The single-phase (spinel) for all the prepared samples was affirmed by the XRD. The hyperfine magnetic field (HMF), quadrupole splitting, isomeric shift, and line-width disparity were all estimated using Mossbauer spectra. With the increment in the Eu doping, 32 the decrement in the HMF was noticed. The prepared NP paramagnetic contribution grew as the Eu^{3+} level rose. The suggested NSF's S-parameters were measured using the co-axial approach. Natural ferromagnetic resonance (NFMR) occurrences allowed for significant EM energy absorption in the range of 2.5-9.5 GHz. Furthermore, the frequency features of the NSFs were greatly altered by the rise in Eu substitution. The resonant amplitude changed abnormally (more than four times). The findings indicate that the prepared materials are applicable to radio-electronic gadgets [121].

Ayman et al. (2020) employed the CoF/MXene composite by ultrasonication method. CoF/MXene has a C_{sp} 594 F g^{-1}, 1046.25 F g^{-1}, and 1268.75 F g^{-1} at a current density of 1 A g^{-1}. CoF/ MXene exhibit the Sp. Capacity 440 C g^{-1} at 1 A g^{-1}. The charge transfer resistance of the material is 0.25 ohm. CoF/MXene composite cyclic stability and capacitance retention of ~97% till 5000 cycles [50].

Bhagwan et al. (2019) applied a facile, rapid, and cost-effective combustion process was used to synthesize zinc cobaltate (ZCO) nanoparticles. To achieve acceptable crystallinity and a suitable morphology in ZCO, several calcination temperatures were utilized. The impact on the electrochemical activity of the SC with the temperature was examined. The excellent C_{sp} at 1 A g^{-1} for optimized sample yields to be 843 F g^{-1}. The aqueous asymmetric supercapacitor was made using the optimum sample. The P and E at 1 A g^{-1} for asymmetric SC were evaluated to be 716 W kg^{-1} and 26.28 Wh kg^{-1}. The parallel-connected 14 LEDs and fan were operated with the two asymmetric SCs connected in series. Based on the foregoing findings, optimized ZCO appears to be favorable for the SC electrode [122].

Javed et al. (2019) used a co-precipitation approach to make $Ni_{0.65}Zn_{0.35}Nd_xFe_{2-x}O_4$ nanoparticles. The electromagnetic and structural characteristics of the prepared samples can be tuned with doping (RE). The electric, magnetic, spectral, and structural behavior of the prepared samples was examined utilizing I-V measurements, VSM, FTIR, and XRD. Excluding x = 0.075, for all the prepared samples the development of the single-phase (spinel) was avowed by

the XRD. The nonlinear trend in the magnetic, electric, and structural study was perceived with the doping of Nd^{3+}. The vibrations in the prepared samples were explained by the FTIR [123].

Cai et al. (2019) altered the composition ratio, to produce rGO-$NiFe_2O_4$ nanohybrids with $NiFe_2O_4$ dispersed over a 2-D rGO substrate. $NiFe_2O_4$ levels might interfere with the ideal condition of transportation of ions and conduction of the electron, thereby lowering C_{sp}. The weight capacitance of the G-N3 (30 wt. % $NiFe_2O_4$) SC electrode is four times that of pristine $NiFe_2O_4$ at 0.5 A g^{-1}. Furthermore, this G-N3 SC electrode has excellent rate performance as well as long-term cycle stability. Quantitative electrochemical kinetics experiments are also used to investigate a surface capacitive storage mechanism. The findings suggest that nanoscale tailoring may be a more reliable route to developing novel SC electrodes [124].

Chilwar et al. (2019) employed a chemical spray approach to preparing a thin film of Al^{3+} doped $LiFe_2O_4$. The single-phase (spinel) development of the prepared sample was assured by XRD pattern analysis. The decrement in the lattice constant was noticed with the doping of Al^{3+}. FTIR study exhibits the effective integration of the dopant in the $LiFe_2O_4$. The agglomerated spherical-shaped grain was perceived in the FESEM. The bandgap lies in the range of 2.36 and 2.04 eV, which is estimated utilizing the Tauc plot. With increasing Al^{3+} content, the saturation magnetization (M_s) drops, but the coercivity (H_c) increases. With increasing Al^{3+} concentrations, the dielectric characteristics deteriorated [125].

Bandyopadhyay et al. (2019) employed a facile hydrothermal approach to preparing porous 3-D Zn-Ni-Co oxide/$NiMoO_4$ over Ni foam for SC. The hierarchical porous Zn-Ni-Co oxide/$NiMoO_4$ exhibits excellent reversible Faradaic reaction, by having quick ions mobility, porous structure, stability, and magnificent conductivity. It was perceived that the asymmetric SC exhibits an excellent life span, $C_{sp,}$ and quick charge-discharge rate if Fe_2O_3/rGO and Zn Ni-Co oxide/$NiMoO_4$ were utilized as an anode and cathode material respectively [126].

Shokri et al. (2018) utilized a simple co-precipitation approach to preparing $Co_xSn_{1-x}Fe_2O_4$ NPs. The optical, morphological, magnetic, and structural characteristics of the prepared samples were examined utilizing DRS, EDX, FESEM, VSM, FTIR, and XRD. The development of the cubic spinel structure was verified by XRD and FTIR findings. With the doping of the Co, the lattice constant first increments (up to x = 0.25) and then decreases (above x = 0.25). For $x < 0.25$ and $x > 0.25$, the shifting of the υ1 peak towards the lower and higher wavenumber respectively was perceived in the FTIR. For x = 0.50 the value of the anisotropy constant, Mr, and M_s were extremely higher, and then decrements above x = 0.50 [127].

Chandel et al. (2018) utilized the facile in-situ approach for the production of $CuFe_2O_4$-rGO NC. Density functional theory was employed to examine the interaction of rGo with $CuFe_2O_4$ inside the prepared NC. The excellent C_{sp} of the NC were exhibited, due to their synergic action. The prepared NC in the weight % ratio of 96:04 showed remarkable catalytic efficiency. This efficiency was much greater than that of pristine $CuFe_2O_4$ in each of these processes. The prepared NC also outperformed pristine $CuFe_2O_4$ in terms of supercapacitance. The C_{sp} of the NC at 2 A g^{-1} was estimated to be 797 F g^{-1} and hold excellent capacitive retention (92 %) beyond 2000 cycles [128].

Ismail et al. (2018) successfully worked in preparing $Mn_{0.5}Zn_{0.5}Fe_2O_4$ spinel ferrite for the first time for high-performance supercapacitor electrodes. The $Mn_{0.5}Zn_{0.5}Fe_2O_4$ spinel ferrite so formed has a mesoporous nanostructure, narrow pore size dissemination, and high surface-to-volume ratio. The electrode prepared by utilizing $Mn_{0.5}Zn_{0.5}Fe_2O_4$ exhibits a very high value of C_{sp} (783 Fg^{-1}) in 0.5 M H_2SO_4 and has a very high coulombic efficiency. The P and E at 1.0 A g^{-1} for the $Mn_{0.5}Zn_{0.5}Fe_2O_4$ are 899.7 W kg^{-1} and 15.8 Wh kg^{-1} which is comparatively larger than the P and E of $MnFe_2O_4$ and $ZnFe_2O_4$. This makes $Mn_{0.5}Zn_{0.5}Fe_2O_4$ a favorable material for high-performance SC applications [129].

Bashir et al. (2018) have employed the nanoparticle Cu doped in the nickel ferrite ($Cu_xNi_{1-x}Fe_2O_4$) via. The coprecipitation method and reduced graphene oxide (rGO) are prepared by the Hummer method. XRD study reveals that doped and undoped samples exhibit the single phase without any presence of the impurity, $Cu_xNi_{1-x}Fe_2O_4$/ rGo composite doesn't influence the crystal structure. SEM reveals the sample exhibits a cubic structure. Nanocomposite shows the distribution of ferrite ($Cu_xNi_{1-x}Fe_2O_4$) and rGO sheet lateral dimension in the range of 20 nm to 80 nm. The individual ferrite shows a capacitance of 65 % after 1000 cycles. The electrochemical properties enhanced the capacitance retention of 65 % to 75 % of doped ($Cu_xNi_{1-x}Fe_2O_4$). 2D material (rGO) is conductive which also enhanced the capacitance of the electrode from 65 % to 85 % [130].

Bhongale et al. (2018) utilized the oxalate co-precipitation approach to prepare $Mg_xCd_{1-x}Nd_{0.03}Fe_{1.97}O_4$ using a unique microwave sintering procedure. Sintering of the prepared sample was done in a microwave oven for 10 minutes. The structural characteristics of the prepared sample were investigated utilizing FTIR, SEM, and XRD. The development of the spinel structure in the prepared sample was assured by the XRD. Despite the absorption peaks, two sharp peaks were noticed near 400 and 600 cm^{-1} in the FTIR study. The magnetic characteristics

of the produced samples are reliant on the grain size and per the VSM analysis. The processed sample's superior magnetic characteristics make them ideal for use as a recording medium. The microwave sintering process allows for the rapid production of spinel ferrites [131].

Vignesh et al. (2018) utilized a facile and minimal-cost co-precipitation technique for the production of $MnFe_2O_4$. The 3.5 M KOH was utilized for the electrochemical investigation and it was revealed that at 0.2 A g^{-1}, the excellent C_{sp} (245 F g^{-1}) with capacitive retention of 105 % beyond 10,000 cycles. The P and E were perceived to be 1207 W kg^{-1} and 12.6 Wh kg^{-1} respectively and thus make $MnFe_2O_4$ a favorable material for SC [132].

Aparna et al. (2018) this work report the utilization of a solvothermal method using a solvent as ethylene glycol to synthesize metal ferrites (MFe_2O_4, M=Fe, Co, Ni, Mn Cu, Zn). The crystallite size of the metal ferrites varies from 20 to 35 nm and the average particle size is 50 – 140 nm investigated from the XRD plots and FESEM micrographs. At a scan rate of 2 mV s^{-1} specific capacitance of metal ferrites (MFe_2O_4, M=Fe, Co, Ni, Mn, Cu, Zn) were determined to be 101 F g^{-1}, 444.78 F g^{-1}, 109.26 F g^{-1}, 190 F g^{-1}, 250 F g^{-1}, 138.95 F g^{-1}. $CoFe_2O_4$ ferrite has a higher specific capacitance than the other metal ferrites [133].

Bashir et al. (2017) studied the nanocomposite Mn doped in the copper ferrite $Mn_xCu_{1-x}Fe_2O_4$ / rGO synthesis by ultrasonication method, $Mn_xCu_{1-x}Fe_2O_4$ ferrite via. Coprecipitation method, and rGO by modified Hummer method. Raman spectroscopy reveals the three prominent peaks in the range 1000 – 3000 cm^{-1}. XRD study reveals the cubic structure. The electrochemical properties CV study reveals that increases in the scan rate capacitance don't decrease the trend. $Mn_xCu_{1-x}Fe_2O_4$ / rGO nanocomposite is a best contender for the supercapacitor electrode [134].

Shah et al. (2017) have studied the $BaPr_xFe_{2-x}O_4$ (x = 0.0, 0.025, 0.05, 0.075, 0.10) spinel ferrites have been prepared by the sol-gel technique. X-ray diffraction (XRD) study reveals that all the sample exhibits the fcc spinel phase. Scanning electron microscopy (SEM) reveals that all the samples showed inhomogeneous grain size distribution. $BaFe_2O_4$ exhibit exhibits a multi-domain structure. When Pr is substituted in $BaFe_2O_4$ ferrite material exhibits the single domain. M-H hysteresis loop showed all the samples exhibit the soft nature of ferrites. Increasing the Pr^{3+} concentration in the barium spinel ferrite, reduced the saturation magnetization (M_s) and remanence (R). Coercivity (H_c) and anisotropy constant (K_1) both

enhanced with the Pr^{3+} concentration. Pr-doped barium ferrites are a potential candidate for high-density magnetic recording applications [135].

Thakur et al. (2017) employed the co-precipitation approach to preparing $Mn_{0.5}Zn_{0.5}Fe_2O_4$. The prepared sample crystallite size (average) at 1373, 1173, and 973 K was evaluated to be 67.42, 39.02, and 11.38 nm respectively. The secondary phase Fe_2O_3 was removed during sintering at 1373 K, revealing a single-phase cubical spinel structure. The spinel structure of the prepared samples was assured by the existence of the two sharp bands near 400 and 600 cm^{-1}. The production of homogeneous nanoparticles may be seen in FESEM pictures. The peak of the absorption spectra shifts to a higher wavelength from 214 nm to 285 nm as the sintering temperature rises. The redshift in the PL and decrement in the bandgap energy were noticed with the sintering temperature [136].

Mousa et al. (2017) successfully prepared the ternary NC which consists of Nanoferrite (Fe_3O_4, $NiFe_2O_4$, $CoFe_2O_4$), graphene, and PANI. This ternary NC so formed was then characterized for its structural and electrochemical properties. The development of the single-phase (spinel) in the prepared samples was avowed by the XRD. The fiber structure of PANI was confirmed by TEM micrographs which is very useful for the transfer of electrolyte ions. It has been analyzed that the ternary NCs so formed show an excellent performance than individual and binary NCs. These ternary NCs at 1 A g^{-1} have a very high value of C_{sp} 1123 F g^{-1}. The magnificent P and E of the prepared NC at 1 A g^{-1} were perceived to be 2680 W kg^{-1} and 240 Wh kg^{-1} along with the capacitive retention of 98.2 % beyond 2000 cycles [137].

Praveena et al. (2016) employed a minimal-cost sol-gel approach to preparing the $Ni_{0.4}Zn_{0.2}Mn_{0.4}Fe_2O_4$ NPs. All of the samples had grain sizes ranging from 18 to 30 nanometers. The hysteresis loops indicate a high saturation magnetization and low coercivity, indicating that the material is magnetically soft. Permittivity's imaginary and real constituents are almost constant up to 1 GHz, then rise as the frequency is increased. The permeability is governed by Snoek's law, which states that the value of μ' increases as the temperature rises, and the resonance frequency rises as well. The reflection coefficient, on the other hand, rises with sintering temperature, with the largest loss occurring in the 100 MHz-1 GHz region. The largest reflection loss in the sample sintered at 700 ^{O}C is due to absorption, destructive interference, and many internal reflections in the sample. For all the samples sintered at different temperatures, the quality factor is constant up to 380 MHz and rises with frequency [138].

Liu et al. (2015) focused on preparing the Mn-doped spinel ferrite and its usage as a catalyst. The prepared sample, cationic distribution, and structural characteristics were examined by employing TG-DSC, XPS, Raman, and XRD. The temperature-programmed reduction was employed for estimating the decline in the catalytic activity of the prepared sample. The Mn doping enhances the O_2 content of the lattice, accelerates ferrite reduction, and improves the oxidative activity of the Mn and Fe catalyst's surface. In the presence of water vapor, the investigated catalyst exhibits great stability and superior activity, which is of practical importance. In light of the fluctuation in the physicochemical and microstructural characteristics of the prepared ferrite, the impact of Mn doping on formaldehyde oxidation was explored [139].

Zha et al. (2015) employed a simple two-step approach to preparing $MnFe_2O_4$ Carbon black-PANI NC. The prepared NC at the 5 A g^{-1} manifests superb capacitive retention of 80 % after 10,000 cycles and at 40 A g^{-1} excellent capability rate of 98%. Furthermore, this synthesized NC has outstanding C_{sp}, which accounts for its usage as a minimal-cost SC material for working electrodes [29].

Tholkappiyan et al. (2015) successfully prepared manganese cobaltite nanoparticles under two distinct circumstances. To affirm the phase (spinel) and purity of the prepared sample FTIR and XRD were employed. The elemental analysis and composition of the prepared samples were examined with the XPS. FESEM manifests the sponge-like and flake-like morphology of the Mn (C-C) and Mn (C-H) respectively. The nonporous characteristics of the prepared sample were investigated employing the BET. The two factors viz. state and shape of the prepared material are highly responsible for its electrochemical activity. Because of its flake-like shape, EIS spectra suggest that hydrothermally synthesized $MnCo_2O_4$ has a reduced diffusion resistance. $MnCo_2O_4$ synthesized by a controlled synthesis process has superior capacitance performance and is regarded as a favorable material for the SC as per the electrochemical results [140].

Bahiraei et al. (2014) utilized a sol-gel approach to produce MgCuZn ferrite under varying temperature conditions. They examined the magnetic and structural characteristics of the resulting samples across different temperature ranges. X-ray diffraction (XRD) analysis verified the formation of a single-phase (spinel) structure. Microscopic examinations showed an even distribution of grains and suggested that alterations in sintering temperature had a notable impact on grain elongation and specimen density. The samples demonstrated higher M_s, permeability, grain size, and density as the sintering temperatures increased [141].

Cai et al. (2014) exploited a facile co-deposition approach for the preparation of 1-D nano-sheets of $NiCo_2O_4$-CNT. The hydroxide nano-sheet precursor was then thermally transformed into $NiCo_2O_4$ nano-sheets, with the overall shape and structure being preserved throughout the process. For $NiCo_2O_4$, the CNT acts as a conducting substrate, thereby resulting in excellent electrochemical activity. The prepared sample at 0.5 A g^{-1} manifests superb C_s of 1038 F g^{-1} and has a capacitive retention of 100 % after 1000 cycles. Moreover, a substantial amount of $NiCo_2O_4$ was deposited onto CNT which makes it favorable for SC [142].

Patil et al. (2013) exploited the sol-gel approach to prepare $ZnFe_2O_4$, $ZnMnO_4$, $ZnCrO_4$, and $ZnTiO_4$. The development of the tetragonal (by doping Mn) and spinel (by doping Ti and Cr) phases was avowed by the XRD. The two sharp absorption peaks in the wavenumber ranging from 400-600 cm^{-1} in the FTIR ratify the development of the spinel structure. The agglomerated spherical-shaped particles were perceived in the FESEM for all the prepared specimens. EDX validates the initial composition utilized in the synthesis. VSM revealed the ferromagnetic characteristics of the prepared samples [143].

Rahimi et al. (2013) employed a sol-gel method to synthesize $Ni_{0.3}Zn_{0.7}Fe_2O_4$ ferrite nanoparticles (NPs). The structural and magnetic properties of the prepared sample were significantly affected by the sintering temperature. X-ray diffraction (XRD) analysis confirmed the formation of a single-phase structure in the prepared samples. The average crystallite size ranged from 13 to 58 nm. As the crystallite size increased, so did the saturation magnetization (M_s), while the coercivity initially increased and then decreased, as observed in magnetic studies of sintered samples at different temperatures. AC susceptibility studies on $Ni_{0.3}Zn_{0.7}Fe_2O_4$ NPs suggested a possible interaction among the NPs leading to behavior similar to superspin glasses [144].

Kumbhar et al. (2012) employed a simple chemical technique to produce a thin layer of $CoFe_2O_4$ on an SS substrate. XRD and FTIR analyses confirmed the formation of $CoFe_2O_4$ spinel ferrite. The nanostructured morphology provides a significant surface area, advantageous for supercapacitors. The specific capacitance (C_s) recorded at 366 F g^{-1} suggests its potential for energy storage in supercapacitors [145].

Hilli et al. (2011) had adopted a typical chemical solid reaction approach, to prepare $(Li_{0.5}Fe_{0.5})_{0.5}Ni_{0.5}Gd_yFe_{2-y}O_4$. The microstructure was studied about sintering temperature. The prepared samples exhibit the development of the single-phase (spinel) as per the XRD spectra. A higher doping concentration of Gd in the grain may limit grain development. However,

temperature (sintering), has a substantial influence on the size of the grain as per the SEM. It shows that n-type charge carriers are the majority, implying that electron hopping is the primary method of 44 conduction. The resistivity rose as the Gd substitution increased, but it reduced dramatically when the sintering temperature climbed [146].

Mane et al. (2011) utilized a sol-gel auto-combustion method to synthesize $Cu_{0.7-x}Co_xZn_{0.3}Fe_2O_4$ spinel ferrites, with x varying between 0.0 and 0.5. They observed that the lattice constant increases as the concentration of Co increases. In the synthesized ferrites, Co and Cu ions occupy the octahedral sites, Zn ions occupy the tetrahedral sites, and Fe ions are distributed across both tetrahedral and octahedral sites. The saturation magnetization initially fluctuates, increasing and then decreasing, as the Co content varies [74].

Su et al. (2009) employed the traditional mixed oxide process to prepare $Mg_{0.4}Cu_{0.2}Zn_{0.4}Fe_{1.96}O_4$ and $Ni_{0.4}Cu_{0.2}Zn_{0.4}Fe_{1.96}O_4$. Both types of ferrite samples attained sufficient density when sintered at 900 °C. Owing to the low weight (atomic) of Mg in contrast to the Ni, the density of $Mg_{0.4}Cu_{0.2}Zn_{0.4}Fe_{1.96}O_4$ ferrite was lower. The microstructures of these two types of ferrite samples did not differ significantly. At all sintering temperatures, the prepared $Mg_{0.35}Cu_{0.05}Zn_{0.60}Fe_2O_4$ would have a higher permeability than its counterparts which is on account of the reduction of magnetostrictive and magnetocrystalline constant of $Mg_{0.35}Cu_{0.05}Zn_{0.60}Fe_2O_4$. The contents of Fe^{3+} and Fe^{2+} in the prepared samples do not tend to be influenced by Mg^{2+} or Ni^{2+}, there were no significant variations in permittivity between the two types of ferrite samples [147].

Bhame et al. (2008) The study delved into the magnetostrictive properties of polycrystalline cobalt ferrite manufactured using the traditional ceramic process, focusing on sintering temperature and dwell duration. It was discovered that the degree of magnetostriction is significantly influenced by the microstructure of the final sintered product. Specifically, magnetostrictive strain amplifies when the sintered material features small, evenly distributed grains with decreased porosity. Notably, higher magnetostriction was noted in samples sintered at a lower temperature of 1100°C. These findings were further validated by examining the microstructural and magnetostrictive traits of various additives during the sintering phase [148].

2.2. Research Gap

After surveying numerous literatures in the field of the spinel ferrite - MXenes for energy storage supercapacitors (SCs), a few research gaps were noted and stated below:

- Ferrites have low electronic conductivity and it is required to synthesize ferrite-based composites that can be used as an electrode material for supercapacitors.
- MXenes exhibit outstanding conductivity, adjustable active surface, and excellent mechanical strength, which is ideal for energy storage devices.
- The literature regarding the spinel ferrite – Ti_3C_2 MXene NC used for energy storage SC or many other applications had the blending procedure was very less exploited.
- In most of the literature, Specific capacitance (C_{sp}) for spinel ferrite and Ti_3C_2 MXene were found to be very low, which has to be improved for high-performance energy storage SCs. To enhance the electrochemical activity with the nanocomposite (NCs) of Ternary Spinel ferrite and Ti_3C_2 MXene.
- No research work in the existing literature that compositionally investigates the electrochemical properties of Spinel ferrite, and $Ti_3C_2T_x$ MXenes as synthesized in this research.

To address these research gaps, my current objectives focus on identifying the best spinel ferrite material and synthesizing its nanocomposite (NC) with $Ti_3C_2T_x$ MXenes using simple techniques for energy storage applications. The emphasis is on producing the nanocomposite material in large quantities, ensuring it is eco-friendly, easily accessible, and cost-effective for the benefit of society.

2.3. Objective of the Present Work

The main aim and objectives of the study of the present research are:

1. Investigation of physical properties of rare-earth/transition metal-doped spinel ferrites.
2. Investigation of dielectric and magnetic properties of nanocomposites of synthesized spinel ferrites and MXenes.
3. Electrochemical study of nanocomposites of spinel ferrites and MXenes for energy storage devices.

2.4. Expected Outcome

The project's goal is to create new composite materials that could address and enhance the specific capacitance of the supercapacitor. These advanced composites have the potential to cover electronic equipment such as computers, mobile phones, vehicles, and many more. This project aims to develop solutions that improve environmental quality, enable safe electronic operation, and contribute to commercial applications.

CHAPTER - 3

Method of Synthesis

3. Introduction

The synthesis method plays a significant role in the production of the Spinel ferrite, MXene, and Spinel ferrite–MXene composite. The best synthesis techniques out of the several known techniques as discussed in the chapter, the sol-gel auto combustion, etching method, and physical blending have been utilized for the synthesis of the spinel ferrite, MXene, and spinel ferrite - MXene NC respectively. The synthesis methodology heavily influenced several well-known properties of spinel ferrite, MXene, and spinel ferrite – MXene NC including structural, morphological, magnetic, and electrochemical properties. These properties have a more significant impact on the prepared material's composition, dopant type, and sintering temperature. Furthermore, the electrochemical performance of the prepared materials for supercapacitor electrode preparation is heavily dependent on the type of substrate, binder, conducting material, and electrolyte used. The detailed processes for preparing the materials using the above-mentioned techniques, as well as the properties to be studied, are discussed in detail below in the form of a Table 3.1, 3.2, 3.3, and 3.4.

3.1. Synthesis Method for Spinel Ferrite

The structural, morphological, magnetic, electrical, optical, and electrochemical properties of spinel ferrites mainly depend on their synthesis method. Various methods have been utilized to synthesize spinel ferrites, such as ceramic, co-precipitation, solid-state, hydrothermal, microwave, spray pyrolysis, and sol-gel auto-combustion methods, as depicted in Fig. 3.1. Many researchers have applied this method for the synthesis of spinel ferrites. Bhandare et al. synthesized $Co_{0.5}Mg_xNi_{0.5-x}Fe_2O_4$ ($0 \leq x \leq 0.4$) spinel ferrite using the sol-gel autocombustion method and observed a single-phase spinel structure. The saturation magnetization M_s randomly increases and decreases with increasing dopant concentration [149][150]. At (x = 0.0), coercivity (H_c) attained the maximum value with the substitution of dopant, and the value of H_c randomly increased or decreased. Peng et al. adopted a hydrothermal method to synthesize $CoFe_{2-x}Gd_xO_4$ nanoparticle (x = 0 – 0.25) at 200 °C and confirmed the crystalline nature of the sample using XRD analysis. M_s decreases with increasing concentration of the dopant and exhibits a small particle size [151].

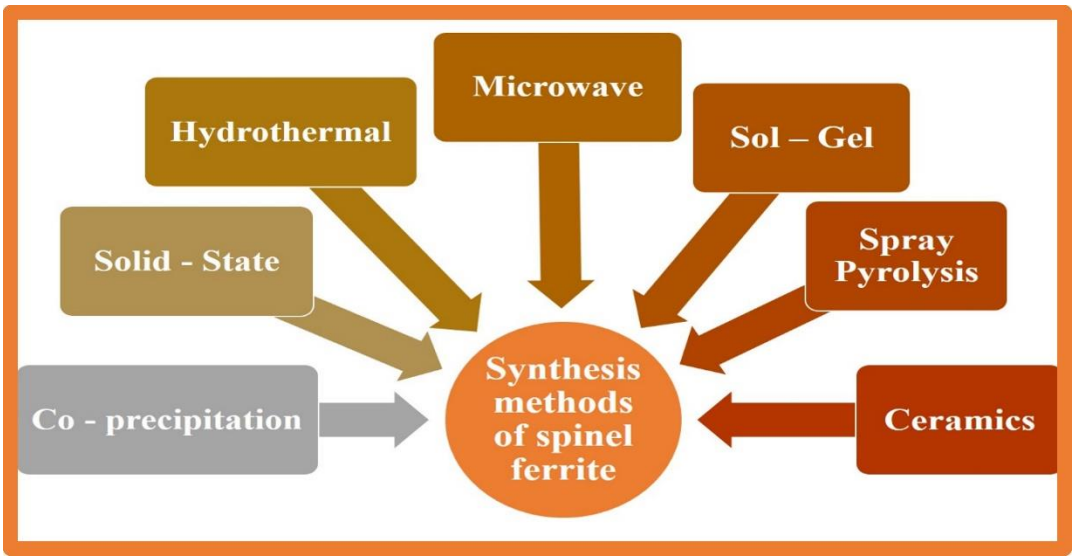

Fig. 3.1. Synthesis methods for spinel ferrite.

The sol-gel method is preferred over the other techniques mentioned above due to its low cost, nanosized structure formation, mass production, homogeneity, formulation of the porous product, minimum time for product synthesis, and formation of the flawless product. Moreover, the utilization of distilled water as a solvent in the sol-gel procedure makes this procedure environmentally friendly [152][153].

3.2. Sol-Gel Method

For the preparation of nanosized oxides of the ferrites, the sol-gel auto combustion method is used. In the preparation process, an exothermic reaction takes place between fuels and oxidized, it is a wet chemical method. In the present work, nitrates are used as oxidants and citric acid as fuel. This method is the most appropriate method to synthesize ferrites over other synthesis methods like solid state method, hydrothermal method, ceramic method, and co-precipitation method. Sol-gel auto combustion method provides controlled morphology, and homogeneity in the samples, time-saving, requires low temperature, and is the cheapest method because the precursors are nitrates and do not require costly equipment. The sol-gel process is mostly used in the production of magnetic nanoparticles. Under steady stirring, metal nitrates metal chlorides, and water solutions are combined, and if we are dealing with the citrate sol-gel technique, we add an adequate quantity of citric acid to the solution while continuing to stir. Following that, a basic solution is added to the solution drop by drop while the solution is constantly stirred. As a result, the pH of the solution is maintained between 7 and 9, and the solution is evaporated at 80 degrees Celsius. A muffle furnace at a temperature of 1000 °C for

5 hours was used to calcine the gel, black fluffy material that had developed after drying and sintering. Following calcination, the resultant ferrite-based nanomaterial was suitable for further investigation into its various characteristics. Researchers are focusing on increasing the quality of the items by making several alterations to the procedure, which they are testing out via a vast number of trials. Fig. 3.2 depicts a schematic representation of the sol-gel method's working mechanism [154].

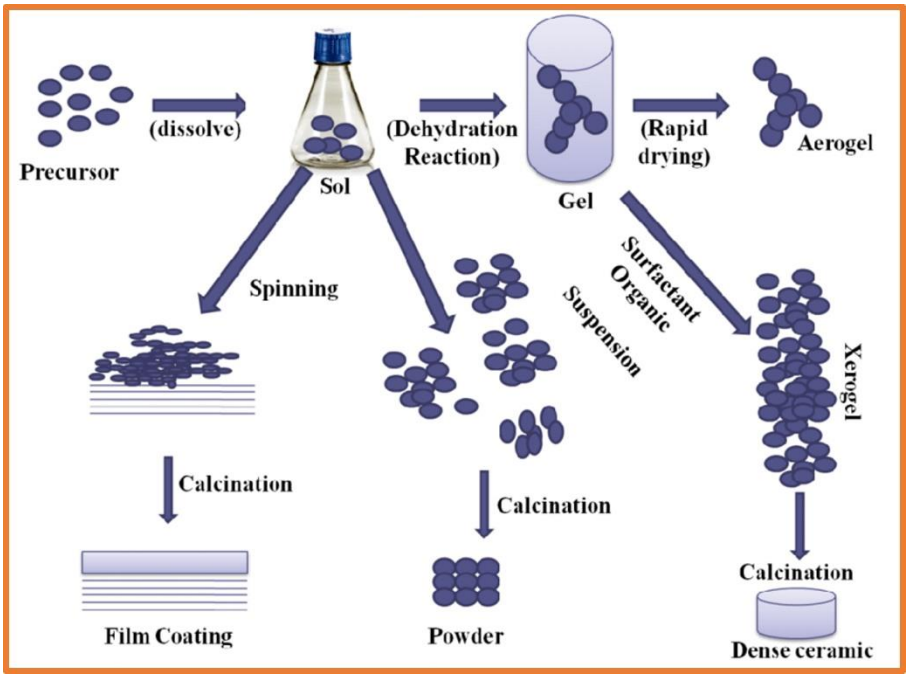

Fig. 3.2. Schematic of the synthesis of the Sol-gel method [155].

3.3. Sol-Gel Autocombustion Method

Sol auto combustion is also known as self-propagation, self-combustion, auto-ignition, and gel thermal decomposition. It also has the advantages of auto combustion, cheap precursors, simple equipment, inexpensiveness, simplicity, and the resulting active nanosized powder and low synthesis temperatures. Analytical reagent (AR) grade chemicals were used for the production of spinel ferrites. The procedure of the sol-gel auto-combustion method is described in Fig. 3.3.

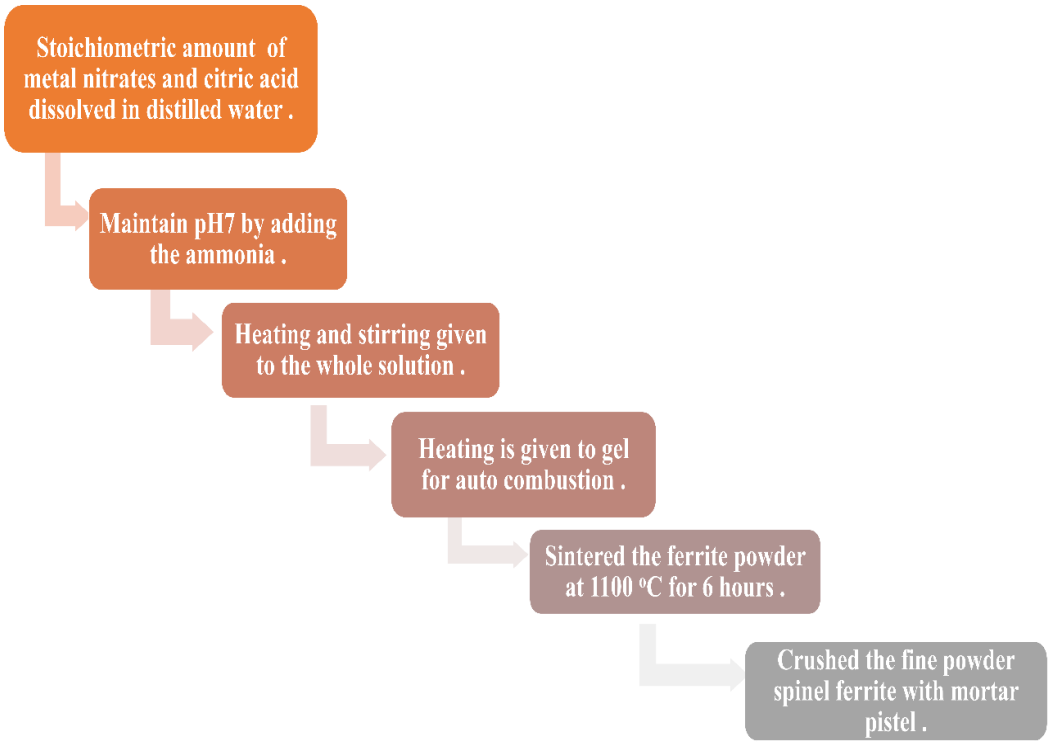

Fig. 3.3. Schematic of the synthesis of the Sol-gel auto combustion method.

3.4. Synthesis of $Zn_{0.2}Mg_{0.8}Fe_2O_4$ Spinel Ferrite

AR grade chemicals were used to synthesize the $Zn_{0.2}Mg_{0.8}Fe_2O_4$ spinel ferrite as in Fig. 3.4. the detailed procedures for the production of spinel ferrite, as well as the characteristics evaluated using different characterization techniques, are included in **Table 3.1**.

Table 3.1 depicts the synthesis procedure of $Zn_{0.2}Mg_{0.8}Fe_2O_4$.

	Material name: Zinc manganese spinel ferrite ($Zn_{0.2}Mg_{0.8}Fe_2O_4$)
	Synthesis method: Sol-gel method
	Sintering temperature at 400 °C, 600 °C, 800 °C
	Chemical used (AR): $Zn(NO_3)_2.6H_2O$, $Co(NO_3)_2.6H_2O$, $Fe(NO_3)_3.9H_2O$, Citric acid
	Metal cation and Citric acid ratio: 1:1
Amount of 100 ml distilled water used for mixing of nitrates and citric acid	
Stirrer the metal nitrate solution for 30 minutes and obtain a clear solution	
	Balance the pH7 by utilizing the ammonia solution
	Magnetic stirring and heating are given to make a gel for 4h at 120 °C

Only heating is given to gel for auto combustion process for 1h at 100 ºC
Further heating of the as a burnt powder to form a fluffy powder for 8-10 h at 80 – 100 ºC
Sintering in a muffle furnace is done for 4h at 400 ºC, 600 ºC, 800 ºC
Grinding of the powder is done by using a mortar and pestel
Properties studied: Structural (XRD and FTIR), Morphology (FESEM), Elemetal (EDX), and Magnetic (VSM)

(0.2) [Zn $(NO_3)_2.6H_2O$)] + (0.8) [Mg $(NO_3)_2.6H_2O$)] + (2) [$Fe(NO_3)_3.9H_2O$)] → $Zn_{0.2}Mg_{0.8}Fe_2O_4$ + H_2O + volatiles

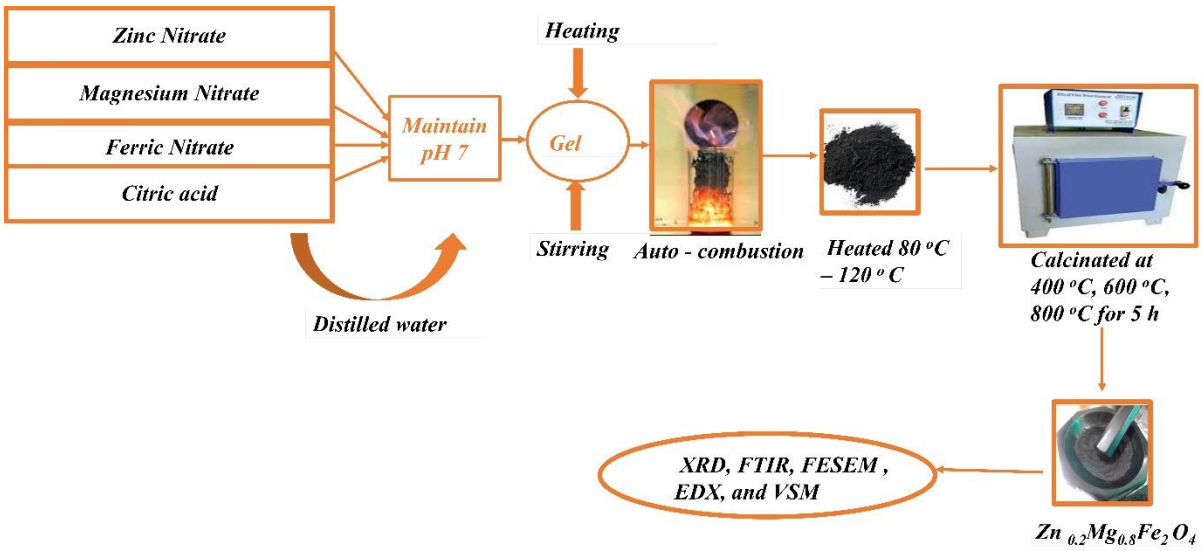

Fig. 3.4. depicts the Schematic of the synthesis of $Zn_{0.2}Mg_{0.8}Fe_2O_4$ spinel ferrite.

3.5. Synthesis of $Mn_xCo_{0.5-x}Ni_{0.5}Fe_2O_4$ Spinel Ferrite (x = 0.0, 0.2, 0.4)

For the production of $Mn_xCo_{0.5-x}Ni_{0.5}Fe_2O_4$ (x = 0.0, 0.2, and 0.4), AR-grade chemicals were utilized as manifested in Fig. 3.5. Table 3.2 lists the detailed processes for producing spinel ferrite, as well as the properties studied employing several characterization techniques.

Table 3.2 manifests the synthesis procedure of the $Mn_xCo_{0.5-x}Ni_{0.5}Fe_2O_4$ ferrite

Material name:	Manganese doped Cobalt spinel ferrite $Mn_xCo_{0.5-x}Ni_{0.5}Fe_2O_4$ ferrite (x = 0.0, 0.2, 0.4)
	Synthesis method: Sol-gel method
	Sintering temperature at 1100 °C
	Chemical used (AR): $Mn(NO_3)_2.6H_2O$, $Co(NO_3)_2.6H_2O$, $Ni(NO_3)_2.6H_2O$ $Fe(NO_3)_3.9H_2O$, Citric acid
	Metal cation and Citric acid ratio: 1:1
Amount of 100 ml distilled water used for mixing of nitrates and citric acid	
Stirrer the metal nitrate solution for 30 minutes and obtain a clear solution	
	Balance the pH7 by utilizing the ammonia solution
	Magnetic stirring and heating are given to make gel for 4h at 120 °C
	Only heating is given to gel for auto combustion process for 1h at 100 °C
Further heating of the as a burnt powder to form a fluffy powder for 8-10 h at 80 – 100 °C	
Sintering in a muffle furnace is done for 4h at 1100 °C	
Grinding of the powder is done by using a mortar and pestel	
Properties studied: Structural (XRD and FTIR), Morphology (FESEM), Elemetal (EDX), Magnetic (VSM), and Dielectric	

(x) [Mn $(NO_3)_2.6H_2O$)] + (0.5-x) [Co $(NO_3)_2.6H_2O$)] + 0.5 [Ni $(NO_3)_2.6H_2O$] + (2) [$Fe(NO_3)_3.9H_2O$)] → $Mn_xCo_{0.5-x}Ni_{0.5}Fe_2O_4$ + H_2O + volatiles

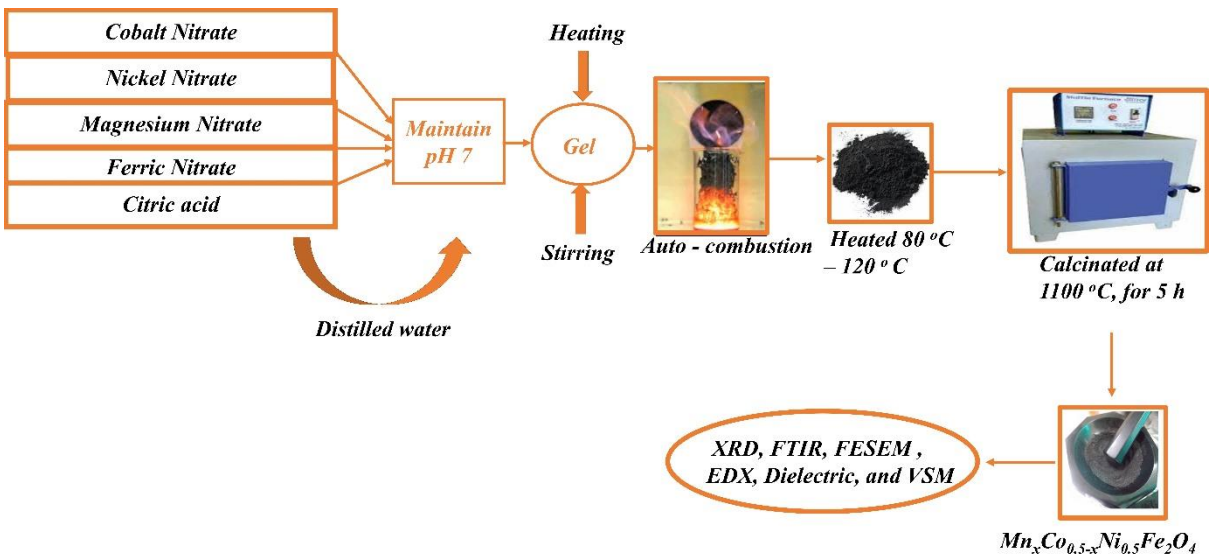

Fig. 3.5. represents the synthesis of $Mn_xCo_{0.5-x}Ni_{0.5}Fe_2O_4$ ferrite.

3.6. Synthesis of $Pr_xMn_{0.5}Co_{0.5}Fe_{2-x}O_4$ Spinel Ferrite (x = 0.00, 0.01, 0.02, 0.03, 0.04)

Synthesis of nanoparticle $Pr_xMn_{0.5}Co_{0.5}Fe_{2-x}O_4$ (x = 0.00, 0.01, 0.02, 0.03, and 0.04) was performed by sol-gel route as in Fig. 3.6. Table 3.3 Detailed procedure for the synthesis of $Pr_xMn_{0.5}Co_{0.5}Fe_{2-x}O_4$ ferrite and also characterization technique.

(0.5) [Mn $(NO_3)_2.6H_2O$)] + (0.5) [Co $(NO_3)_2.6H_2O$)] + x [Pr $(NO_3)_3.6H_2O$] + (2 − x) [Fe $(NO_3)_3.9H_2O$)] → $Pr_xMn_{0.5}Co_{0.5}Fe_{2-x}O_4$ + H_2O + volatiles

Table 3.3. Detailed procedure for the synthesis of $Pr_xMn_{0.5}Co_{0.5}Fe_{2-x}O_4$ ferrite.

Material name:	$Pr_xMn_{0.5}Co_{0.5}Fe_{2-x}O_4$ ferrite (x = 0.00, 0.01, 0.02, 0.03, 0.04)
	Synthesis method: Sol-gel method
	Sintering temperature at 1100 ºC
	Chemical used (AR): $Pr(NO_3)_3.9H_2O$, $Mn(NO_3)_2.6H_2O$, $Co(NO_3)_2.6H_2O$, $Fe(NO_3)_3.9H_2O$, Citric acid
	Metal cation and Citric acid ratio: 1:1
Amount of 100 ml distilled water used for mixing of nitrates and citric acid	
Stirrer the metal nitrate solution for 30 minutes and obtain a clear solution	
	Balance the pH7 by utilizing the ammonia solution
	Magnetic stirring and heating are given to make gel for 4h at 120 ºC
	Only heating is given to gel for auto combustion process for 1h at 100 ºC
Further heating of the as a burnt powder to form a fluffy powder for 8-10 h at 80 – 100 ºC	
Sintering in a muffle furnace is done for 4h at 1100 ºC	
Grinding of the powder is done by using a mortar and pestel	
Properties studied: Structural (XRD and FTIR), Morphology (FESEM), Elemetal (EDX), Magnetic (VSM)	

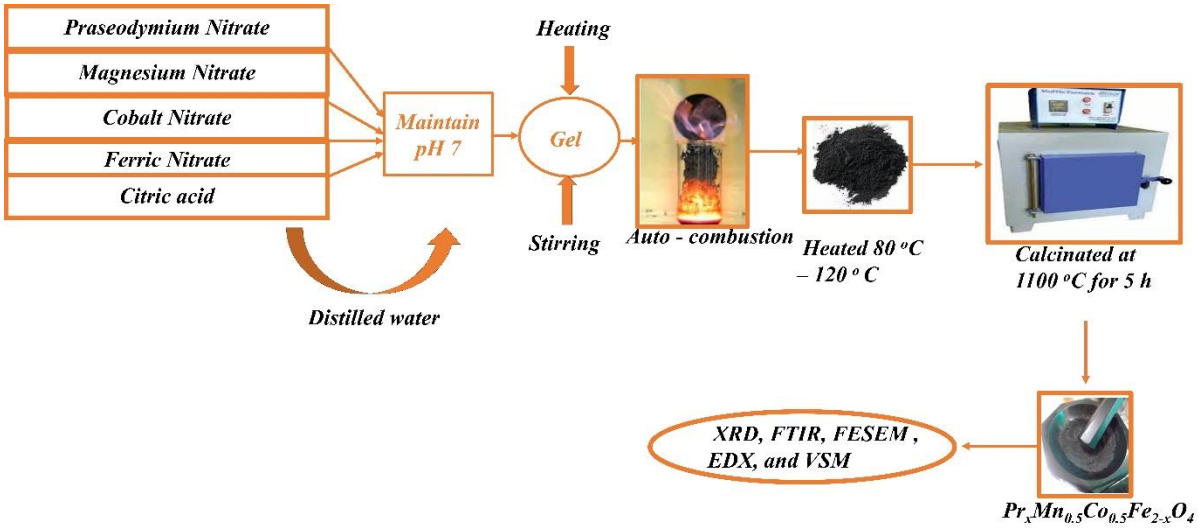

Fig. 3.6. Synthesis steps of $Pr_xMn_{0.5}Co_{0.5}Fe_{2-x}O_4$ spinel ferrite.

3.7. Synthesis of $Pr_{0.02}Mn_{0.5}Co_{0.5}Fe_{1.98}O_4$ Spinel Ferrite (x = 0.02)

$Pr_{0.02}Mn_{0.5}Co_{0.5}Fe_{1.98}O_4$ utilized sol-gel auto combustion technique as in Fig. 3.7.

Table 3.4. Detailed procedure for the synthesis of $Pr_{0.02}Mn_{0.5}Co_{0.5}Fe_{1.98}O_4$ ferrite.

Material name: $Pr_{0.02}Mn_{0.5}Co_{0.5}Fe_{1.98}O_4$ ferrite (x = 0.02)	
	Synthesis method: Sol-gel method
	Sintering temperature at 1100 °C
	Chemical used (AR): $Pr(NO_3)_3.9H_2O$, $Mn(NO_3)_2.6H_2O$, $Co(NO_3)_2.6H_2O$, $Fe(NO_3)_3.9H_2O$, Citric acid
	Metal cation and Citric acid ratio: 1:1
Amount of 100 ml distilled water used for mixing of nitrates and citric acid	
Stirrer the metal nitrate solution for 30 minutes and obtain a clear solution	
	Balance the pH7 by utilizing the ammonia solution
	Magnetic stirring and heating are given to make gel for 4h at 120 °C
	Only heating is given to gel for auto combustion process for 1h at 100 °C
Further heating of the as a burnt powder to form a fluffy powder for 8-10 h at 80 – 100 °C	
Sintering in a muffle furnace is done for 4h at 1100 °C	
Grinding of the powder is done by using a mortar and pestel	

Properties studied: Structural (XRD and FTIR), Morphology (FESEM and HRTEM), Elemetal (EDX and XPS), Magnetic (VSM)

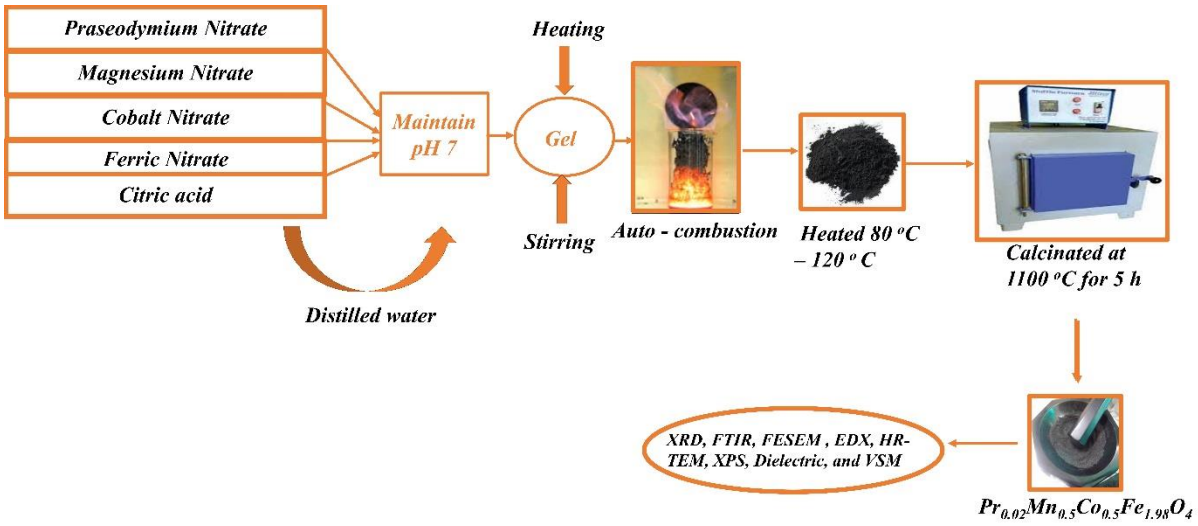

Fig. 3.7. Schematic synthesis of the $Pr_{0.02}Mn_{0.5}Co_{0.5}Fe_{1.98}O_4$ spinel ferrite.

3.8. Synthesis of Ti_3C_2 MXene

The chemical etching method is utilized to synthesize Ti_3C_2 MXene as in Fig. 3.8. Ti_3AlC_2 is a MAX phase used to etch the 'Al' using the etching method. In this method, 50 ml of HCl was poured into a Teflon bottle and swirled for 20 min. 3g LiF was added to the HCl and mixed properly for 30 min. Then, 2g of MAX-phase Ti_3AlC_2 is added to the HCl + LiF solution. The whole solution was kept at room temperature and continuous stirring for 48 h. The whole solution was then centrifuged at 4500 rpm and washed with distilled water until a pH of 7 was obtained. After vacuum filtration, the powder was oven to 90 ° C for 6 h. Properties to study for material XRD, FESEM, HR-TEM, XPS, VSM, Dielectric, CV, GCD, and EIS.

$$4Ti_3AlC_2 + 14LiF + 14HCl = 3Ti_3C_2 + Ti_3C_2F_2 + 2AlF_3 + Li_3AlF_6 + AlCl_3 + 11LiCl + 7H_2$$

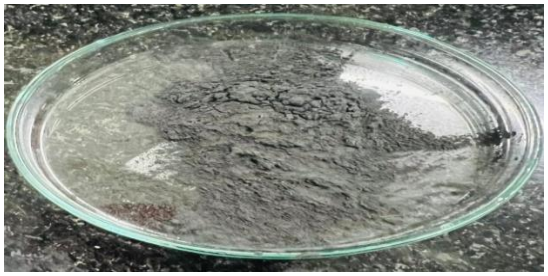

Fig. 3.8. Fine powder of Ti_3C_2 by using Fluoride etching method.

3.9. Synthesis Method of Spinel Ferrite – MXene Nanocomposite

Scientists working on the MXene-based nanocomposite material primarily use two methods for its synthesis, namely in situ polymerization and blending or direct compounding [156], as presented in Fig. 3.9.

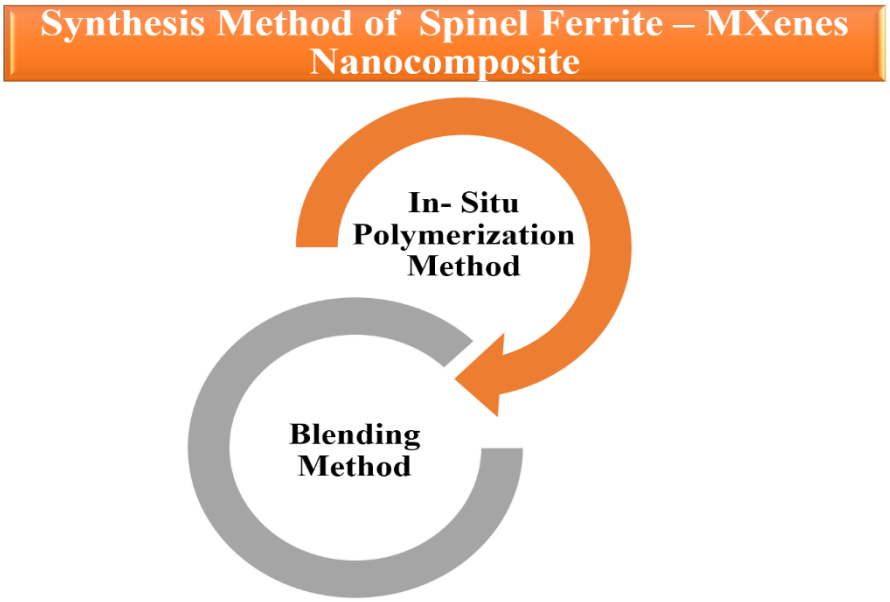

Fig. 3.9 Method for the synthesis of spinel ferrite – MXene nanocomposite.

The blending method is used for the synthesis of spinel ferrite–MXene-based nanocomposites. This method is advantageous owing to ease of synthesis, reduced time, and low cost. Furthermore, in the blending method, it is more difficult to achieve a proper distribution of the nanoparticles in MXene than in the in situ polymerization method [156].

3.10. Blending Method

Blending, also known as direct compounding, has been proposed as a quick and easy way to create 2D nanocomposites (NCs). As shown in Fig. 3.10, the most common blending procedures are solution, emulsion, melt, mechanical, and physical. These blending processes entail the direct incorporation of nanoparticles (NPs) into MXene in the required proportions. MXene and NP preforms were prepared separately before being combined to form the NCs. Apart from the benefits, there are some drawbacks to this procedure, such as non-uniform NP distribution within MXenes due to NP agglomeration [50][156].

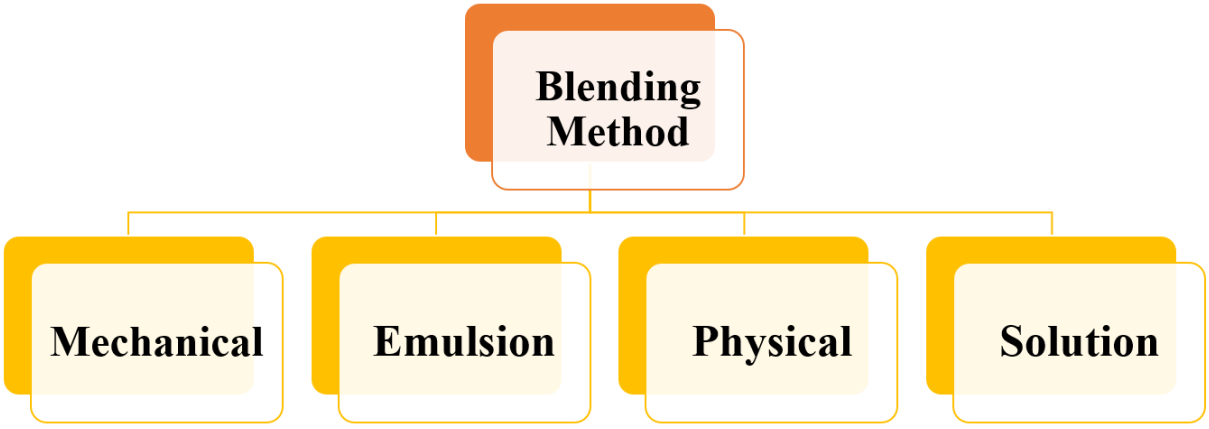

Fig. 3.10. Blending method for the synthesis of the MXene nanocomposite.

3.11. Synthesis of $Pr_{0.02}Mn_{0.5}Co_{0.5}Fe_{1.98}O_4$ - Ti_3C_2 MXene nanocomposite

A Physical blending technique was used for the synthesis of the nanocomposites. The weight ratio of Mxene (Ti_3C_2) and spinel ferrite ($Pr_{0.02}Mn_{0.5}Co_{0.5}Fe_{1.98}O_4$) is taken to be 1:5, which was physically blended with the mortar pestle and homogenized, as shown in Fig. 3.11. Various properties study XRD, FESEM, HR-TEM, XPS, VSM, Dielectric, CV, GCD, and EIS.

$Pr_{0.02}Co_{0.5}Mn_{0.5}Fe_{1.98}O_4 + Ti_3C_2 \rightarrow Pr_{0.02}Co_{0.5}Mn_{0.5}Fe_{1.98}O_4$ - Ti_3C_2

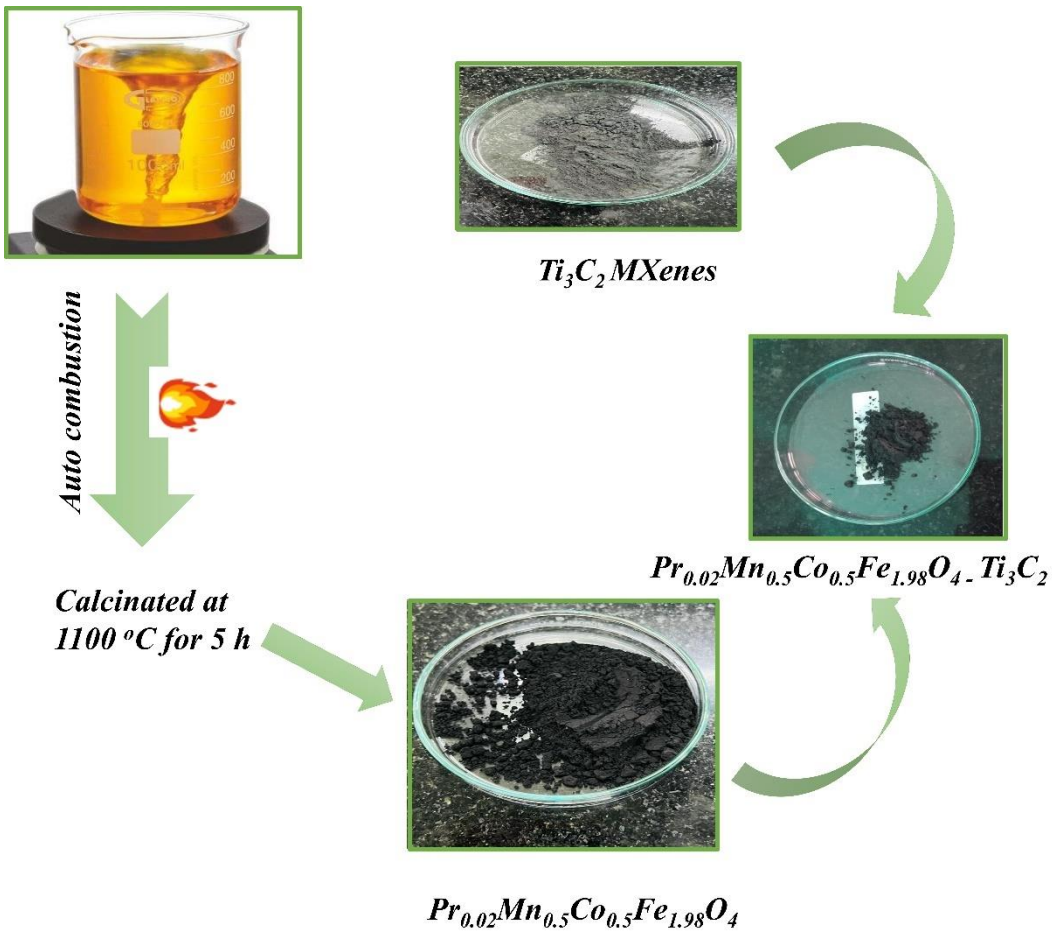

Fig. 3.11. depicts the physical blending method of the $Pr_{0.02}Co_{0.5}Mn_{0.5}Fe_{1.98}O_4$ - Ti_3C_2.

3.12. Fabrication of Electrochemical Electrode

A three-electrode apparatus was used to conduct the electrochemical examination at room temperature. The working electrode (ink-loaded nickel foam), reference electrode (Ag/AgCl), and counter electrode (platinum wire) were the three electrodes used. The experiment was carried out with 3 M KOH as the electrolyte. To remove the nickel oxide layer, nickel foam (1 cm × 1 cm) was sonicated in 3 M HCl at 50 °C for 1 h before being used as a working electrode and manifested in Fig. 3.6. The nickel foam was then repeatedly rinsed with ethanol and distilled water before being dried at 60 °C for 3 h. The ink drop casting method was adopted to prepare electrodes of $Pr_{0.02}Mn_{0.5}Co_{0.5}Fe_{1.98}O_4$, Ti_3C_2, and $Pr_{0.02}Mn_{0.5}Co_{0.5}Fe_{1.98}O_4 – Ti_3C_2$ as in Fig. 3.12. The active material mass ($Pr_{0.02}Mn_{0.5}Co_{0.5}Fe_{1.98}O_4$, Ti_3C_2, and $Pr_{0.02}Mn_{0.5}Co_{0.5}Fe_{1.98}O_4 – Ti_3C_2$) (70 wt%), acetylene black as a conductive agent (10 wt%), and

polyvinylidene fluoride (PVA) as a binder (10 wt%) were homogenously mixed with four drops of n-methyl-2-pyrrolidone (NMP) as a solvent. The ink loaded onto the nickel foam with an area (1 cm×1 cm) was dried at 65 °C for 10 h. However, similar techniques were used to prepare the working electrodes of Ti_3C_2 MXene and $Pr_{0.02}Mn_{0.5}Co_{0.5}Fe_{1.98}O_4 – Ti_3C_2$ nanocomposites.

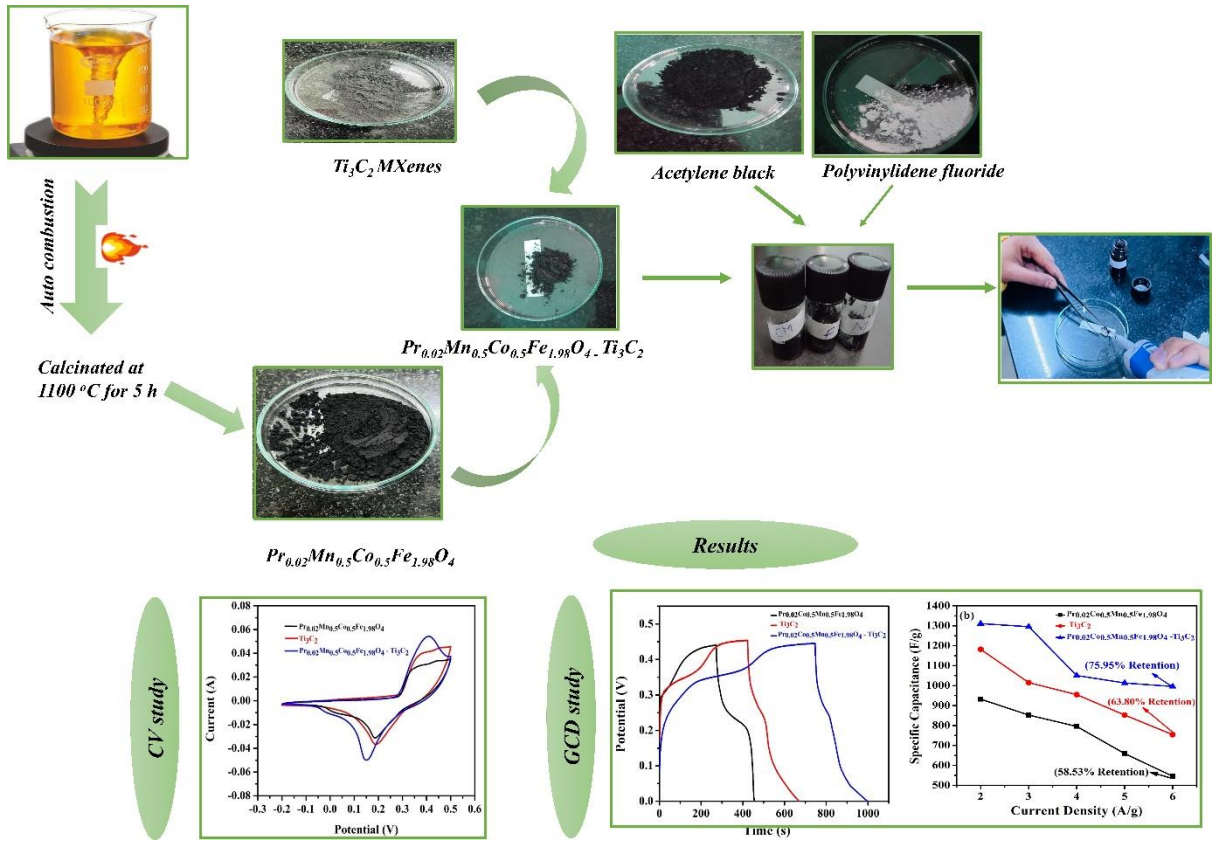

Fig. 3.12. Steps of fabrication of electrode $Pr_{0.02}Mn_{0.5}Co_{0.5}Fe_{1.98}O_4$, Ti_3C_2, and $Pr_{0.02}Mn_{0.5}Co_{0.5}Fe_{1.98}O_4 – Ti_3C_2$.

CHAPTER 4

Characterization Technique

4. Characterization Techniques

The structural, morphological, magnetic, and electrochemical characteristics of the prepared samples were investigated using the following characterization techniques.

4.1. X-ray diffraction (XRD)

This technique is widely used to study the crystallographic details of materials [157]. XRD is the most frequently employed analytical tool for determining the crystallinity of a prepared specimen and for accumulating information on the phase and dimensions of the unit cell of the material. It is a non-destructive and non-contact technique that provides structural information, lattice parameters, grain size, structural defects, structural epixity, and phase information. XRD is a constructive interference of monochromatic radiation that scatters at specific angles within a specimen's lattice planes, and atomic variation determines peak intensities. An X-ray wavelength range of 10^{-3} – 10^{-1} nm is produced from an X-ray tube with a high-velocity electron by bombarding a metal target [158]. The fundamental principle of the identification technique is based on constructive interference, which occurs in cathode ray tubes and produces a monochromatic beam of X-rays from a crystalline sample. The X-ray beam interacts with the object and scatters with the same energy as that of the input photons in random directions. This analysis is applicable only to crystalline or semicrystalline matter. As a result, if the sample under examination has a regular atomic arrangement, the dispersed light is oriented in specific directions determined by the X-ray wavelength, crystal lattice dimensions, and orientation [159].

X-rays are a form of electromagnetic energy that originates from the electron clouds of atoms. Fig. 4.1 shows that the monochromatic X-ray beam is collimated and bombarded onto the specimen. As the sample and detecting sensor are turned on, the intensity of the diffracted or reflected X-rays is gathered and measured in a range of angles (2θ) with respect to the incident X-ray beam [160]. Interference due to the X-ray diffracted beam from a crystallographic plane is observed as a peak related to Bragg's angle (θ) and the detector records the X-ray signal. Then, it converts the signal to a count rate that is connected to an output device such as a printer or computer monitor. As in Eq. (4.1) when the incident angles fulfill Bragg's condition a constructive interference pattern is produced [89].

$$2d \sin \theta = n \lambda \qquad (4.1)$$

where d is the plane spacing, θ is the Bragg angle, n is the order of diffraction, and λ is the X-rays of wavelength. XRD tests were performed on a Powder X-ray diffractometer (Bruker D8 Advance).To identify the phases of the materials, the X-ray powder diffraction data were compared with the Joint Committee Powder Diffraction Standards (JCPDS) or American Standards for Testing of Materials (ASTM) [161].

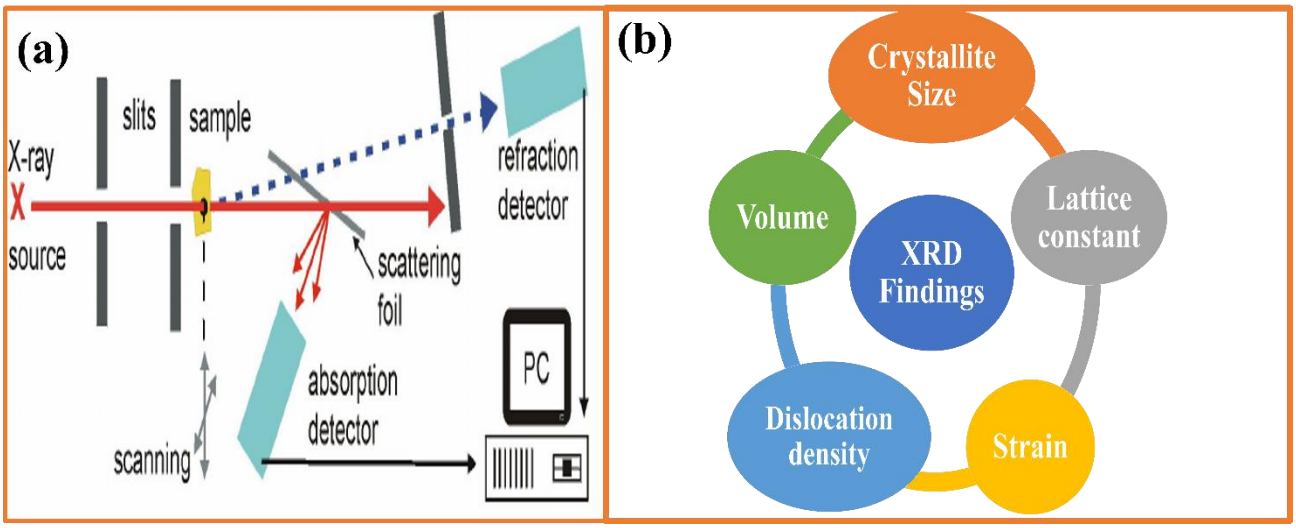

Fig. 4.1. (a) Schematic of the principle of X-ray diffraction. (b) Findings of XRD.

4.2. Fourier Transform Infrared Spectroscopy (FTIR)

FTIR spectroscopy was used to investigate the interactions between the infrared and the sample. Its work is to investigate the vibrational properties of molecules in matter. This method can be used to identify the various functional groups and residues in a sample. The IR region, which extends from (0.7-1) to (200-350) μm can be categorized into three ranges as follows: Near IR 13000 - 4000 cm^{-1}, Mid IR between 4000-400cm^{-1} Far infrared between 400-10 cm^{-1} [162]. Far-infrared has low energy; therefore, it is used to study fundamental and rotational vibrations. Mid-infrared with moderate energy is used to study coupled rotational–vibrational structures. Near IR has high energy, so it is used for exciting overtone vibrations. For characterization purposes, the mid-infrared spectrum is used. Infrared radiation is passed through the material to be absorbed by the molecules it contains in FTIR spectroscopy. The vibration frequencies of the molecules must be equal to those of radiation so that matter can absorb energy. When light strikes a sample, one part of it is reflected, another is absorbed, and the third is transmitted. The exact frequencies of energy absorbed by the specimen match the

vibrational energy of the functional group in the sample. A detector collects the transmitted light that carries the molecular information of the sample [163]. The mid-infrared frequencies in FTIR are measured by the interferometer in a few seconds. The interferometer is used to analyze the energy transmitted through the material. The interferometer contains a beam splitter, stable mirror, and moving mirror. that split the falling IR radiation into two parts. One beam is set so that it can retain a fixed path length and create a path difference for the other beam that varies according to the moving mirror. These two beams interfere constructively, and a beam is emitted from the interferometer, which is known as an interferogram. The emitted beam consists of all information about the sample. With the help of a mathematical technique software named Fourier transformation, all the information is decoded from the individual frequencies. Nicolet FTIR interferometer IR prestige-21 with model-8400S was used as the FTIR spectrometer [164][165] [166]. The FTIR spectrum interpretation is simple because the wavenumber is proportional to energy and frequency. Fig. 4.2 depicts the principle of FTIR.

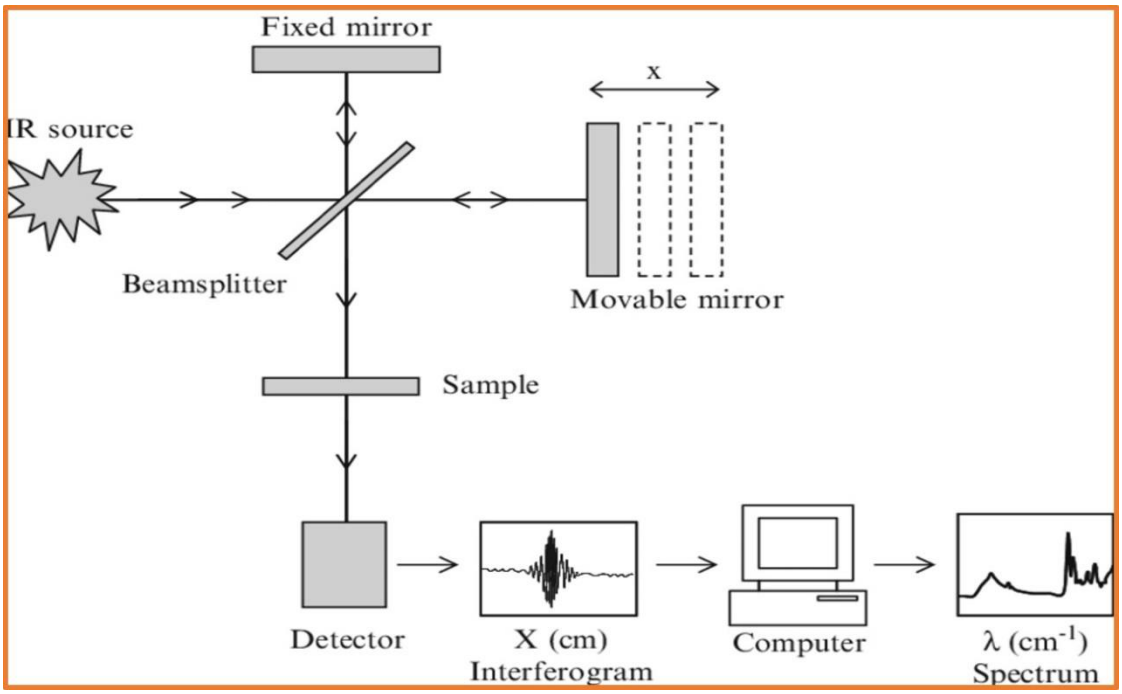

Fig. 4.2. Principle of FTIR spectroscopy.

4.3. X-Ray Photoelectron Spectroscopy (XPS)

X-ray photoelectron spectroscopy (XPS) is an analytical method used to investigate specimen surfaces and chemical compositions. X-ray photoelectrons (XPS) is a well-known non-damaging, surface-sensitive, and quantitative surface analysis tool. XPS offers elementary composition, empirical pure material formula, surface contamination, and chemical/electronic element state details. Ion beam grafting (depth profiling) can characterize the homogeneity of the elemental composition over the top surface (profiling or mapping) as well as the elementary composition. Historically, Robinson and Young's work in 1930 was an important step forward in photoelectron spectrometry. In the 1950s, Siegbahn's group investigated the first precision electron spectrometer, but by the end of the 1960s, it was the first commercial XPS instrument. The application of XPS to material science increased dramatically by around 1985, when digital systems, multi-channel detection, and higher analyzers were developed. XPS is one of the most advanced and complete modern surface-research instruments. The XPS technique enables the identification of various material types such as metals, alloys, polymers, semiconductors, geologic and biological samples, and any surface supporting a high-vacuum device. When X-rays strike a material under vacuum, the innermost orbital electrons are ejected at the sample surface. The number of electrons ejected and their kinetic energy (K.E) are used to obtain the XPS spectra. The electron number indicates the element proportion in the sample. The binding energy of the emitted electron demonstrates the oxidation state of each element. The binding energy (B.E) of the emitted electron is determined from the, as given in Eq. (4.2).

$$E_{binding} = E_{photon} - E_{kinetic} - \Phi \quad (4.2)$$

Where, $E_{binding}$ and $E_{kinetic}$ refer to the B.E and K.E of the emitted electron, respectively, E_{photon} is the energy of the X-ray photon used and Φ is the work function [167][168]. The energy of the produced photoelectrons is then measured using an electron energy analyzer. X-ray photoelectron spectroscopy (XPS) measurement was using a spectrometer (Thermo Scientific K-Alpha). The resulting binding energy-dependent intensity allows the determination of the surface chemical state, elemental breakdown, and elemental quantities [169][170]. Various components of the XPS instrument are depicted in Fig. 4.3(a) and the XPS findings are shown in Fig. 4.3(b).

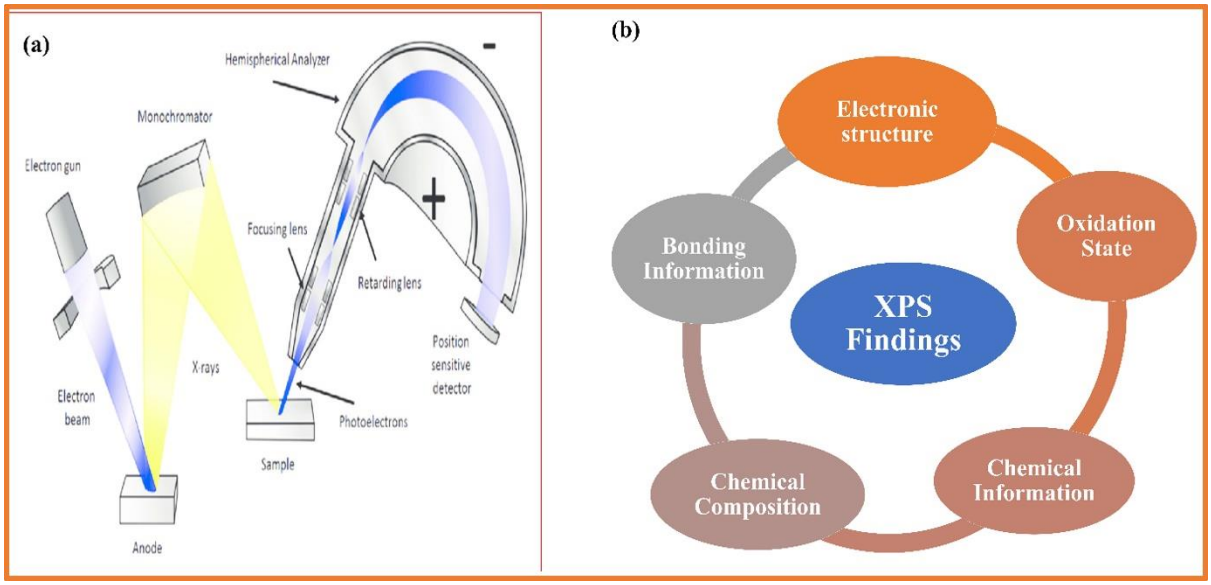

Fig. 4.3. (a) Working of XPS **(b)** Findings of XPS.

4.4. Field Emission Scanning Electron Microscopy (FESEM)

FESEM is an essential electron microscopic technique for analyzing micrographs and investigating the structural properties of microstructured materials in high-resolution specimens at depths ranging from 10,000 to 300,000 times [171]. The fundamental concept behind FESEM is to scan the samples with electrons rather than light. Electrons can be produced by an electron gun or field emission source and then accelerated using a field emission source gradient. To focus the beam, it is passed through an electromagnetic lens, which allows it to fall on the samples. Various types of electrons are emitted from the sample. Secondary electrons are useful for generating sample surface images [172]. The electrons either disappear without any interaction or are dispersed within the cloud with a potential. The ejection of electrons from the specimen occurs because of the number of interactions between the specimen and the electron beam. This interaction involves the emission of Auger electrons, back-scattered electrons, and secondary electrons. The secondary electrons and backscattered electrons are separated, depending on the energy [173]. FESEM was used to confirm the surface morphology (FE-SEM: JEOL JSM-7610 F Plus). The detector collects secondary electrons and produces electrical signals, which are amplified and converted into scan images that appear on the screen as a digital image of a sample surface. Fig. 4.4 depicts the FESEM results.

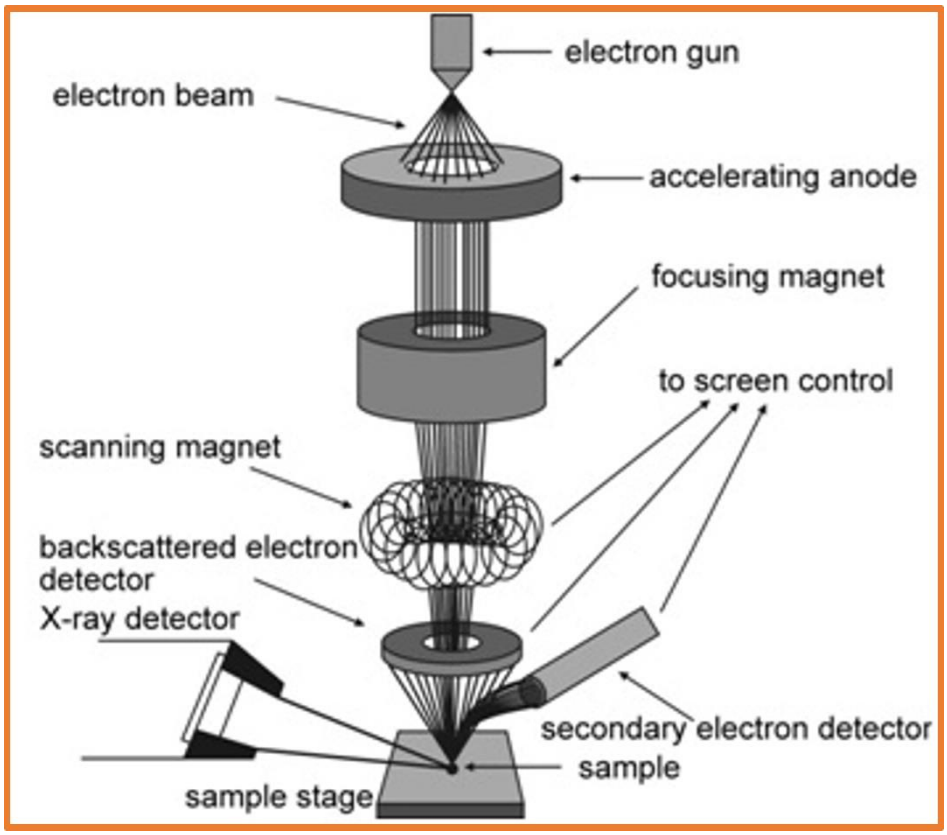

Fig. 4.4. depicts the working principle of the FESEM.

4.5. Energy Dispersive X-Ray Spectroscopy (EDX)

Heinrich (1968) determined the quantification technique for determining the intensity of X-rays. EDX is used to determine the elemental composition and ratio of specimens [174]. EDX is mainly based on the concept that a specific atomic structure of an element can exhibit a distinct set of peaks in its emission spectrum [175]. The K, L, and M shells of the electron around an atom's nucleus are schematically depicted in Fig. 4.5. In EDX electrons are bombarded on the sample to induce the emission of X-rays, which may exit and emit from the innermost layer, and the outermost layer electron fills the hole and emits energy in the form of X-rays [176]. The difference in energy is equal to the energy between the two shells in which electronic transitions occur, allowing the identification of the elements present in the test specimen. The low detection limit varies from ~ 0.1 to several atomic percentages, reliant on the element and matrix of the sample. The chemical composition was determined by EDX

spectroscopy (EDX: OXFORD EDX LN2 free). An X-ray spectrometer can examine radiation and identify test sample elements based on their wavelength (characteristic) [177].

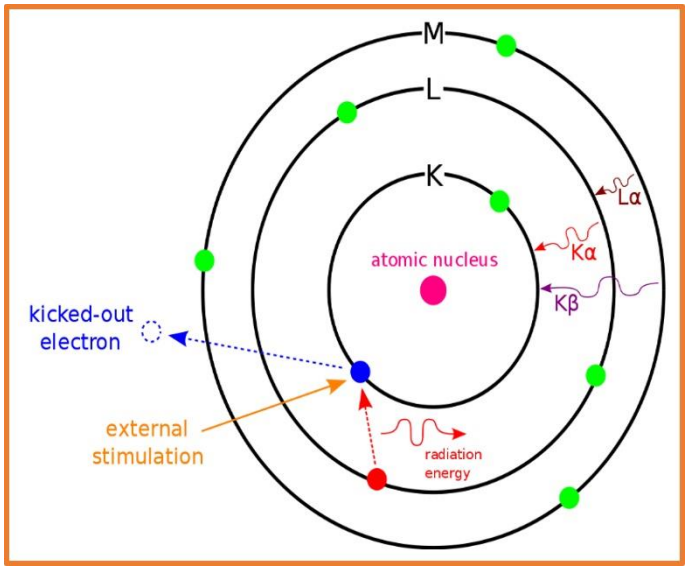

Fig. 4.5. depicts the principle of EDX spectroscopy.

4.6. High-Resolution Transmission Electron Microscopy (HR-TEM)

Transmission electron microscopy (TEM) is used to determine the morphology, crystallography, size, and elemental composition by transmitting a focused electron beam through the sample. TEM is capable of providing both atomic-resolution images and chemical information. They usually have a spatial resolution of 1 nm. [178]. HRTEM can be used to determine the sample composition, electronic structure, and chemical bonding. The HRTEM instruments are depicted in Fig. 4.6(a). The various findings of HRTEM are depicted in Fig. 4.6(b). TEM can be used to focus on a single nanoparticle and derive its chemical and structural information. TEM works on the principle of electron diffraction. The electron beam emitted from the filament passes through various electromagnetic lenses to strike the specimen. The smaller the wavelength of the electron beam, the higher the desired resolution. The majority of the beam striking the specimen is transmitted, which is focused to obtain an image. However, aberrations in the lenses limit the resolution of TEM. HRTEM is an imaging mode in TEM that is used to investigate crystal structures. The electrons interact with the thin sample to produce electron waves that undergo a phase change in the image plane [178]. With HRTEM, crystal structures and defects in the crystal can be imaged effectively. It is also equipped with a Bruker

Xflash 6TI30 with an LN2-free detector for elemental composition studies. The instrument includes both dark-field and bright-field imaging with selected area electron diffraction (SAED) patterns [179][180].

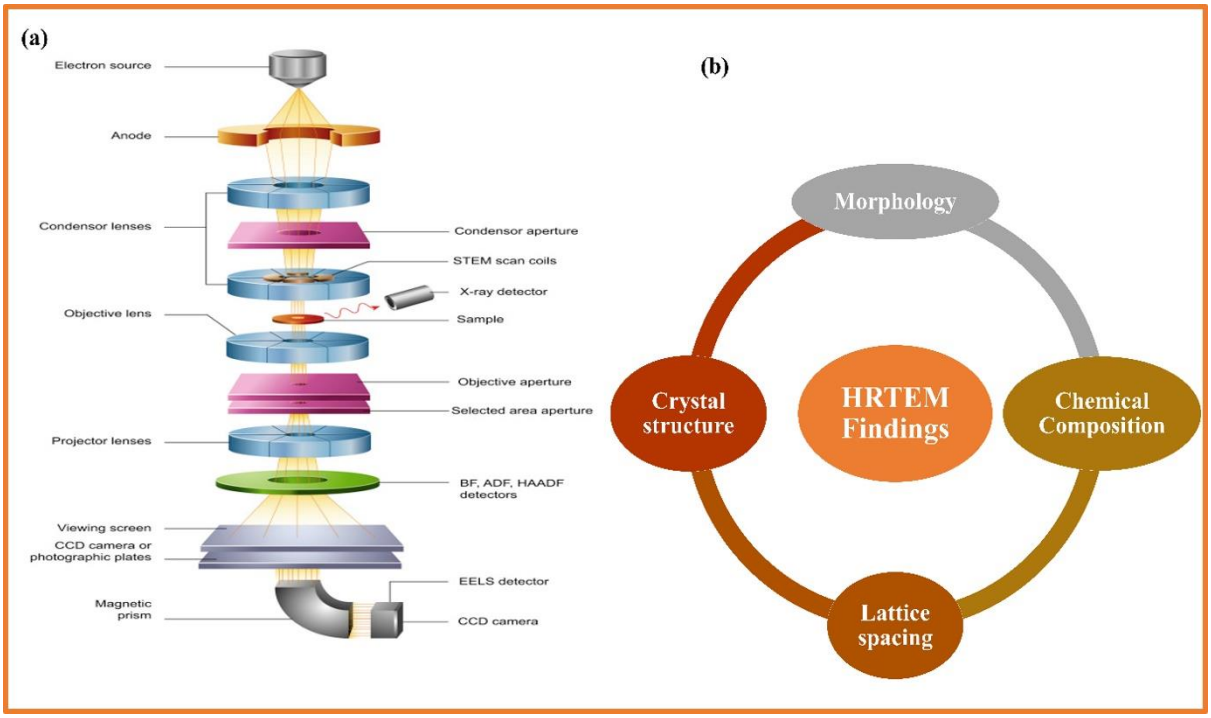

Fig. 4.6(a) working of HRTEM and **(b)** HRTEM findings.

4.7. Vibrating Sample Magnetometer (VSM)

A VSM is a piece of scientific equipment that analyzes magnetic properties using Faraday's Law of Induction, also known as a Foner magnetometer. In 1959, Simon Foner designed the VSM at the MIT Lincoln Laboratory [181]. VSM is a useful technique for determining the characteristics of magnetic materials. The experimental sample is placed in a sample holder, which is then sandwiched between two sets of pickup coils connected to an electromagnet. Because of the uniformity of the electromagnet's magnetic field, magnetization is induced in the sample. The sample holder, which holds the sample inside, is designed to vibrate mechanically in a sinusoidal pattern [182]. When a vibrating component produces a variation in the magnetic field of the sample, Faraday's law of electromagnetic induction produces an electric field corresponding to the magnetization. The magnetic properties of spinel ferrite were investigated using a VSM (VSM-EZ9).Variations in magnetic flux cause a voltage

in the pickup coils that is proportional to the magnetization of the sample [183][184]. These changes are converted into a graph of magnetization (M) against the applied magnetic field by software in a computer connected to the VSM equipment (H), as shown in Fig. 4.7

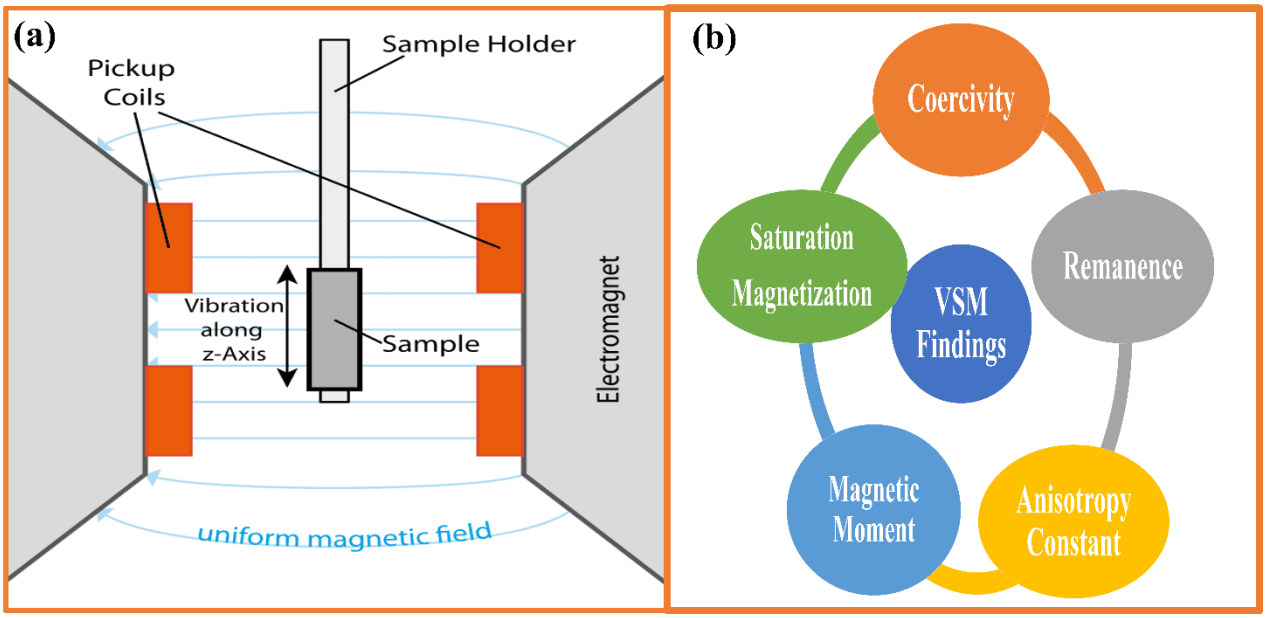

Fig. 4.7. (a) manifests the principle of the VSM. **(b)** Findings of VSM.

4.8. Impedance Analyzer

An impedance analyzer is a component of electrical devices that examines impedance and admittance. When voltage is provided to a circuit or device, the overall opposition offered to the flow of periodic current (AC test signal) is called impedance. The real and imaginary components are part of the periodic current [185]. The impedance can be written as Eq. (4.3) when the connection is made in series.

$$Z = R + jX \tag{4.3}$$

where X is the reactance (which is the imaginary component of impedance), R is the resistance (which is the real component of impedance), and j is an imaginary number. By plotting the x-axis as resistance and the y-axis as the reactance, the impedance can be calculated [186]. Wynne Kerr impedance analyzer (Model 6500). In general, the device under test (DUT) is provided with AC voltage, and impedance (Z) and capacitance (C) are used to assess the

DUT's response. The angle (θ) formed by the impedance (Z) along the x-axis is also measured [187]. Various dielectric parameters, such as the real part of permittivity (ε), the imaginary part of permittivity (ε'), dielectric tangent loss (tanδ), and AC conductivity, can be calculated using acquired data, such as impedance (Z), capacitance (C), and angle (θ). Fig. 4.8 manifests the universal impedance analyzer [187].

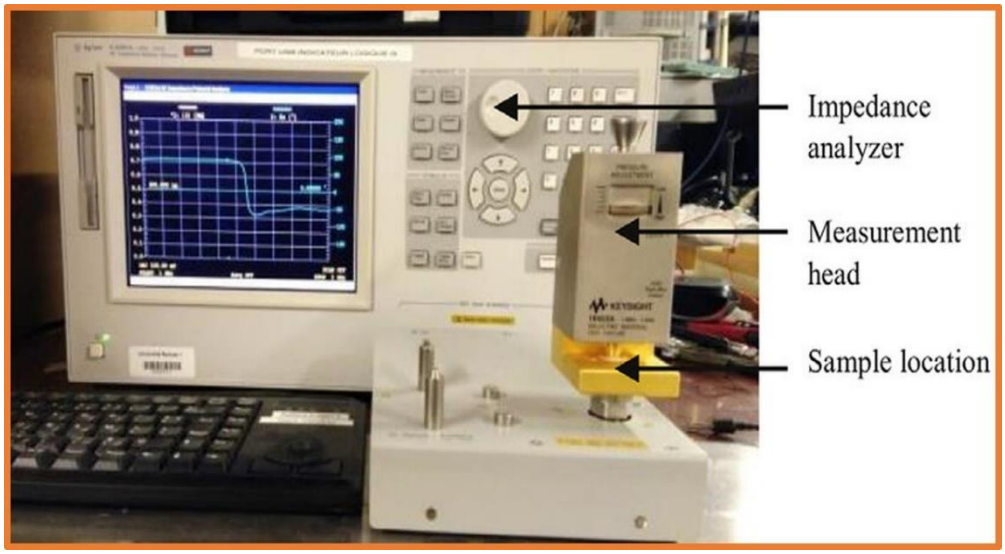

Fig. 4.8. Universal impedance analyzer.

4.9. Electrochemical Design

For supercapacitor testing, two-cell configurations such as a 3-electrode system and a 2-electrode system are used in this study. In a three-electrode setup, the active material is coated in a minimal amount onto the current collector and is tested for its super-capacitive nature. While a two-electrode setup resembles a full-working supercapacitor. Briefly, for a 3-electrode system, the working electrode was prepared by mixing particular ratios of the active electrode material, conductive additive (carbon black), and a binder (PVDF) with an organic solvent (NMP) and made into a slurry which was coated onto the current collector (graphite foil/ carbon fiber). The Platinum foil was used as the counter electrode with Ag/AgCl as the reference electrode [116]. An aqueous electrolyte such as KOH was used throughout this project. Electrochemical measurements were performed using a three-electrode system with a gamry potentiostat/galvanostat interface (5000E). The schematic depicting the three-electrode setup is shown in Fig. 4.9.

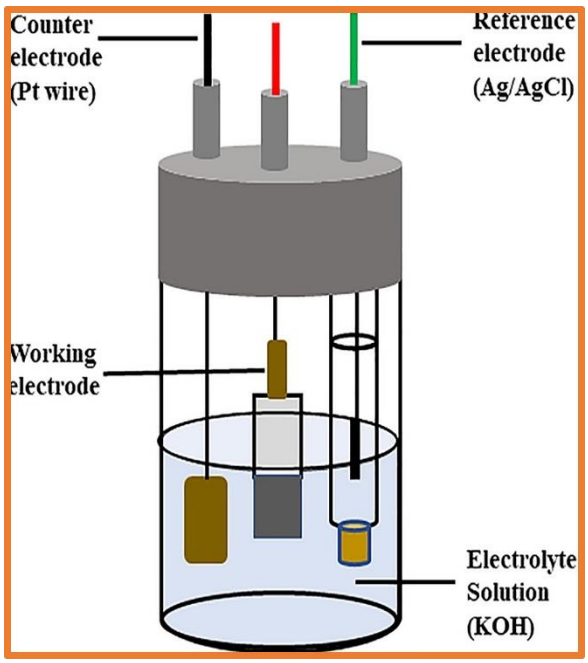

Fig. 4.9. Schematic of a 3-electrode setup [188].

4.10. Electrochemical Techniques

The performance of the supercapacitor electrode can be evaluated using various electrochemical techniques, which will be discussed in this section. Specific capacitance is an important parameter in deciding the performance of the electrode materials, and this can be calculated using electrochemical techniques. A two-electrode system is used for a supercapacitor (SC) device to investigate its performance [12]. In electrochemical investigations, a three-electrode (half-cell) system is employed to identify the specific electrochemical properties of a material. Two working electrodes are sandwiched between a solid electrolyte that acts as a separator in two-electrode systems. An illustration of a two-electrode setup that is comparable to a packed SC cell and provides a more precise illustration of the electrochemical performance of the electrode in the device is shown in Fig. 4.10 (a) [189]. At the specified potential window on the electrochemical system, the working electrodes of the half-cells had twice the potential window as the electrodes in the full-cells [190].

In a half-cell, three-electrode systems, i.e., working electrode, reference electrode, and counter electrode, are immersed in an electrolyte. A three-electrode cell system is schematically depicted in Fig. 4.10(b) [191]. The electrochemical workspace device measures the potential difference between the working and reference electrodes to monitor the current flowing from the counter to the working electrode. The current generated is directly related to the voltage established between the active and reference electrodes. Subsequently, this current is transformed into a voltage via a current-to-voltage converter and recorded with a timestamp by the data acquisition system. It's important to note that an ideal electrometer should have a high electrical resistance to minimize input currents. Any current flowing through a reference electrode can alter the true potential, potentially impacting data accuracy [192].

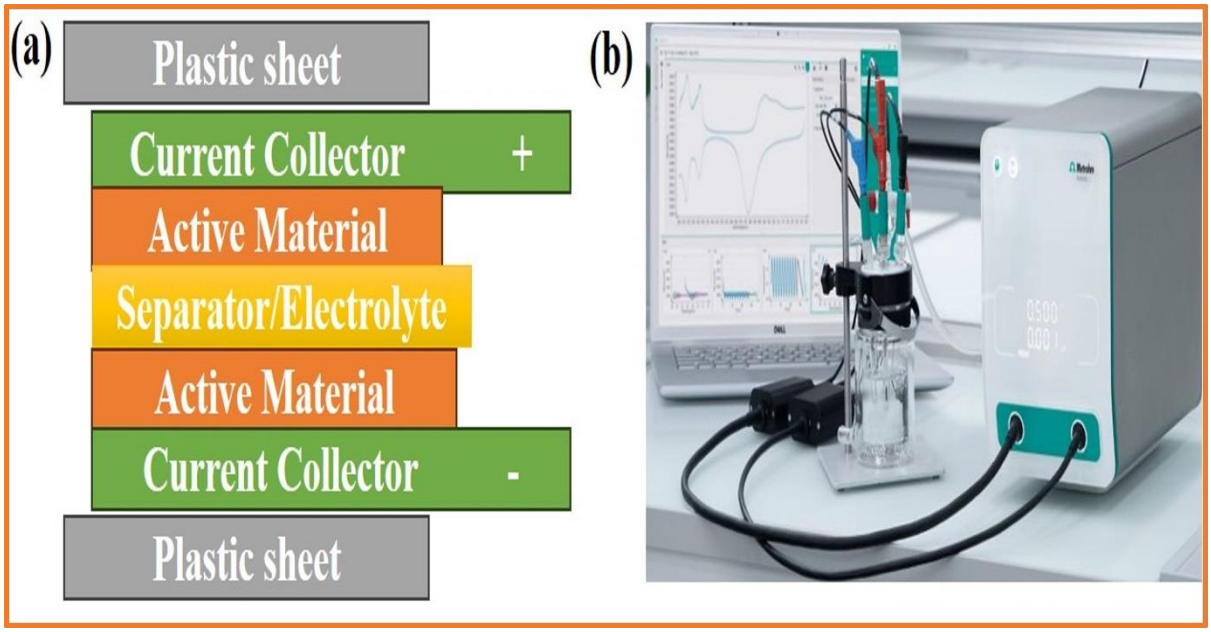

Fig. 4.10. (a) depicts the two-electrode device and **(b)** three-electrode cells [192].

4.11. Cyclic Voltammetry (CV)

This is a potentiodynamic technique where the charge response of a material is recorded with respect to the changing voltage applied. In this technique, a potential is applied to the working electrode, and the potential sweeps a cycle between the initial and the final potential. Voltage is applied at a constant sweep rate (dV/dt) and the resultant current between the voltage range is recorded. However, the type of electrolyte limits the total potential range. A plot of the obtained current versus the applied voltage gives the cyclic voltammogram [193]. Fig. 4.11 shows the comparison of CV curves for EDLC and a pseudocapacitor.

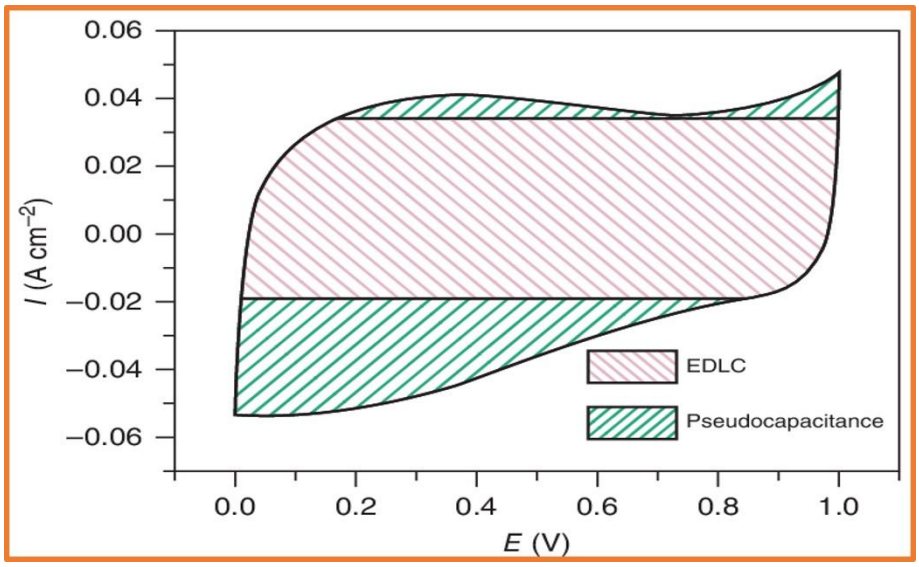

Fig. 4.11. Comparison of CV curves for EDLC and a pseudocapacitor [194].

For an EDLC, the shape of the CV is like a parallelogram (deformed rectangular shape) and the CV of a pseudocapacitor shows prominent peaks indicating the redox reactions taking place. The CV curve of a pseudocapacitor has separate peaks representing oxidation and reduction. Multiple CV curves are often recorded for varying scan rates as shown in Fig. 4.12. Multi curves enable the system to attain a steady state. In this work, we have used multiple CV curves. From the CV curves, the specific capacitance of the electrode material can be calculated using Eq. (4.4) [9].

$$C_{sp} = \frac{1}{mv\Delta V}\int_{Vi}^{vf} I(V)\, dV \qquad (4.4)$$

where C_s is the specific capacitance (F/g), I_{max} is the maximum current in both directions (A), m is the mass of the active material (g) and ν is the scan rate (V/s). As the scan rate increases, the value of the specific capacitance decreases as both are inversely proportional to each other. CV is also used to test the degree of reversibility of the electrode. An exact mirror voltammogram represents a highly reversible system. At extremely high scan rates there is rapid changing of potential which leads to sluggish transport of ions. This sluggish transport of ions leads to poor utilization of pores in a porous electrode thereby declining the performance [195][196].

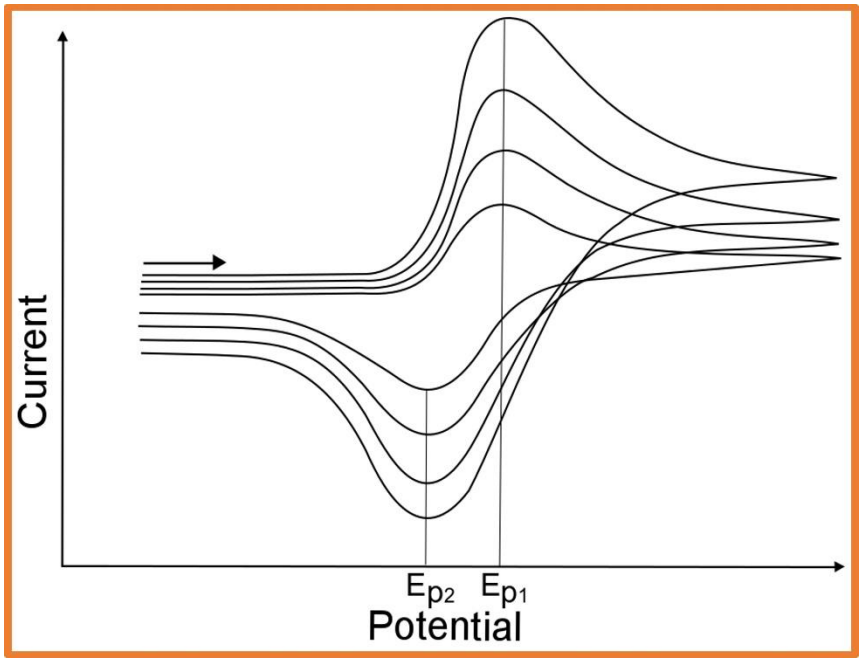

Fig. 4.12. CV curves for varying scan rates [193].

4.12. Galvanic Charge Discharge (GCD)

Galvanostatic charge-discharge (GCD) experiments, also known as chronopotentiometry (CP), provide essential data on cyclic life, equivalent series resistance (ESR), energy (E), power (P), and specific capacitance (Cs). In this technique, a constant current is applied to the working electrode, and the resulting potential relative to the reference electrode is measured. During charging and discharging at a fixed current density, the amount of charge transferred between the electrodes remains constant. The change in potential over time is recorded and varies according to the current density [197]. Fig. 4.13 A schematic of the GCD curve is shown. However, for characterizing the cycle life of supercapacitors (SCs), a two-electrode test cell is preferable as it closely simulates practical operating conditions [107]. The charge-discharge curve reveals the charge storage mechanism of the specified electrode. A non-linear curve suggests that charges are stored through a pseudocapacitive (PC) mechanism, while a linear curve indicates storage by an electric double-layer capacitance (EDLC) mechanism [36]. C_{sp} can be determined using Eq. (4.5) [62]

$$C_{sp} = \frac{I_m \times \Delta t}{\Delta V} \qquad (4.5)$$

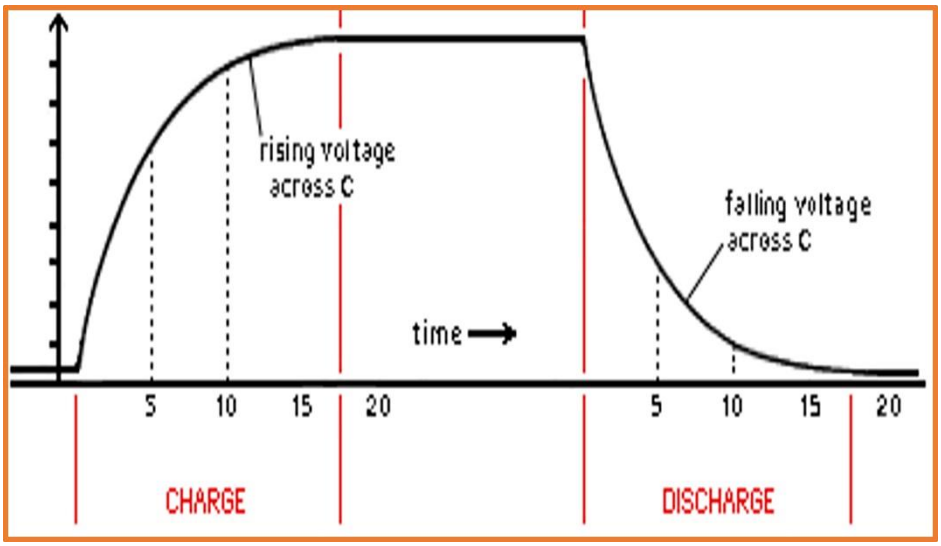

Fig. 4.13. depicts the charging and discharging curve of the GCD [36].

4.13. Electrochemical impedance analyzer

EIS is also a powerful technique for determining the performance of a supercapacitor. The resistance in the cell can be evaluated using this technique. An AC potential is applied to the cell over a frequency range, and the resultant current is measured. A tiny AC signal (5 to 50 mV) is supplied to the supercapacitor (SC) cell in the frequency range of 10 Hz–1 MHz. The resultant signals are current responses that apply alternating current signals. Nyquist and Bode plots can be used to analyze and interpret EIS spectra [198].

In Fig. 4.14, a Nyquist plot is presented with equivalent circuits that include four elements: R_s (ohmic resistance), R_s+R_{ct} (charge transfer resistance), CPE (constant phase element), and W (Warburg impedance). The use of Electrochemical Impedance Spectroscopy (EIS) is crucial for distinguishing between frequency-dependent and frequency-independent electrical components observed in the Nyquist plot [199]. To model complex electrochemical processes near the electrode-electrolyte interface, equivalent circuit models are constructed based on fundamental electric circuit elements such as capacitors and resistors. Unlike resistors, which lack frequency dependence and imaginary components, inductors and capacitors contribute an imaginary component to impedance [200].

The Nyquist plot shown in Fig. 4.14 provides a visual representation of both the real and imaginary impedance components. In this plot, the imaginary components are depicted on the Y-axis, while the X-axis represents the real components of impedance. An inset diagram within the figure exhibits a fitted equivalent circuit that correlates with the Nyquist plot. Notably, the

semicircular loop visible in the plot is linked to the charge transfer resistance [201]. Moreover, the concept of solution resistance is of significance within the impedance of an electrochemical cell. Variables such as temperature, ion type, ion concentration, and the structure of the current pathway are determinants of the electrolytic solution's resistance. Additionally, the kinetics of charge transfer are fixed and influenced by factors such as reaction type, temperature, concentration, and potential of reaction products. Warburg impedance, which is affected by ionic diffusion, is characterized by a decrease in impedance at higher frequencies due to shorter diffusion paths for reactants. Conversely, lower frequencies lead to longer diffusion paths and increased Warburg impedance.

In the Nyquist plot, Warburg impedance is represented by a diagonal line inclined at 45°, indicating the mass transport of ions. Furthermore, the real-axis intercept at higher frequencies corresponds to ohmic resistance. With decreasing frequency, reactants encounter longer diffusion distances, resulting in an elevation of Warburg impedance [202][203].

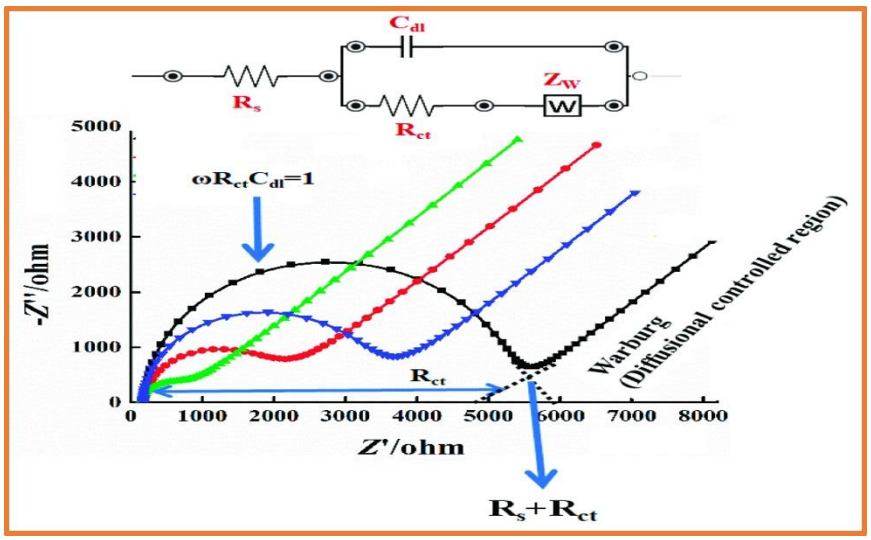

Fig. 4.14. depicts the principle of EIS [203].

CHAPTER-5

Result and Discussion

5. Sintering Temperature Impact on the Structural-Magnetic Properties of the $Zn_{0.2}Mg_{0.8}Fe_2O_4$ Spinel Ferrite

Abstract

This research work investigated the influence of sintering temperature on the structural and magnetic properties of $Zn_{0.2}Mg_{0.8}Fe_2O_4$ ferrite synthesized by the sol-gel auto-combustion process at different sintering temperatures (400 ºC, 600 ºC, 800 ºC). XRD study confirmed the $Zn_{0.2}Mg_{0.8}Fe_2O_4$ ferrite exhibits cubic symmetry. The crystallite size and unit cell volume increase as the sintering temperature increases. FTIR spectrum shows the vibrational band near 600 cm^{-1} to 400 cm^{-1} which corresponds to the tetrahedral and octahedral sites respectively. FESEM micrographs show the inhomogenous microstructure and agglomeration due to the existence of magnetic interactions. EDX study indicates the presence of all the elements in the sample.VSM reveals that saturation magnetization increases as the temperature increases. The soft ferromagnetic nature was exhibited by all the prepared samples owing to its low coercivity value and found its application in power and electromagnetic devices.

5.1. Experimental Method

Spinel ferrite $Zn_{0.2}Mg_{0.8}Fe_2O_4$ (400 ºC, 600 ºC, 800 ºC) can be generated by using the sol-gel auto combustion method. The AR grade chemicals $Zn(NO_3)_2.6H_2O$, $Mg(NO_3)_2.6H_2O$, $Fe(NO_3)_2.9H_2O$, and citric acid were used. All nitrates and citric acid have been taken in an equal amount of 1:1 and dissolved in the deionized water. Add a few drops of ammonia hydroxide to the mixture of nitrates and balance the pH value to 7. So, the solution is heated at 80 ºC for 6 hrs, the gel is formed in a brownish color. The gel is further heated and undergoes an auto combustion process. Then the fluffy powder is sintered at various temperatures (400 ºC,600 ºC, 800 ºC) and ground the powder with a mortar pestel.

5.2. Characterization Techniques

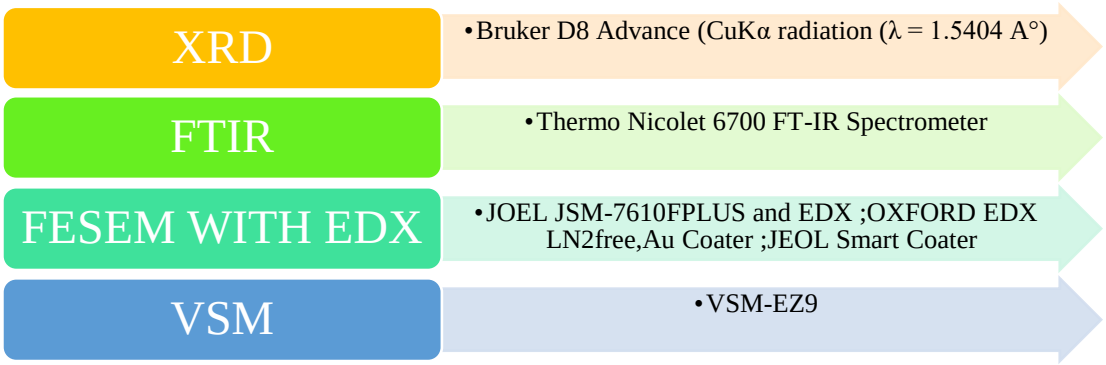

Fig. 5.1. depicts the characterization techniques**.**

5.3. RESULT AND DISCUSSION

5.3.1. X-ray diffraction (XRD) study

XRD pattern of $Zn_{0.2}Mg_{0.8}Fe_2O_4$ (x = 400 ºC, 600 ºC, 800 ºC) spinel ferrite can be amalgamated by using the sol-gel auto combustion method process as manifest in Fig. 5.2(a). $Zn_{0.2}Mg_{0.8}Fe_2O_4$ ferrite exhibits the single-phase and no impurity peaks are present. It exhibits the Fd-3m space symmetry. As per the JCPDS no.22-1012 (Zn ferrite) and 88-1943(Mg ferrite) the characteristic peaks are (220), (311), (400), (422), (511), (440) which confirm the face-centered cubic structure, but the most prominent peak is (311) [204]. Table 5.1 depicts the lattice constant (a_o), volume of the unit cell (V), and crystallite size (D). The lattice parameters can be calculated by using this Eq. (5.1) [205].

$$a_o = d\sqrt{h^2 + k^2 + l^2} \qquad (5.1)$$

where d is the interlayer distance spacing, a_o is the lattice constant, and hkl is the miller indices of the plane. The lattice constant increases as the temperature increases due to the larger ionic radii of Zn^{2+} (0.74 Å) and Mg^{2+} (0.72 Å) than the Fe^{2+} (0.64 Å) as in Fig. 5.2(b). The unit cell volume is increased as the lattice constant increases [206]. Lattice constant is directly proportional to the volume of the unit cell. Using the Debye Scherrer formula determine the crystallite size of the intense peak (311) by Eq. (5.2) [65].

$$D = \frac{k\lambda}{\beta \cos\theta} \qquad (5.2)$$

where D is the crystallite size, K (0.9) is scherrer constant, λ is the wavelength, β is the full-width half maxima, and θ is the Bragg angle corresponding to the peaks. The crystallite size of $Zn_{0.2}Mg_{0.8}Fe_2O_4$ range is 14 nm - 32nm increasing the sintering temperature, FWHM is reduced which shows the growth in grain increased as well as the crystallite size is increased[207]. At 800 ºC motion of the atom increased which increased the grain growth and also enhanced the crystallinity of the material. With temperature, crystallite size increases may be attributed to the coalescence process [149] . At 800 ºC the crystallite size of the prominent peak (311) is maximum.

Table 5.1 Lattice parameters of $Zn_{0.2}Mg_{0.8}Fe_2O_4$.

Sintering temperature	**Crystallite size(nm)**	**a (Å)**	**Volume(Å)^3**
400 ºC	14.6	8.39	590
600 ºC	27.6	8.41	595
800 ºC	32.5	8.42	599

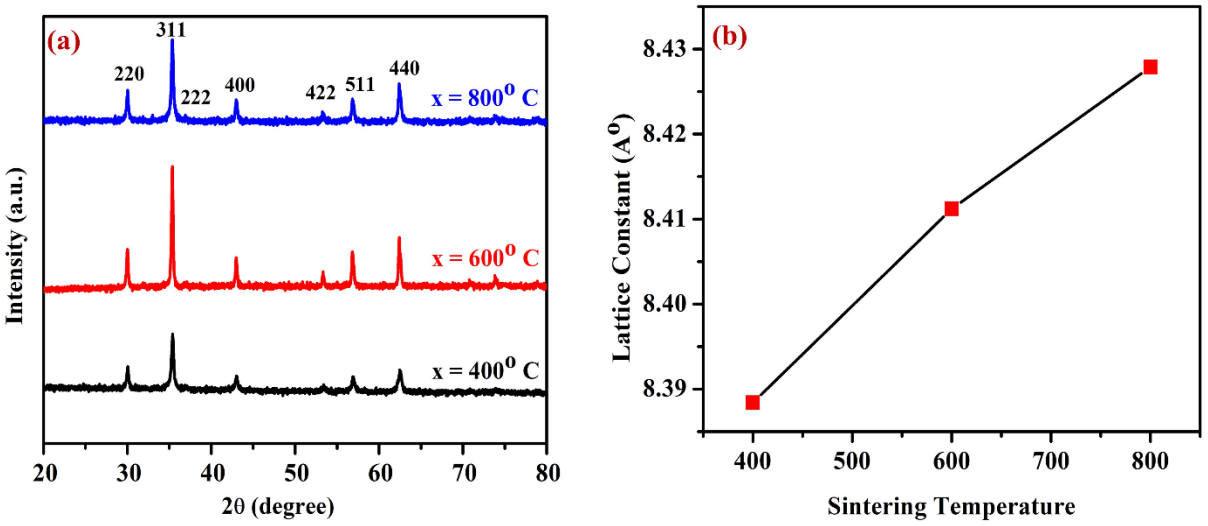

Fig. 5.2(a) XRD plot $Zn_{0.2}Mg_{0.8}Fe_2O_4$ (b) the Lattice constant vs sintering temperature**.**

5.3.2. Fourier Transformation Infrared Spectroscopy (FTIR)

The FTIR graph $Zn_{0.2}Mg_{0.8}Fe_2O_4$ ferrites synthesized at the temperatures 400 ºC,600 ºC, and 800 ºC as manifest in Fig. 5.3. The presence of v_1 absorption band lies near about 535.18 cm^{-1} and the second v_2 absorption lies near about 357.18 cm^{-1} [63]. The absorption band v_1 has attributed the stretching vibration to the tetrahedral atoms. The second v_2 absorption band corresponds to the octahedral atoms which affirms the spinel structure of the prepared material. The band 1516.34cm^{-1} exhibits stretching vibrations and also shows the presence of carboxyl acid [79]. As synthesized the sample of distilled water is used and the band appears near the 3570 cm^{-1} presence of the O-H bond for absorbing water molecules. The band 2357.10 cm^{-1} is attributed to the atmospheric CO_2 [78].

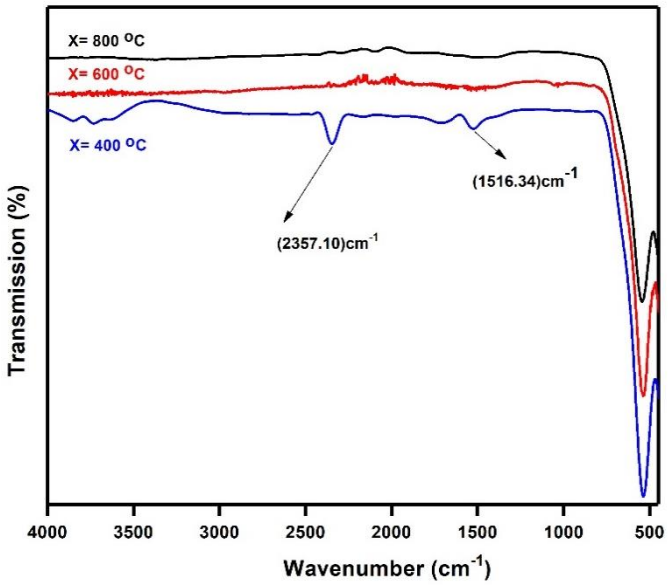

Fig. 5.3. FTIR spectra of $Zn_{0.2}Mg_{0.8}Fe_2O_4$ ferrite.

5.3.3. Field Emission Scanning Electron Microscopy (FESEM)

Fig. 5.4 depicts the $Zn_{0.2}Mg_{0.8}Fe_2O_4$ (x = 400 ºC,600 ºC, 800 ºC) spinel ferrite micrograph and histogram plot. The microstructure of the $Zn_{0.2}Mg_{0.8}Fe_2O_4$ ferrite shows the inhomogeneous size, grain growth, and assemblage of the grains [208]. The micrograph fesem reveals the agglomeration of particles due to the magnetic interaction between the nearby particles. The particle size was determined to be 506.12 nm, 548.84 nm, and 564.58 nm at temperatures 400

ºC, 600 ºC, 800 ºC respectively. The average size of the particle calculated, increases with increasing temperature. The element may lead to an enhancement of particle growth or inhibit particle growth which depends on the nature of the interaction [163].

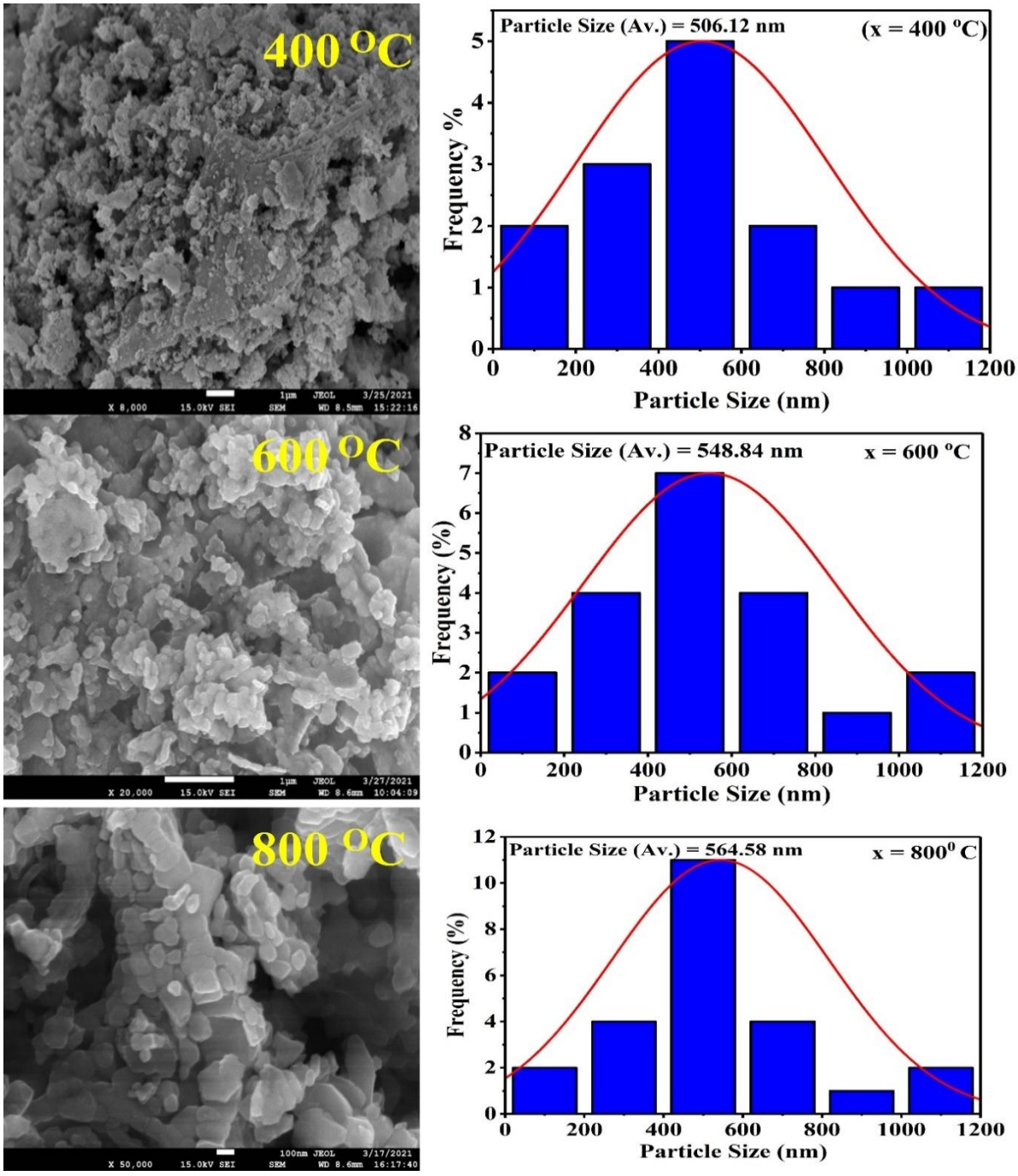

Fig. 5.4. the microstructure and particle size histogram of $Zn_{0.2}Mg_{0.8}Fe_2O_4$ ferrites.

5.3.4. Energy Dispersive X-Ray

Fig. 5.5(a)(b) manifests the EDX spectra to verify the element composition and elemental mapping of the prepared sample $Zn_{0.2}Mg_{0.8}Fe_2O_4$. At 800 ºC $Zn_{0.2}Mg_{0.8}Fe_2O_4$ exhibits the pure phase as compared to 600 ºC and 400 ºC. At the 800 ºC $Zn_{0.2}Mg_{0.8}Fe_2O_4$ ferrite shows all elements peaks viz Zn, Mg, Fe, O and homogenously diffusion in the spinel ferrite without the presence of the impurity [79]. This study indicates that pure $Zn_{0.2}Mg_{0.8}Fe_2O_4$ may be produced successfully by the constituents at T_s 800 ºC. Table 5.2 represents the experimental value and theoretical value of the atomic percent (at %) and weight percent (wt %) of the $Zn_{0.2}Mg_{0.8}Fe_2O_4$ sample.

Table 5.2 the Theoretical and Experimental value of atomic% and weight % $Zn_{0.2}Mg_{0.8}Fe_2O_4$.

Sintering temperature	Weight and Atomic percent	Value	Element				Total
			Zn	Mg	Fe	O	
800 ºC	Atomic percent	Experimental	3.45	11.86	30.64	53.97	100
		Theoretical	2.85	11.42	28.56	57.14	100
	Weight percent	Experimental	7.47	9.38	55.30	31.91	100
		Theoretical	6.29	9.35	53.72	30.61	100

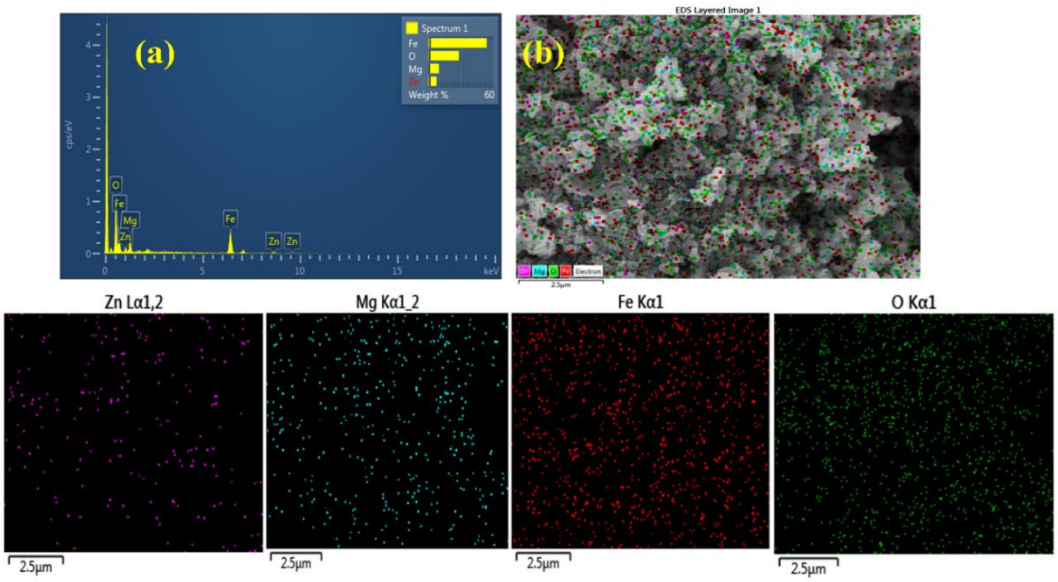

Fig. 5.5 a) the elemental mapping of Zn $_{0.2}$Mg$_{0.8}$Fe$_2$O$_4$ferrite b) represents the EDX spectra of Zn $_{0.2}$Mg$_{0.8}$Fe$_2$O$_4$.

5.3.5. VIBRATING SAMPLE MAGNETOMETER (VSM)

Fig. 5.6 examines the M-H hysteresis loop of Zn $_{0.2}$Mg$_{0.8}$Fe$_2$O$_4$ synthesized sample at room temperature by applying a magnetic field range is -20 to +20 Koe. Table 5.3 depicts the value of saturation magnetization (M_s), remanent magnetization (M_r), and coercivity (H_c), magnetic moment (μ_B), squareness ratio (SR). The saturation magnetization is mainly depending on the lattice exchange interaction i.e A-A, B-B, A-B [209] . The saturation magnetization is increased as the sintering temperature is increased due to the crystallite size being increased. The squareness ratio is determined by Eq. (5.3) [74].

$$SR=M_r/M_s \qquad (5.3)$$

where SR is the squareness ratio, M_r is the remanent magnetization, and M_s is the saturation magnetization. For the sintering ferrites at all temperatures, the squareness ratio lies between the 0.178 - 0.151 [210]. It reveals that the sample is randomly oriented at the multi-domain. The magnetic moment of the particles can grow with increasing particle size. The magnetic moments can be calculated using Eq. (5.4) [211].

$$n_B = \frac{M \times M_S}{5585} \qquad (5.4)$$

where n_B magnetic moment, M molecular mass, and M_s is saturation magnetization. The magnetic moment increases as the temperature increases. At high T_s, the influence on the crystallization and grain size can be occurred which can show the enhancement of the lattice. Coercivity is decreased with an increase the temperature. As the crystallite size increases from 14.6 nm to 32.5 nm, the saturation magnetization M_s also increases (from 30.166 emu/g to 44.987 emu/g). This trend can be attributed to a reduction in surface spin disorder. Smaller crystallites have a higher surface-to-volume ratio, which increases spin canting at the particle surface, reducing the net magnetization. Larger particle sizes facilitate a shift to multi-domain behavior, reducing H_c. Coercivity is inversely proportional to the saturation magnetization (M_s). $Zn_{0.2}Mg_{0.8}Fe_2O_4$ spinel ferrite exhibits soft ferrite in nature.The synthesized $Zn_{0.2}Mg_{0.8}Fe_2O_4$ spinel ferrite has been used in the application of magnetic recording and electronic devices [79].

Table 5.3 The magnetic parameters of $Zn_{0.2}Mg_{0.8}Fe_2O_4$

Sintering temperature	**M_s(emu/g)**	**M_r(emu/g)**	**H_c (Oe)**	**SR**	**$n_B(\mu_B)$**
400 °C	30.166	5.40	65.577	0.178	1.12
600 °C	34.920	5.42	52.847	0.155	1.29
800 °C	44.987	6.79	49.605	0.151	1.67

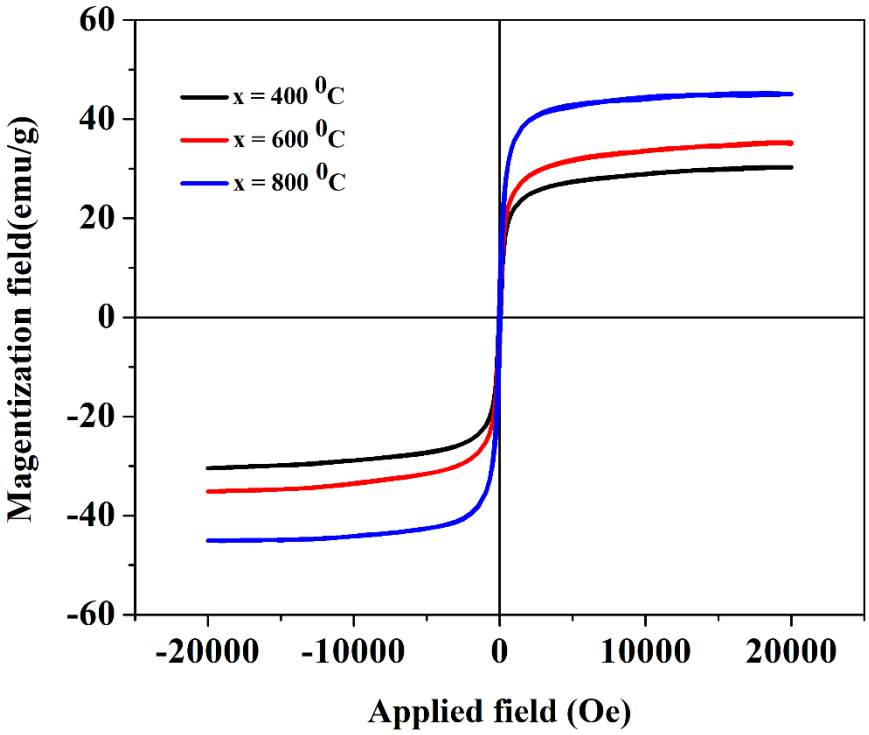

Fig. 5.6 M-H curve of Zn $_{0.2}$Mg$_{0.8}$Fe$_2$ O$_4$ ferrite.

5.4. CONCLUSION

$Zn_{0.2}Mg_{0.8}Fe_2O_4$ (x = 400 ºC, 600 ºC, 800 ºC) spinel ferrite is successfully synthesized by the sol-gel auto combustion technique and studies the different characteristic properties such as structural, morphology, and magnetic properties. XRD spectrum examined spinel ferrite exhibit single phase. Crystallite size is increased with the temperature increase lies between 14 nm - 32nm. FTIR reveals the presence of the functional group and spinel phase formation. The particle size range is 506.12 nm - 564.58 nm. Magnetic properties reveal prepared sample exhibits a soft ferromagnetic nature owing to its low coercivity value and found its application in power and electromagnetic devices. This material can be used in LEDs, transistors, and sensors.

CHAPTER – 6

Result and Discussion

6. Manganese Doped Co-Ni Spinel Ferrite: Investigation of Structural, Morphological, Magnetic, and Dielectric Properties

Abstract

The structural, morphological, magnetic, and dielectric properties of $Mn_xCo_{0.5-x}Ni_{0.5}Fe_2O_4$ (x = 0.0, 0.2, and 0.4) synthesized by sol-gel auto-combustion are reported in this paper. X-ray diffraction (XRD) pattern of the samples confirms the formation of a single-phase spinel ferrite and the crystallite size (*D*) is in the range of 32.60 - 33.62 nm. Fourier transform infrared (FTIR) spectra have a vibrational band at 534.20 cm^{-1} and 420.13 cm^{-1} which corresponds to the tetrahedral and octahedral sites of the $Mn_xCo_{0.5-x}Ni_{0.5}Fe_2O_4$ respectively. Field emission scanning electron microscope (FESEM) reveals the cubic morphology of the synthesized spinel ferrite with inhomogeneous grain size. Vibrating sample magnetometer (VSM) analysis showed the ferromagnetic nature of all samples. All the samples exhibit a multi-domain because the value of M_r/M_s lies in the range of 0.153 – 0.336. Dielectric properties reveal the hopping of the charge carrier which has improved the conduction mechanism of the $Mn_xCo_{0.5-x}Ni_{0.5}Fe_2O_4$.

Keywords: Spinel Ferrite, Structural Properties, Magnetic Properties, Dielectric Properties.

6.1. Materials and methods

6.1.1. Chemicals Requirement

In this research, highly pure (99–99.5%) analytical reagent (AR) grade chemicals viz., manganese nitrates (Mn $(NO_3)_2.6\ H_2O$), nickel nitrates (Ni $(NO_3)_3.6H_2O$), cobalt nitrates (Co $(NO_3)_2.6H_2O$), ferric nitrates (Fe $(NO_3)_3.9H_2O$), and citric acid ($C_6H_8O_7.H_2O$) were used to prepare spinel ferrite.

6.1.2 Synthesis of spinel ferrite with Mn^{2+} substitution

Sol-gel auto-combustion method was adopted to synthesize the manganese-doped cobalt-nickel spinel ferrite ($Mn_xCo_{0.5-x}Ni_{0.5}Fe_2O_4$) as in Fig. 6.1. AR-grade chemicals were dissolved in 100 ml of de-ionized water. Citric acid was used as a fueling agent and all metal nitrates were used as an oxidant in a 1:1 ratio. The nitrates solution was continuously swirled

until the desired homogenous solution was achieved. To attain the pH value of 7, ammonium hydroxide solution is added drop-by-drop. After the gel formation, spinning has been stopped. The gel was heated at 80 ºC for 3 hours to get ash. The ash was further heated at 80 ºC for 9-10 h. The material so formed was sintering at 1100 ºC for 6 h in the muffle furnace. Finally, the powdered sample of the ferrite was crushed in an agate motor with the pestle to produce the homogenized fine powder of the synthesized ferrite.

Fig. 6.1. Schematic of the synthesis of $Mn_xCo_{0.5-x}Ni_{0.5}Fe_2O_4$ spinel ferrite.

6.2. Characterization Technique

The phase of the prepared sample was studied using a Powder X-ray diffractometer (Bruker D8 Advance) with CuKα radiation at λ = 1.5406 Å from 20°-80° in 0.02° increments. FTIR with diamond ATR (Perkin Elmer spectrum 2) affirms the spinel structure of the prepared spinel ferrites. FESEM (FE-SEM: JEOL JSM-7610 F Plus) confirms the surface morphology while chemical composition is confirmed by the energy dispersive x-ray analysis (EDX spectrum) (EDX: OXFORD EDX LN2 free). The magnetic properties of spinel ferrite were investigated using a VSM (VSM-EZ9). Wynne Kerr impedance analyzer (Model 6500) is utilized to determine the dielectric properties.

6.3. Results and Discussions

6.3.1. XRD analysis

The XRD pattern of the $Mn_xCo_{0.5-x}Ni_{0.5}Fe_2O_4$ (x = 0.0, 0.2, 0.4) ferrite is shown in Fig. 6.2. The phase structure of the synthesized Mn-doped Co–Ni spinel ferrite were investigated using X-ray diffraction, and various lattice parameters viz. lattice constant (a_o), unit cell volume (V_{cell}), crystallite size (D), lattice strain (ε), dislocation density (δ), and hopping length L_{tetra} and L_{octa} are reported in Table 6.1. The diffraction pattern has miller indices (hkl) corresponding to (111), (220), (311), (222), (400), (422), (511), and (440) which is according to the JCPDS card no. 10-0325 for (Ni ferrite) and JCPDS card no. 22-1086 (Co ferrite) [114]. This authenticates the presence of a face-centered cubic (fcc) arrangement and having a space group of Fd-3m in our synthesized $Mn_xCo_{0.5-x}Ni_{0.5}Fe_2O_4$ samples [212]. These peaks exhibit a single-phase crystalline structure without any extra impurity present in them. The highest intensity characteristic diffraction peak is (311). The a_o can be calculated by Eq. (6.1) [213] as mentioned in Table (6.1).

$$a_o = d\sqrt{h^2 + k^2 + l^2} \qquad (6.1)$$

Here, hkl are characteristic diffracting peaks, d is the interlayer spacing, and a_o is the lattice constant. The peaks are slightly shifted toward the lower 2θ and due to this the lattice constant increases as the Mn^{2+} concentration increases which is according to Vegard's law. When the Mn^{2+} is substituted into Co-Ni ferrite with varying concentrations (x = 0.0, 0.2, 0.4), the lattice constant (a_o) increases from 8.349 to 8.360 Å. Similar to this was reported in the literature by Mahajan et *al*. [79]. This increase in lattice constant is because of the Mn^{2+} ion replacing the Co^{2+} ions. The Mn^{2+} has a high ionic radii of 0.80 Å than the Co^{2+} ion with ionic radii of 0.78 Å as in Fig. 6.3(a)[79][214].

Table 6.1

Structural parameters of the $Mn_xCo_{0.5-x}Ni_{0.5}Fe_2O_4$ samples.

Mn Concentration (x)	a_o (Å)	V (Å)	D (nm)	ε	δ (m^{-2})	L_{tetra}	L_{octa}
x = 0.0	8.349	581.97	32.60	3.450	0.927	3.615	2.951

x = 0.2	8.352	582.64	33.99	3.312	0.854	3.616	2.952
x = 0.4	8.360	584.44	33.62	3.352	0.873	3.619	2.955

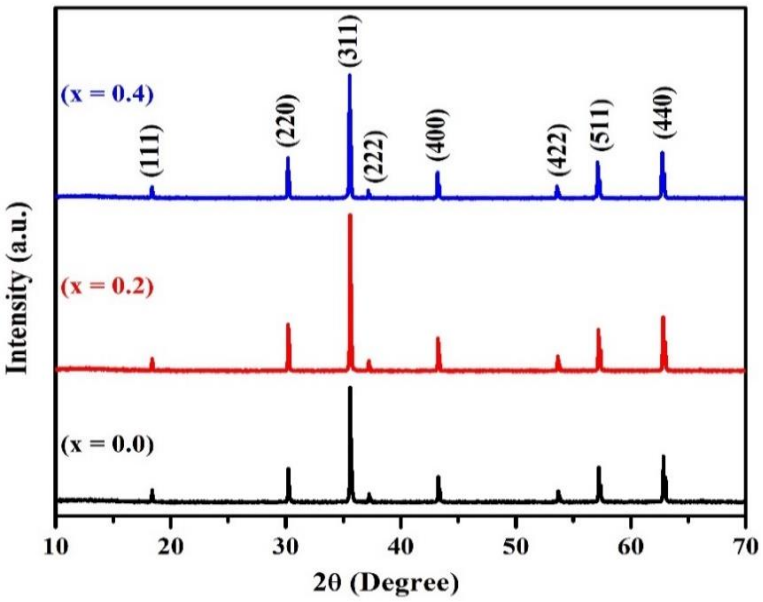

Fig. 6.2. XRD plot of $Mn_xCo_{0.5-x}Ni_{0.5}Fe_2O_4$ samples.

Table 6.2

Interplanar spacing (d) at different hkl planes for $Mn_xCo_{0.5-x}Ni_{0.5}Fe_2O_4$ samples.

Hkl	*d*(Å)		
	x = 0.0	x = 0.2	x = 0.4
(111)	4.823	4.821	4.819
(220)	2.955	2.951	2.952
(311)	2.520	2.517	2.518
(222)	2.413	2.410	2.411
(400)	2.090	2.087	2.088
(422)	1.707	1.704	1.705
(511)	1.609	1.607	1.608
(440)	1.479	1.476	1.477

By using Bragg's law, the interplanar spacing (d) can be evaluated using Eq. (6.2) [215].

$$d = \frac{n\lambda}{2\sin\theta} \tag{6.2}$$

Where λ = 1.5406 Å represents the X-ray wavelength, n is the order of the diffraction peak, and θ is Bragg's angle. The d-spacing values for the prepared samples as obtained using X Powder software are in Table 6.2. The unit cell volume (V_{cell}) is dependent on the lattice constant and therefore increases as the doping content increases as exhibited by Fig. 6.3(b) [216][217]. This ionic radius difference increases V_{cell}, and as a result, the unit cell of the synthesized spinel ferrite expands [79]. The crystallite size (D) for the high-intensity peak (311) can be evaluated by using Eq. 6.3 [65].

$$D = \frac{k\lambda}{\beta\cos\theta} \tag{6.3}$$

Here, β is full-width half maxima and k is the Scherrer constant which is 0.9. The lattice strain and dislocation density can be calculated by Eq. (6.4) and Eq. (6.5) [64].

$$\delta = \frac{1}{D^2} \tag{6.4}$$

$$\varepsilon = \frac{\beta}{4Tan\theta} \tag{6.5}$$

The crystallite size was determined to be in the nanoscale range using the Debye-Scherrer formulae. The D of the sample firstly increases from 32.60 (x = 0.0) nm to 33.99 nm (x = 0.2) and then decreases to 33.62 nm (x = 0.4). This agrees with other works observed by Jabbar et *al.* [214]. This irregular crystallite size is because the Mn^{2+} cation can randomly be present on both tetrahedral and octahedral sites and Mn^{2+} has high ionic radii of 0.80 Å than the Co^{2+} ion with ionic radii of 0.78 Å [79]. Table 6.2 reports the lattice strain and dislocation density which decreases from x = 0.0 to 0.2 and then increases at x = 0.4, due to the ionic radii difference of the metal cations Ni (0.69Å), Co^{2+}(0.78 Å), Mn^{2+}(0.80 Å), Fe^{3+}(0.64 Å). This randomness creates non-uniform strain in the crystal lattice and breaks them into non-uniform nanoparticles of sporadic shape. Strain creates inhomogeneity in the lattice and distortion induced in the lattice during the synthesis process [218][219].

The jumping length can be calculated by Eq. (6.6) and Eq. (6.7) [65].

$$L_{tetra} = \frac{a_o\sqrt{3}}{4} \tag{6.6}$$

$$L_{octa} = \frac{a_o\sqrt{2}}{4} \qquad (6.7)$$

Where L_{tetra} and L_{octa} are the jumping length, and a_o is the lattice constant. Table 6.2. shows the hopping length of the L_{tetra}(A) and L_{octa}(B) sites. Hopping length increases as the Mn^{2+} concentration increases due to the ionic radii difference of the Mn^{2+}(0.80Å) larger than the Co^{2+} (0.78 Å) these magnetic ions are separated, which increases the hopping length as similar to this was reported in the literature by Ali et *al.*[210].

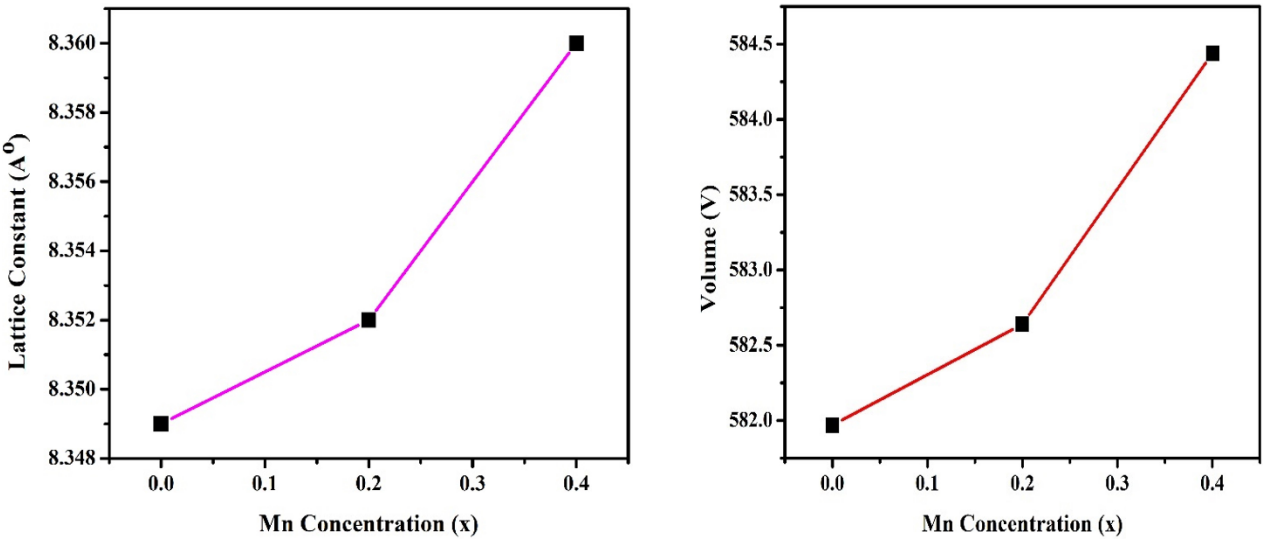

Fig. 6.3. (a) Lattice constant (a_o) and (b) unit cell volume (V) as a function of Mn concentration.

6.3.2. FTIR analysis

The Infrared spectroscopy is especially useful for assessing the quality, chemical bonding, and spinel structure of synthesized samples. The FTIR spectrum at the ambient temperature for all synthesized samples with varying Mn content in the 400 to 4000 cm^{-1} range is presented in Fig. 6.4 [220]. The FTIR spectra peaks manifest the positions of metal cations in the lattice sites. Metal cations exist in tetrahedral and octahedral lattice sites in spinel ferrite, as evidenced by the spatial positioning of oxygen ions. Vibrational bands were observed in the wavenumber range of 400 to 600 cm^{-1} for all samples with different Mn concentrations. Similar to this was reported in the literature by Hammad et *al.* [221]. A peak at 534.20 cm^{-1} belongs to the tetrahedral complex and a peak at 420.13 cm^{-1} belongs to the octahedral complex which is attributed to the stretching vibrations and affirms the spinel structure of our prepared samples [205]. The difference in bond length of metal-oxygen ions in the tetrahedral and

octahedral sites results in a difference in the frequency of the vibrational bands (v_1 and v_2) [222]. The frail adsorption bands at 2328 cm^{-1} and 2364 cm^{-1} were because of the existence of O-H and CO_2, respectively [223]. The occurrence of O-H and CO_2 vibrations was due to moisture absorption from the atmosphere [224]. The presence of a peak at 1100 cm^{-1} confirms the absence of N-O in the synthesized sample. The absence of vibration bands around the peak 1395, 1672, and 3147 cm^{-1} confirmed the removal of citric acid during the sintering process and demonstrated the faultlessness of our prepared $Mn_xCo_{0.5-x}Ni_{0.5}Fe_2O_4$ spinel ferrite [79].

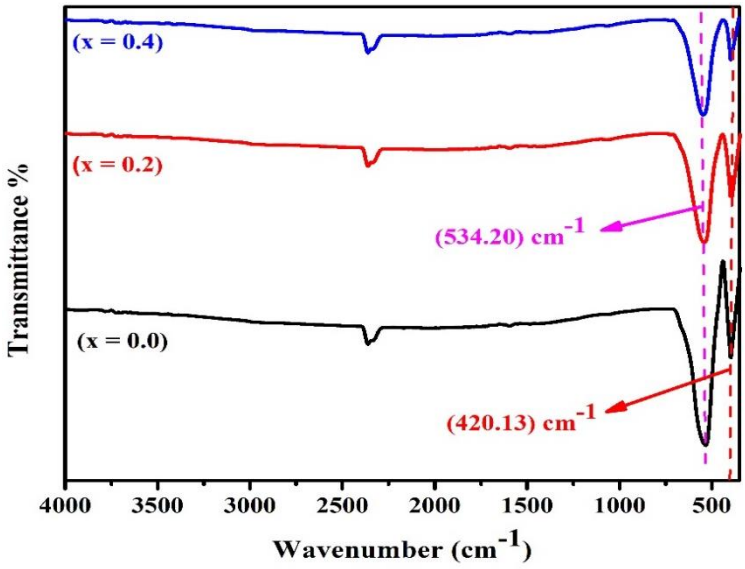

Fig. 6.4. FTIR spectra of $Mn_xCo_{0.5-x}Ni_{0.5}Fe_2O_4$ samples.

6.3.3. FESEM and EDX analysis

To investigate the morphological properties of the synthesized material, FESEM micrographs of the samples were provided. Micrographs and average particle sizes of the synthesized $Mn_xCo_{0.5-x}Ni_{0.5}Fe_2O_4$ (x = 0.0, 0.2, 0.4) sample are presented in Fig. 6.5. The figure reveals the agglomeration of particles due to the magnetic interaction between the nearby particles. These samples show an inhomogeneous nature and are irregular in size and shape [79]. According to FESEM micrographs, the grains of all the samples were in the nanoscale range, with distinct voids and pores that could be attributed to gas emissions (CO_2, NO_2, H_2O, etc.) during the synthesis. From the histogram, the average particle size had been evaluated using the ImageJ software. According to the

FESEM particle size distribution, the estimated average ferrite nanoparticle sizes were determined to be 246.53 nm, 252.73 nm, and 337.39 nm for x = 0.0, x = 0.2, and x = 0.4 respectively. These values are in the same order as those reported by Hasan et *al*. [225]. The average size of the particle calculated, increases with increasing doping concentration. The dopant element may lead to an enhancement of particle growth or inhibit particle growth which depends on the nature of the interaction. In our study, the increase in the size of particles may be a result of the enhancement of particle boundary mobility by the Mn^{2+} concentration [226]. Moreover, the particle sizes in the FESEM were found to be bigger than the crystallite size obtained in the XRD result. This variation in the crystallite and particle size may be attributed to the agglomeration of particles as can be observed in FESEM micrographs [227].

EDX spectra in Fig. 6.6(a) verify the elemental stoichiometry of the synthesized $Mn_xCo_{0.5-x}Ni_{0.5}Fe_2O_4$ (x = 0.0, 0.2, 0.4) samples. The undoped ferrite (x = 0.0) exhibits the peaks belonging to Co, Ni, Fe, and O, whereas, the doped ferrites (x = 0.2 and 0.4) exhibit the peaks belonging to Mn, Co, Ni, Fe, and O. For all the synthesized samples EDX spectra avows the experimental stoichiometry without any impurity present in it. Table 6.3 represents the experimental value of the atomic percent (*at. %*) and weight percent (*wt. %*) of $Mn_xCo_{0.5-x}Ni_{0.5}Fe_2O_4$ (x = 0.0, 0.2, 0.4) samples. The theoretical and experimental values of the *at. %* and *wt. %* are closely associated which affirms the accuracy of our synthesized samples [79][228]. Fig. 6.6(b) depicts the elemental mapping of the doped Mn^{2+} spinel ferrites with the uniform propagation of the $Mn_xCo_{0.5-x}Ni_{0.5}Fe_2O_4$ spinel ferrite.

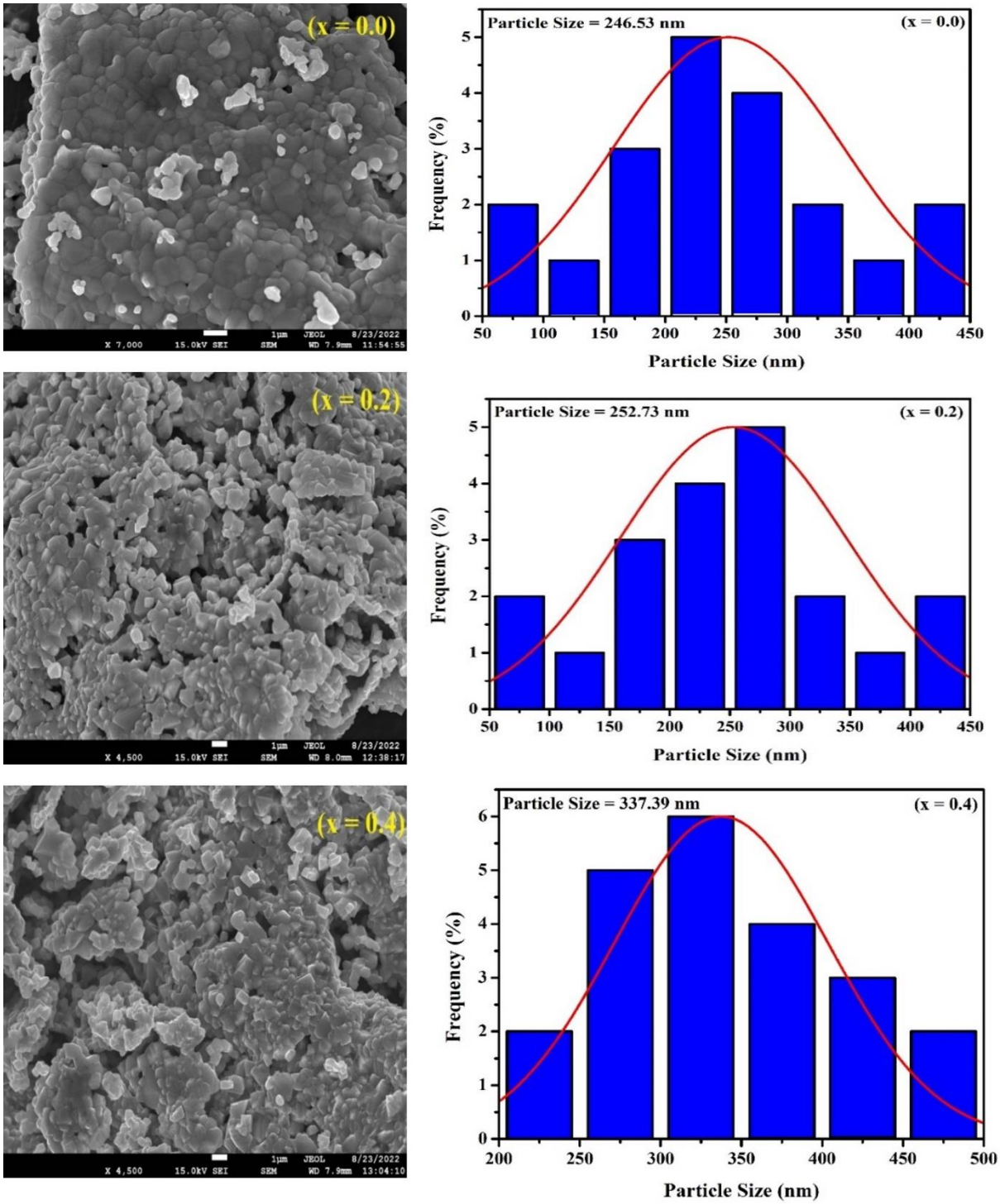

Fig. 6.5. FESEM micrograph and particle size of MnxCo0.5-xNi0.5Fe2O4 sample.

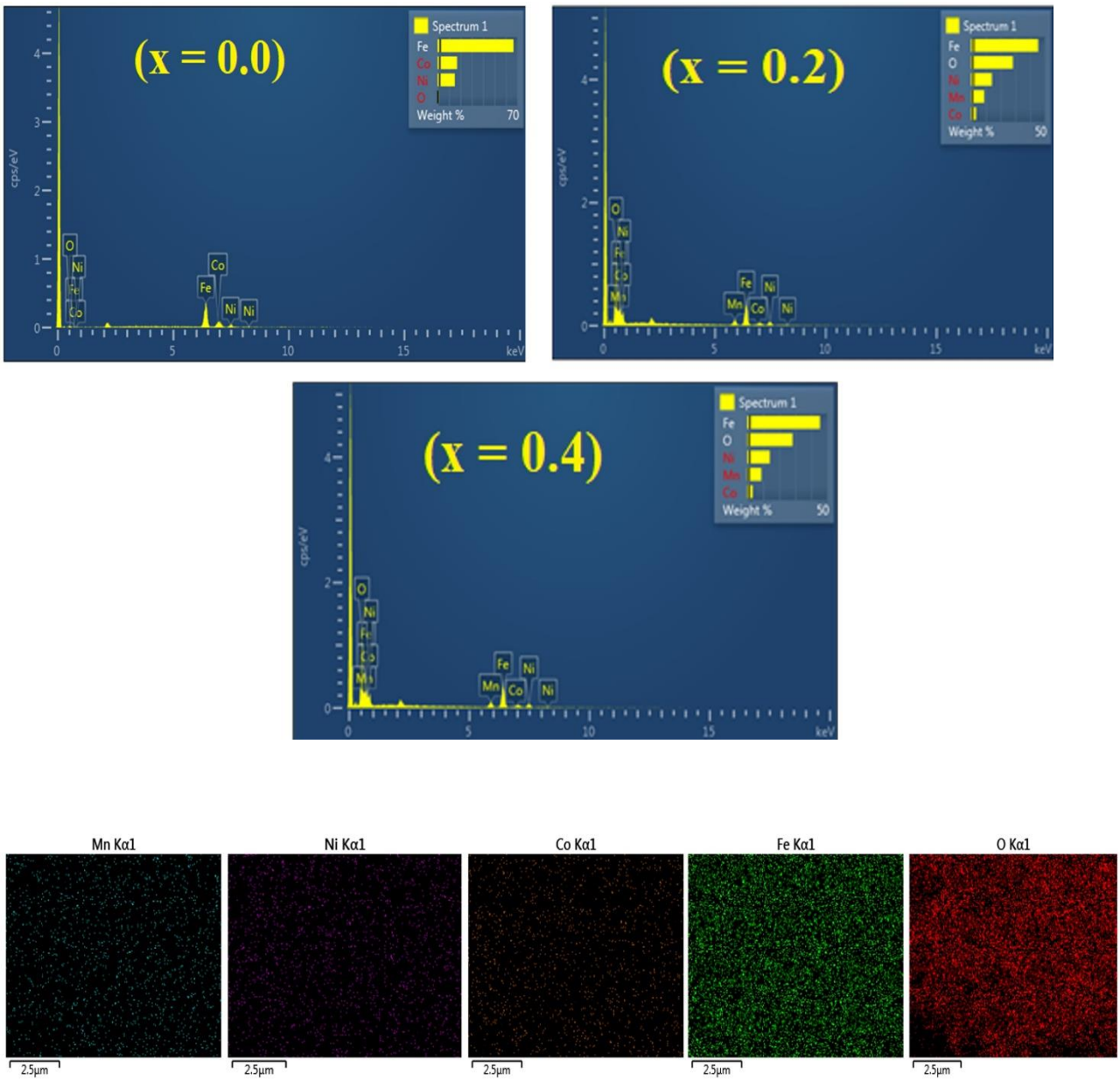

Fig. 6.6 (a) EDX spectra of $Mn_xCo_{0.5-x}Ni_{0.5}Fe_2O_4$ samples and (b) elemental mapping of $Mn_{0.2}Co_{0.3}Ni_{0.5}Fe_2O_4$.

Table 6. 3

Experimental and theoretical values of *at*. % and *wt. %* for $Mn_xCo_{0.5-x}Ni_{0.5}Fe_2O_4$ samples.

Mn concentration (x)	**Value**	**Weight %and Atomic %**	**Element**					**Total**
			Mn	Ni	Co	Fe	O	
0.0	Theoretical	Weight %	0.0	12.99	14.29	46.44	26.29	100
	Experimental	Weight %	0.0	12.52	12.58	47.70	27.18	100
0.2	Theoretical	Weight %	5.73	13.01	4.88	50.34	26.03	100
	Experimental	Weight %	4.70	12.56	7.57	47.86	27.27	100
0.4	Theoretical	Weight %	8.81	14.04	3.28	45.48	28.39	100
	Experimental	Weight %	9.45	12.61	2.53	48.03	27.37	100
0.0	Theoretical	Atomic %	0.0	7.14	7.14	28.57	57.14	100
	Experimental	Atomic %	0.0	7.53	8.25	28.30	55.92	100
0.2	Theoretical	Atomic %	2.85	7.14	4.28	28.57	57.14	100
	Experimental	Atomic %	3.55	7.55	2.82	30.69	55.39	100
0.4	Theoretical	Atomic %	5.71	7.14	1.42	28.57	57.14	100
	Experimental	Atomic %	5.27	7.86	1.83	26.75	58.29	100

6.3.4. VSM analysis

The M-H hysteresis plot for the synthesized $Mn_xCo_{0.5-x}Ni_{0.5}Fe_2O_4$ sample at room temperature in the magnetic field range of -30 KOe to +30 KOe is presented in Fig. 6.7. Table 6.4 reveals the magnetic parameters such as remanence (M_r), coercivity (H_c), saturation magnetization (M_s), anisotropy constant (K), and squareness ratio (SR). The M-H plot shows the S-shape hysteresis loop which attributes that the material is ferromagnetic. The saturation magnetization decreased from 55.26 (x = 0.0) to 52.52 emu/g (x = 0.2) and then it increases to 63.42 emu/g (x = 0.4) with the Mn^{2+} dopant as exhibited in Fig. 6.8(a). The reduction in M_s is a direct result of crystallite size miniaturization. When the particle size changes from bulk to nanoscale, the M_s decreases as the size of the nanoparticles decreases due to the presence of some level of spin canting in the entire volume of the nanoparticles. Similar to this was reported in the literature by Nabavi *et al*. [229]. Various factors viz. weak interaction, and lattice defects

are responsible for the M_s decrement. The magnetic moment n_B is listed in Table 4. The crystal lattice also exhibits three types of superexchange interaction A-A, B-B, and A-B [230][231]. The Yaffle-Kittel suggested magnetization was based on three sub-lattice models. According to the Neel two sub-lattice model cation distribution for (x = 0.0, 0.2, and 0.4) is presented in Eq. (6.8) (6.9) [163][232].

$$(Fe^{3+})_A[Ni^{2+}_{0.5}Co^{2+}_{0.5}FeO_4]_B \quad (6.8)$$

$$(Mn^{2+}_xFe^{3+})_A[Mn^{2+}_xCo^{2+}_{0.5-x}Ni^{2+}_{0.5}Fe\ O_4]_B \quad (6.9)$$

Cobalt and Nickel ferrite both are inverse ferrite in that the divalent cation (Co^{2+}, Ni^{2+}) can occupy the B site and the trivalent cation (Fe^{3+}) can occupy the A and B sites, where, A is tetrahedral and B is the octahedral site [233]. Mn^{2+} acquires any lattice site (A or B).

From the above equation, the magnetic moment of the A-site is smaller than the B-site, therefore the magnetic moment theoretically increases as the Mn^{2+} concentration increases. These metals have the theoretical magnetic moment as Ni^{2+}($2\mu_B$), Mn^{2+}($5\mu_B$), Co^{2+}(3 μ_B), and Fe^{2+}(5 μ_B) [234]. The net magnetic moment is $M_{net} = |M_B - M_A|$. The experimental magnetic moment decreased as calculated using Eq. (6.10) [65].

$$n_B = \frac{M_S \times Mw}{5585} \quad (6.10)$$

where Mw is the molecular weight of the composition, and M_s is the saturation magnetization. As Mn^{2+} concentration increases, M_s is reduced irregularly, and the magnetic moment also reduces due to the weak A-B exchange interaction. Magnetic spin is the cause of the disorder crystal structure of the synthesized $Mn_xCo_{0.5-x}Ni_{0.5}Fe_2O_4$ spinel ferrite [227].

The anisotropy constant (K) can be calculated using Eq. (6.11) [223].

$$K = \frac{H_c \times M_S}{0.961} \quad (6.11)$$

where H_c and M_s are the coercivity and saturation magnetization respectively. In Table 6.4 K increases as the Mn^{2+} content increases because the anisotropy constant is dependent on the coercivity and saturation magnetization. Magnetic anisotropy is influenced by the crystal

structure and the distribution of metal cations. The Mn^{2+} cations have a larger ionic radius than the Co^{2+} cations, and their substitution for Co^{2+} cations can distort the spinel structure, creating local magnetic anisotropy. This leads to a more pronounced uniaxial magnetic anisotropy in the material, which increases the coercivity. Mn ions have a higher spin and orbital magnetic moment [79]. Mn^{2+} ions replace the Co^{2+} ions, due to which Co^{2+} ions decrease, as a result, the anisotropy constant and coercivity increase [218]. The larger crystallite sizes reduce surface area-to-volume ratios, which can decrease spin disorder at the particle surface and thereby increase M_s. However, variations in cation distribution or crystallinity (influenced by synthesis conditions) may cause slight fluctuations in M_s, the rise in coercivity with increased crystallite size suggests the particles might be transitioning from a single-domain to a multi-domain structure. Generally, multi-domain particles have higher coercivity because the domain wall pinning requires a higher external field to reorient.

The squareness ratio SR (M_r/M_s) with different concentrations of Mn^{2+} is calculated using Eq. (6.12) [235]. The value of M_r/M_s increases by increasing the concentration of the Mn dopant. The value of M_r/M_s lies between 0.153 to 0.336 and reveals the multi-domain spinel ferrite nanoparticles [223]. According to Ali *et al*., the $CoIn_xFe_{2-x}O_4$ spinel ferrite exhibits the superparamagnetic property when the particle size is decreasing then multi-domain particles reduce to a single domain but in the reported study the particle size increases (246.53 nm to 337.39 nm) which confirms the occurrence of multi-domain [210].

$$SR = \frac{M_r}{M_s} \qquad (6.12)$$

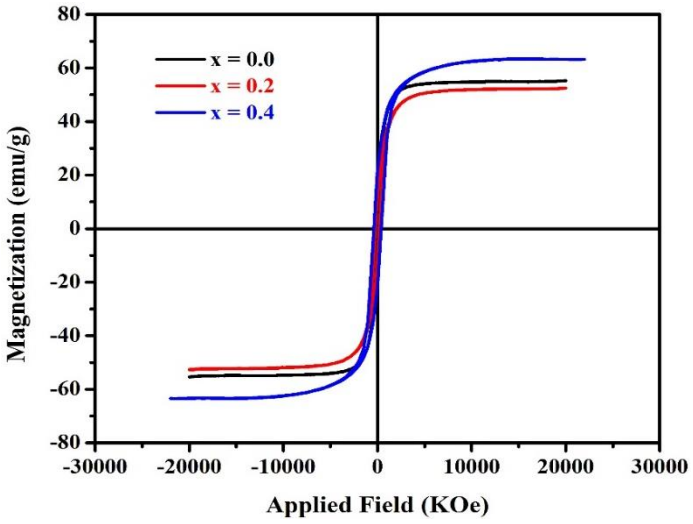

Fig. 6.7. M-H hysteresis plot of $Mn_xCo_{0.5-x}Ni_{0.5}Fe_2O_4$ samples.

The value of coercivity obtained from VSM results varies with several factors viz. size, morphology, micro-strain, and anisotropy constant of the incorporated samples. The coercivity increases as the Mn^{2+} content increases due to the magneto-crystalline anisotropy as in Fig. 6.8(b) [218]. The coercivity may also increase due to the presence of cobalt ferrite which is a hard ferrite. Owing to their high coercivity, this material has been used in recording magnetic media, electronic devices, and data processing. However, the magnetic moment decreases with increasing Mn concentration as a result, it reduces the A-B interaction [218].

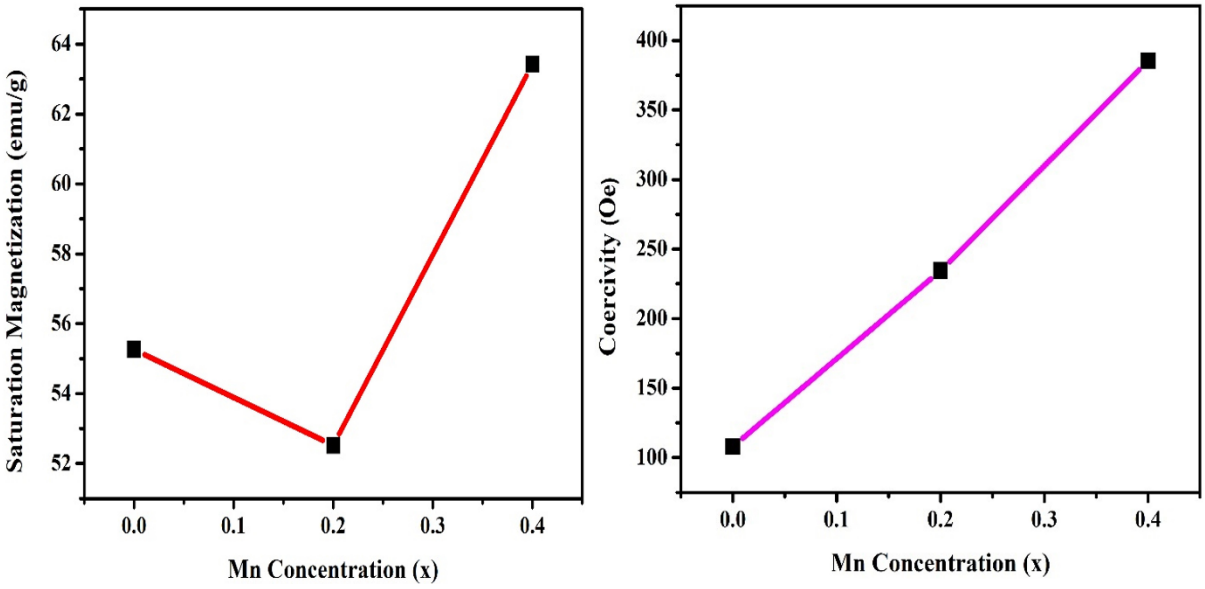

Fig. 6.8. (a) saturation magnetization as a function of Mn concentration (b) coercivity as a function of Mn concentration.

Table 6.4

Magnetic parameters of $Mn_xCo_{0.5-x}Ni_{0.5}Fe_2O_4$ samples.

Mn Concentration (x)	**0.0**	**0.2**	**0.4**
Saturation Magnetization M_s (emu/g)	55.26	52.52	63.42
Remanence M_r (emu/g)	8.50	12.00	21.32
Coercivity H_c (Oe)	108.03	234.42	385.38

Ratio of squareness (*SR*)	0.153	0.228	0.336
Anisotropy Constant *K* (erg/cc)	6218.47	12824.74	25459.16
Magnetic moment n^t_B (μ_B)	2.5	4.4	6.3
Magnetic moment n^o_B (μ_B)	2.6	2.3	2.1

6.3.5. Dielectric property analysis

The frequency dependence of real (ε') and imaginary (ε'') parts of permittivity are in Fig. 6.9(a, b), and dielectric loss ($tan\ \delta$) are in Fig. 6.9(c). The ε', ε'' can be measured by the Eq. (6.13) (6.14) [236].

$$\varepsilon' = \frac{C}{C_0} = \frac{\mathrm{Ct}}{\varepsilon_0 \mathrm{A}} \tag{6.13}$$

$$\varepsilon'' = \frac{G}{wC_0} = \frac{Gdi}{\varepsilon_0 wA} \tag{6.14}$$

Here, t is the thickness of pellets, ε_0 is the permittivity of free space 8.85×10^{-12} F/m, A is the area of pellets, and C is the capacitance of a dielectric material. As the frequency (log f) increased, the dielectric constant decreased slowly and attained a constant value at one point. This trend was attained because of the different types of polarization viz. ionic, electronic dipolar, and space charge. In ferrites, electrons are exchanged between the ions and dipoles, which align themselves with Fe^{2+} to Fe^{3+} and Mn^{2+} to Mn^{3+} [237]. Furthermore, at low-frequency hopping of e^- between ferric (Fe^{3+}) and ferrous (Fe^{2+}) atoms ions promote large polarization, and hence dielectric constant increases. According to Maxwell Wagner's Koops theory, the dielectric curve shows the dispersion and explains the two-layer structure. According to the Koop model, the spinel ferrite consists of well-conducting grains separated by highly resistive boundaries [238][239]. The dielectric constant was found to be maximum at minimum frequency because the grain boundaries were more active when compared to the grains i.e., the reason the dielectric constant is high at the low frequency. When the applied electric field, the scattered electrons are accommodated on resistive grain boundaries and then combined to form a space charge polarization. However, at low frequency, the dielectric constant is high and then

decreases with increasing frequency [238][77]. For the undoped sample (x = 0.0) dielectric constant ε' is less as compared to the doped sample (x = 0.2, 0.4). The dielectric constant can be explained with the help of FESEM (particle size). As a result, the FESEM particle size of (x = 0.4) is larger as compared to the (x = 0.0, 0.2). It found that the sample grains are fine and give high dielectric constant because of the large surface of ratio area to volume [207].

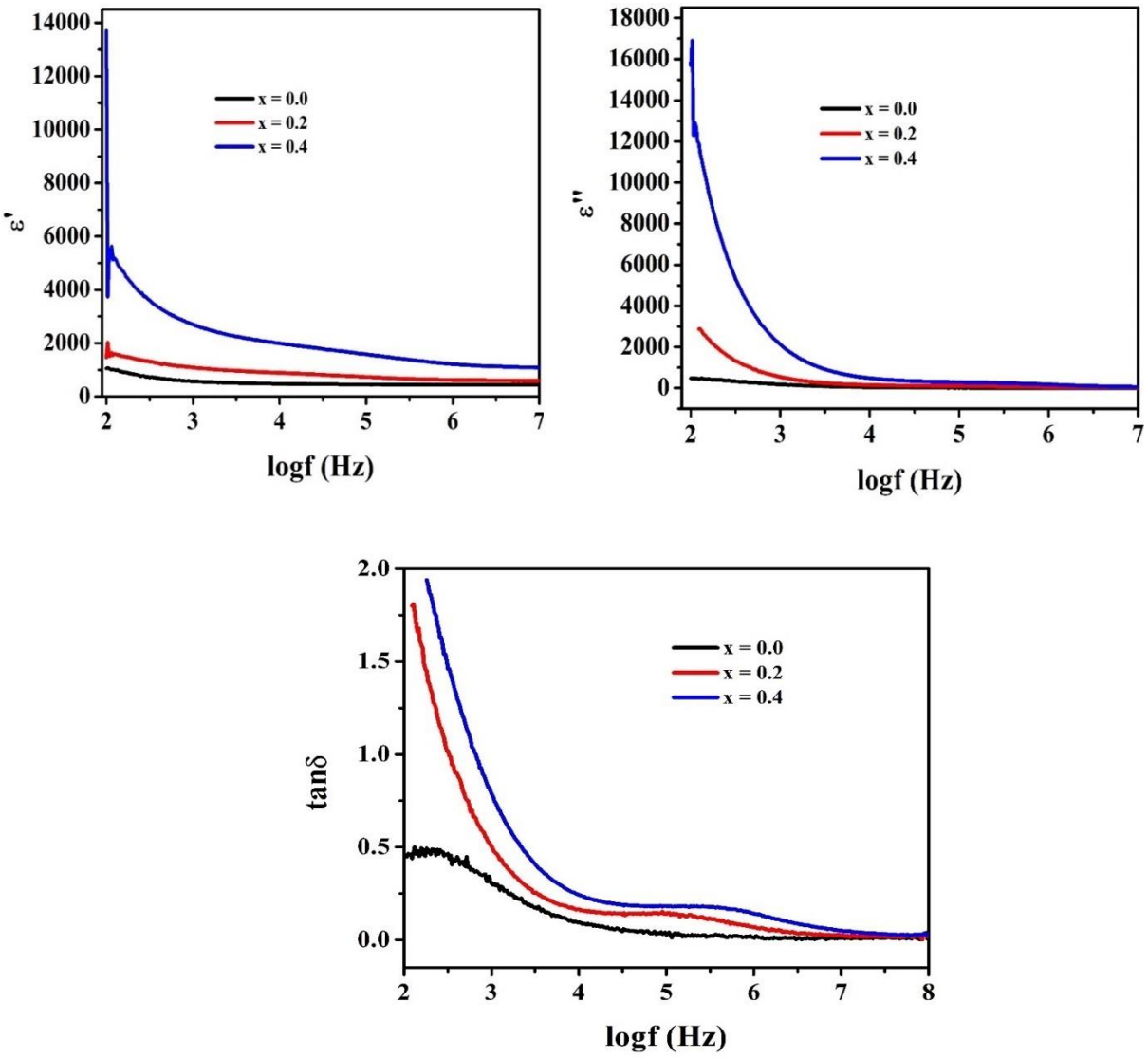

Fig .6.9 (a)Dielectric constant (ε') vs frequency (b) dielectric loss (ε'') with frequency (c) dielectric loss (tanδ) with frequency $Mn_xCo_{0.5-x}Ni_{0.5}Fe_2O_4$ samples.

The dielectric loss (tanδ) factor can be calculated by Eq. (6.15) [239].

$$tan\delta = \frac{\varepsilon''}{\varepsilon\prime} = \frac{G}{wC} \qquad (6.15)$$

The dielectric loss of the $Mn_xCo_{0.5-x}Ni_{0.5}Fe_2O_4$ ferrites showed a lag in polarization when an electric field was applied. The dielectric loss factor is due to domain wall resonance domain defects, non-uniform domain wall movements, and varying flux densities. The dielectric loss is caused by the resonance obtained at the walls of the domains. And also, when charge carries transport from grain-grain boundaries of ferrites the direction of polarization changes in the presence of applied field which causes dissipation in energy [240]. At high frequency, dielectric losses are reticent in the domain wall where the magnetization is changed by rotation [237][239]. At higher frequencies, a small quantity of energy is enough for the exchange of electrons between Fe^{2+} and Fe^{3+} giving low resistivity and a low value of loss tangent. At x = 0.2, and 0.4 concentration sample shows a hump at mid of frequencies, which happened due to the exchange of electrons between ions frequency is matched with the applied frequency. Similar to this was reported in the literature by Padmasree et *al*. [241].

6.4. Conclusion

Single-phase cubic spinel ferrite ($Mn_xCo_{0.5-x}Ni_{0.5}Fe_2O_4$) was successfully prepared by sol-gel route. The lattice constant (a_o) and the volume of the unit cell show an increment with the addition of the Mn as a result, the unit cell of the synthesized spinel ferrite expands. This can be related to the fact that Mn^{2+} has high ionic radii of 0.80 Å as compared to the Co^{2+} ion having ionic radii of 0.78 Å. The FTIR affirms the formation of spinel ferrite $Mn_xCo_{0.5-x}Ni_{0.5}Fe_2O_4$. The particle size varies from 246.53 to 337.39 nm as exhibited by the FESEM study. Because of the porous morphology demonstrated by all of the FESEM micrographs, the synthesized samples are useful for energy storage applications. The M-H hysteresis loop reveals the increase in coercivity from 108.03 Oe – 385.38 Oe. Saturation magnetization randomly decreased which then increased directly thereby affecting the crystallite size. The dielectric constant was found to be high at low frequencies because the grain boundaries were more active. Owing to the high coercivity and good remanence of these prepared materials, they are applicable in recording devices, switching, and microwave devices.

Chapter -7

Result and Discussion

7. Crystal structure, morphological, and magnetic properties of ternary nanohybrid $Pr_xMn_{0.5}Co_{0.5}Fe_{2-x}O_4$ ($0.00 < x < 0.04$) spinel ferrite

Abstract

Rare earth Pr^{3+} ion substituted in the Mn - Co spinel ferrite was prepared via. sol-gel route. The phase composition of the prepared samples was analyzed by X-ray diffraction (XRD). Rietveld refinement confirms the single phase for the samples (x = 0.0, 0.01, 0.02) and shows a secondary phase for the samples with higher concentrations of Pr^{3+} (x = 0.03 and 0.04). The absorption band occurs within 400 – 600 cm^{-1} which affirms the formation of spinel ferrite by the Fourier transform infrared (FTIR) spectra. Field emission scanning electron microscopy (FESEM) micrograph reveals the presence of porous morphology and non-uniform grain growth inhomogeneous in size and shape due to the agglomeration present in the prepared sample. A vibrating sample magnetometer (VSM) study reveals all the samples exhibit a ferromagnetic nature. The coercivity (H_c) increases from 441.78 to 557.32 Oe and then decreases to 503.48 Oe. Owing to the basis of large surface area, presence of pore size, and soft magnetic nature synthesized spinel ferrites are best suitable for supercapacitor electrode material.

Keywords: Spinel ferrites, Structural Properties, Magnetic Properties, Morphology.

7.1. Experimental Procedure

7.1.1. Sample Preparation

Synthesis of nanoparticle $Pr_xMn_{0.5}Co_{0.5}Fe_{2-x}O_4$ (x = 0.00, 0.01, 0.02, 0.03, and 0.04) was performed by sol-gel route as in Fig. 7.1. The stoichiometric amount of metal nitrates AR-grade chemicals (Mn $(NO_3)_2.6H_2O$), (Co $(NO_3)_2.6H_2O$), and (Pr $(NO_3)_3.6H_2O$), and (Fe $(NO_3)_3.9H_2O$) were dissolved in 200 ml of the distilled water. Citric acid and metal nitrates were mixed in a 1:1 ratio. Citric acid (CA) was used as a chelating agent. NH_3 was added dropwise to maintain pH 7. The metal nitrates solution was stirred vigorously to achieve a homogeneous solution. The stirring was stopped, heat the solution at 80 ° C, and the gel was formed. After 3h the product was self-combustion. A fluffy powder was formed and heated at 90 °C. The reticular material was grounded and sintered in a furnace at 1100 ° C for 6 h.

(0.5) [Mn $(NO_3)_2.6H_2O$)] + (0.5) [Co $(NO_3)_2.6H_2O$)] + x [Pr $(NO_3)_3.6H_2O$] + (2 − x) [Fe $(NO_3)_3.9H_2O$)] → $Pr_xMn_{0.5}Co_{0.5}Fe_{2-x}O_4$ + H_2O + volatiles

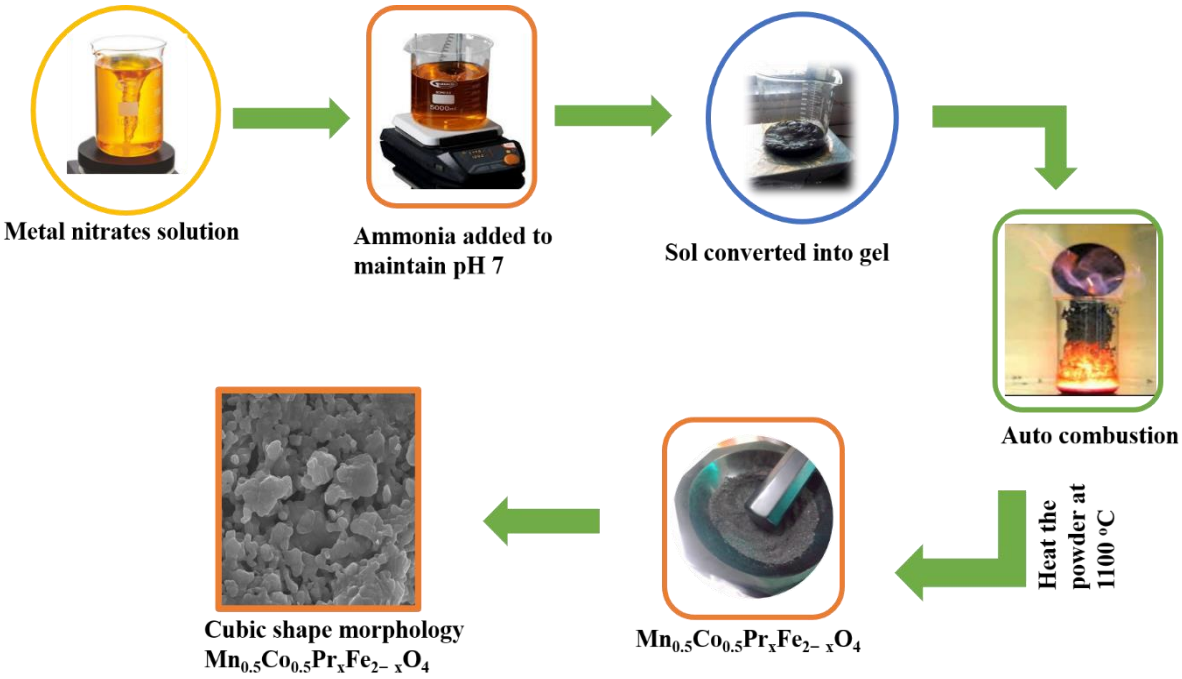

Fig. 7.1. Schematic of the synthesis of $Pr_xMn_{0.5}Co_{0.5}Fe_{2-x}O_4$ spinel ferrite.

7.2. Materials characterizations

The properties of the synthesized RE-doped Mn–Ni ferrite were evaluated using XRD, FTIR, FESEM with EDX, and VSM. To determine the phase identification and crystallographic structure of the materials, X-ray diffraction (Bruker D8 Advance) was used with Cu-Kα radiation having wavelength λ = 1.5404 in the 2θ range from 20 ° – 80 °. Further, the crystallite size of the sample is obtained from the XRD pattern by applying Scherrer's equation. The Fourier transform infrared spectra are recorded using (Perkin Elmer Spectrum2) and followed by the KBr pressed pellet technique to determine the structures of the calcined ferrite material. The morphologies were identified by FESEM (FE-SEM: JEOL JSM-7610 F Plus) and elemental composition was identified by EDAX (EDX: OXFORD EDX LN2 free). The magnetic properties have been measured at room temperature by using a Vibrating Sample Magnetometer (VSM-EZ9).

7.3. Result and Discussion

7.3.1. XRD study

The phase identification of the prepared samples $Pr_xMn_{0.5}Co_{0.5}Fe_{2-x}O_4$ (x =0.00-0.04) was done using the XRD analysis. Fig. 7.2(a) displays the XRD patterns of $Pr_xMn_{0.5}Co_{0.5}Fe_{2-x}O_4$ spinel ferrite. The observed peaks were indexed using the JCPDS card 22-1086 with cubic structure and Fd-3m as space group [59]. We observed that a pure sample (single phase) was obtained for the sample with x varying from 0.00 to 0.02. This may indicate that the substituted atom (Pr) properly occupied the crystallography sites. However, with the increase of Pr-concentration in the sample (x=0.03 and x=0.04), a strange peak (secondary phase) was also formed. Since a single phase was observed in samples for x between 0.00-0.03, we cannot assimilate this impurity (secondary phase) to the incomplete reaction as reported by Tchouank et *al*. [211] but the presence of this impurity could be due to the fact that the saturation in Pr^{3+} was reached which would favor the formation of another compound (*) which refers to Pr-ferrite with JCPDS card 19-1012 and Pnma as space group. To confirm the XRD observations, we performed the Rietveld Refinement using the FullProf suite package. To carry out all the refined parameters, the following conditions were used: the cycles of refinement were 30, the pseudo-Voigt function was used the define the peak morphology, and the background was defined by the linear interpolation. Fig. 7.2 (b)-(e) depicts the Rietveld refinement of prepared samples. The black plot (Yobs) refers to the experimental data, the red plot represents the theoretical data (Ycal), the background is in blue line and the small lines in green give the position for each plane. The reliability factors R_p (Profile fitting R-value), R_{wp} (Weighted profile R-value), and R_{exp} (anticipated R-value), the goodness of fit (GoF), and chi-square (χ^2) for all the samples were found in the following range: $10.4\% \leq R_p \leq 19.6\%$, $10.4\% \leq R_{wp} \leq 16.8\%$, $8.68\% \leq R_{exp} \leq 11.5\ \%$, and $1.2 \leq GoF \leq 1.4$ Table 7.1. From these figures, it was noticed that Yobs and Ycal perfectly match for x=0.00-0.02. However, an extra peak occurred between 30° and 35° for x=0.03 and x=0.04. The identified peaks in the XRD patterns refer to the diffraction planes (220), (311), (222), (400), (422), (511), (440), (620), and (533). From these peaks, the average value of lattice constant (a) and volume of the unit cell (V) of all the samples was determined by using the equation discussed elsewhere [209][204]. It was found that for x varying from 0.00 to 0.01, the values of a and V increase then they decrease for x greater than 0.02. The lattice parameter decreases with the substitution of Mn^{2+} ions with Co^{2+} ions, to accommodate the Mn^{2+} ion of relatively larger ionic radii (0.80 Å) as compared to that of Co^{2+} ion (0.78 Å) [242]. With further substitution of Fe^{3+} ions with Pr^{3+} ions, the lattice parameter decreased attributing to the larger ionic radii of Pr^{3+} (1.013Å) ion as compared to Fe^{3+} (0.64 Å) ion shown in Table

7.1. This can be observed from the XRD patterns in which the positions of the peak shifted towards higher values of Bragg angle and then towards lower values Fig. 7.3. This observation was done for the peaks between 62° and 63° but it can be observed for any peak. In general, by replacing an ion with another ion with a larger ionic radius, the unit cell volume tends to increase. In this work, Fe^{3+} ions (r(Fe^{3+})=0.645Å) were replaced by Pr^{3+} ions (r(Pr^{3+})=1.013Å). Thus, observed variation in *a* and *V* could be related to the possible interactions between ions of the system.

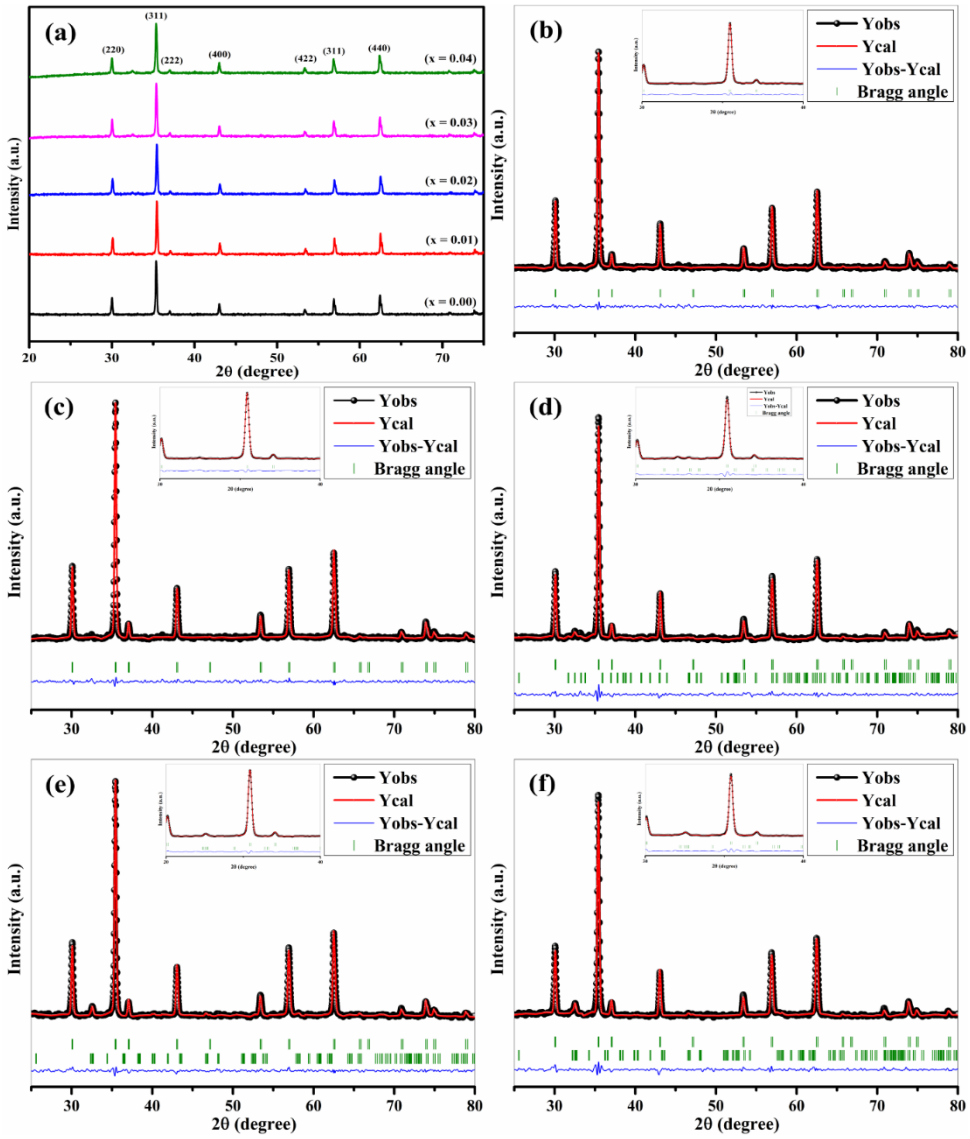

Fig. 7.2 (a) XRD patterns and Rietveld refinement of $Pr_xMn_{0.5}Co_{0.5}Fe_{2-x}O_4$ (b) x=0.00, (c) x=0.01, (d) x=0.02, (e) x=0.03, (f) x=0.04.

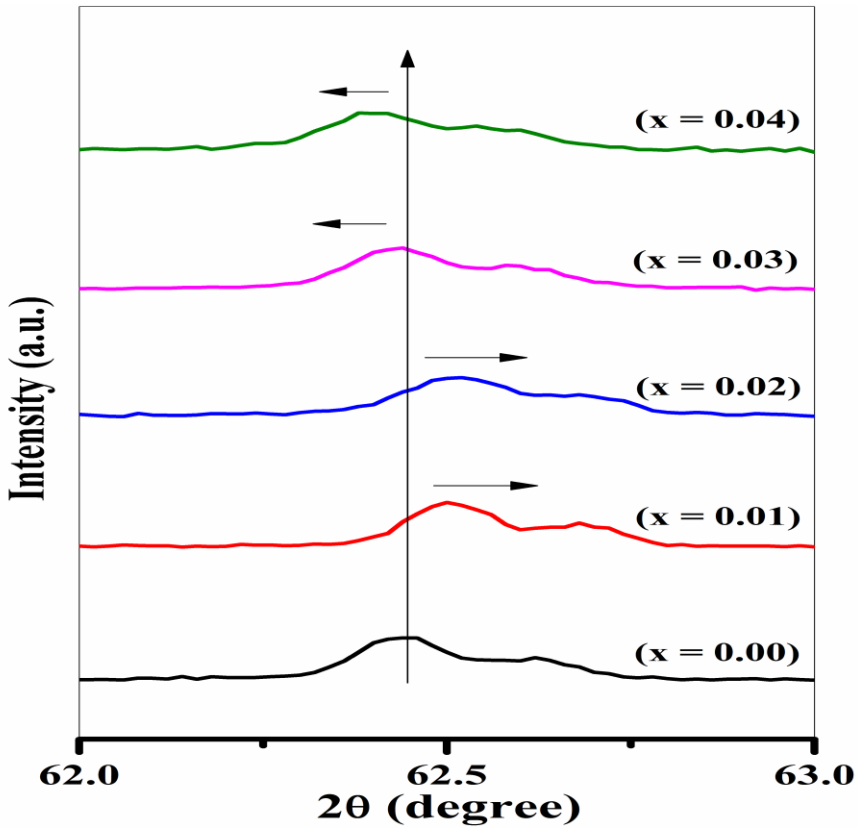

Fig. 7.3. Shift in 2θ (~ 62.45°) value of $Pr_xMn_{0.5}Co_{0.5}Fe_{2-x}O_4$ samples.

The crystallite size (D) of prepared samples was assessed using the Debye–Scherrer formula Eq. (7.1) and the values are listed in Table 7.1**.** The values of D were obtained in the range of 43-45 nm. It was reported that if the values of D are inferior to 50 nm then the material is a suitable candidate for media recording applications [230]. Hence, it could be deduced that the prepared samples are potential candidates for media recording applications.

$$D = \frac{k\lambda}{\beta \cos\theta} \qquad (7.1)$$

where k is constant having a value of 0.95, λ is wavelength 1.5406 nm, 2θ is Bragg angle, and β is the full-width half maxima. Strain and dislocation density was calculated from the below Eq. (7.2)(7.3) [59].

$$\varepsilon = \frac{\beta}{4Tan\theta} \qquad (7.2)$$

$$\delta = \frac{1}{D^2} \quad (7.3)$$

For the incorporated sample, crystallite size is decreased with increased Pr^{3+} concentration due to segregation near the grain boundaries, which hampers its movement. Strain and dislocation density increases but at x = 0.03 to 0.04 it decreases due to the metal cation randomly present in the tetrahedral and octahedral sites. The variation in metal cations that are arranged induces strain within the lattice sites, leading to their fragmentation into irregular particles of varying shapes. [79].

Hopping length in tetrahedral sites (L_A) and in octahedral sites (L_B) which are nothing but the distance between the magnetic ions were calculated from Eq. (7.4) and Eq. (7.5) [243]. It was found that L_A and L_B show the same variability with the lattice constant. This observation was expected since they are proportional to the lattice constant *a*. The hopping length values in tetrahedral and octahedral sites were found to lie in the range of 3.6408-3.6405 nm and 2.9723 – 2.9721 nm. These values are in the same order as those reported by Zipare et *al*. [244]. The fact that the hopping length in the octahedral site (B-sites) is less than that of a tetrahedral site (A-sites) could indicate that it is more probable to have a hopping of an electron in the B-sites compared to the A-sites [243][245].

$$L_A = a\sqrt{3}/_4 \quad (7.4)$$

$$L_B = a\sqrt{2}/_4 \quad (7.5)$$

To understand the distribution of electrons in the prepared samples, we did the electron density of the refined structures through the GFourier program using the Fullprof Suite software. Indeed, the electron density gives information about the probability of finding electrons at a specific location within an orbital. Fig. 7.4 shows the 2D and 3D electron density mapping of $Pr_xMn_{0.5}Co_{0.5}Fe_{2-x}O_4$ for x=0.00 and x=0.01. The 2D map is the projection of the 3D map on the plane (x, y) as shown in Fig. 7.4. The plan with the highest value of density was considered. From Fig. 7.4, it can be seen that electrons are more concentrated around cobalt atoms as compared to oxygen atoms. The red, orange, and yellow contours around Co atoms could refer to the distribution of the valence d orbitals electrons whereas the blue contour around the O atoms could refer to the distribution of 2s and 2p orbitals electrons [243].

Table 7.1.

Lattice parameters (a and c), the volume of unit cell (V_{cell}), crystallite size (D), Dislocation density (δ), Lattice strain (ε), Hopping length in tetrahedral and octahedral sites (L_A and L_B), reliability factors (R_p, R_{wp} and R_{exp}), Bragg R-factor (R_{bragg}), goodness of fit (GoF) and chi-square (χ^2) of prepared samples.

Amount of x	***x* = 0.00**	***x* = 0.01**	***x* = 0.02**	***x* = 0.03**	***x* = 0.04**
***D* (nm)**	45.00	44.06	43.27	44.90	44.89
***a* (Å)**	8.408	8.417	8.413	8.407	8.407
***V* (Å^3)**	594.476	596.402	595.491	594.305	594.359
Dislocation density (δ)	0.493	0.514	0.533	0.495	0.496
Lattice strain (ε)	0.257	0.262	0.267	0.258	0.258
***L_A* (nm)**	3.640	3.6447	3.6428	3.6404	3.6405
***L_B* (nm)**	2.972	2.9755	2.9740	2.9720	2.9721
***a*(Å) (Rietveld)**	8.40	8.40	8.40	8.40	8.40
***V*(Å^3) (Rietveld)**	591.984	592.857	592.201	593.088	593.636
***R_{bragg}* (%)**	2.54	2.17	3.41	21.6	3.54
***R_p* (%)**	12.1	10.4	17.9	16.7	19.6
***R_{wp}* (%)**	12.7	10.4	15.7	15.1	16.8
***R_{exp}* (%)**	8.89	8.68	10.8	10.9	11.5
Rf-factor	2.77	3.00	2.79	12.5	2.98
GoF	1.4	1.2	1.4	1.4	1.4
χ^2	2.038	1.437	2.131	1.933	2.144

Number of phases	1	1	1	2	2

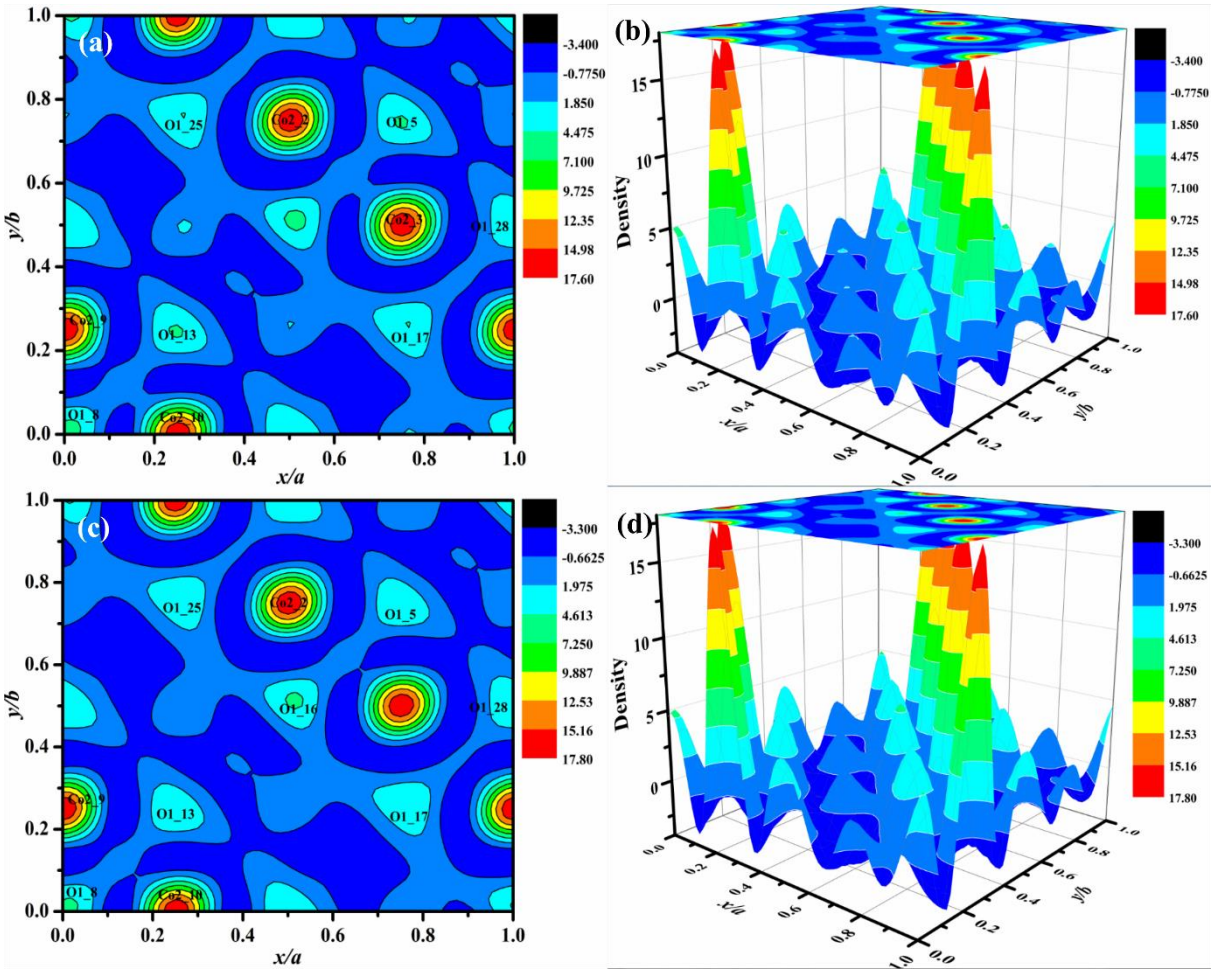

Fig. 7.4. 2D electron density mapping ((a) and (c)) and 3D electron density mapping ((b) and (d)) of $Pr_xMn_{0.5}Co_{0.5}Fe_{2-x}O_4$ ($x = 0.00$ and $x = 0.01$).

7.3.2. FTIR study

For further information about the structure, the FTIR spectra for all the synthesis samples $Pr_xMn_{0.5}Co_{0.5}Fe_{2-x}O_4$ ($0.00 < x < 0.04$) were taken in the range of 4000 cm^{-1} to 400 cm^{-1} in Fig. 7.5 respectively. Two frequency bands (υ_1 and υ_2) were observed. At the high–frequency band (υ_1) range lies 542.54 cm^{-1} indicates the stretching vibrations of M-O complexes at the tetrahedral site (A) but at the lesser frequency band (υ_2) range is 453.57 cm^{-1} indicates the intrinsic vibrations M-O complexes at the octahedral site (B) [246]. The difference in peak position at frequency υ_1 (542.24 cm^{-1}) and υ_2 (453.57 cm^{-1}) is observed due to a change in bond

length ($Fe^{3+} – O^{2–}$) at tetrahedral and octahedral sites [247]. These two absorption bands reveal the formation of spinel ferrite [248]. The absence of peaks near the wavenumber at 1385, 1572, and 3137 cm^{-1} reveals citric acid ($C_6H_8O_7$) has been evacuated in our synthesized spinel ferrite [59].

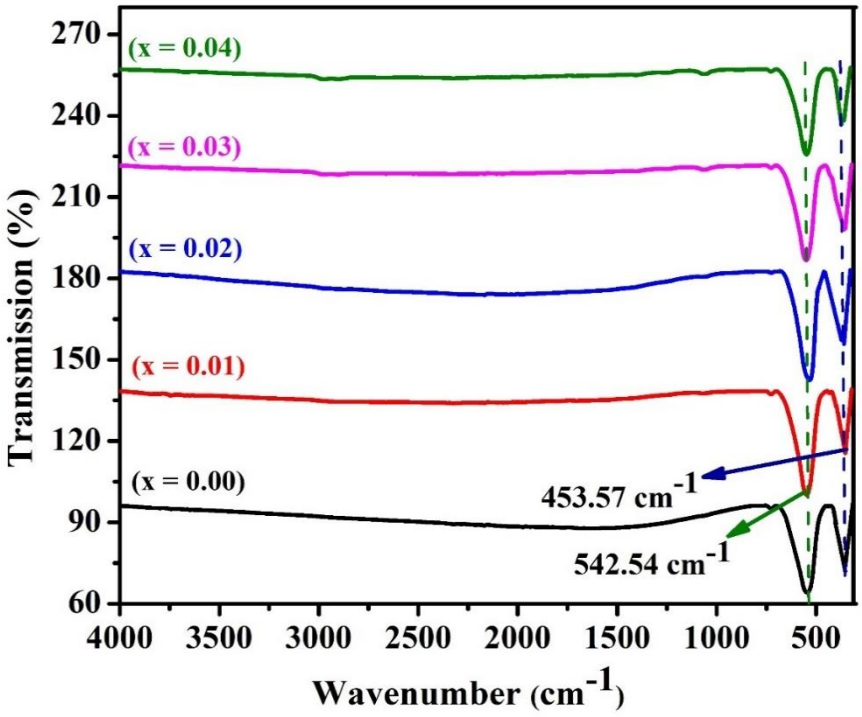

Fig. 7.5. FTIR spectra of $Pr_xMn_{0.5}Co_{0.5}Fe_{2-x}O_4$ ($0.00 < x < 0.04$).

7.3.3. FESEM with EDX study

The field emission scanning electron micrograph (FESEM) and particle size histogram for $Pr_xMn_{0.5}Co_{0.5}Fe_{2-x}O_4$ ($0.00 < x < 0.04$) NPs are shown in Fig. 7.6 respectively. The micrographs for all the samples reveal that the grains exhibit agglomerations, irregular shapes and sizes, and non–uniform grain growth. In the FESEM micrographs, agglomerations were observed owing to the presence of magnetic interactions in the NPs, as well as the electrostatic nature of the surfactant during the synthesis process [249]. For the (x = 0.00, 0.01, 0.02, 0.03, and 0.04) the particle size is 373.55 nm, 397.88 nm, 396.12 nm, 498.71 nm, and 245.69 nm respectively. The variation in the particle size can be attributed to the grain size owing to the rare earth dopant Pr^{3+} cations. As per the space charge model, the increase in trivalent dopant (Pr^{3+}) cations at the grain boundary area leads to a concentration gradient between the interior

of the grain and the grain boundary. This gradient reduces the mobility of cations along the grain boundary, resulting in decreased densification and grain growth rates [65]. For all the samples of FESEM micrographs determine some voids and pores, which were attributed to the emission of gases (CO_2, NO_2, H_2O, etc.) during sample synthesis. These pores are helpful for gas-detection applications and energy-storage devices (supercapacitors, batteries, etc.) [233]. The EDX spectra revealed the elemental mapping and composition of the stoichiometric ratios of the $Pr_xMn_{0.5}Co_{0.5}Fe_{2-x}O_4$ NPs as in Fig. 7.7. The EDX spectrum of the undoped sample revealed elements viz. Mn, Co, Fe, and O at ($x = 0.00$). The doped sample at ($x = 0.01, 0.02, 0.03, 0.04$) reveals elements viz. Pr, Mn, Co, Fe, and O were present without impurities in the incorporated sample. Table 7.2 reports the theoretical and experimental values of atomic percentage (%), indicating the accuracy of the synthesis process [233]. For $x = 0.03$ and $x = 0.04$ a large difference has been observed in the theoretical and experimental due to the secondary phase has been observed in the XRD pattern. Fig. 7.8 indicates the elemental mapping of the $Pr_{0.01}Mn_{0.5}Co_{0.5}Fe_{1.99}O_4$, revealing the presence of elements viz. Co, Mn, Pr, Fe. and O, and their uniform distribution in a specific spinel ferrite.

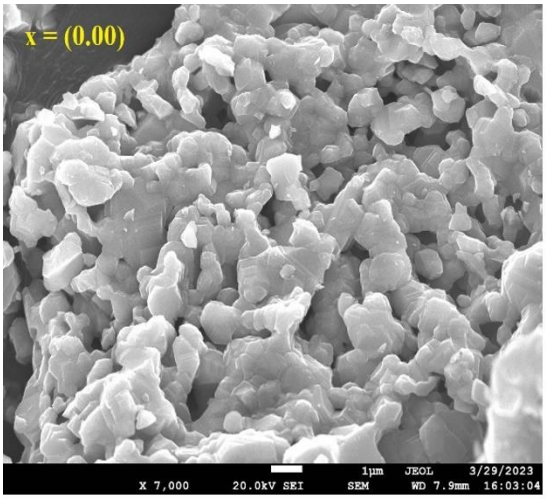
x = (0.00)
X 7,000 20.0kV SEI 1μm SEM JEOL WD 7.9mm 3/29/2023 16:03:04

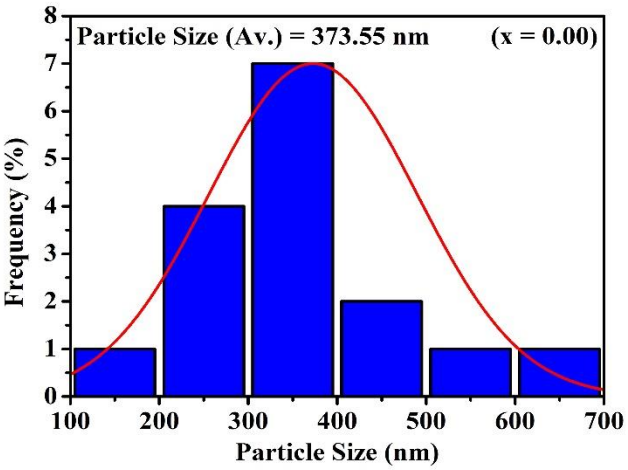
Particle Size (Av.) = 373.55 nm
(x = 0.00)
Frequency (%)
Particle Size (nm)
0 1 2 3 4 5 6 7 8
100 200 300 400 500 600 700

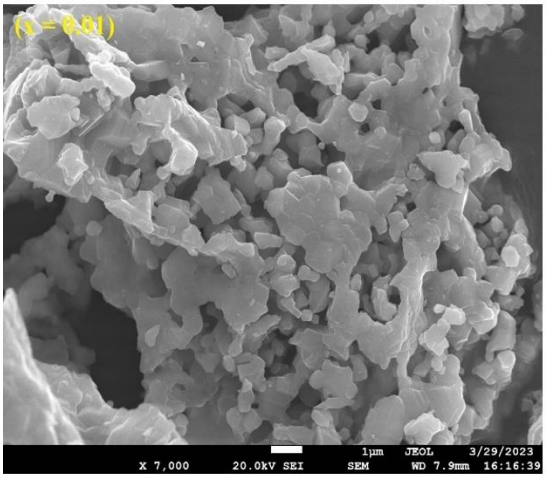
(x = 0.01)
X 7,000 20.0kV SEI 1μm SEM JEOL WD 7.9mm 3/29/2023 16:16:39

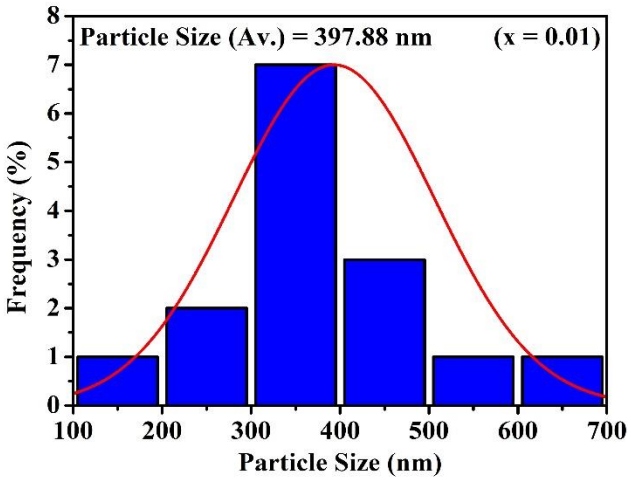
Particle Size (Av.) = 397.88 nm
(x = 0.01)
Frequency (%)
Particle Size (nm)
0 1 2 3 4 5 6 7 8
100 200 300 400 500 600 700

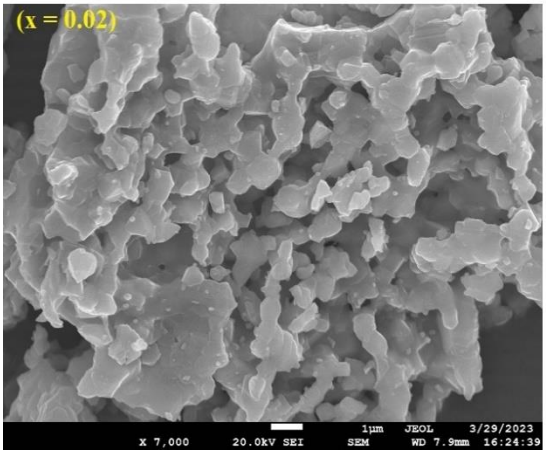
(x = 0.02)
X 7,000 20.0kV SEI 1μm SEM JEOL WD 7.9mm 3/29/2023 16:24:39

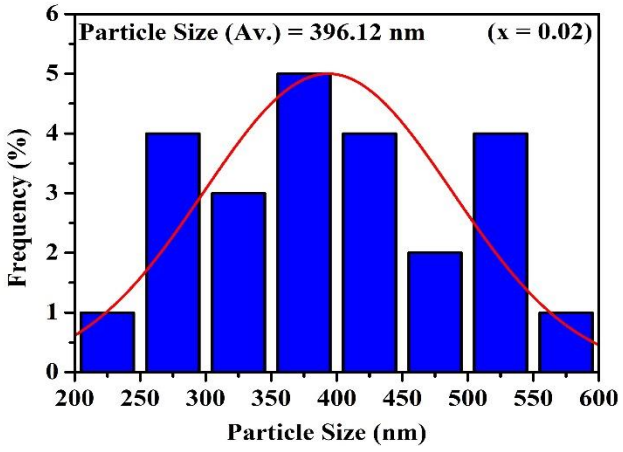
Particle Size (Av.) = 396.12 nm
(x = 0.02)
Frequency (%)
Particle Size (nm)
0 1 2 3 4 5 6
200 250 300 350 400 450 500 550 600

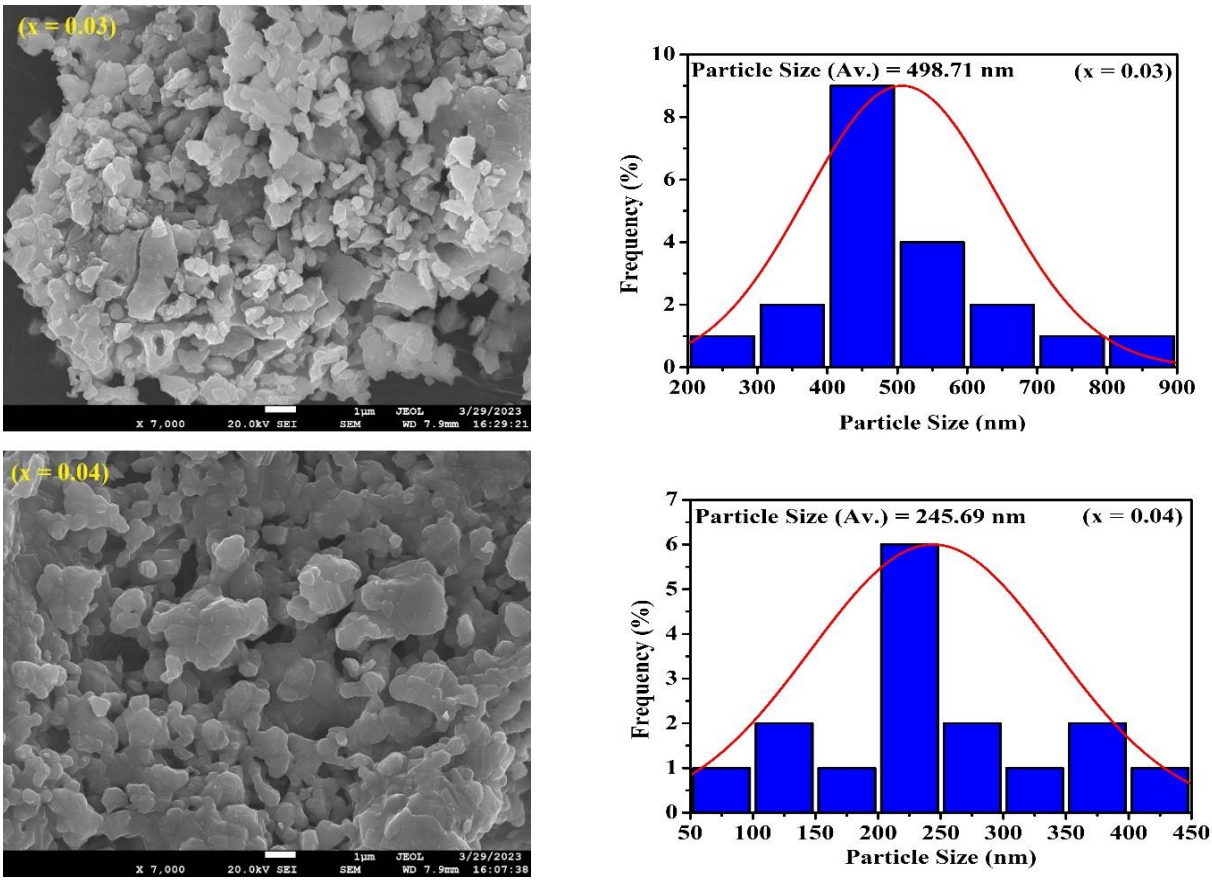

Fig. 7.6. FESEM micrograph and particle size histogram $Pr_xMn_{0.5}Co_{0.5}Fe_{2-x}O_4$ ($0.00 < x < 0.04$).

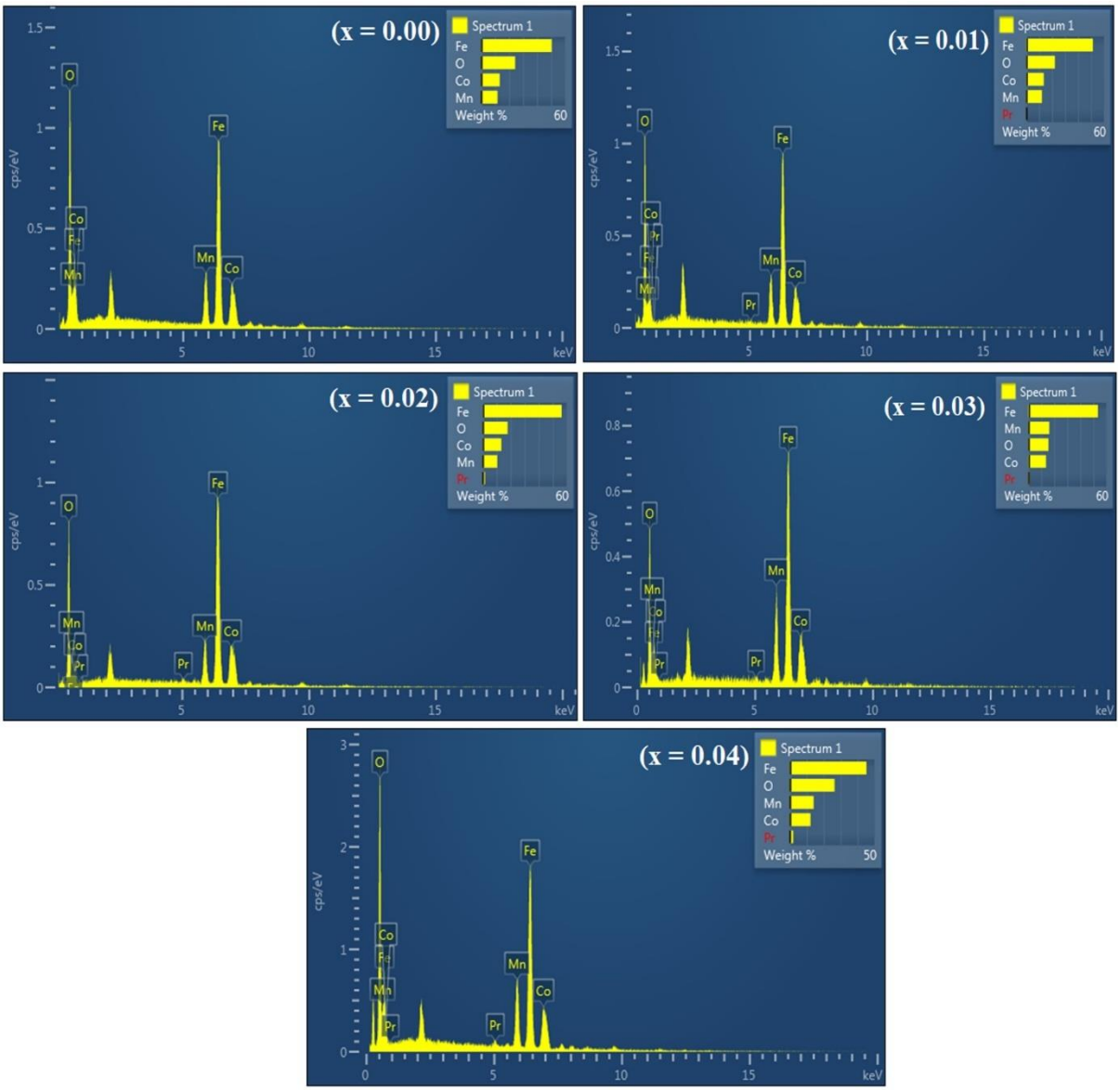

Fig. 7.7. EDX spectra of the $Pr_xMn_{0.5}Co_{0.5}Fe_{2-x}O_4$ ($0.00 < x < 0.04$).

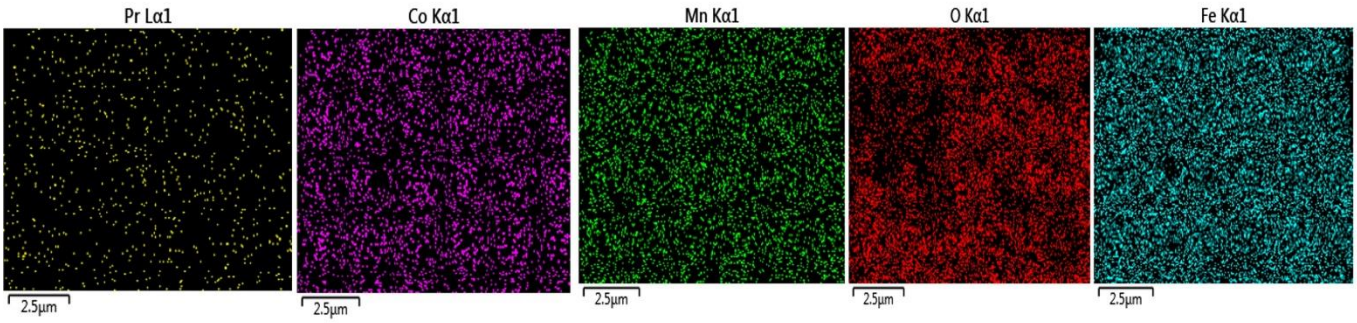

Fig. 7.8. Elemental mapping of the doped spinel ferrite $Pr_{0.04}Mn_{0.5}Co_{0.5}Fe_{1.96}O_4$.

Table 7.2

Theoretical and Experimental Value of atomic percent at % of $Pr_xMn_{0.5}Co_{0.5}Fe_{2-x}O_4$.

Pr concentration (x)	Value	Element at %					Total
		Pr	Mn	Co	Fe	O	
0.00	Theoretical	0.00	7.14	7.14	28.57	57.14	100
	Experimental	0.00	7.47	7.90	31.54	53.09	100
0.01	Theoretical	0.14	7.14	7.14	28.42	57.14	100
	Experimental	0.12	8.03	8.34	33.34	50.16	100
0.02	Theoretical	0.28	7.14	7.14	28.28	57.14	100
	Experimental	0.49	7.47	8.89	39.44	43.71	100
0.03	Theoretical	0.42	7.14	7.14	28.14	57.14	100
	Experimental	0.36	11.96	9.42	38.93	39.33	100
0.04	Theoretical	0.57	7.14	7.14	28.00	57.14	100
	Experimental	0.42	12.23	11.46	39.63	35.33	100

7.3.4. VSM study

The M vs H hysteresis graph of $Pr_xMn_{0.5}Co_{0.5}Fe_{2-x}O_4$ (x = 0.00, 0.01, 0.02, 0.03, and 0.04) is shown in Fig. 7.9. with a magnetic field range of -15Koe to +15 Koe. Table 7.3 lists the magnetic parameters of saturation magnetization (M_s), remanence magnetization (M_r), coercivity (H_c), anisotropy constant (K_1), squareness ratio (R), and magnetic moment (n_B). The magnetic curves for all samples showed an S-type curve and a ferromagnetic nature [12]. The magnetic properties of spinel ferrite depend on A-B interactions, cation distribution, and particle

size. The Pr^{3+} content increases, M_s increases ($x = 0.00,0.01, 0.03$) then decreases ($x = 0.02,0.04$) is depended on the cation distribution in the tetrahedral and octahedral sites as shown in Fig. 7.10(a). The increase in M_s can be explained viz. high crystallinity and decreasing spin disorder on the surface of the nanoparticles. The lower M_s is found in several oxides such as Al_2O_3, In_2O_3, CeO_2, MgO, and MgO with nano-size dimensions. This magnetic behavior is expected to originate from the exchange interactions between localized spin moments of electrons [204]. According to Wadne *et al*., pure BFMO has lower saturation magnetization as compared to the Eu substituted in BFMO. Such an enhancement in M_s could be related to the presence of the orthorhombic phase which leads to the suppression of SMSS in Eu substituted BFMO [250]. The reduction in M_s directly affected the reduction in crystallite size. Because the ionic radii of Pr^{3+} ions are higher than those of Co^{2+} and Mn^{2+} ions, Pr^{3+} ions occupy octahedral sites in the lattice. When the saturation magnetization is reduced, the size of the nanoparticles also changes owing to spin canting [16]. As a result, the decrease in M_s can be explained by the hypothesis of magnetic dead sheets (spin disarray) on the surface of the nanoparticles, while a reduction in saturation magnetization with an increase in the Pr^{3+} content [35]. The magnetic interactions can be explained based on magnetization behavior. The super-exchange process allows the cations to interact magnetically through the intermediary oxygen ions in three ways: A-A, B-B, and A-B. Cations at the tetrahedral and octahedral sites are represented by A and B, respectively. Table 7.3 demonstrates the cation distribution [251]. Manganese ferrite is a mixed ferrite in that the (Mn^{2+}) acquires any lattice site (A or B). Cobalt ferrite is inverse ferrite in that the divalent cation (Co^{2+}) can occupy the B site and the trivalent cation (Fe^{3+}) can occupy the A and B sites, where the A site is tetrahedral and the B site is octahedral [163]. Pr is a trivalent cation (Pr^{3+}) that can occupy the octahedral site.

Table 7.3

Cation Distribution of the $Pr_xMn_{0.5}Co_{0.5}Fe_{2-x}O_4$ (x = 0.00, 0.01, 0.02, 0.03, and 0.04).

Pr Concentration	Cation Distribution	
	Tetrahedral (A) site	Octahedral (B) site
$x = 0.00$	$(Mn_{0.25}Fe_1)$	$[Mn_{0.25}Co_{0.5}Fe_1]$
$x = 0.01$	$(Mn_{0.25}Fe_1)$	$[Pr_{0.01}Mn_{0.25}Co_{0.5}Fe_{1.99}]$
$x = 0.02$	$(Mn_{0.25}Fe_1)$	$[Pr_{0.02}Mn_{0.25}Co_{0.5}Fe_{1.98}]$
$x = 0.03$	$(Mn_{0.25}Fe_1)$	$[Pr_{0.03}Mn_{0.25}Co_{0.5}Fe_{1.97}]$
$x = 0.04$	$(Mn_{0.25}Fe_1)$	$[Pr_{0.04}Mn_{0.25}Co_{0.5}Fe_{1.96}]$

$$n_B = \frac{M \times M_S}{5585} \qquad (7.6)$$

M_s can also be explained based on n_B, also computed by Eq. (7.6) as shown in Fig. 7.10(a). where M is the molecular weight and M_s is the saturation magnetization. The magnetic moment increased (x = 0.00 (1.66μ_B), (x = 0.01 (3.54 μ_B) then decreased (x = 0.02 (2.66 μ_B), again increased (x = 0.03 (3.89 μ_B), and then decreased (x = 0.04 (2.71 μ_B). The substitution of Pr^{3+} ions replaces Fe^{3+} ions from the B site. The Fe^{3+} ions reside on tetrahedral as well as on the octahedral sites, while Pr^{3+} ions (1.013 Å) occupy the octahedral site due to the larger ionic radius as compared to Fe^{3+} ions (0.64 Å). So, there is a lesser chance of Pr^{3+} to reside on the tetrahedral site. As Pr^{3+} is non-magnetic. As a result, the magnetic moment on the B–site reduced, but the magnetization on the A-sublattice remained unchanged. The transfer of Fe^{3+} ions from the B site to the A site may decrease the M_s. The saturation magnetization and remanence are reduced by weakening the A–B interaction. As the Pr^{3+} content increases, M_s randomly increases and decreases, and the magnetic moment also follows the same trend of increases and decreases, which debilitates the A-B exchange interaction and causes disorder of consecutive magnetic spins in the crystal structure of the spinel ferrite nanoparticles [210]. The reduction in Ms directly affected the reduction in crystallite size. Because the ionic radii of Pr^{3+} ions are higher than those of Co^{2+} and Mn^{2+} ions, Pr^{3+} ions occupy octahedral sites in the lattice. When the saturation magnetization is reduced, the size of the nanoparticles also changes owing to spin canting. As a result, the decrease in Ms can be explained by the hypothesis of magnetic deadsheets (spin disarray) on the surface of the nanoparticles, while a reduction in saturation magnetization with an increase in the Pr^{3+} content. The coercivity increases as particle size increases. This increase in Hc with particle size due to the particles approaching a critical size, where they are likely near the single- to multi-domain transition threshold. At this size, the particles have increased magnetic anisotropy.

The Stoner-Wohlfarth model was used to calculate the anisotropy constant (K_1) using Eq. (7.7) [238] as shown in Fig. 7.10(b).

$$K_1 = \frac{H_c \times M_S}{0.96} \qquad (7.7)$$

The coercivity (H_c) increased from 441.78 Oe (x = 0.00), 490.39 Oe (x = 0.01), 557.32 Oe (x = 0.02) and then decreased 523.12 Oe (x = 0.03), 503.48 Oe (x = 0.04) as in Fig. 7.10(b). According to the above relation, the anisotropy constant is directly dependent on H_c and M_s because the anomalous behavior of the coercivity is related to the cation distribution and the anisotropy constant. Table 7.4 lists the K_1 values for different concentrations of Pr^{3+}. The

anisotropy constant K_1 increased (x = 0.00, 0.01, and 0.03), owing to the Pr^{3+} ions occupying the octahedral sites. Thus, the coercivity increases owing to structural distortion and lattice change [127]. The two phenomena are: (i) a high anisotropy constant associated with the strain leads to an increase in H_c. (ii) the movement of the Mn^{2+} ions from the octahedral and tetrahedral sites to reduce the coercivity at the higher concentration of the Pr^{3+} (x = 0.03, 0.04) [252]. Coercivity may be strongly influenced by various factors, such as crystallite size, magnetic particle morphology and size distribution, saturation magnetization, porosity, anisotropy constant, grain size, and magnetic domain [21]. In the present study, a lower value of coercivity (H_c) indicates that the material is soft ferrite, which is suitable for power applications, energy storage devices, sensors, and multilayer chip inductors. The squareness ratio and magnetic moment were calculated using Eq. (7.8)[245].

$$R = \frac{M_r}{M_s} \tag{7.8}$$

For all the samples the values of M_r/M_s lie within the range of 0.28 ~ 0.34. The material magnetic hardness can also be determined by using the values of M_r/M_s. It can be observed in the literature that the materials having M_r/M_S above 0.5 show the single-domain structure and lower values (<0.5) oriented from the multi-domain structures [204]. The materials exhibit a multi-domain structure and reveal magnetostatics interaction between the nanoparticles [79].

Table 7.4

Magnetic parameters of $Pr_xMn_{0.5}Co_{0.5}Fe_{2-x}O_4$ samples.

Pr concentration (x)	M_s (emu/g)	H_c (Oe)	M_r (emu/g)	K_1 (erg/cc)	R	n_B (μ_B)
x = 0.00	40.05	441.78	11.5	18430.5	0.28	1.66
x = 0.01	84.91	490.39	25.56	43373.9	0.30	3.54
x = 0.02	63.62	557.32	18.53	36934.0	0.29	2.49
x = 0.03	92.56	523.12	30.98	50437.4	0.33	3.89
x = 0.04	64.27	503.48	22.22	33706.9	0.34	2.71

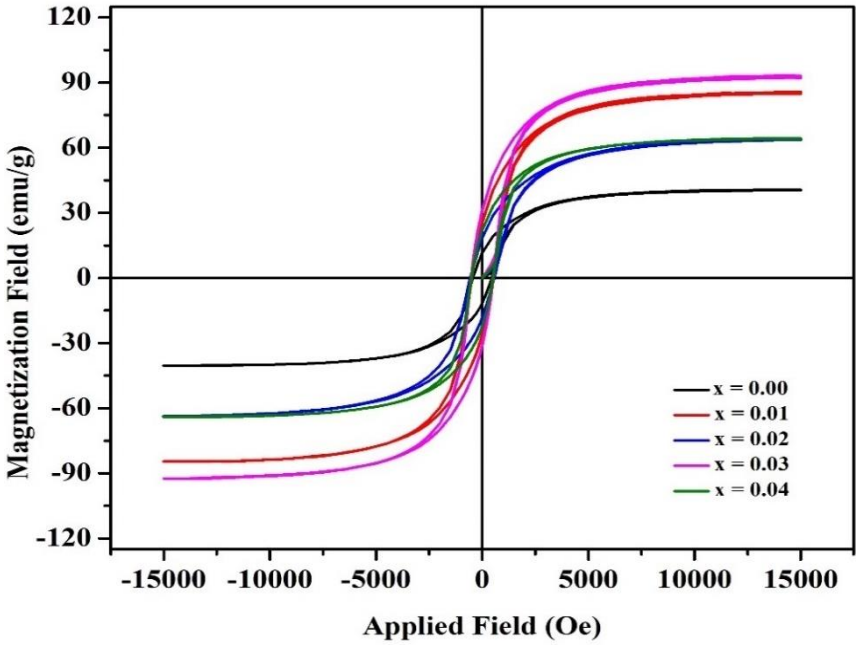

Fig. 7.9. VSM plots for $Pr_xMn_{0.5}Co_{0.5}Fe_{2-x}O_4$ ($0.00 < x < 0.04$).

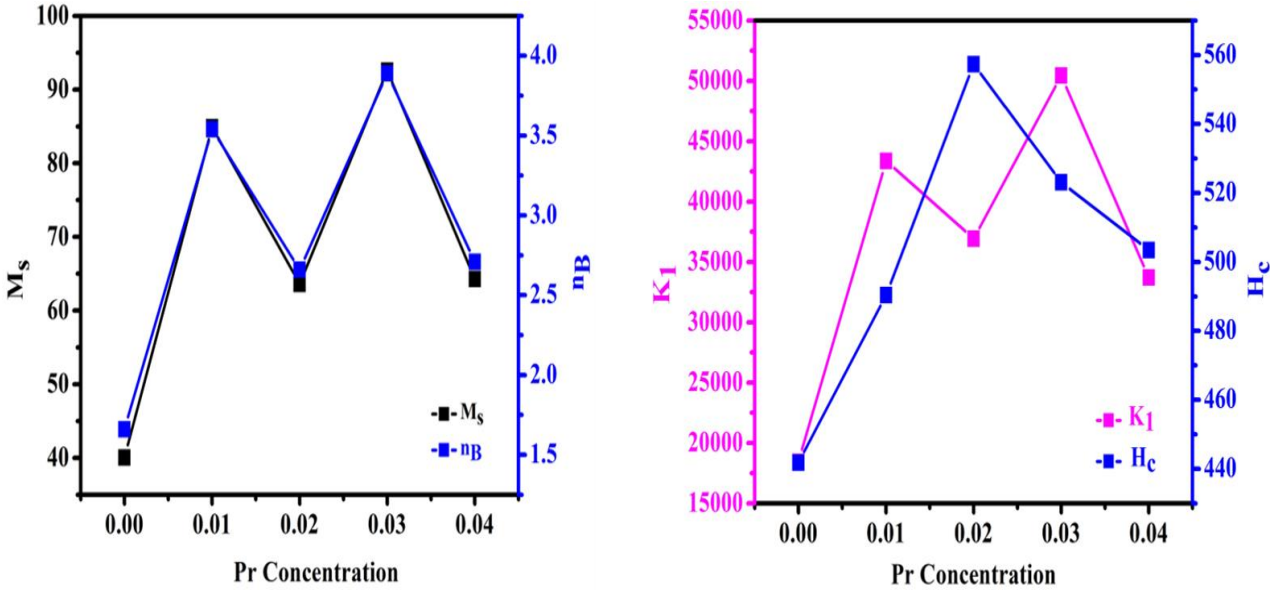

Fig. 7.10(a) Saturation Magnetization (M_s), Magnetic Moment (n_B) representation of $Pr_xMn_{0.5}Co_{0.5}Fe_{2-x}O_4$ (b) Anisotropy constant (K_1), Coercivity (H_c) representation of $Pr_xMn_{0.5}Co_{0.5}Fe_{2-x}O_4$.

7.4. Conclusion

In the present study, we fabricated $Pr_xMn_{0.5}Co_{0.5}Fe_{2-x}O_4$ using a cost-effective sol-gel auto-combustion method, and their structural and magnetic properties were analyzed. The crystallite size first decreases and then increases due to the Pr^{3+} having high ionic radii than the Fe^{3+} ions. The synthesized material $Pr_xMn_{0.5}Co_{0.5}Fe_{2-x}O_4$ is found to be the best suitable match for the supercapactior electrode, and gas sensing because of the porous morphology exhibited by all the FESEM micrographs. The EDX spectra determine the atomic percent (at%) values, which were in close concordance with the theoretical values. For $x = 0.03$ and $x = 0.04$ however, the large difference in the theoretical and experimental value occurred owe to the secondary phase which has been observed in the XRD pattern. The absorption band fall in the usual range υ_1 (542.24 cm^{-1}) and υ_2 (453.57 cm^{-1}) which confirmed the formation of spinel ferrite. The magnetic soft nature of the synthesized samples makes them suitable for energy storage devices. The squareness ratio for all the samples was noticed to be less than 0.5 which affirms the existence of the multi-domain structure. Owing to the above-mentioned characterized features it is deduced that $Pr_xMn_{0.5}Co_{0.5}Fe_{2-x}O_4$ spinel ferrites can be potential candidates for supercapacitor electrode material.

Chapter – 8

Result and Discussion

8. PrMnCo-Ti_3C_2 MXene nanocomposite-based supercapacitor for enhanced electrochemical performance

Abstract

The popularity of MXene has increased amongst researchers owing to its marvelous electrochemical properties. The current research work explores the synthesis of nanocomposites $Pr_{0.02}Mn_{0.5}Co_{0.5}Fe_{1.98}O_4$ – Ti_3C_2) which is most suitable for supercapacitor applications. The sol-gel method was used to synthesize the spinel ferrite ($Pr_{0.02}Mn_{0.5}Co_{0.5}Fe_{1.98}O_4$) and the etching method for Ti_3C_2 MXene's. The final ($Pr_{0.02}Mn_{0.5}Co_{0.5}Fe_{1.98}O_4$ – Ti_3C_2) nanocomposite was prepared by using physical blending. The X-ray diffraction (XRD) analysis revealed the enhancement of the crystallite size of the $Pr_{0.02}Mn_{0.5}Co_{0.5}Fe_{1.98}O_4$ – Ti_3C_2 nanocomposite compared to the $Pr_{0.02}Mn_{0.5}Co_{0.5}Fe_{1.98}O_4$, and Ti_3C_2. Field emission electron microscopy (FESEM) affirms the porous morphology that helps to enhance the electrochemical activity. The average crystallite size (D) $Pr_{0.02}Mn_{0.5}Co_{0.5}Fe_{1.98}O_4$, Ti_3C_2, and $Pr_{0.02}Mn_{0.5}Co_{0.5}Fe_{1.98}O_4$ - Ti_3C_2 samples which are found to be 38 nm, 15 nm, and 31 nm respectively. The XPS results in $Pr_{0.02}Mn_{0.5}Co_{0.5}Fe_{1.98}O_4$ - Ti_3C_2 composite affirms the presence of peaks viz. Ti 2p, Pr 3d, Mn 2p, Co 2p, Fe 2p, C 1s, O 1s. The electrochemical properties of the $Pr_{0.02}Mn_{0.5}Co_{0.5}Fe_{1.98}O_4$ – Ti_3C_2 nanocomposite were found to be superior to those of $Pr_{0.02}Mn_{0.5}Co_{0.5}Fe_{1.98}O_4$ and Ti_3C_2. The specific capacitances of the $Pr_{0.02}Mn_{0.5}Co_{0.5}Fe_{1.98}O_4$ – Ti_3C_2, Ti_3C_2, and $Pr_{0.02}Mn_{0.5}Co_{0.5}Fe_2O_4$ electrodes 1310.54 F g^{-1}, 1181.95 F g^{-1}, and 947.81 F g^{-1} at a current density of 2 A g^{-1}. The nanocomposite showed good electrochemical performance and hence it is a promising material for supercapacitors.

Keywords: MXene's, X-ray Diffraction, Nanocomposite, Specific Capacitance

8.1. Methods

8.1.1. Preparation of the Spinel ferrites

AR grade nitrates including [Pr $(NO_3)_2.6H_2O$], [Fe $(NO_3)_2{\cdot}9H_2O$], [Mn $(NO_3)_2.6\ H_2O$], [Co $(NO_3)_2.6\ H_2O$] were used. $Pr_xCo_{0.5}Mn_{0.5}Fe_{2-x}O_4$ sol-gel auto combustion technique was

applied to prepare the material. Metal nitrate and citric acid in an equal ratio of 1:1 were dissolved in the distilled water. The solution maintained the pH value of 7 by adding ammonia hydroxide and stirring. Subsequently, heated the solution to obtain the gel formation by swrilling and then auto combustion. Ash was formed and annealed at 1100 °C in a muffle furnace. Then, the powder was ground with a mortar pestle.

(0.5) [Mn $(NO_3)_2.6H_2O$)] + (0.5) [Co $(NO_3)_2.6H_2O$)] + x [Pr $(NO_3)_3.6H_2O$] + (2 − x) [Fe $(NO_3)_3.9H_2O$)] → $Mn_{0.5}Co_{0.5}Pr_xFe_{2-x}O_4 + H_2O$ + volatiles

8.1.2. Preparation of the Mxene (Ti_3C_2)

Ti_3AlC_2 is a MAX phase used to etch the 'Al' using the etching method. For MXene synthesis, HCl was poured into a Teflon bottle and swirled for 20 min. LiF was added to the HCl and mixed properly for 30 min. Then, MAX-phase Ti_3AlC_2 was added to the HCl + LiF solution and swirled for 48 h. The whole solution was then centrifuged at 4500 rpm and washed with distilled water until a pH of 7 was obtained. After vacuum filtration, the powder was oven to 90 ° C for 6 h.

$4Ti_3AlC_2 + 14LiF + 14HCl = 3Ti_3C_2 + Ti_3C_2F_2 + 2AlF_3 + Li_3AlF_6 + AlCl_3 + 11LiCl + 7H_2$

8.1.3. Preparation of $Pr_{0.02}Mn_{0.5}Co_{0.5}Fe_{1.98}O_4$ - Ti_3C_2 MXene composite

A physical blending technique was approached for the synthesis of the nanocomposites. The weight ratio of Mxene (Ti_3C_2) and spinel ferrite ($Pr_{0.02}Mn_{0.5}Co_{0.5}Fe_{1.98}O_4$) was taken to be 1:5, which was physically blended with the mortar pestle and homogenized, as shown in Fig. 8.1.

$Pr_{0.02}Co_{0.5}Mn_{0.5}Fe_{1.98}O_4 + Ti_3C_2 \rightarrow Pr_{0.02}Co_{0.5}Mn_{0.5}Fe_{1.98}O_4$ - Ti_3C_2

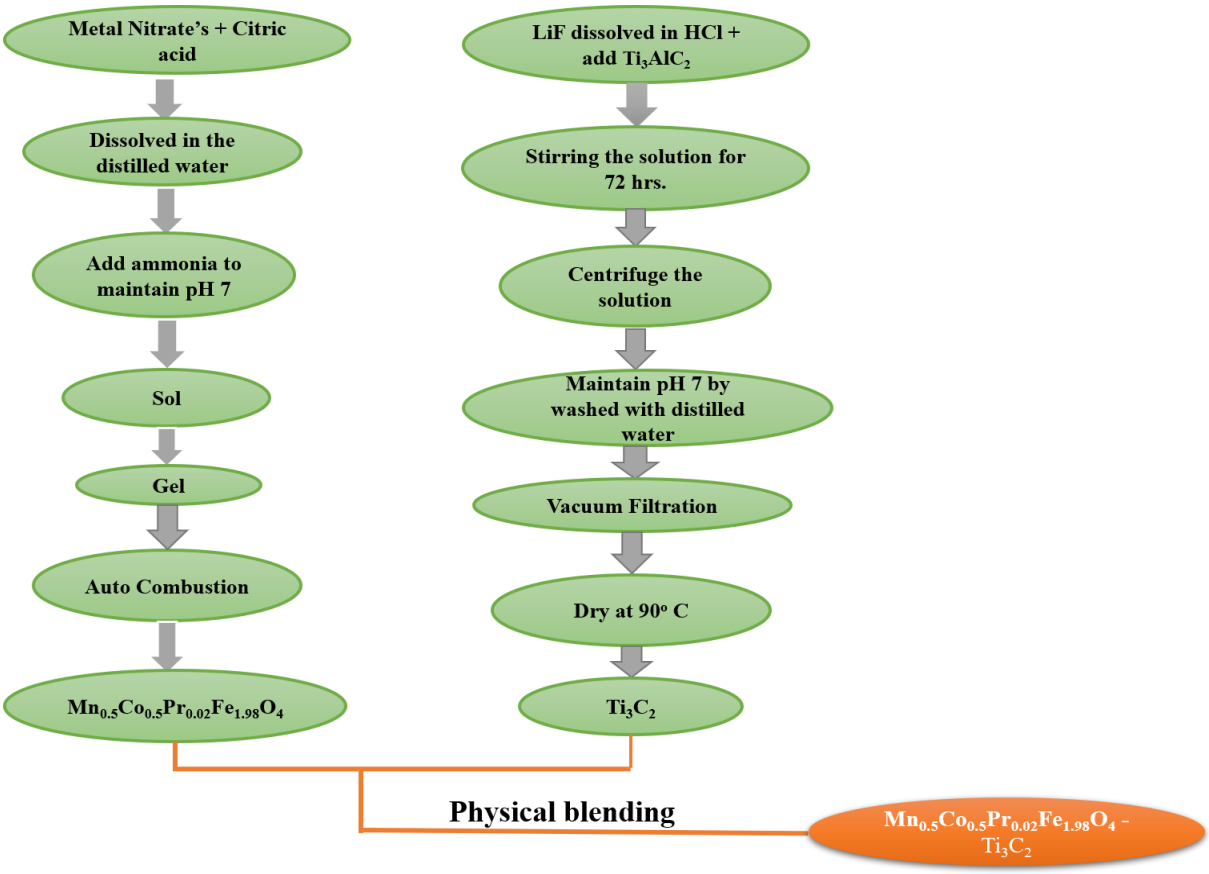

Fig. 8.1. Preparation method of the $Pr_xMn_{0.5}Co_{0.5}Fe_{2-x}O_4$, Ti_3C_2, $Pr_{0.02}Mn_{0.5}Co_{0.5}Fe_{1.98}O_4$ - Ti_3C_2 composite.

8.1.4. Preparation of electrode

The ink drop casting method was adopted to prepare electrodes of $Pr_{0.02}Mn_{0.5}Co_{0.5}Fe_{1.98}O_4$, Ti_3C_2, and $Pr_{0.02}Mn_{0.5}Co_{0.5}Fe_{1.98}O_4 - Ti_3C_2$. The active material mass ($Pr_{0.02}Mn_{0.5}Co_{0.5}Fe_{1.98}O_4$, Ti_3C_2, and $Pr_{0.02}Mn_{0.5}Co_{0.5}Fe_{1.98}O_4 - Ti_3C_2$) (70 wt%), acetylene black as a conductive agent (20 wt%), and polyvinylidene fluoride (PVA) as a binder (10 wt%) were homogenously mixed with four drops of n-methyl-2-pyrrolidone (NMP) as a solvent. The ink loaded onto the nickel foam with an area (1 cm×1 cm) was dried at 65 °C for 10 h. However, similar techniques were used to prepare the working electrodes of Ti_3C_2 MXene and $Pr_{0.02}Mn_{0.5}Co_{0.5}Fe_{1.98}O_4 - Ti_3C_2$ nanocomposites.

8.2. Materials Characterizations

XRD tests were performed on a Powder X-ray diffractometer (Bruker D8 Advance) for phase identification of the samples. Cu-Kα radiation was employed having a wavelength of λ = 1.5406 (Å) from 20° - 80° in increments of 0.02°. FESEM was used to confirm the surface morphology (FE-SEM: JEOL JSM-7610 F Plus), and the chemical composition was determined by EDX spectroscopy (EDX: OXFORD EDX LN2 free). High-resolution transmission electron microscopy (HR-TEM) (JEOL, Model-JEM 2100) was used for the surface features. X-ray photoelectron spectroscopy (XPS) measurement was performed at a pressure lesser than 10^{-7} Pa using a spectrometer (Thermo Scientific K-Alpha). The magnetic properties of spinel ferrite were investigated using a VSM (VSM-EZ9). Wynne Kerr impedance analyzer (Model 6500) is utilized to determine the dielectric properties. Electrochemical measurements were performed using a three-electrode system with a gamry potentiostat/galvanostat interface (5000E), Ag/AgCl as the reference electrode, platinum as the counter electrode, and the coated active material on nickel foam as the working electrode. Electrolyte 3M KOH aqueous solution was used for cyclic voltammetry (CV), galvanostatic charge-discharge (GCD), and electrochemical impedance spectroscopy (EIS).

8.3. Results and Discussion

8.3.1. XRD Study

X-ray patterns of the synthesized materials $Pr_xMn_{0.5}Co_{0.5}Fe_{2-x}O_4$ are shown in Fig. 8.2. The sample exhibited a single phase (x = 0.00). The secondary phase ($PrFeO_3$) is observed at x ≥ 0. 01. As per the JCPDS no. Pr ferrite (00-019-1012) [253], Mn ferrite (74-2403) [254], Co ferrite (22-1086) [255] confirm the x-ray diffraction peaks are (220), (112), (311), (222), (400), (422), (511), and (440). Peak (311) has a high peak intensity. The secondary phase occurs due to the high reactivity of Fe^{3+} ions with Pr^{3+} ions at the grain boundary [64]. The X-ray patterns indicate that all the samples have a face-centered cubic crystal structure with the Fd-3m space group. The Pr-doped manganese-cobalt ferrite was analyzed for different parameters such as lattice constant (a_o), crystalline size (D), surface area (S), porosity (P), dislocation density, and strain, as shown in Table 8.1. The lattice constant a_o can be measured as Eq. (8.1)[256].

$$a_o = d\sqrt{h^2 + k^2 + l^2} \qquad (8.1)$$

where a_o is the lattice constant, and d is the interlayer spacing. As the concentration of Pr^{3+} increased, the lattice constant (a_o) increased, except for (x = 0.02, 0.03) as shown in Table 8.1 because of the substitution of the Pr^{3+} ions in the Fe^{3+} ions but Pr^{3+} (1.013 Å) ions have higher ionic radii than Fe^{3+} (0.64 Å) ions. When the Pr^{3+} ion is doped in the $Mn_{0.5}Co_{0.5}Fe_2O_4$ spinel lattice some of the Fe^{3+} ions replace the Pr^{3+} ions resulting in the expansion of the (x = 0.02, 0.05) unit cell [257]. The crystallite size can be calculated by Debye Scherrer's formula $Pr_xCoMnFe_{2-x}O_4$ spinel ferrite as Eq. (8.2) [78].

$$D = \frac{k\lambda}{\beta \cos\theta} \tag{8.2}$$

$$\delta = \frac{1}{D^2} \tag{8.3}$$

$$\varepsilon = \frac{\beta}{4Tan\theta} \tag{8.4}$$

where k is the Scherrer constant, θ is the Bragg angle, β is the full width at half maximum, and λ is the wavelength of X-ray radiation. The crystallite sizes exhibit an irregular trend for the $Pr_xMn_{0.5}Co_{0.5}Fe_{2-x}O_4$ (x = 0.0, 0.01, 0.02, 0.03, 0.04) spinel ferrite as in Table 8.1. The calculated strain and dislocation densities are listed in Table 8.1. The irregular variation observed in the crystallite size is due to the presence of Mn^{2+} ions, which are randomly present at both tetrahedral sites and octahedral sites. The dislocation density and microstrain increase and then decrease owing to the metal cation's random presence in the tetrahedral and octahedral sites. The inhomogeneous strain in the lattice sites is caused by the randomness of the metal cations, breaking them into irregular particles of a sporadic shape [256][258]. This inhomogeneous behavior is due to the different ions present in the lattice with distinct ionic radii Pr^{3+} (1.013 Å), Mn^{2+} (0.80 Å), Co^{2+} (0.78 Å), Fe^{2+} (0.64 Å). The undoped sample has less deformation in the crystallographic structure compared to the other crystallographic structures.

$$D_x = \frac{ZM}{Na^3} \tag{8.5}$$

$$D_{bulk} = \frac{m}{\pi r^2 h} \tag{8.6}$$

$$S = \frac{6000}{D.D_x} \quad (8.7)$$

$$P = 1 - \frac{d_{bulk}}{d_x} \times 100 \quad (8.8)$$

where 'N' is Avogadro's number, 'M' is the molecular weight, 'a_o' is the lattice constant, m is the mass, r is the radius of the pallets, and h is the thickness of the pallets. The X-ray density, bulk density, surface area, and porosity are calculated using Eq. (8.5) (8.6) (8.7) (8.8) and presented in Table 8.1. X-ray density increased with Pr^{3+} concentration due to its high molecular mass than Fe^{3+}. This is because X-ray density relatively depends on the molecular mass of the elements present in the material and also depends on the small grain size of spinel ferrite [258]. The bulk densities of the specimens were determined and presented in Table 8.1. The bulk density (D_{bulk}) shows an inhomogeneous trend and the thickness and mass of the pellets vary. The decrease in bulk density revealed an enhancement in porosity [258]. The *S* increased due to the reduction in crystallite size which increases the X-ray density [259]. All the samples had excellent porosity with $Pr_{0.02}Mn_{0.5}Co_{0.5}Fe_{1.98}O_4$ (x = 0.02) having the highest porosity of the others. These pores are beneficial for energy storage devices (supercapacitors and batteries) as the electrolyte ions easily reach the electrode [79].

Table 8.1 Structural parameters of the $Pr_xMn_{0.5}Co_{0.5}Fe_{2-x}O_4$ (x = 0.00, 0.01, 0.02, 0.03, 0.04).

Compositions	a_o	D	δ	ε	S	D_x	D_{bulk}	P %
x = 0.00	8.408	45	0.493	2.535	25.65	5.19	2.00	61.51
x = 0.01	8.417	44	0.515	2.592	26.19	5.19	1.99	61.72
x = 0.02	8.414	43	0.533	2.638	26.55	5.22	1.96	62.46
x = 0.03	8.407	45	0.493	2.540	25.46	5.24	1.98	62.26
x = 0.04	8.408	45	0.494	2.541	25.35	5.27	1.98	62.45

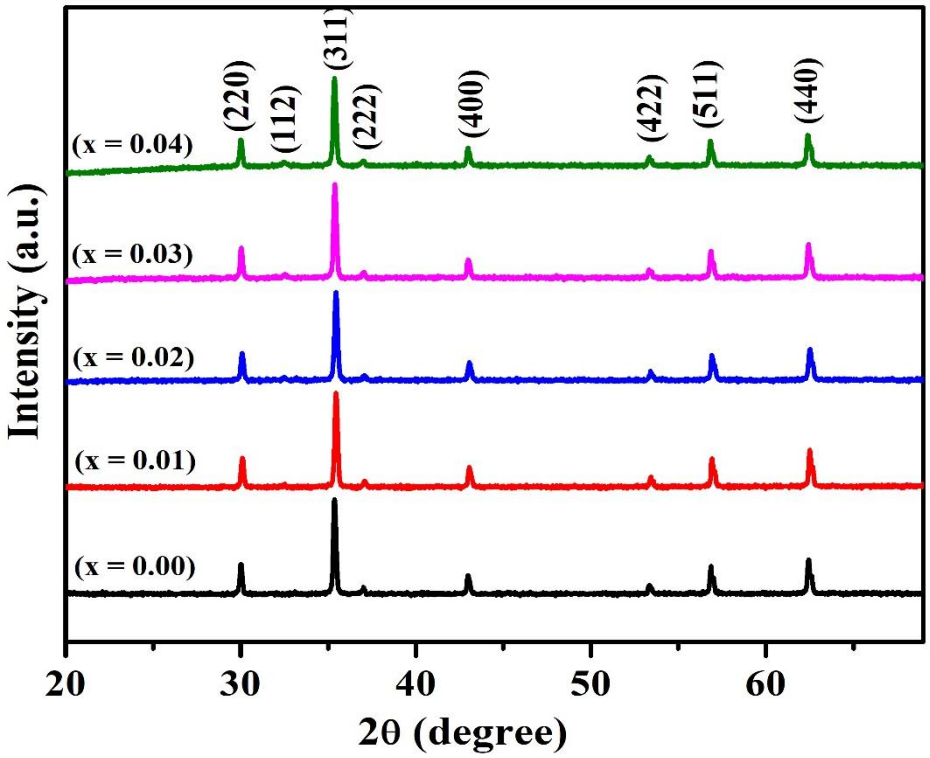

Fig. 8.2. X-ray diffraction pattern of $Pr_xMn_{0.5}Co_{0.5}Fe_{2-x}O_4$ sample.

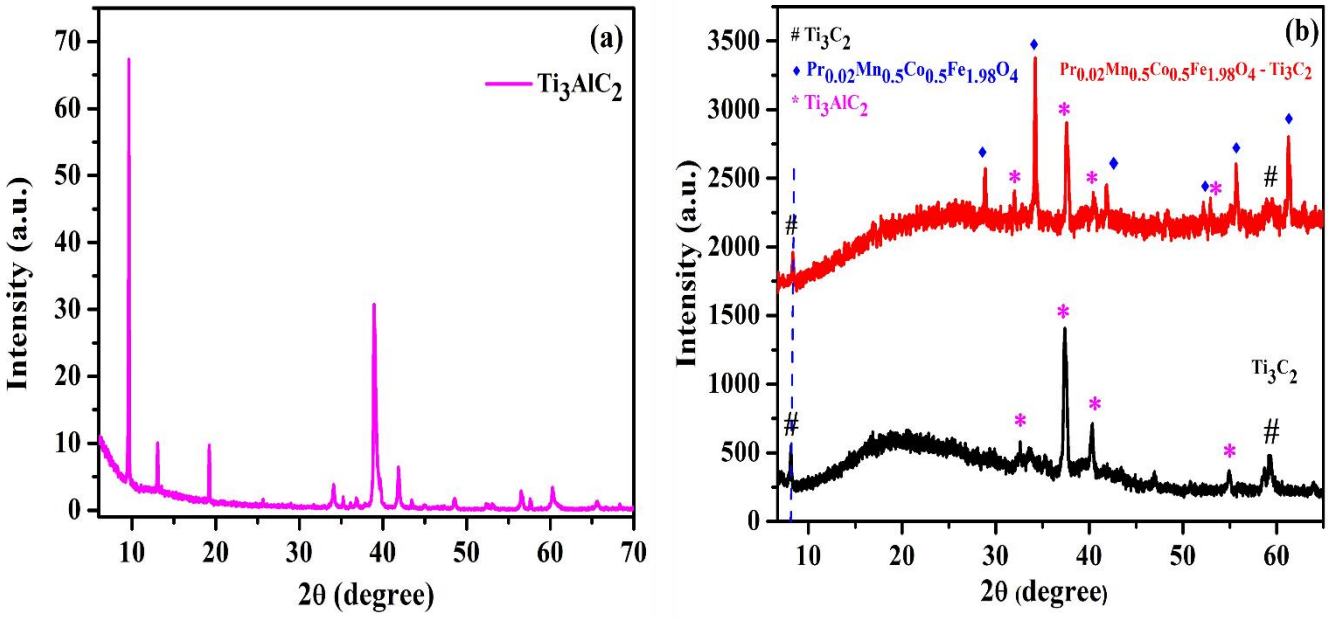

Fig. 8.3. XRD pattern of (a) MAX phase, (b) Ti_3C_2, and $Pr_{0.02}Mn_{0.5}Co_{0.5}Fe_{1.98}O_4$ - Ti_3C_2.

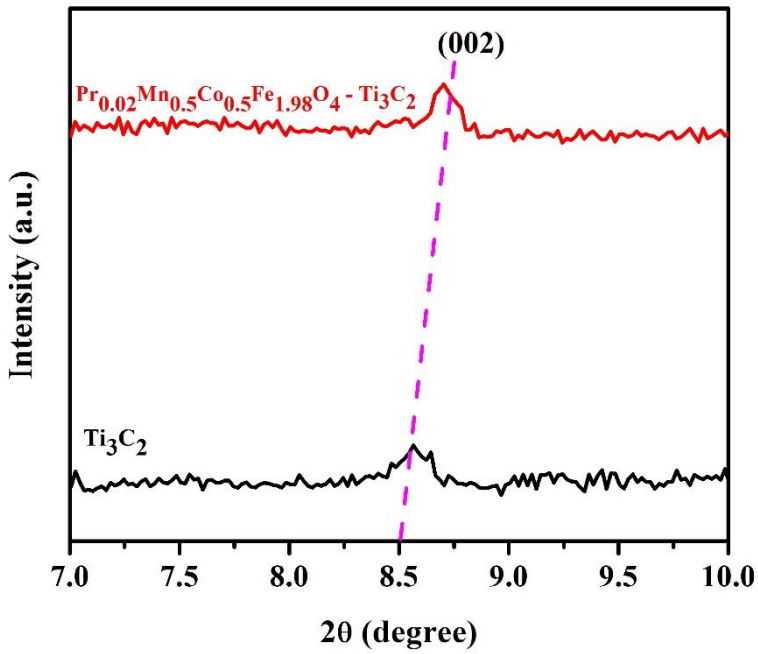

Fig. 8.4. 2θ (~8.5 °) Ti_3C_2, and $Pr_{0.02}Mn_{0.5}Co_{0.5}Fe_{1.98}O_4$ -Ti_3C_2 samples.

The peak (002) at 2θ = 8.5 ° demonstrates the Ti_3C_2 and has a 2D accordion structure [260]. A slight backward shift was observed in the (002) peak after the conversion of the Ti_3AlC_2 MAX phase into Ti_3C_2, which confirms the formation of the MXene material as in Fig.8.3(a)(b). The typical distinct characteristic peaks at 8.5 ° and 60 ° correspond to the (002) and (110) planes of MXene [261]. The reduced intensity of the characteristic peak is 40 ° after the etching process which demonstrates the Ti_3AlC_2 changed into the Ti_3C_2. The XRD pattern confirms the Ti_3C_2 peak (002) in the nanocomposite, which could be related to the entrance of $Pr_{0.02}Mn_{0.5}Co_{0.5}Fe_{1.98}O_4$ spinel ferrite into the Ti_3C_2. Furthermore, the characteristic peaks of $Pr_{0.02}Mn_{0.5}Co_{0.5}Fe_{1.98}O_4$ and Ti_3C_2 could be seen in the prepared samples, indicating their existence. The downward shift of the (002) peak corresponding to $Pr_{0.02}Mn_{0.5}Co_{0.5}Fe_{1.98}O_4$ - Ti_3C_2 composite demonstrated a slight increase in the d-spacing as in Fig. 8.4 [262] The $Pr_{0.02}Mn_{0.5}Co_{0.5}Fe_{1.98}O_4$ - Ti_3C_2 nanocomposite results in effective intercalation between $Pr_{0.02}Mn_{0.5}Co_{0.5}Fe_{1.98}O_4$ and Ti_3C_2 MXene's matrix [99][62]. The $Pr_{0.02}Mn_{0.5}Co_{0.5}Fe_{1.98}O_4$ - Ti_3C_2 nanocomposite exhibited all the crystalline peaks of the $Pr_{0.02}Mn_{0.5}Co_{0.5}Fe_{1.98}O_4$ ferrite with no position change. The hkl (002) peaks of the $Pr_{0.02}Mn_{0.5}Co_{0.5}Fe_{1.98}O_4$ - Ti_3C_2 nanocomposite crystallite size was higher than that Ti_3C_2 as evaluated by the Debye Scherrer constant as shown in Table 8.2 [263]. This increase in the nanocomposite crystallite size

confirms the encapsulation of $Pr_{0.02}Mn_{0.5}Co_{0.5}Fe_{1.98}O_4$ spinel ferrite nanoparticles with Ti_3C_2 MXene.

Table 8.2

Structural parameters of the Ti_3C_2, and $Pr_{0.02}Mn_{0.5}Co_{0.5}Fe_{1.98}O_4$ – Ti_3C_2.

Sample	hkl	β	2θ	D (nm)
Ti_3C_2	(002)	0.46	8.5	17
$Pr_{0.02}CoMnFe_{1.98}O_4$ - Ti_3C_2	(002)	0.261	8.5	30

8.3.2. FESEM with EDX Study

The surface morphology and particle size of $Pr_{0.02}Mn_{0.5}Co_{0.5}Fe_{1.98}O_4$, Ti_3C_2, and $Pr_{0.02}Mn_{0.5}Co_{0.5}Fe_{1.98}O_4$ - Ti_3C_2 were investigated using the FESEM micrograph as depicted in Fig. 8.5. The FESEM micrograph of $Pr_{0.02}Mn_{0.5}Co_{0.5}Fe_{1.98}O_4$ was inhomogeneous in shape and size but showed a porous morphology. During the synthesis process, some gases are discharged which gives rise to pores [79][150][264]. Ti_3C_2 exhibited an accordion-like morphology. A parallel arrangement in the as-prepared MXene layers was detected which indicates the specific etching direction of 'Al.' The $Pr_{0.02}Mn_{0.5}Co_{0.5}Fe_{1.98}O_4$ - Ti_3C_2 nanocomposite reveals that the nanoparticles and MXenes are embedded with openings between the layers. The presence of nanoparticles between the MXene layers prevents restacking. MXenes prevent nanoparticle agglomeration which enhances nanocomposite pores. Because of the ease of access of the electrolyte to the electrode, these pores enhance electrochemical activity [259]. FESEM micrographs were used to calculate the particle size using ImageJ software. In Fig. 8.5 histogram is plotted for all the incorporated samples to estimate the average particle size in the nanosize range. EDX study provides information on the elemental composition of the $Pr_{0.02}Mn_{0.5}Co_{0.5}Fe_{1.98}O_4$, Ti_3C_2, and $Pr_{0.02}Mn_{0.5}Co_{0.5}Fe_{1.98}O_4$ - Ti_3C_2 as shown in Fig. 8.6. The EDX of $Pr_{0.02}Mn_{0.5}Co_{0.5}Fe_{1.98}O_4$ ferrite reveals the element Pr, Mn, Co, Fe, O, and Ti_3C_2, display the element Ti, C, and O, and nanocomposite of $Pr_{0.02}Mn_{0.5}Co_{0.5}Fe_{1.98}O_4$ - Ti_3C_2 reveals the elements Pr, Mn, Co, Fe, O, Ti, and C. No additional peaks were observed for any sample [79]. Fig. 8.7 depicts the uniform distribution of elements over the entire nanocomposite sample. Table 8.3 represents the atomic % and weight % of all the samples and reflects the weight ratios of the $Pr_{0.02}Mn_{0.5}Co_{0.5}Fe_{1.98}O_4$, Ti_3C_2, and $Pr_{0.02}Mn_{0.5}Co_{0.5}Fe_{1.98}O_4$ - Ti_3C_2.

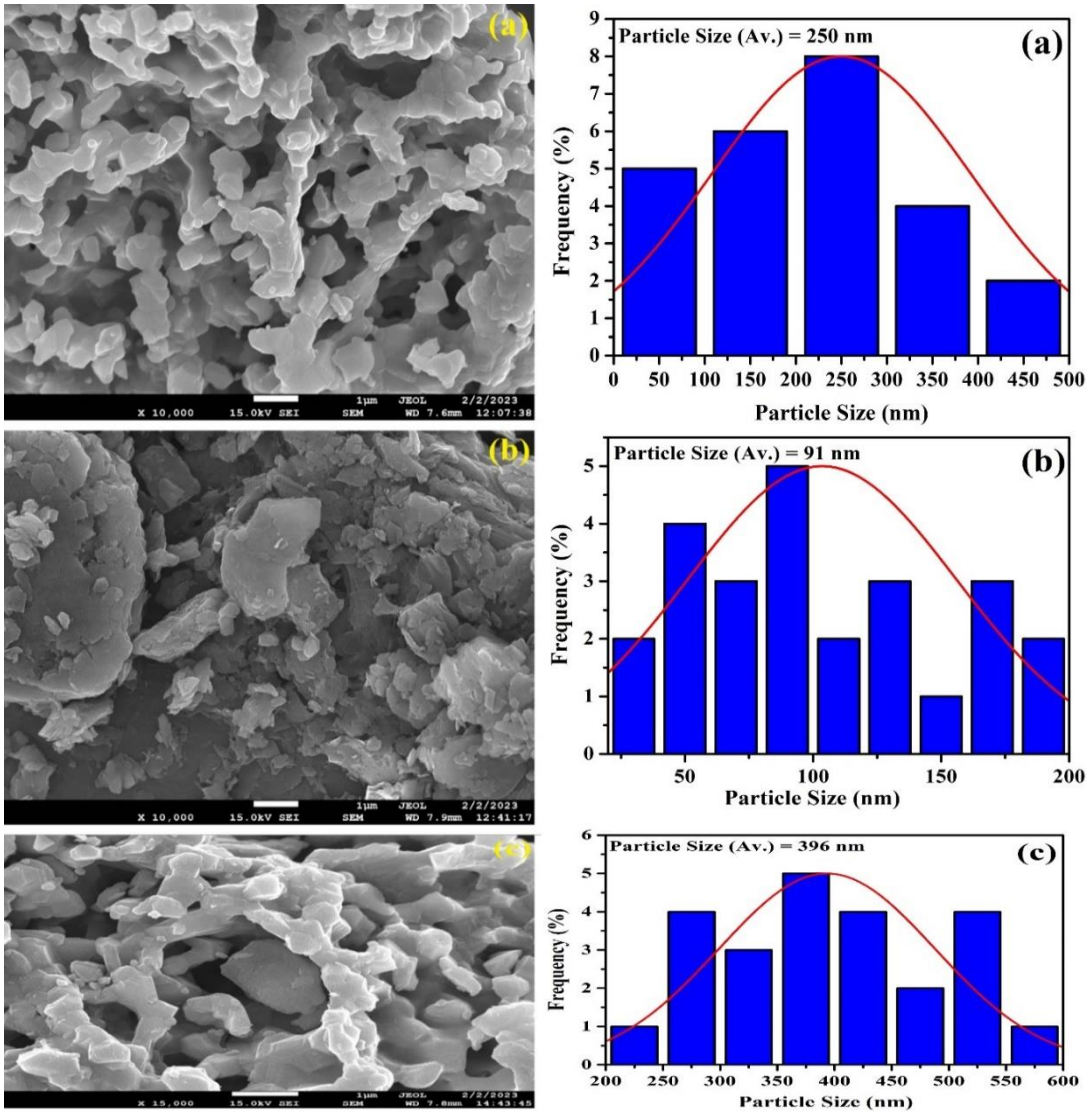

Fig. 8.5. FESEM images and histogram of (a) $Pr_{0.02}Mn_{0.5}Co_{0.5}Fe_{1.98}O_4$, (b) Ti_3C_2, and (c) $Pr_{0.02}Mn_{0.5}Co_{0.5}Fe_{1.98}O_4$ - Ti_3C_2.

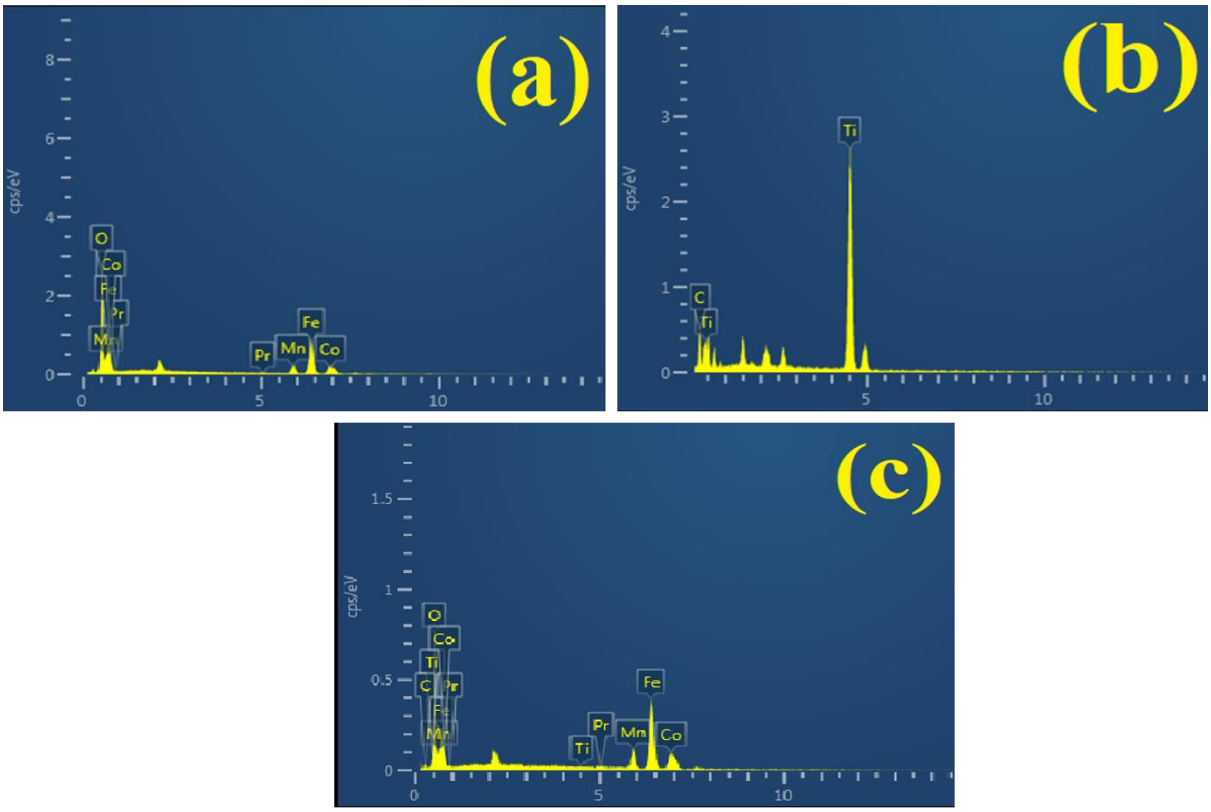

Fig. 8.6. EDX spectra of (a) $Pr_{0.02}Mn_{0.5}Co_{0.5}Fe_{1.98}O_4$, (b) Ti_3C_2, and (c) $Pr_{0.02}Mn_{0.5}Co_{0.5}Fe_{1.98}O_4$ -Ti_3C_2

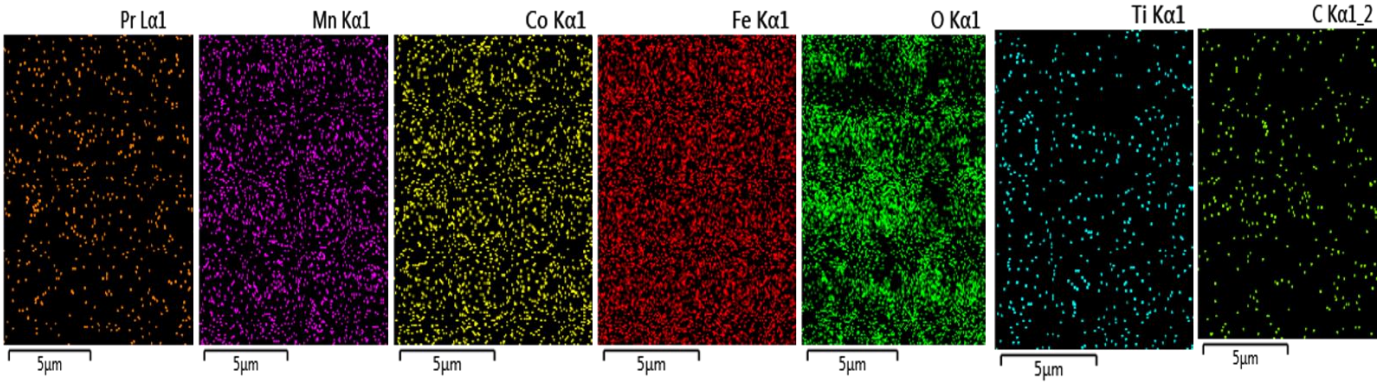

Fig. 8.7 Elemental mapping of $Pr_{0.02}Mn_{0.5}Co_{0.5}Fe_{1.98}O_4$ - Ti_3C_2 nanocomposite.

Table 8.3 Atomic % and Weight % of the $Pr_{0.02}Mn_{0.5}Co_{0.5}Fe_{1.98}O_4$, Ti_3C_2, and $Pr_{0.02}Mn_{0.5}Co_{0.5}Fe_{1.98}O_4 - Ti_3C_2$.

Sample	Weight % and Atomic %	Elements							Total
		Pr	Mn	Co	Fe	O	Ti	C	
$Pr_{0.02}Mn_{0.5}Co_{0.5}Fe_{1.98}O_4$	Atomic %	0.37	5.95	8.47	30.59	54.65	0	0	100
	Weight%	1.38	9.46	14.44	49.42	25.29	0	0	100
Ti_3C_2	Atomic %	0	0	0	0	0	46.84	53.84	100
	Weight %	0	0	0	0	0	22.74	77.26	100
$Pr_{0.02}Mn_{0.5}Co_{0.5}Fe_{1.98}O_4 - Ti_3C_2$	Atomic %	0.03	0.91	1.11	4.62	45.31	8.37	39.64	100
	Weight %	0.24	2.53	3.29	13.04	36.61	20.24	24.05	100

8.3.3. HR-TEM Study

High-resolution transmission electron microscope (HR-TEM) images were further investigated to determine the morphology and topography of our prepared samples. As noticed from Fig. 8.8 $Pr_{0.02}Mn_{0.5}Co_{0.5}Fe_{1.98}O_4$ (ferrite) depicts the agglomerations and non–uniform size of the crystallite (D) [265]. Ti_3C_2 (MXene) was ultra-thin and flexible presenting a sheet-like morphology [262]. The HR-TEM micrograph of the $Pr_{0.02}Mn_{0.5}Co_{0.5}Fe_{1.98}O_4$ - Ti_3C_2 (composite) clearly showed the thin layer structure of Ti_3C_2 and the attachment of ferrite spherical nanoparticles on the MXene layers [95]. The average crystallite size (D) has been evaluated by using the ImageJ software and then the histogram is plotted for $Pr_{0.02}Mn_{0.5}Co_{0.5}Fe_{1.98}O_4$, Ti_3C_2, and $Pr_{0.02}Mn_{0.5}Co_{0.5}Fe_{1.98}O_4$ - Ti_3C_2 samples to calculate the D which is found to be 38 nm, 15 nm, and 31 nm respectively. It is worth noting that the average crystallite size evaluated by the HR-TEM is in close agreement with the crystallite size as evaluated from XRD data and hence affirms the immaculateness of our prepared samples.

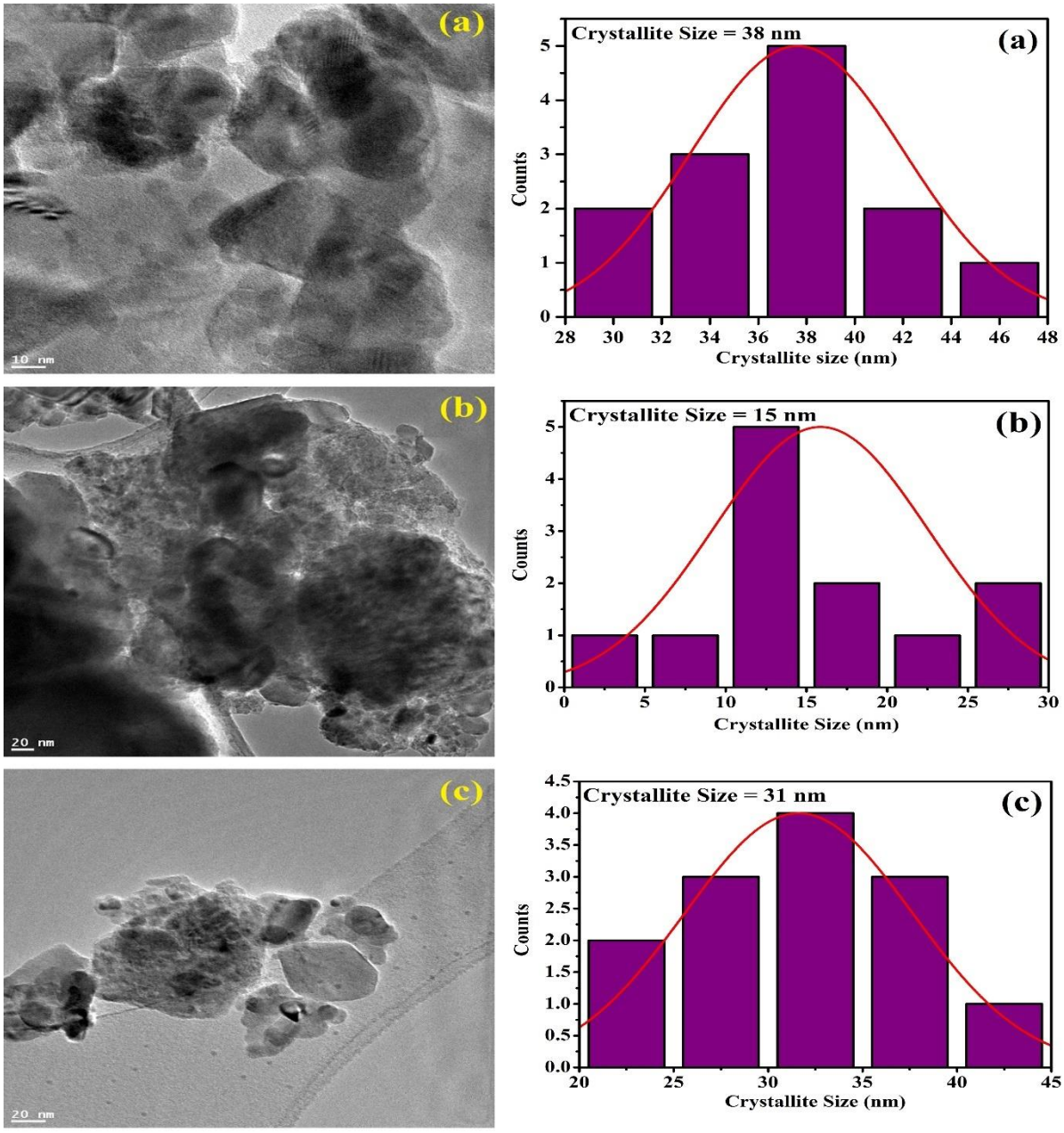

Fig. 8.8. HRTEM images and histogram of (a) $Pr_{0.02}Mn_{0.5}Co_{0.5}Fe_{1.98}O_4$, (b) Ti_3C_2, and (c) $Pr_{0.02}Mn_{0.5}Co_{0.5}Fe_{1.98}O_4$ -Ti_3C_2.

8.3.4. X-ray photoelectron spectroscopy (XPS) Study

The XPS technology provides detailed information about the element composition and valence states found in nanomaterials. Fig. 8.9 are the XPS spectra of synthesized $Pr_{0.02}Mn_{0.5}Co_{0.5}Fe_{1.98}O_4$ spinel ferrites, Ti_3C_2 MXene, and the $Pr_{0.02}Mn_{0.5}Co_{0.5}Fe_{1.98}O_4 - Ti_3C_2$ composite. The C 1s peak at 284.5 eV was used for charge correction purposes. In the O 1s spectrum, two primary peaks labeled as O 1s (O_C) and O 1s(O_L) correspond to the bonding arrangements of oxygen atoms within the sample [266]. The O 1s (O_L) binding energy signifies the energy associated with the oxygen atom's single bond, while O 1s(O_C) corresponds to the energy of the double bond, measured at 530.1 eV and 531.5 eV, respectively, as depicted in Fig. 8.10(a). In Fig. 8.10(b), the deconvoluted spectrum peak of Mn^{2+} exhibits two asymmetric peaks of Mn $2p_{3/2}$ and Mn $2p_{1/2}$, with binding energy values of 641.9 eV and 653.2 eV, respectively. The Mn $2p_{3/2}$ peak comprises two peaks at 639.89 eV and 641.34 eV, indicating the presence of Mn (II) and Mn (III) states, respectively [266]. In Fig. 8.10(c), the XPS spectra of the Co element in the 2p region show that the main metal peaks' binding energies in the Co $2p_{3/2}$ and Co $2p_{1/2}$ regions are located at 780.4 eV and 796.5 eV, respectively, with an additional satellite peak at a higher binding energy. The Co $2p_{3/2}$ peak exhibits three primary asymmetric peaks, indicating the presence of two unequal bond lattice positions: the tetrahedron and the octahedron. This variation stems from the differing occupancy levels of Co^{2+} ions within the spinel ferrite lattice structure. The appearance of the two asymmetric peaks at 782.7 eV (T_h) and 780.1 eV (O_h) is attributed to the tetrahedral and octahedral bonds formed between Co^{2+} and oxygen. The third asymmetric peak corresponds to the satellite peaks observed at the higher binding energy [236]. The Fe $2p_{1/2}$ and Fe $2p_{3/2}$ peaks, approximately centered at 723.5 eV and 710.0 eV, respectively, as shown in Fig. 8.10(d), exhibit further resolution into multiple peaks at approximately 724.7 eV, 723.1 eV, 712.5 eV, 710.5 eV, and 709.3 eV. Specifically, the peaks at approximately 709.3 eV and 723.1 eV correspond to Fe^{2+} ions, while those around 710.5 eV and 724.7 eV indicate Fe^{3+} ions. Furthermore, satellite peaks observed at 712.6 eV, 719 eV, 729 eV, and 734 eV result from electronic transitions attributed to the charge transfer of Fe ions during ferrite formation [267]. Fig. 8.10(e) depicts the Pr 3d photoelectron spectrum in the ferrite centered at 938 eV, which is consistent with the peak of the Pr 3d peak as reported in the work of Rosenberger *et al.*[169].Fig. 8.11(a) Ti_3C_2 MXene spectrum Ti 2p which can be deconvoluted into three doublets corresponding to Ti $2p_{3/2}$ and Ti $2p_{1/2}$ of Ti - C, Ti (II), and Ti

- O, respectively. Fig. 8.11(b)presents C1s XPS spectrum which can be fitted into three peaks at 284.8, 286.2, and 288.4 eV assigned to C-C, C-OH, and O-C=O groups, respectively. Fig. 8.11(c) The deconvoluted spectrums of the O 1s region are centered at 529.7 and 531.8 eV corresponding to $Ti_3C_2O_x$ and $Ti_3C_2(OH)_x$. These XPS results are in agreement with the reported values, confirming that the MXene is synthesized successfully with surface-terminating functional groups [72]. In Fig. 8.12 the $Pr_{0.02}Mn_{0.5}Co_{0.5}Fe_{1.98}O_4$ - Ti_3C_2 composite, confirms the presence of peaks viz. Ti 2p, Pr 3d, Mn 2p, Co 2p, Fe 2p, C 1s, and O 1s. As a result, $Pr_{0.02}Mn_{0.5}Co_{0.5}Fe_{1.98}O_4$, and Ti_3C_2 portray the immaculate of our synthesized spinel ferrite and verify our EDX results.

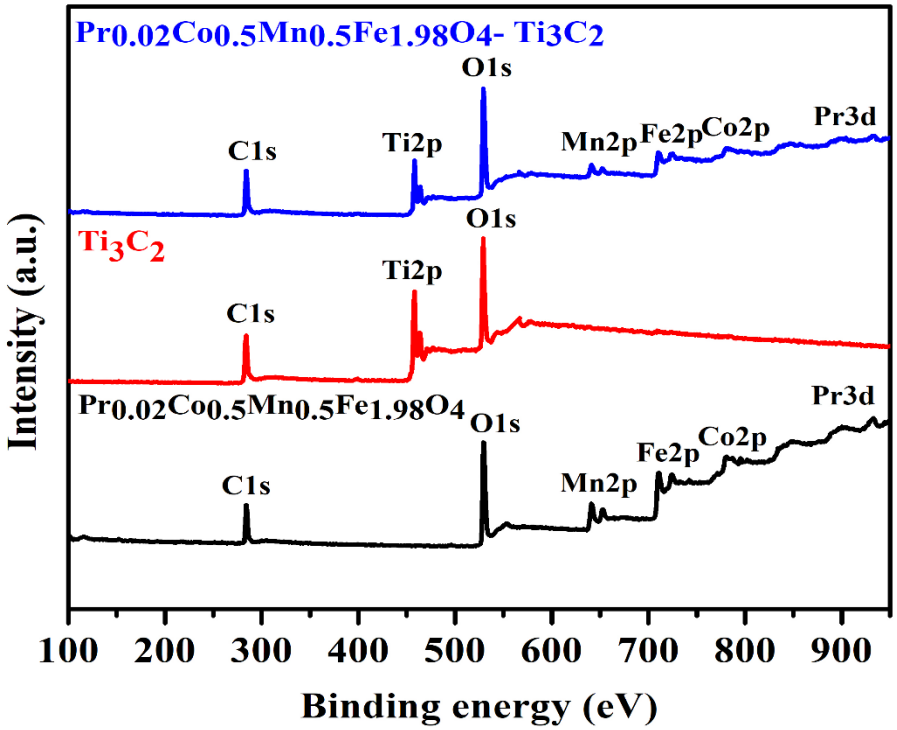

Fig. 8.9. All spectrum peaks $Pr_{0.02}Mn_{0.5}Co_{0.5}Fe_{1.98}O_4$, Ti_3C_2, and $Pr_{0.02}Mn_{0.5}Co_{0.5}Fe_{1.98}O_4$ - Ti_3C_2.

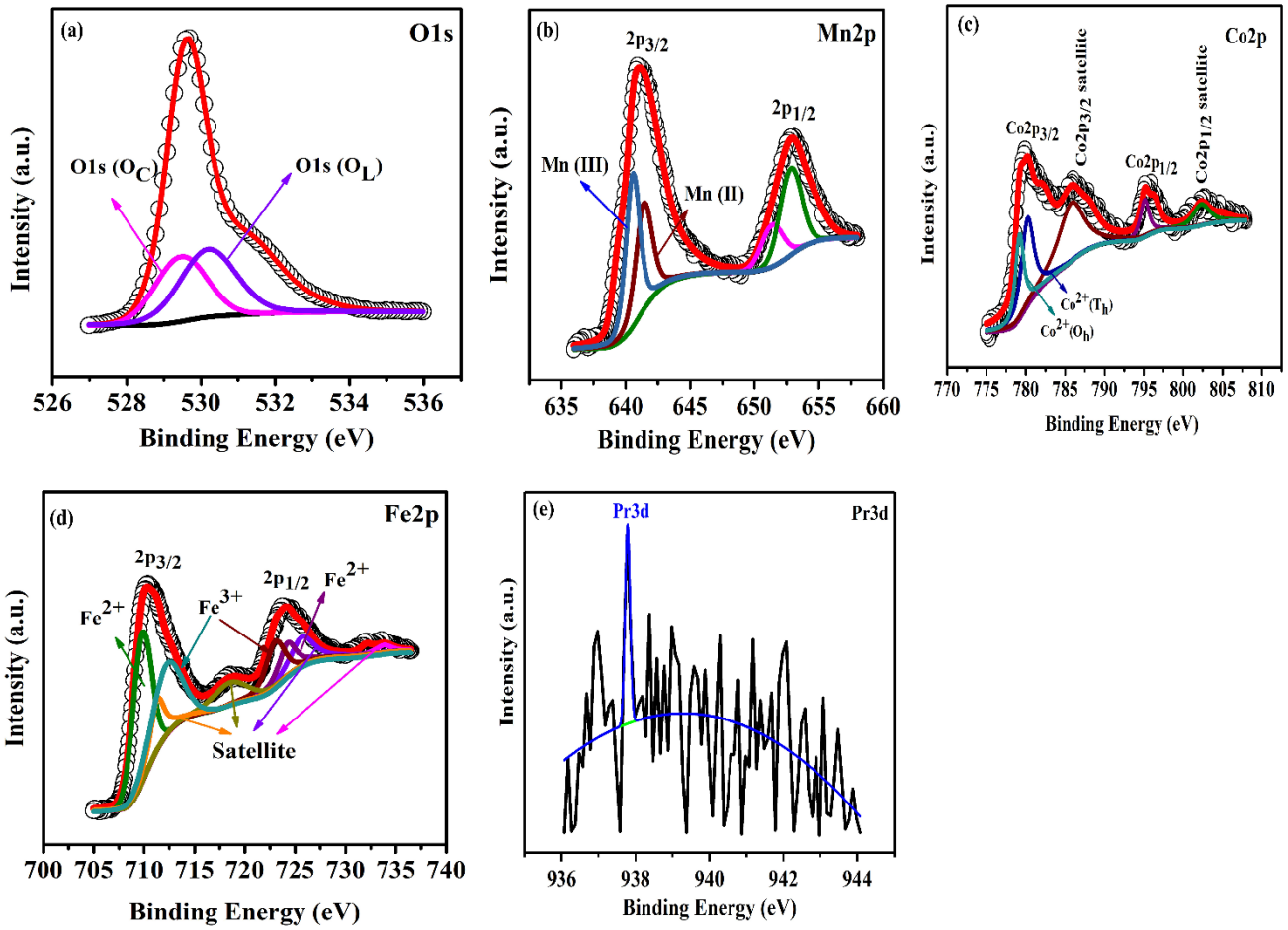

Fig. 8.10. Deconvoluted XPS spectra of (a) O1s, (b) M2p, (c) Co2p, (d) Fe2p, and (e) Pr3d.

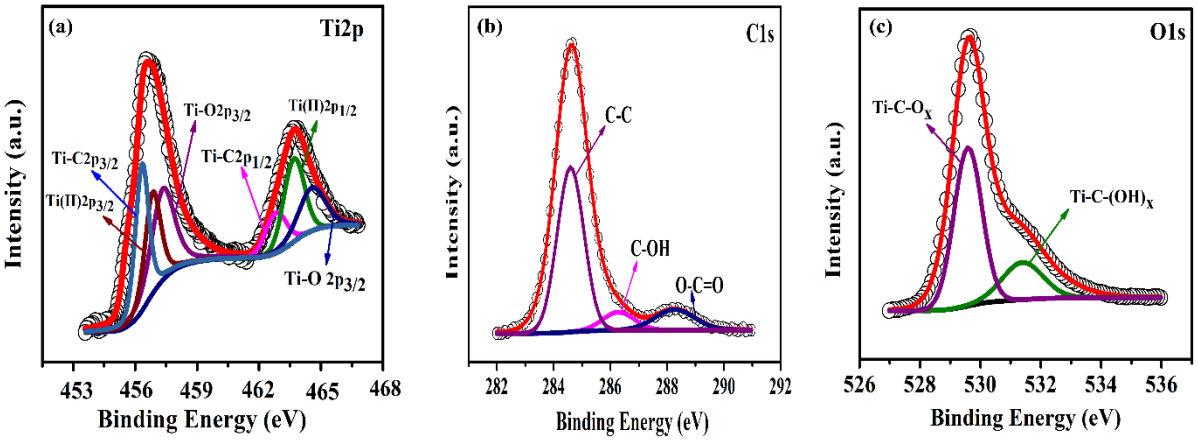

Fig. 8.11. Deconvoluted XPS spectra of (a) Ti2p, (b) C1s, and (c) O1s.

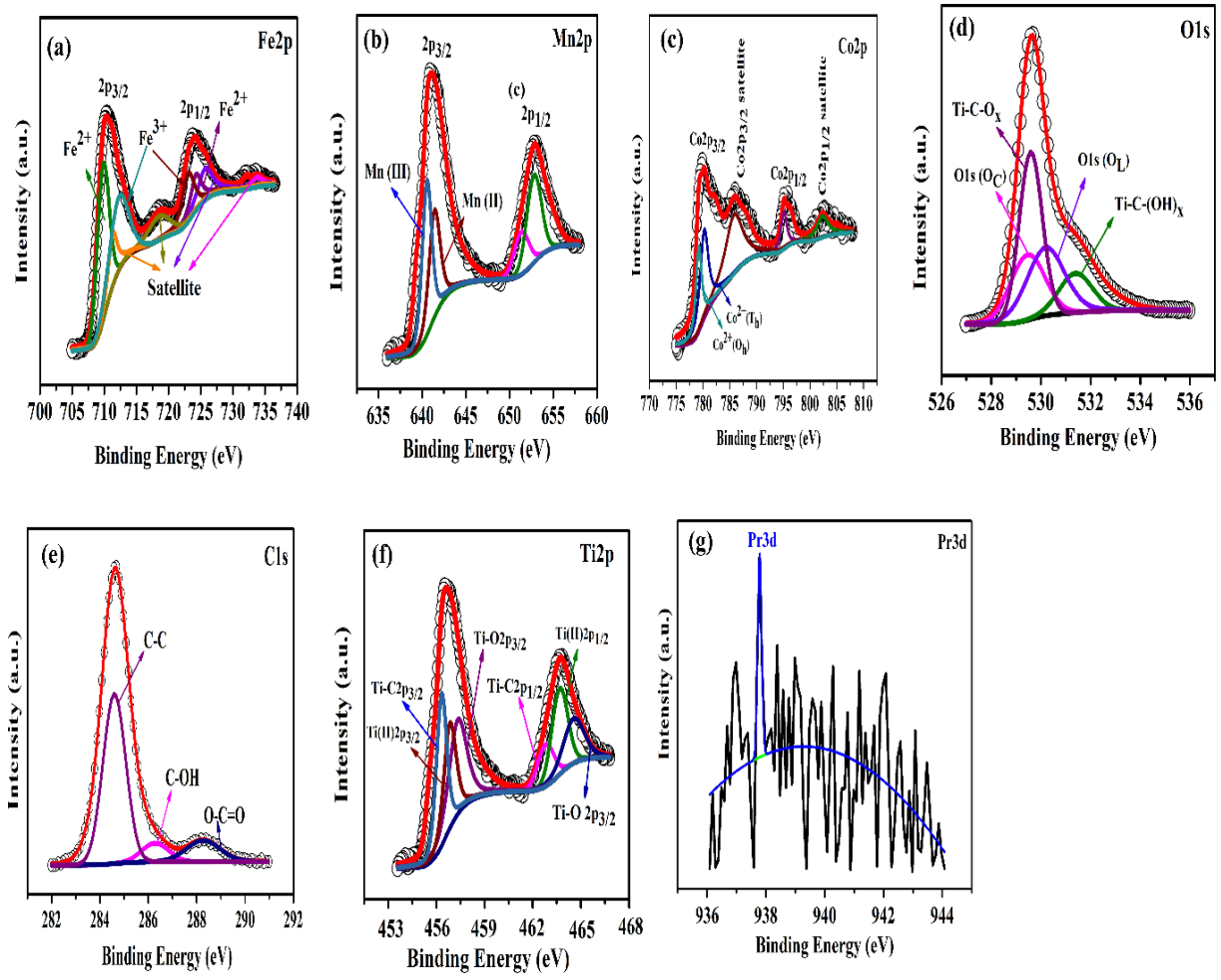

Fig. 8.12. Deconvoluted XPS spectra of (a) Fe2p, (b) Mn2p, (c) Co2p, (d) O1s, (e) C1s, (f) Ti2p, (g) Pr3d.

8.3.5. Magnetic Study

Fig. 8.13 depicts the M-H hysteresis loops using the VSM technique for the Spinel ferrite, MXene, and composite. Table 8.4 represents the values obtained from the coercivity (H_c), saturation magnetization (M_s), remanent (M_r), squareness ratio (SR), and magnetic moment (n_B). K_1 was calculated by using the formula given below Eq. (8.9) [257].

$$K_1 = \frac{M_S \times H_C}{0.96} \qquad (8.9)$$

The $Pr_{0.02}Mn_{0.5}Co_{0.5}Fe_{1.98}O_4$ spinel ferrite exhibits a high M_s as compared to the Ti_3C_2, and $Pr_{0.02}Mn_{0.5}Co_{0.5}Fe_{1.98}O_4$ - Ti_3C_2. By adding the Ti_3C_2 with the $Pr_{0.02}Mn_{0.5}Co_{0.5}Fe_{1.98}O_4$ spinel ferrite the magnetization reduced for the Ti_3C_2 (62.99 e mu/g) and $Pr_{0.02}Mn_{0.5}Co_{0.5}Fe_{1.98}O_4$

(40.49 emu/g) [268]. The reduced M_S might result from substituting the non-magnetic Ti_3C_2 MXene with the $Pr_{0.02}Mn_{0.5}Co_{0.5}Fe_{1.98}O_4$ spinel ferrite, reducing the netmagnetic moment. The saturation magnetization of $Pr_{0.02}Mn_{0.5}Co_{0.5}Fe_{1.98}O_4$ - Ti_3C_2 composite can be correlated with the presence of MXene, small size, and surface defect of ferrite crystallites. In addition, the strain between the MXene surface and Pr0.02Mn0.5Co0.5Fe1.98O4 should take partial responsibility for this as well. The particle size in the spinel ferrite increases, it can lead to a decrease in coercivity. Larger particles tend to have fewer domain walls, reducing domain wall pinning and making it easier for domains to reorient, resulting in lower coercivity. The squareness ratio of the prepared samples lies within the range of 0.28-0.29, they all exhibit a multi-domain structure [156].

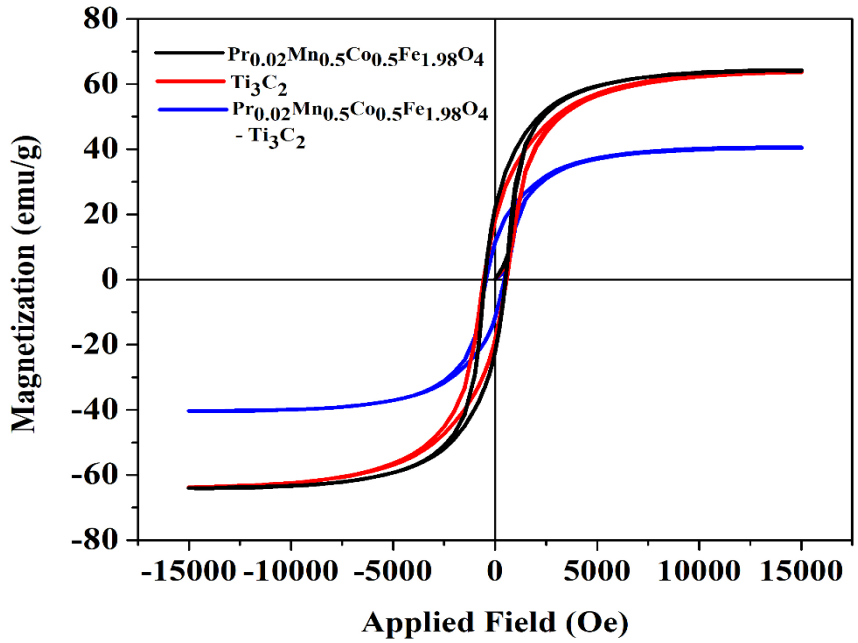

Fig. 8.13. M-H loop of the $Pr_{0.02}Mn_{0.5}Co_{0.5}Fe_{1.98}O_4$, Ti_3C_2, $Pr_{0.02}Mn_{0.5}Co_{0.5}Fe_{1.98}O_4 – Ti_3C_2$.

Table 8.4 Magnetic parameters of $Pr_{0.02}Mn_{0.5}Co_{0.5}Fe_{1.98}O_4$, Ti_3C_2, $Pr_{0.02}Mn_{0.5}Co_{0.5}Fe_{1.98}O_4 – Ti_3C_2$.

Sample	M_s	H_c	M_r	SR	n_B
$Pr_{0.02}Mn_{0.5}Co_{0.5}Fe_{1.98}O_4$	63.62	557.32	18.53	0.29	2.49
Ti_3C_2	62.99	505.64	18.14	0.28	1.89

$Pr_{0.02}Mn_{0.5}Co_{0.5}Fe_{1.98}O_4$ - Ti_3C_2	40.49	426.14	11.57	0.28	2.80

8.3.6. Dielectric Study

Fig. 8.14 displays the real (ε') and imaginary (ε") permittivity components of the synthesized $Pr_{0.02}Mn_{0.5}Co_{0.5}Fe_{1.98}O_4$ – Ti_3C_2 composite across a frequency range of 1-6 GHz. Typically, the real permittivity component signifies the storage capacity of dielectric and magnetic energy, while the imaginary component indicates the corresponding energy loss. Incorporating Ti_3C_2 MXene led to an upsurge in the composite's permittivity [269]. The electrical conductivity contributes to an elevated complex permittivity, aligning with the free electron theory. Consequently, the observed enhancements primarily arise from Ti_3C_2's exceptional electrical conductivity, substantiated by both theoretical projections and experimental validations. Ti_3C_2 demonstrates metallic-like conductivity owing to its substantial electron density near the Fermi level [N(Ef)], as anticipated by density functional theory. According to Shahzad et al., Ti_3C_2 exhibits an electrical conductivity of up to 4600 Scm^{-1}[135]. Thus, the substantial aspect ratio of 2D Ti_3C_2 facilitates the establishment of a conductive network within the PrMnCo ferrite, acting as an electron transporter and strengthening the electrical conductivity of $Pr_{0.02}Mn_{0.5}Co_{0.5}Fe_{1.98}O_4$ – Ti_3C_2 composites.

The real (ε') and imaginary (ε") permittivity values showed an initial decline between 1 and 4 GHz, followed by stabilization at a consistent level, indicating a distinct frequency-dependent dielectric response commonly seen in carbon/magnetic composites. This phenomenon, known as frequency dispersion, arises from the delayed alignment of induced charges with the alternating external field at higher frequencies, leading to reduced electronic oscillations. The dielectric properties of materials are influenced by electronic, ionic, space charge, Debye dipole, and interfacial polarization [270]. In $Pr_{0.02}Mn_{0.5}Co_{0.5}Fe_{1.98}O_4$ – Ti_3C_2 composites, the main contributors to dielectric behavior are space charge, Debye dipole, and interfacial polarization. These findings are in line with observations made by Liu et al. in co-doped Ni–Zn ferrite/graphene (CNZF/GN) composites, indicating similarities in dielectric properties between the systems. The Debye dipolar relaxation effect in $Pr_{0.02}Mn_{0.5}Co_{0.5}Fe_{1.98}O_4$ – Ti_3C_2 composites can be explained by several factors. During alternating electromagnetic wave radiation, delays in induced charges at interfaces such as ferrite–ferrite, ferrite–Ti_3C_2, and Ti_3C_2–Ti_3C_2 encountering the external field lead to relaxation and conversion of

electromagnetic energy into thermal energy. Furthermore, lattice defects and functional groups generated during the synthesis of Ti_3C_2 and $Pr_{0.02}Mn_{0.5}Co_{0.5}Fe_{1.98}O_4$ – Ti_3C_2 composites promote additional carriers between ferrite and Ti_3C_2, facilitating Debye relaxation. Additionally, in the $Pr_{0.02}Mn_{0.5}Co_{0.5}Fe_{1.98}O_4$ – Ti_3C_2 heterogeneous system, the accumulation of virtual charges at interfaces with varying conductivities and dielectric constants results in interfacial polarization known as Maxwell–Wagner polarization [271].

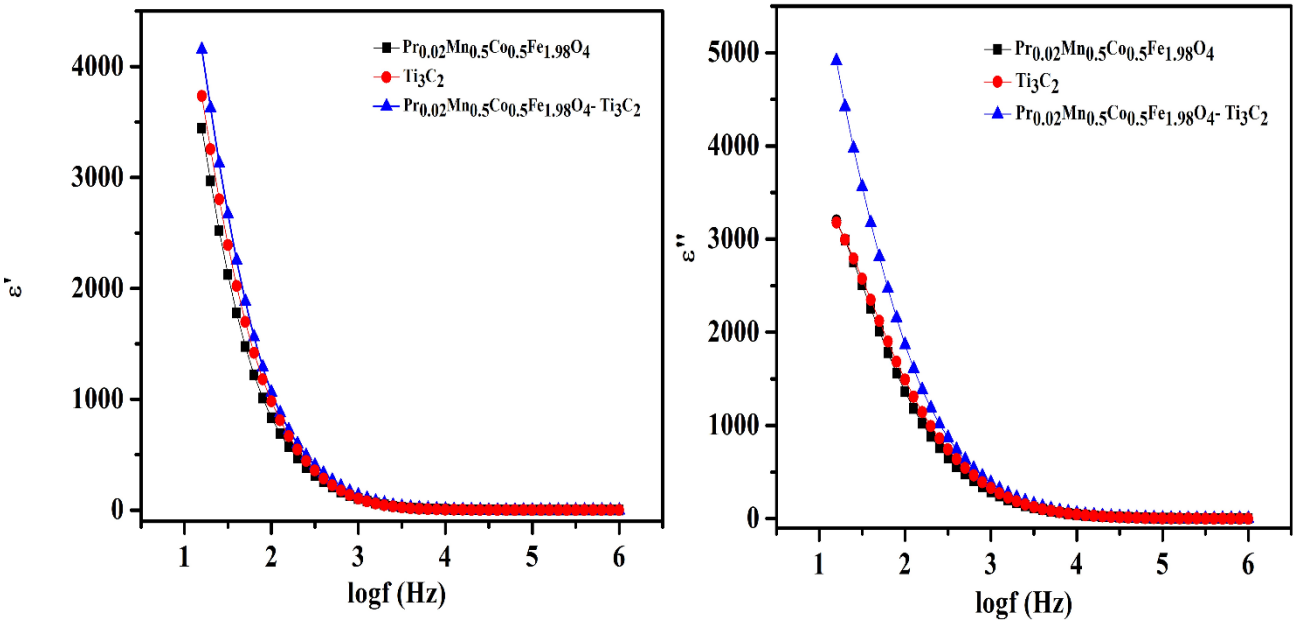

Fig. 8.14. depicts the real permittivity and imaginary permittivity of the $Pr_{0.02}Mn_{0.5}Co_{0.5}Fe_{1.98}O_4$, Ti_3C_2, and $Pr_{0.02}Mn_{0.5}Co_{0.5}Fe_{1.98}O_4$ – Ti_3C_2.

8.4. Electrochemical Study

8.4.1 CV Study

The Cyclic voltammetry (CV) of all materials was obtained using a three-electrode system in an electrochemical cell. The electrochemical cell has active working electrodes $Pr_{0.02}Mn_{0.5}Co_{0.5}Fe_{1.98}O_4$, Ti_3C_2, $Pr_{0.02}Mn_{0.5}Co_{0.5}Fe_{1.98}O_4$ - Ti_3C_2 reference electrode Ag/AgCl and platinum as a counter electrode having 3M KOH as an electrolyte, potential window range -0.2 to 0.5 V and scanning rate (10 – 100mV s^{-1}). Fig. 8.15 depicts the CV curves for the $Pr_{0.02}Mn_{0.5}Co_{0.5}Fe_{1.98}O_4$, Ti_3C_2, and $Pr_{0.02}Mn_{0.5}Co_{0.5}Fe_{1.98}O_4$ - Ti_3C_2 nanocomposite at 10 mVs^{-1}. The specific capacitance of the working electrode was calculated using Eq. (8.10) as depicted in Table 8.5.

$$C_{sp} = \frac{1}{mv\Delta V}\int_{Vi}^{vf} I(V)\, dV \qquad (8.10)$$

where ∫I (V)dV is the area of CV curves, m (mg) is an active material mass coated on the electrode, and ΔV (V) is the difference of the potential window. These CV curves manifest a non-rectangular shape which affirms the appearance of faradic behavior in all materials [272][260]. The redox reaction causes a shift in the anodic and cathodic peaks towards higher and lower potentials respectively oxidation and reduction are observed as the scan rate increases [108]. The $Pr_{0.02}Mn_{0.5}Co_{0.5}Fe_{1.98}O_4$ - Ti_3C_2 composite exhibited a large surface area, high specific capacitance, and better conductivity than MXene and spinel ferrite. While decreasing the internal resistance MXenes improved the charge carrier mobility. Fig. 16(a) depicts the CV curves for the $Pr_{0.02}Mn_{0.5}Co_{0.5}Fe_{1.98}O_4$ - Ti_3C_2 composite at scan rates of 10, 20, 40, 60, 80, and 100 mV s^{-1}. As the scan rate increased the peak current increased without any significant change in the structure of the CV curves. The specific capacitance was determined to be 10 mVs^{-1} for $Pr_{0.02}Mn_{0.5}Co_{0.5}Fe_{1.98}O_4$ (765.72 F g^{-1}), Ti_3C_2 (924.50 F g^{-1}), and $Pr_{0.02}Mn_{0.5}Co_{0.5}Fe_{1.98}O_4$ - Ti_3C_2 (1134.27 F g^{-1}). The $Pr_{0.02}Mn_{0.5}Co_{0.5}Fe_{1.98}O_4$ - Ti_3C_2 composite had a high specific capacitance which is superior to that reported in a previous study as shown in Table 8.7. With increases in the scan rate, as a result, decrement in the specific capacitance for $Pr_{0.02}Mn_{0.5}Co_{0.5}Fe_{1.98}O_4$, Ti_3C_2, and $Pr_{0.02}Mn_{0.5}Co_{0.5}Fe_{1.98}O_4$ - Ti_3C_2. At a high scan rate, the specific capacitance is reduced because the inner active site cannot endure the redox transition entirely owing to the diffusion effect of a proton inside the electrode. The specific capacitance in the decreasing trend demonstrates that the area of the electrode has a significant impact at high charging and discharging rates [273]. For all scan rates, the $Pr_{0.02}Mn_{0.5}Co_{0.5}Fe_{1.98}O_4$ - Ti_3C_2 nanocomposite had a higher specific capacitance than the $Pr_{0.02}Mn_{0.5}Co_{0.5}Fe_{1.98}O_4$ and Ti_3C_2 individual materials, as shown in Fig. 16(b).

Table 8.5 Electrochemical parameters from CV curve of $Pr_{0.02}Mn_{0.5}Co_{0.5}Fe_{1.98}O_4$, Ti_3C_2, $Pr_{0.02}Mn_{0.5}Co_{0.5}Fe_{1.98}O_4$ – Ti_3C_2 nanocomposite.

Sample	v (mV s^{-1})	Voltage (V)	C_{sp}
$Pr_{0.02}Mn_{0.5}Co_{0.5}Fe_{1.98}O_4$	10	0.7	765.72
	20	0.7	567.16
	40	0.7	535.76
	60	0.7	491.23

	100	0.7	368.723
Ti_3C_2	10	0.7	924.50
	20	0.7	704.78
	40	0.7	534.02
	60	0.7	521.10
	100	0.7	439.44
$Pr_{0.02}Mn_{0.5}Co_{0.5}Fe_{1.98}O_4$ - Ti_3C_2	10	0.7	1134.27
	20	0.7	914.57
	40	0.7	842.20
	60	0.7	713.61
	100	0.7	685.50

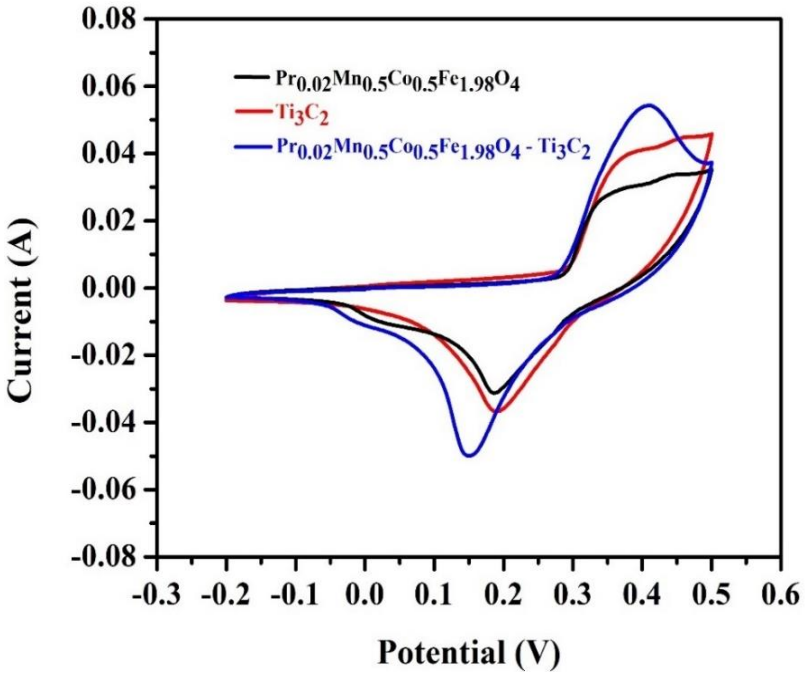

Fig. 8.15. CV curve of $Pr_{0.02}Mn_{0.5}Co_{0.5}Fe_{1.98}O_4$, Ti_3C_2, $Pr_{0.02}Mn_{0.5}Co_{0.5}Fe_{1.98}O_4$ – Ti_3C_2 at scan rate 10 mVs^{-1}.

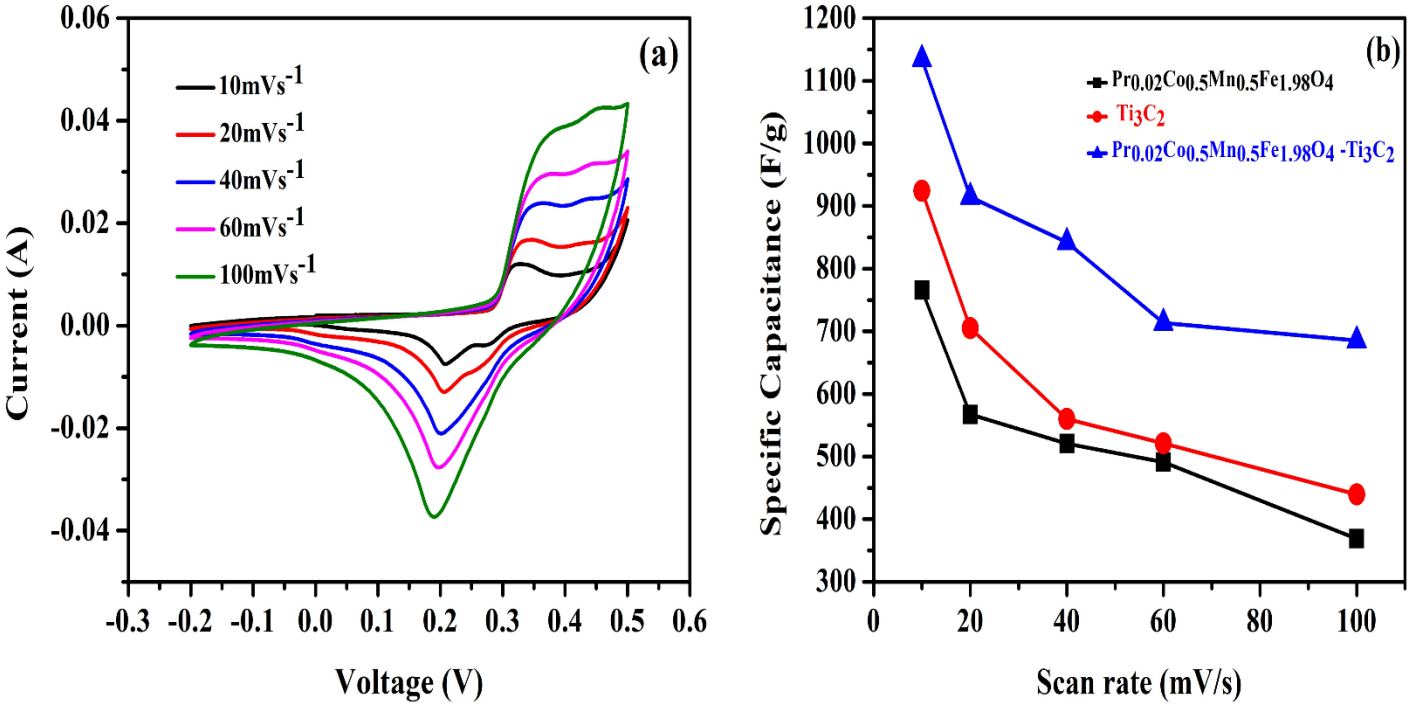

Fig. 8.16. CV curves of (a) $Pr_{0.02}Mn_{0.5}Co_{0.5}Fe_{1.98}O_4$ – Ti_3C_2 at different scan rates, and (b) Specific capacitance as a function of scan rate.

8.4.2 Galvanic Charge–Discharge (GCD) Study

The GCD analysis of $Pr_{0.02}Mn_{0.5}Co_{0.5}Fe_{1.98}O_4$, Ti_3C_2, and $Pr_{0.02}Mn_{0.5}Co_{0.5}Fe_{1.98}O_4$ - Ti_3C_2 was carried 3M KOH at different current density (2-6 A g^{-1}) and potential rate (0.0 – 0.5 V). The GCD curves demonstrate nonlinear behavior, which indicates redox reaction and pseudocapacitive behavior [263]. The specific capacitance was calculated at different current density (2 – 6A g^{-1}) through the given Eq. (8.11) [28].

$$C_{sp} = \frac{I_m \times \Delta t}{\Delta V} \qquad (8.11)$$

where I_m is the current density (2 - 6 A g^{-1}), Δt is the charging-discharging time, and ΔV is the potential rate (0.0-0.5 V). The specific capacitance (C_{sp}) of $Pr_{0.02}Mn_{0.5}Co_{0.5}Fe_{1.98}O_4$ (931.81F g^{-1}), Ti_3C_2 (1181.95 F g^{-1}), $Pr_{0.02}Mn_{0.5}Co_{0.5}Fe_{1.98}O_4$ - Ti_3C_2 (1310.54 F g^{-1}) were calculated at current density 2 A g^{-1} as in Fig. 8.17. At different current density (2,3,4,5, and 6 A g^{-1}) the specific capacitance of $Pr_{0.02}Mn_{0.5}Co_{0.5}Fe_{1.98}O_4$, Ti_3C_2, and $Pr_{0.02}Mn_{0.5}Co_{0.5}Fe_{1.98}O_4$ - Ti_3C_2 were evaluated as depicted in Table 8.6 and Fig. 8.18(a). The current density increases leading to a decrement in the specific capacitance. When the high current density is applied, the specific

capacitance decreased which can be attributed to the slow rate of the redox reaction. This is because deep ion penetration occurs at the inner site of the electrode surface which is not favorable at high current density and constrains the outer surface leading to the total specific capacitance (C_{sp}) of the material to decreased [274]. The C_{sp} of the $Pr_{0.02}Mn_{0.5}Co_{0.5}Fe_{1.98}O_4$ - Ti_3C_2 nanocomposite has a higher value of 1310.54 F g^{-1} at 2 A g^{-1} than the $Pr_{0.02}Mn_{0.5}Co_{0.5}Fe_{1.98}O_4$ and Ti_3C_2 in the literature as presented in Table 8.7. The specific capacitance retentions of $Pr_{0.02}Mn_{0.5}Co_{0.5}Fe_{1.98}O_4$, Ti_3C_2, and $Pr_{0.02}Mn_{0.5}Co_{0.5}Fe_{1.98}O_4$ - Ti_3C_2 at a current density of 6 A g^{-1} were 58.53 %, 63.80 %, and 75.95 %, respectively as in the Fig. 18(b). The nanocomposite exhibited a higher specific capacitance retention than the individual $Pr_{0.02}Mn_{0.5}Co_{0.5}Fe_{1.98}O_4$ and Ti_3C_2. The nanocomposite shows high retention owing to the presence of the conducting material (MXene) [275]. Ti_3C_2 improves the conductivity of nanocomposite. The specific capacitance of the composite is high owing to the doping of rare earth elements and the presence of MXenes. Doping with rare-earth elements enhances the electrochemical activity of the electrode. The ionic radii of Fe^{3+} (0.64 Å) are less than the ionic radii of Pr^{3+} (1.013 Å) which causes the deformation in the structure of $Mn_{0.5}Co_{0.5}Fe_{2-x}O_4$. This is because, when the exchange reaction, the diffusion rate of protons increased. For doped samples, Pr^{3+} ions replaced Fe^{3+} ions in the lattice $Mn_{0.5}Co_{0.5}Fe_{2-x}O_4$, which formed an adequate positive defect. Therefore, the possibility of proton transfer increases, and electrons can easily escape from $Mn_{0.5}Co_{0.5}Fe_{2-x}O_4$ [274]. Ti_3C_2 is a conductive material with high electrical conductivity when incorporated into the composite material. It can improve the overall electrical conductivity of the composite. Ti_3C_2 has a layered structure with a large specific surface area. This property provides a high number of active sites for electrochemical reactions to occur such as redox reactions. The increased active surface area can enhance the overall electrochemical activity and improve the performance of the composite material. Also, a large surface area facilitates ion diffusion, enabling efficient ion storage and transport within the composite material. This characteristic is particularly beneficial for supercapacitors [276]. Ti_3C_2 has a 2D lamellar structure that allows for fast ion intercalation which facilitates to access the large surface of MXenes and allows for fast reaction in pseudocapacitive store charge and high performance. The entire process significantly enhanced the electrochemical properties of the material. The increased active surface area can enhance the overall electrochemical activity and improve the performance of the composite material. Also,a large surface area facilitates ion diffusion, enabling efficient ion storage and transport withinthe composite material. It enhance the specific caapcitance of the material. Porous structures can facilitate faster ion movement, impacting the overall charge/discharge rates. The pororsity of all the sample is 61.51%-

62.45%.These pores are beneficial for energy storage devices (supercapacitors and batteries) as the electrolyte ions easily reach the electrode

Table 8.6 GCD parameters of $Pr_{0.02}Mn_{0.5}Co_{0.5}Fe_{1.98}O_4$, Ti_3C_2, $Pr_{0.02}Mn_{0.5}Co_{0.5}Fe_{1.98}O_4$ - Ti_3C_2 nanocomposite.

Sample	I_m (Ag^{-1})	Δt (s)	ΔV (V)	C_{sp} ($F\ g^{-1}$)
$Pr_{0.02}Mn_{0.5}Co_{0.5}Fe_{1.98}O_4$	2	205	0.44	931.81
	3	125	0.44	852.27
	4	87.5	0.44	795.45
	5	58	0.44	659.18
	6	40	0.44	545.45
Ti_3C_2 Mxene	2	260.03	0.44	1181.95
	3	148.90	0.44	1015.27
	4	105	0.44	954.54
	5	75	0.44	852.27
	6	55.30	0.44	754.09
$Pr_{0.02}Mn_{0.5}Co_{0.5}Fe_{1.98}O_4$ - Ti_3C_2	2	288.32	0.44	1310.54
	3	190	0.44	1295.45
	4	115.56	0.44	1050.62
	5	89.15	0.44	1013.06
	6	73	0.44	995. 45

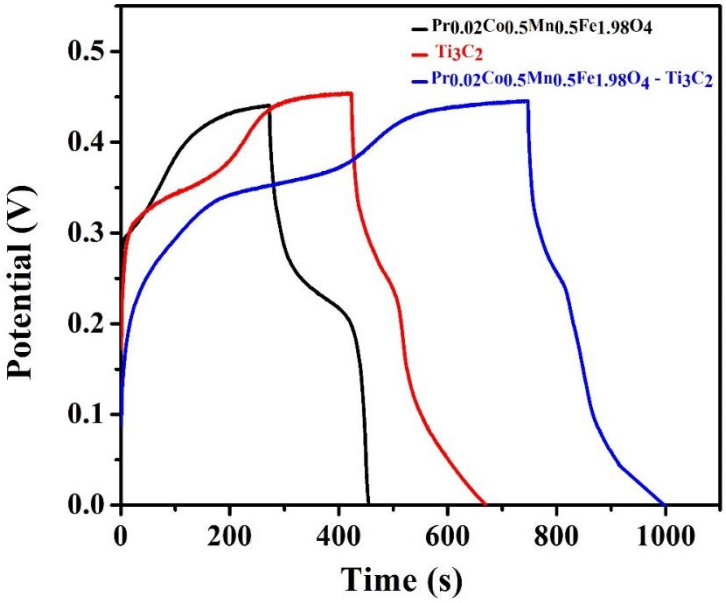

Fig. 8.17. GCD curves of $Pr_{0.02}Mn_{0.5}Co_{0.5}Fe_{1.98}O_4$, Ti_3C_2, $Pr_{0.02}Mn_{0.5}Co_{0.5}Fe_{1.98}O_4$ – Ti_3C_2 nanocomposite at 2 Ag^{-1}.

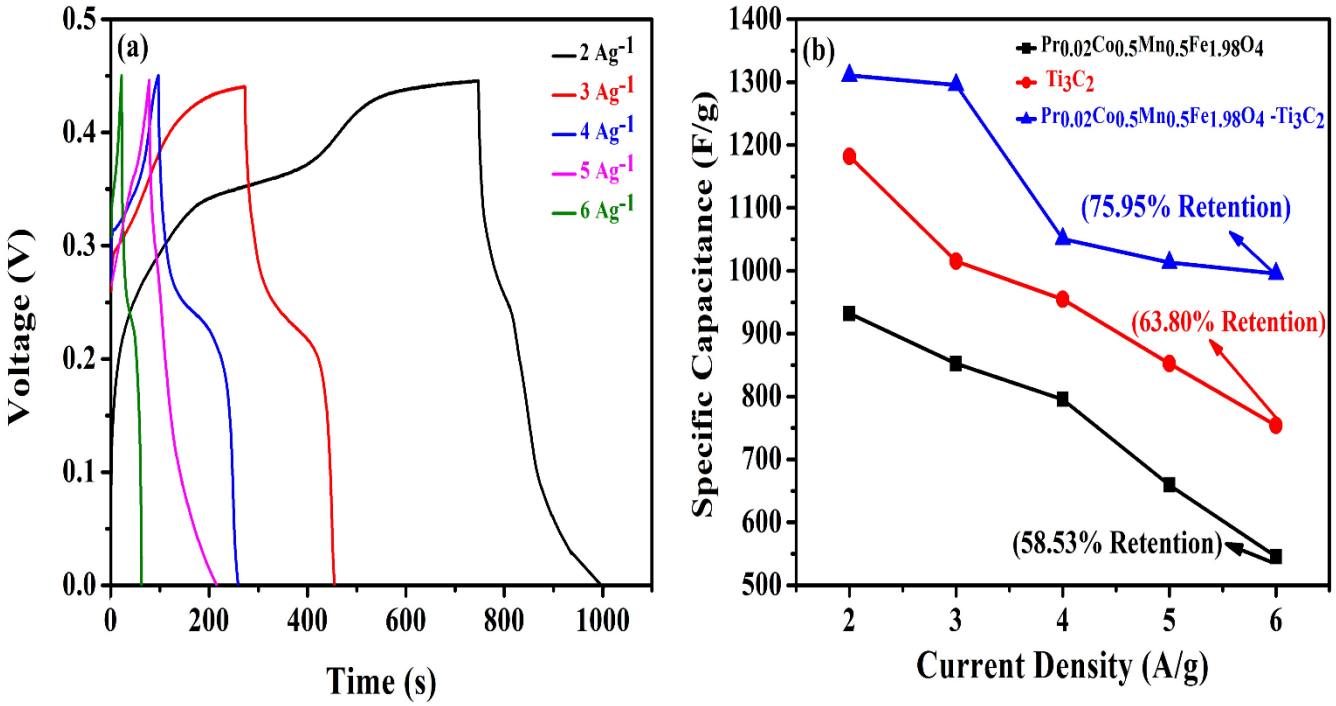

Fig. 8.18 (a) GCD curves of $Pr_{0.02}Mn_{0.5}Co_{0.5}Fe_{1.98}O_4$ - Ti_3C_2 nanocomposite at different current densities, and (b) Specific capacitance as a function of current density.

Table 8.7 Super capacity performance of $Pr_{0.02}Mn_{0.5}Co_{0.5}Fe_{1.98}O_4 – Ti_3C_2$ compared with some other ferrites, conducting material, and composite-based ferrites.

Material	Synthesis method	Electrolyte	CV (F g^{-1})	GCD (F g^{-1})	References
$Ce_{0.5}CoFe_{1.5}O_4$	Hydrothermal method	1M KOH	926	426	[28]
$Al_{0.8}Cu_{0.1}Co_{0.1}Fe_2O_4$	Sol-gel method	1M KOH	256	93	[274]
$CuCoFe_2O_4$	Sol-gel method	1M KOH	221.1	76.9	[275]
Ti_3C_2	Etching method (using HF)	0.1M KOH	323.17	1046.25	[96]
$Mn_{0.3}Co_{0.2}Zn_{0.5}Fe_2O_4$-PANI	Mechanical blending method	3M KOH	286.91	226.25	[62]
$CoFe_2O_4$- MXene	Coprecipitation Method	0.1M KOH	440	1268.75	[50]
$CoFe_2O_4$- Graphene	Hydrothermal method	6M KOH	256	196	[277]
$Pr_{0.02}Mn_{0.5}Co_{0.5}Fe_{1.98}O_4 – Ti_3C_2$	Mechanical blending method	3M KOH	1134.27	1310.54	This work

8.4.3 EIS Study

The electron transfer and electrical resistance property of the prepared material $Pr_{0.02}Mn_{0.5}Co_{0.5}Fe_{1.98}O_4$, Ti_3C_2, $Pr_{0.02}Mn_{0.5}Co_{0.5}Fe_{1.98}O_4$ - Ti_3C_2 can be determined by the EIS analysis. Fig. 8.19 depicts the Nyquist plot of $Pr_{0.02}Mn_{0.5}Co_{0.5}Fe_{1.98}O_4$, Ti_3C_2, and $Pr_{0.02}Mn_{0.5}Co_{0.5}Fe_{1.98}O_4$ - Ti_3C_2 applying 5mV and a frequency of 100 kHz to 0.1 Hz. In the Nyquist plot at high frequencies, the semicircle represents the Faraday charge transfer resistance (R_{ct}), and at low frequencies, the straight-line slope depicts the Warburg resistance (W_d), which represents the continuous diffusion/transport between the pores and electrolyte of the electro-active material during the redox reactions [278]. The equivalent series resistance of the material $Pr_{0.02}Mn_{0.5}Co_{0.5}Fe_{1.98}O_4$, Ti_3C_2, and $Pr_{0.02}Mn_{0.5}Co_{0.5}Fe_{1.98}O_4$ - Ti_3C_2 are evaluated by the intercept of the semicircle X - axis are 1.75 Ω, 0.74 Ω, 0.31 Ω. R_{ct} is inversely proportional to

the specific capacitance. The higher the value of R_{ct}, the lower the specific capacitance of the supercapacitors. The order of the R_{ct} value $Pr_{0.02}Mn_{0.5}Co_{0.5}Fe_{1.98}O_4$>, Ti_3C_2>, $Pr_{0.02}Mn_{0.5}Co_{0.5}Fe_{1.98}O_4$ - Ti_3C_2. $Pr_{0.02}Mn_{0.5}Co_{0.5}Fe_{1.98}O_4$ - Ti_3C_2 improved the charge transfer in the supercapacitor owing to its lower R_{ct} value [279]. The $Pr_{0.02}Mn_{0.5}Co_{0.5}Fe_{1.98}O_4$ - Ti_3C_2 nanocomposite showed high charge transfer in the electrode, and the nanocomposite had high ionic and electronic conductivity. $Pr_{0.02}Mn_{0.5}Co_{0.5}Fe_{1.98}O_4$ - Ti_3C_2 nanocomposite exhibits better capacitance than the individual $Pr_{0.02}Mn_{0.5}Co_{0.5}Fe_{1.98}O_4$ and Ti_3C_2 which also confirms the CV and GCD results. The slope of the $Pr_{0.02}Mn_{0.5}Co_{0.5}Fe_{1.98}O_4$ - Ti_3C_2 nanocomposite is much closer to 90^0 than that of $Pr_{0.02}Mn_{0.5}Co_{0.5}Fe_{1.98}O_4$, Ti_3C_2. $Pr_{0.02}Mn_{0.5}Co_{0.5}Fe_{1.98}O_4$ - Ti_3C_2 demonstrated better capacitance behavior, which is consistent with the CV results [62]. Consequently, the physical blending of $Pr_{0.02}Mn_{0.5}Co_{0.5}Fe_{1.98}O_4$ - Ti_3C_2 produces a synergistic effect, enhancing the electrochemical properties of the synthesized nanocomposite electrode.

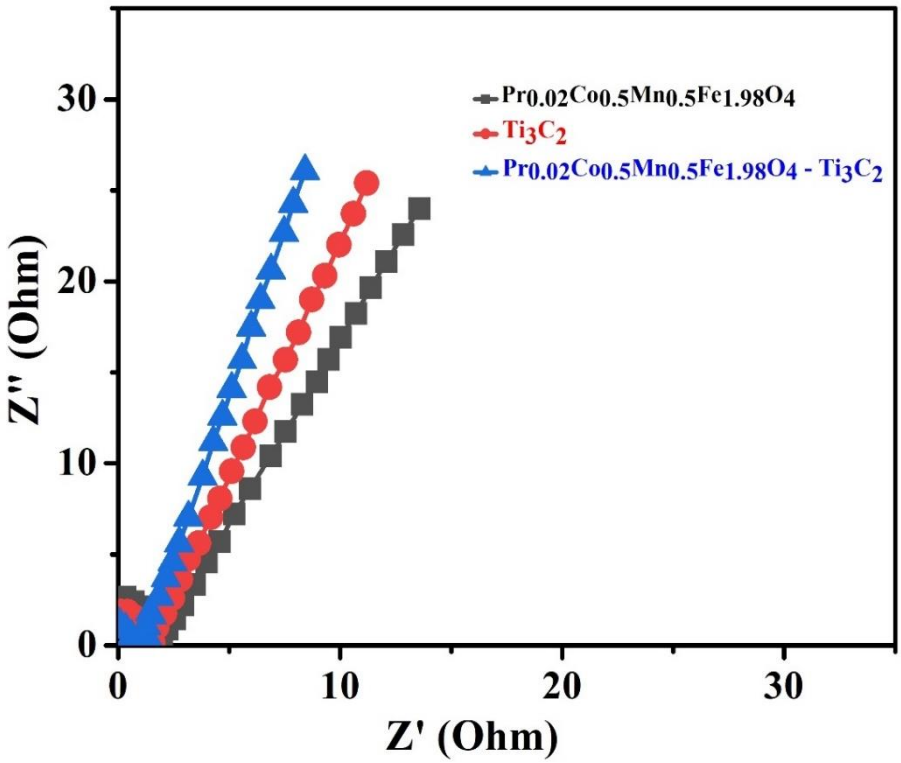

Fig. 8.19. Nyquist plot of $Pr_{0.02}Mn_{0.5}Co_{0.5}Fe_{1.98}O_4$, Ti_3C_2, and $Pr_{0.02}Mn_{0.5}Co_{0.5}Fe_{1.98}O_4$ - Ti_3C_2 nanocomposite.

8.5. Conclusion

A simple and cost-effective method was adopted to synthesize the novel material $Pr_{0.02}Mn_{0.5}Co_{0.5}Fe_{1.98}O_4$ - Ti_3C_2 as the supercapacitor electrode using sol-gel auto combustion

method, and physical blending. The enhancement in the crystallite size of the $Pr_{0.02}Mn_{0.5}Co_{0.5}Fe_{1.98}O_4$ - Ti_3C_2 nanocomposite confirms the encapsulation of ferrite nanoparticles with MXene. EDX confirms the presence of the element's composition and stoichiometry ratios of the materials. HR-TEM is in close agreement with the crystallite size as evaluated from XRD data and hence affirms the immaculateness of our prepared samples. XPS analysis affirmed that Pr^{3+} metal ions were successfully incorporated into the manganese cobalt ferrite lattice and further confirmed the spinel nature and Ti_3C_2 of synthesized material in the nanocomposite. The excellent electrochemical activity of the $Pr_{0.02}Mn_{0.5}Co_{0.5}Fe_{1.98}O_4$ - Ti_3C_2 nanocomposite was demonstrated by CV, GCD, and EIS. The highest C_{sp} was achieved to be 1310.54 Fg^{-1} at 2 mVs^{-1} with a capacitance retention of 75.95 % at 6 Ag^{-1}. EIS results also revealed the superior electrochemical properties of the $Pr_{0.02}Mn_{0.5}Co_{0.5}Fe_{1.98}O_4$ - Ti_3C_2 composite by providing only 0.25 Ω a charge transfer resistance. In the future, ternary nanocomposites will be prepared using MoS_2 and rGO to strengthen C_s. We hope that this study will lead to further possibilities for investigating novel spinel ferrite-based nanocomposites for supercapacitor applications.

CHAPTER – 9

Summary and Conclusion

The present research work investigated the impact of sintering temperature on the magnetic as well as structural characteristics of $Zn_{0.2}Mg_{0.8}Fe_2O_4$ spinel ferrite synthesized by cost-effective sol-gel auto combustion process at various sintering temperatures (400 ºC, 600 ºC, 800 ºC). The cubic symmetry of the $Zn_{0.2}Mg_{0.8}Fe_2O_4$ ferrite was confirmed by XRD analysis. The lattice constant increases as the temperature increases because the Zn^{2+} (0.74 Å) and Mg^{2+} (0.72 Å) have larger ionic radii than the Fe^{2+} (0.64 Å) As the sintering temperature rises, the crystallite size of $Zn_{0.2}Mg_{0.8}Fe_2O_4$ increases from 14 nm to 32 nm. FTIR study reveals the presence of the v_1 absorption band is near 535.18 cm^{-1} and the presence of the v_2 absorption band is near 357.18 cm^{-1} which affirms the formation of $Zn_{0.2}Mg_{0.8}Fe_2O_4$ spinel ferrite. The micrograph fesem reveals the agglomeration of particles due to the magnetic interaction between the nearby particles. The particle size was determined to be 506.12 nm, 548.84 nm, and 564.58 nm corresponding x = 400 ºC, 600 ºC, 800 ºC temperature using ImageJ software. EDX study revealed at the 800 ºC $Zn_{0.2}Mg_{0.8}Fe_2O_4$ ferrite shows all elements peaks viz Zn, Co, Fe, O, and homogenously diffusion in the spinel ferrite without the presence of impurity. Magnetic properties demonstrate $Zn_{0.2}Mg_{0.8}Fe_2O_4$ spinel ferrite exhibits soft ferrite in nature. The saturation magnetization is increased from 30.166 emu/g – 44.987 emu/g as the sintering temperature is increased due to the crystallite size is increased. The squareness ratio is between 0.178 - 0.151. It demonstrates that the sample is oriented at the multi-domain. Owing to these properties it affirms that the synthesized $Zn_{0.2}Mg_{0.8}Fe_2O_4$ spinel ferrite has been used in the application of magnetic recording and electronic devices.

Further, the $Mn_xCo_{0.5-x}Ni_{0.5}Fe_2O_4$ (x = 0.0, 0.2, and 0.4) was synthesized by using the sol-gel auto-combustion method. The phase structure of $Mn_xCo_{0.5-x}Ni_{0.5}Fe_2O_4$ (x = 0.0, 0.2, and 0.4) exhibits the single-phase crystalline structure without any extra impurity present which is confirmed by the XRD studies. The lattice constant (a_o) increases from 8.349 - 8.360 Å due to the Mn^{2+} has a high ionic radii of 0.80 Å than the Co^{2+} ion with ionic radii of 0.78 Å. The *D* of the sample firstly increases from 32.60 (x = 0.0) nm to 33.99 nm (x = 0.2) and then decreases to 33.62 nm (x = 0.4) by utilizing the Debye Scherrer formula. The peaks at 1395, 1672, and 3147 cm^{-1} demonstrated the absence of citric acid during the sintering process and indicated the faultlessness of our prepared $Mn_xCo_{0.5-x}Ni_{0.5}Fe_2O_4$ spinel ferrite. FESEM micrographs indicate the samples are inhomogeneous in nature and irregular in size and shape, the

grains of all the samples were in the nanoscale range, with the presence of distinct voids and pores that could be attributed to gas emissions (CO_2, NO_2, H_2O, etc.) during the synthesis. The theoretical and experimental values of at. % and wt.% are very similar, confirming the precision of our synthesized samples by utilizing EDX spectra. The M-H plot reveals that all samples exhibit a ferromagnetic nature. The saturation magnetization decreased from 55.26 emu/g - 63.42 emu/g with the Mn^{2+} dopant. The reduction in M_s is a direct result of crystallite size miniaturization. The dielectric constant was found to be high at low frequencies because the grain boundaries were more active. Owing to the large surface area, porous size, high coercivity, and good remanence of the materials, they are applicable in recording devices, switching, and microwave devices and also used as a supercapacitor electrode material.

Further, the Rare earth Pr^{3+} ion substituted in the Mn - Co spinel ferrite was prepared via. sol-gel route. The phase composition of the prepared samples was analyzed by X-ray diffraction (XRD). Rietveld refinement confirms the single phase for the samples (x = 0.0, 0.01, 0.02) and shows a secondary phase for the samples with higher concentrations of Pr^{3+} (x = 0.03 and 0.04). The values of *D* were obtained in the range of 43-45 nm. It was reported that if the values of *D* are inferior to 50 nm, then the material is a suitable candidate for media recording applications. The hopping length values in tetrahedral and octahedral sites were found to lie in the range of 3.6408-3.6405 nm and 2.9723 – 2.9721 nm. In 2D and 3D electron density the red, orange, and yellow contours around Co atoms could refer to the distribution of the valence d orbitals electrons whereas the blue contour around the O atoms could refer to the distribution of 2s and 2p orbitals electrons. Two frequency bands (υ_1 and υ_2) were observed. At the high–frequency band (υ_1) range lies 542.54 cm^{-1} indicates the stretching vibrations of M-O complexes at the tetrahedral site (A) but at the lesser frequency band (υ_2) range is 453.57 cm^{-1} indicates the intrinsic vibrations M-O complexes at the octahedral site (B). $Pr_xMn_{0.5}Co_{0.5}Fe_{2-x}O_4$ is found to be the best suitable match for the supercapactior electrode, and gas sensing because of the porous morphology exhibited by all the FESEM micrographs. The EDX spectra determine the atomic percent (at%) values, which were in close concordance with the theoretical values. For $x = 0.03$ and $x = 0.04$. However, the large difference in the theoretical and experimental value occurred owe to the secondary phase which has been observed in the XRD pattern. The magnetic properties of $Pr_xMn_{0.5}Co_{0.5}Fe_{2-x}O_4$ ferrite reveal its soft nature. The squareness ratio for all the samples was noticed to be less than 0.5 which affirms the existence of the multi-

domain structure. Owing to the above-mentioned characterized features it is deduced that $Pr_xMn_{0.5}Co_{0.5}Fe_{2-x}O_4$ spinel ferrites can be potential candidates for supercapacitor electrode material.

Owing to the magnificent properties of the prepared $Pr_xMn_{0.5}Co_{0.5}Fe_{2-x}O_4$ (x = 0.00, 0.01, 0.02, 0.03, and 0.04) samples for supercapacitor electrode material as described above, the sample at x = 0.3, viz. $Pr_{0.02}Mn_{0.5}Co_{0.5}Fe_{1.98}O_4$ has a large surface area and high porosity. Taking into consideration the findings of the above studies, the 2D material MXene and novel nanocomposite $Pr_{0.02}Mn_{0.5}Co_{0.5}Fe_{1.98}O_4$ – Ti_3C_2 have been synthesized by the etching method and physical blending method. The XRD pattern confirms the Ti_3C_2 peak (002) in the nanocomposite, which could be related to the entrance of $Pr_{0.02}Mn_{0.5}Co_{0.5}Fe_{1.98}O_4$ spinel ferrite into the Ti_3C_2. Furthermore, the characteristic peaks of $Pr_{0.02}Mn_{0.5}Co_{0.5}Fe_{1.98}O_4$ and Ti_3C_2 could be seen in the prepared samples, indicating their existence. This increase in the nanocomposite crystallite size confirms the encapsulation of $Pr_{0.02}Mn_{0.5}Co_{0.5}Fe_{1.98}O_4$ spinel ferrite nanoparticles with Ti_3C_2 MXene. The $Pr_{0.02}Mn_{0.5}Co_{0.5}Fe_{1.98}O_4$ - Ti_3C_2 nanocomposite reveals that the nanoparticles and MXenes are embedded with openings between the layers. The presence of nanoparticles between the MXene layers prevents restacking. MXenes prevent nanoparticle agglomeration which enhances nanocomposite pores. Because of the ease of access of the electrolyte to the electrode, these pores enhance electrochemical activity. The HR-TEM micrograph of the $Pr_{0.02}Mn_{0.5}Co_{0.5}Fe_{1.98}O_4$ - Ti_3C_2 (composite) clearly showed the thin layer structure of Ti_3C_2 and the attachment of ferrite spherical nanoparticles on the MXene layers. The specific capacitances of the $Pr_{0.02}Mn_{0.5}Co_{0.5}Fe_{1.98}O_4$ – Ti_3C_2, Ti_3C_2, and $Pr_{0.02}Mn_{0.5}Co_{0.5}Fe_2O_4$ electrodes 1310.54 F g^{-1}, 1181.95 F g^{-1}, and 947.81 F g^{-1} at a current density of 2 A g^{-1}. The highest C_{sp} was achieved to be 1310.54 Fg^{-1} at 2 mVs^{-1} with a capacitance retention of 75.95 % at 6 Ag^{-1}. EIS results also revealed the superior electrochemical properties of the $Pr_{0.02}Mn_{0.5}Co_{0.5}Fe_{1.98}O_4$ - Ti_3C_2 composite by providing only 0.25 Ω a charge transfer resistance. The nanocomposite showed good electrochemical performance and hence it is a promising material for supercapacitors.

9.1. Future Scope

This thesis work on Spinel ferrite – MXene based supercapacitor electrodes has introduced a wide scope in the field of energy storage and significantly affects the next generation of modern Spinel ferrite – MXene based electrodes.

1. Citric acid is used as fuel in the present synthesis of spinel ferrites while the use of other fuels like urea, glycine, tartaric acid, etc. can be explored.

2. This work can be extended by the needful modifications of spinel ferrite with ternary composite to further increase its electrochemical performance as a supercapacitor electrode.

3. Modification of $Ti_3C_2T_x$ with metal telluride, CNT, and graphitic-C_3N_4 to further increase its electrochemical efficiency.

We expect that these factors will create more opportunities for researchers in this field to investigate advanced spinel ferrite-based nanocomposites for potential use in upcoming supercapacitor applications.

CHAPTER-10

Bibliography

[1] J. Castro-Gutiérrez, A. Celzard, and V. Fierro, "Energy Storage in Supercapacitors: Focus on Tannin-Derived Carbon Electrodes," *Front. Mater.*, vol. 7, no. July, pp. 1–25, 2020, doi: 10.3389/fmats.2020.00217.

[2] T. Chen *et al.*, "All-solid-state high performance asymmetric supercapacitors based on novel MnS nanocrystal and activated carbon materials," *Sci. Rep.*, vol. 6, no. November 2015, pp. 1–9, 2016, doi: 10.1038/srep23289.

[3] F. Xing *et al.*, "Flameless combustion with liquid fuel: A review focusing on fundamentals and gas turbine application," *Appl. Energy*, vol. 193, pp. 28–51, 2017, doi: 10.1016/j.apenergy.2017.02.010.

[4] J. R. Miller and P. Simon, "Materials science: Electrochemical capacitors for energy management," *Science (80-.).*, vol. 321, no. 5889, pp. 651–652, 2008, doi: 10.1126/science.1158736.

[5] T. Güney, "Renewable energy, non-renewable energy and sustainable development," *Int. J. Sustain. Dev. World Ecol.*, vol. 26, no. 5, pp. 389–397, 2019, doi: 10.1080/13504509.2019.1595214.

[6] B. K. Saikia, S. M. Benoy, M. Bora, J. Tamuly, M. Pandey, and D. Bhattacharya, "A brief review on supercapacitor energy storage devices and utilization of natural carbon resources as their electrode materials," *Fuel*, vol. 282, no. April, p. 118796, 2020, doi: 10.1016/j.fuel.2020.118796.

[7] O. D. Momoh and M. O. Omoigui, "An overview of hybrid electric vehicle technology," *5th IEEE Veh. Power Propuls. Conf. VPPC '09*, pp. 1286–1292, 2009, doi: 10.1109/VPPC.2009.5289703.

[8] O. Krishan and S. Suhag, "An updated review of energy storage systems: Classification and applications in distributed generation power systems incorporating renewable energy resources," *Int. J. Energy Res.*, vol. 43, no. 12, pp. 6171–6210, 2019, doi: 10.1002/er.4285.

[9] H. Sun *et al.*, "Hierarchical 3D electrodes for electrochemical energy storage," *Nat. Rev.*

Mater., vol. 4, no. 1, pp. 45–60, 2019, doi: 10.1038/s41578-018-0069-9.

[10] S. Liu, D. Ni, H. F. Li, K. N. Hui, C. Y. Ouyang, and S. C. Jun, "Effect of cation substitution on the pseudocapacitive performance of spinel cobaltite MCo2O4 (M = Mn, Ni, Cu, and Co)," *J. Mater. Chem. A*, vol. 6, no. 23, pp. 10674–10685, 2018, doi: 10.1039/c8ta00540k.

[11] H. Wang and H. Dai, "Strongly coupled inorganic–nano-carbon hybrid materials for energy storage," *Chem. Soc. Rev.*, vol. 42, no. 7, pp. 3088–3113, 2013, doi: 10.1039/c2cs35307e.

[12] B. K. Kim, S. Sy, A. Yu, and J. Zhang, "Electrochemical Supercapacitors for Energy Storage and Conversion," *Handb. Clean Energy Syst.*, pp. 1–25, 2015, doi: 10.1002/9781118991978.hces112.

[13] M. Manjurul Haque, M. Huq, and M. A. Hakim, "Influence of CuO and sintering temperature on the microstructure and magnetic properties of Mg- Cu- Zn ferrites," *J. Magn. Magn. Mater.*, vol. 320, no. 21, pp. 2792–2799, 2008, doi: 10.1016/j.jmmm.2008.06.017.

[14] M. Winter and R. J. Brodd, "What are batteries, fuel cells, and supercapacitors?," *Chem. Rev.*, vol. 104, no. 10, pp. 4245–4269, 2004, doi: 10.1021/cr020730k.

[15] L. Yu and G. Z. Chen, "Supercapatteries as High-Performance Electrochemical Energy Storage Devices," *Electrochem. Energy Rev.*, vol. 3, no. 2, pp. 271–285, 2020, doi: 10.1007/s41918-020-00063-6.

[16] M. Nagao *et al.*, "All-solid-state lithium–sulfur batteries with three-dimensional mesoporous electrode structures," *J. Power Sources*, vol. 330, pp. 120–126, 2016, doi: 10.1016/j.jpowsour.2016.09.009.

[17] P. J. Hall *et al.*, "Energy storage in electrochemical capacitors: Designing functional materials to improve performance," *Energy Environ. Sci.*, vol. 3, no. 9, pp. 1238–1251, 2010, doi: 10.1039/c0ee00004c.

[18] R. R. Zhang, Y. M. Xu, D. Harrison, J. Fyson, F. L. Qiu, and D. Southee, "Flexible strip supercapacitors for future energy storage," *Int. J. Autom. Comput.*, vol. 12, no. 1, pp. 43–49, 2015, doi: 10.1007/s11633-014-0866-6.

[19] H. Du, Z. Wu, Y. Xu, S. Liu, and H. Yang, "Poly(3,4-ethylenedioxythiophene) based

solid-state polymer supercapacitor with ionic liquid gel polymer electrolyte," *Polymers (Basel).*, vol. 12, no. 2, 2020, doi: 10.3390/polym12020297.

[20] Y. Hu and T. S. Fisher, "Suggested standards for reporting power and energy density in supercapacitor research," *Bull. Mater. Sci.*, vol. 41, no. 5, pp. 10–13, 2018, doi: 10.1007/s12034-018-1641-z.

[21] M. Yassine and D. Fabris, "Performance of commercially available supercapacitors," *Energies*, vol. 10, no. 9, 2017, doi: 10.3390/en10091340.

[22] Z. Qi and G. M. Koenig, "Review Article: Flow battery systems with solid electroactive materials," *J. Vac. Sci. Technol. B, Nanotechnol. Microelectron. Mater. Process. Meas. Phenom.*, vol. 35, no. 4, 2017, doi: 10.1116/1.4983210.

[23] P. Forouzandeh, V. Kumaravel, and S. C. Pillai, "Electrode materials for supercapacitors: A review of recent advances," *Catalysts*, vol. 10, no. 9, pp. 1–73, 2020, doi: 10.3390/catal10090969.

[24] B. Pal, S. Yang, S. Ramesh, V. Thangadurai, and R. Jose, "Electrolyte selection for supercapacitive devices: A critical review," *Nanoscale Adv.*, vol. 1, no. 10, pp. 3807–3835, 2019, doi: 10.1039/c9na00374f.

[25] Bharti *et al.*, "Theories and models of supercapacitors with recent advancements: impact and interpretations," *Nano Express*, vol. 2, no. 2, 2021, doi: 10.1088/2632-959X/abf8c2.

[26] Poonam, K. Sharma, A. Arora, and S. K. Tripathi, "Review of supercapacitors: Materials and devices," *J. Energy Storage*, vol. 21, no. 2, pp. 801–825, Feb. 2019, doi: 10.1016/j.est.2019.01.010.

[27] G. Gautham Prasad, N. Shetty, S. Thakur, Rakshitha, and K. B. Bommegowda, "Supercapacitor technology and its applications: A review," *IOP Conf. Ser. Mater. Sci. Eng.*, vol. 561, no. 1, 2019, doi: 10.1088/1757-899X/561/1/012105.

[28] G. Nabi *et al.*, "Role of cerium-doping in CoFe2O4 electrodes for high performance supercapacitors," *J. Energy Storage*, vol. 29, no. December 2019, 2020, doi: 10.1016/j.est.2020.101452.

[29] D. Zha, P. Xiong, and X. Wang, "Strongly coupled manganese ferrite/carbon black/polyaniline hybrid for low-cost supercapacitors with high rate capability," *Electrochim. Acta*, vol. 185, pp. 218–228, 2015, doi: 10.1016/j.electacta.2015.10.139.

[30] Y. Zhai, Y. Dou, D. Zhao, P. F. Fulvio, R. T. Mayes, and S. Dai, "Carbon Materials for Chemical Capacitive Energy Storage," *Adv. Mater.*, vol. 23, no. 42, pp. 4828–4850, 2011, doi: 10.1002/adma.201100984.

[31] F. Belhachemi, S. Rael, and B. Davat, "Physical based model of power electric double-layer supercapacitors," *Conf. Rec. - IAS Annu. Meet. (IEEE Ind. Appl. Soc.*, vol. 5, no. Upresa 7037, pp. 3069–3076, 2000, doi: 10.1109/ias.2000.882604.

[32] P. Saha and M. Khanra, "Equivalent circuit model of supercapacitor for self-discharge analysis - A comparative study," *Int. Conf. Signal Process. Commun. Power Embed. Syst. SCOPES 2016 - Proc.*, no. 978, pp. 1381–1386, 2017, doi: 10.1109/SCOPES.2016.7955667.

[33] R. Kant and M. B. Singh, "Generalization of the Gouy-Chapman-Stern model of an electric double layer for a morphologically complex electrode: Deterministic and stochastic morphologies," *Phys. Rev. E - Stat. Nonlinear, Soft Matter Phys.*, vol. 88, no. 5, 2013, doi: 10.1103/PhysRevE.88.052303.

[34] M. A. Brown, G. V. Bossa, and S. May, "Emergence of a Stern Layer from the Incorporation of Hydration Interactions into the Gouy-Chapman Model of the Electrical Double Layer," *Langmuir*, vol. 31, no. 42, pp. 11477–11483, 2015, doi: 10.1021/acs.langmuir.5b02389.

[35] H. Zhang, L. Zhang, J. Chen, H. Su, F. Liu, and W. Yang, "One-step synthesis of hierarchically porous carbons for high-performance electric double layer supercapacitors," *J. Power Sources*, vol. 315, pp. 120–126, 2016, doi: 10.1016/j.jpowsour.2016.03.005.

[36] A. Halama, B. Szubzda, and G. Pasciak, "Carbon aerogels as electrode material for electrical double layer supercapacitors - Synthesis and properties," *Electrochim. Acta*, vol. 55, no. 25, pp. 7501–7505, 2010, doi: 10.1016/j.electacta.2010.03.040.

[37] R. Chen, M. Yu, R. P. Sahu, I. K. Puri, and I. Zhitomirsky, "The Development of Pseudocapacitor Electrodes and Devices with High Active Mass Loading," *Adv. Energy Mater.*, vol. 10, no. 20, 2020, doi: 10.1002/aenm.201903848.

[38] Z. Jian, V. Raju, Z. Li, Z. Xing, Y. S. Hu, and X. Ji, "A High-Power Symmetric Na-Ion Pseudocapacitor," *Adv. Funct. Mater.*, vol. 25, no. 36, pp. 5778–5785, 2015, doi:

10.1002/adfm.201502433.

[39] A. Afif, S. M. Rahman, A. Tasfiah Azad, J. Zaini, M. A. Islam, and A. K. Azad, "Advanced materials and technologies for hybrid supercapacitors for energy storage – A review," *J. Energy Storage*, vol. 25, no. July, p. 100852, 2019, doi: 10.1016/j.est.2019.100852.

[40] Z. S. Iro, C. Subramani, and S. S. Dash, "A brief review on electrode materials for supercapacitor," *Int. J. Electrochem. Sci.*, vol. 11, no. 12, pp. 10628–10643, 2016, doi: 10.20964/2016.12.50.

[41] Xian Jian *et al.*, "Carbon-Based Electrode Materials for Supercapacitor: Progress, Challenges and Prospective Solutions," *J. Electr. Eng.*, vol. 4, no. 2, pp. 75–87, 2016, doi: 10.17265/2328-2223/2016.02.004.

[42] L. Zhang and X. S. Zhao, "Carbon-based materials as supercapacitor electrodes," *Chem. Soc. Rev.*, vol. 38, no. 9, pp. 2520–2531, 2009, doi: 10.1039/b813846j.

[43] J. Yao, Q. Pan, S. Yao, L. Duan, and J. Liu, "Mesoporous MnO2 Nanosphere/Graphene Sheets as Electrodes for Supercapacitor Synthesized by a Simple and Inexpensive Reflux Reaction," *Electrochim. Acta*, vol. 238, pp. 30–35, 2017, doi: 10.1016/j.electacta.2017.02.153.

[44] S. Liu, L. Hu, X. Xu, A. A. Al-Ghamdi, and X. Fang, "Nickel Cobaltite Nanostructures for Photoelectric and Catalytic Applications," *Small*, vol. 11, no. 34, pp. 4267–4283, 2015, doi: 10.1002/smll.201500315.

[45] N. Arsalani, A. G. Tabrizi, and L. S. Ghadimi, "Novel PANI/MnFe2O4 nanocomposite for low-cost supercapacitors with high rate capability," *J. Mater. Sci. Mater. Electron.*, vol. 29, no. 7, pp. 6077–6085, 2018, doi: 10.1007/s10854-018-8582-6.

[46] A. Eftekhari, L. Li, and Y. Yang, "Polyaniline supercapacitors," *J. Power Sources*, vol. 347, pp. 86–107, 2017, doi: 10.1016/j.jpowsour.2017.02.054.

[47] S. Banerjee and K. K. Kar, "Conducting polymers as electrode materials for supercapacitors," *Springer Ser. Mater. Sci.*, vol. 302, no. 2009, pp. 333–352, 2020, doi: 10.1007/978-3-030-52359-6_13.

[48] Y. Han, Y. Ge, Y. Chao, C. Wang, and G. G. Wallace, "Recent progress in 2D materials for flexible supercapacitors," *J. Energy Chem.*, vol. 27, no. 1, pp. 57–72, 2018, doi:

10.1016/j.jechem.2017.10.033.

[49] P. Forouzandeh and S. C. Pillai, “Two-dimensional (2D) electrode materials for supercapacitors,” *Mater. Today Proc.*, vol. 41, no. xxxx, pp. 498–505, 2020, doi: 10.1016/j.matpr.2020.05.233.

[50] I. Ayman *et al.*, “Batteries and Energy Storage CoFe2O4 Nanoparticles-Decorated 2D MXene : A Novel Hybrid Material for Supercapacitors Applications Sustainable Energy Technologies Center , College of Engineering , King Saud University , PO,” 2020, doi: 10.1021/acs.energyfuels.0c00959.

[51] Y. Wang and Y. Wang, “Recent progress in MXene layers materials for supercapacitors: High-performance electrodes,” *SmartMat*, vol. 4, no. 1, 2023, doi: 10.1002/smm2.1130.

[52] C. Zhong, Y. Deng, W. Hu, J. Qiao, L. Zhang, and J. Zhang, “A review of electrolyte materials and compositions for electrochemical supercapacitors,” *Chem. Soc. Rev.*, vol. 44, no. 21, pp. 7484–7539, 2015, doi: 10.1039/c5cs00303b.

[53] W. Ye, H. Wang, J. Ning, Y. Zhong, and Y. Hu, “New types of hybrid electrolytes for supercapacitors,” *J. Energy Chem.*, vol. 57, pp. 219–232, 2021, doi: 10.1016/j.jechem.2020.09.016.

[54] S. Amani, N. Sohrabi, R. Mohammadi, and I. Ahadzadeh, “Synthesis and investigation of CoMnFeO4/reduced graphene oxide as ecofriendly electrode material for supercapacitor and its electrochemical performances,” *J. Alloys Compd.*, vol. 937, p. 168020, 2023, doi: 10.1016/j.jallcom.2022.168020.

[55] D. Karabelli, J.-C. Leprêtre, F. Alloin, and J.-Y. Sanchez, “Poly(vinylidene fluoride)-based macroporous separators for supercapacitors,” *Electrochim. Acta*, vol. 57, no. July 2011, pp. 98–103, Dec. 2011, doi: 10.1016/j.electacta.2011.03.033.

[56] R. Srivastava and B. C. Yadav, “Ferrite materials: Introduction, synthesis techniques, and applications as sensors,” *Int. J. Green Nanotechnol. Biomed.*, vol. 4, no. 2, pp. 141–154, 2012, doi: 10.1080/19430892.2012.676918.

[57] M. Kaur, P. Jain, and M. Singh, “Studies on structural and magnetic properties of ternary cobalt magnesium zinc (CMZ) Co0.6-xMgxZn0.4 Fe2O4 (x = 0.0, 0.2, 0.4, 0.6) ferrite nanoparticles,” *Mater. Chem. Phys.*, vol. 162, pp. 332–339, 2015, doi: 10.1016/j.matchemphys.2015.05.075.

[58] K. Sathiyamurthy, C. Rajeevgandhi, L. Guganathan, S. Bharanidharan, and S. Savithiri, "Enhancement of magnetic, supercapacitor applications and theoretical approach on cobalt-doped zinc ferrite nanocomposites," *J. Mater. Sci. Mater. Electron.*, vol. 32, no. 9, pp. 11593–11606, 2021, doi: 10.1007/s10854-021-05764-2.

[59] H. Mahajan, S. Kumar, and A. K. Srivastava, "Synthesis and investigation of structural , morphological , and magnetic properties of the manganese doped cobalt-zinc spinel ferrite," vol. 896, pp. 2–11, 2021.

[60] S. C. Tolani, A. R. Golhar, and K. G. Rewatkar, "A review of morphological, structural behaviour and technological applications of ferrites," *AIP Conf. Proc.*, vol. 2104, no. May, 2019, doi: 10.1063/1.5100459.

[61] H. Qin *et al.*, "Spinel ferrites (MFe2O4): Synthesis, improvement and catalytic application in environment and energy field," *Adv. Colloid Interface Sci.*, vol. 294, no. July, p. 102486, 2021, doi: 10.1016/j.cis.2021.102486.

[62] H. Mahajan *et al.*, "Structural, morphological, and electrochemical investigation of Mn0.3Co0.2Zn0.5Fe2O4-polyaniline nanocomposite for supercapacitor application," *J. Mater. Sci. Mater. Electron.*, vol. 33, no. 35, pp. 26590–26603, 2022, doi: 10.1007/s10854-022-09335-x.

[63] S. Joshi, M. Kumar, H. Pandey, M. Singh, and P. Pal, "Structural, magnetic and dielectric properties of Gd3+ substituted NiFe2O4 nanoparticles," *J. Alloys Compd.*, vol. 768, pp. 287–297, 2018, doi: 10.1016/j.jallcom.2018.07.250.

[64] M. A. Khan, M. U. Islam, M. Ishaque, and I. Z. Rahman, "Effect of Tb substitution on structural, magnetic and electrical properties of magnesium ferrites," *Ceram. Int.*, vol. 37, no. 7, pp. 2519–2526, 2011, doi: 10.1016/j.ceramint.2011.03.063.

[65] I. Mohammed *et al.*, "Structural, morphological, optical, magnetic, and microwave properties of La3+- Mn2+ substituted Zn2-Y-type barium-strontium hexaferrite," *Chinese J. Phys.*, vol. 78, no. April, pp. 377–390, 2022, doi: 10.1016/j.cjph.2022.06.025.

[66] R. C. Pullar, "Hexagonal ferrites: A review of the synthesis, properties and applications of hexaferrite ceramics," *Prog. Mater. Sci.*, vol. 57, no. 7, pp. 1191–1334, 2012, doi: 10.1016/j.pmatsci.2012.04.001.

[67] M. N. Akhtar, M. Babar, S. Qamar, Z. ur Rehman, and M. A. Khan, "Structural Rietveld

refinement and magnetic features of prosademium (Pr) doped Cu nanocrystalline spinel ferrites," *Ceram. Int.*, vol. 45, no. 8, pp. 10187–10195, 2019, doi: 10.1016/j.ceramint.2019.02.069.

[68] M. Niaz Akhtar *et al.*, "Y3Fe5O12 nanoparticulate garnet ferrites: Comprehensive study on the synthesis and characterization fabricated by various routes," *J. Magn. Magn. Mater.*, vol. 368, pp. 393–400, 2014, doi: 10.1016/j.jmmm.2014.06.004.

[69] I. A. Abdel-Latif, "Crystal structure and electrical transport of nano-crystalline strontium-doped neodymium ortho-ferrites," *J. Nanoparticle Res.*, vol. 22, no. 5, 2020, doi: 10.1007/s11051-020-04846-2.

[70] M. Wang *et al.*, "Effect of Sr doped the YFeO3 rare earth ortho-ferrite on structure, magnetic properties, and microwave absorption performance," *Ceram. Int.*, vol. 47, no. 24, pp. 34159–34169, 2021, doi: 10.1016/j.ceramint.2021.08.325.

[71] C. Yuan, H. Bin Wu, Y. Xie, and X. W. Lou, "Mixed transition-metal oxides: Design, synthesis, and energy-related applications," *Angew. Chemie - Int. Ed.*, vol. 53, no. 6, pp. 1488–1504, 2014, doi: 10.1002/anie.201303971.

[72] Y. Wang *et al.*, "A High-Performance, Tailorable, Wearable, and Foldable Solid-State Supercapacitor Enabled by Arranging Pseudocapacitive Groups and MXene Flakes on Textile Electrode Surface," *Adv. Funct. Mater.*, vol. 31, no. 7, pp. 1–12, 2021, doi: 10.1002/adfm.202008185.

[73] V. Verma, M. Kaur, and J. M. Greneche, "Tailored structural, optical and magnetic properties of ternary nanohybrid Mn 0.4 Co 0.6-x Cu x Fe 2 O 4 (x= 0, 0.2, 0.4, 0.6) spinel ferrites," *Ceram. Int.*, vol. 45, no. 8, pp. 10865–10875, 2019, doi: 10.1016/j.ceramint.2019.02.164.

[74] D. R. Mane, D. D. Birajdar, S. Patil, S. E. Shirsath, and R. H. Kadam, "Redistribution of cations and enhancement in magnetic properties of sol-gel synthesized Cu0.7-x Co x Zn0.3Fe 2O4 ($0 \leq x \leq 0.5$)," *J. Sol-Gel Sci. Technol.*, vol. 58, no. 1, pp. 70–79, 2011, doi: 10.1007/s10971-010-2357-8.

[75] A. A. Kadam, S. S. Shinde, S. P. Yadav, P. S. Patil, and K. Y. Rajpure, "Structural, morphological, electrical and magnetic properties of Dy doped Ni-Co substitutional spinel ferrite," *J. Magn. Magn. Mater.*, vol. 329, pp. 59–64, 2013, doi:

10.1016/j.jmmm.2012.10.008.

[76] J. Smit and H. P. J. Wijn, “Physical Properties of Ferrites,” *Adv. Electron. Electron Phys.*, vol. 6, no. C, pp. 69–136, 1954, doi: 10.1016/S0065-2539(08)60132-8.

[77] N. Channa *et al.*, “Nickel-substituted manganese spinel ferrite nanoparticles for high-frequency applications,” *J. Mater. Sci. Mater. Electron.*, vol. 31, no. 2, pp. 1661–1671, 2020, doi: 10.1007/s10854-019-02684-0.

[78] K. Kaur, H. Mahajan, A. Sharma, I. Mohammaed, A. K. Srivastava, and D. Basandrai, “Manganese doped cobalt – nickel spinel ferrite via . sol – gel approach : Insight into structural , morphological , magnetic , and dielectric properties,” *J. Mater. Res.*, pp. 1–13, 2023, doi: 10.1557/s43578-023-01119-1.

[79] H. Mahajan, S. K. Godara, and A. K. Srivastava, “Synthesis and investigation of structural, morphological, and magnetic properties of the manganese doped cobalt-zinc spinel ferrite,” *J. Alloys Compd.*, vol. 896, p. 162966, 2022, doi: 10.1016/j.jallcom.2021.162966.

[80] M. Hu, H. Zhang, T. Hu, B. Fan, X. Wang, and Z. Li, “Emerging 2D MXenes for supercapacitors: Status, challenges and prospects,” *Chem. Soc. Rev.*, vol. 49, no. 18, pp. 6666–6693, 2020, doi: 10.1039/d0cs00175a.

[81] Z. Wang *et al.*, “Unraveling and regulating self-discharge behavior of Ti3C2Tx MXene-based supercapacitors,” *ACS Nano*, vol. 14, no. 4, pp. 4916–4924, 2020, doi: 10.1021/acsnano.0c01056.

[82] Y. Tang, J. Zhu, C. Yang, and F. Wang, “ Enhanced Capacitive Performance Based on Diverse Layered Structure of Two-Dimensional Ti 3 C 2 MXene with Long Etching Time ,” *J. Electrochem. Soc.*, vol. 163, no. 9, pp. A1975–A1982, 2016, doi: 10.1149/2.0921609jes.

[83] N. C. Ghosh and S. P. Harimkar, *Consolidation and synthesis of MAX phases by Spark Plasma Sintering (SPS): A review*. Woodhead Publishing Limited, 2012. doi: 10.1016/B978-1-84569-991-8.50003-5.

[84] Y. Gogotsi and B. Anasori, “The Rise of MXenes,” *ACS Nano*, vol. 13, no. 8, pp. 8491–8494, 2019, doi: 10.1021/acsnano.9b06394.

[85] R. Garg, A. Agarwal, and M. Agarwal, “Synthesis and optimisation of MXene for

supercapacitor application," *J. Mater. Sci. Mater. Electron.*, vol. 31, no. 21, pp. 18614–18626, 2020, doi: 10.1007/s10854-020-04404-5.

[86] X. Zhang, X. Liu, R. Yan, J. Yang, Y. Liu, and S. Dong, "Ion-assisted self-assembly of macroporous MXene films as supercapacitor electrodes," *J. Mater. Chem. C*, vol. 8, no. February, pp. 2008–2013, 2020, doi: 10.1039/C9TC05595A.

[87] R. Shafique *et al.*, "Investigations of 2D Ti3C2(MXene)-CoCr2O4 nanocomposite as an efficient electrode material for electrochemical supercapacitors," *Int. J. Energy Res.*, vol. 46, no. 5, pp. 6689–6701, 2022, doi: 10.1002/er.7605.

[88] S. Venkateshalu and A. N. Grace, "MXenes—A new class of 2D layered materials: Synthesis, properties, applications as supercapacitor electrode and beyond," *Appl. Mater. Today*, vol. 18, p. 100509, 2020, doi: 10.1016/j.apmt.2019.100509.

[89] L. H. Karlsson, J. Birch, J. Halim, M. W. Barsoum, and P. O. Å. Persson, "Atomically Resolved Structural and Chemical Investigation of Single MXene Sheets," *Nano Lett.*, vol. 15, no. 8, pp. 4955–4960, 2015, doi: 10.1021/acs.nanolett.5b00737.

[90] M. Ghidiu, M. R. Lukatskaya, M. Q. Zhao, Y. Gogotsi, and M. W. Barsoum, "Conductive two-dimensional titanium carbide 'clay' with high volumetric capacitance," *Nature*, vol. 516, no. 7529, pp. 78–81, 2015, doi: 10.1038/nature13970.

[91] L. Verger, V. Natu, M. Carey, and M. W. Barsoum, "MXenes: An Introduction of Their Synthesis, Select Properties, and Applications," *Trends Chem.*, vol. 1, no. 7, pp. 656–669, 2019, doi: 10.1016/j.trechm.2019.04.006.

[92] C. J. Zhang *et al.*, "Oxidation Stability of Colloidal Two-Dimensional Titanium Carbides (MXenes)," *Chem. Mater.*, vol. 29, no. 11, pp. 4848–4856, 2017, doi: 10.1021/acs.chemmater.7b00745.

[93] M. Khazaei *et al.*, "Novel electronic and magnetic properties of two-dimensional transition metal carbides and nitrides," *Adv. Funct. Mater.*, vol. 23, no. 17, pp. 2185–2192, 2013, doi: 10.1002/adfm.201202502.

[94] J. N. Coleman *et al.*, "Two-dimensional nanosheets produced by liquid exfoliation of layered materials," *Science (80-.).*, vol. 331, no. 6017, pp. 568–571, 2011, doi: 10.1126/science.1194975.

[95] A. Thirumurugan *et al.*, "MXene/Ferrite Magnetic Nanocomposites for Electrochemical

Supercapacitor Applications," *Micromachines*, vol. 13, no. 10, 2022, doi: 10.3390/mi13101792.

[96] T. Yaqoob *et al.*, "MXene/Ag2CrO4 nanocomposite as supercapacitors electrode," *Materials (Basel).*, vol. 14, no. 20, Oct. 2021, doi: 10.3390/MA14206008.

[97] A. Anwar, U. S. Akther, K. H. Maria, M. K. Alam, A. Kumar, and M. N. I. Khan, "Regulated Ni – Zn – Co ferrites : structural , electrical and magnetic properties tailored by co doping," *J. Mater. Sci. Mater. Electron.*, pp. 1–23, 2024, doi: 10.1007/s10854-023-11748-1.

[98] S. Chai *et al.*, "Manganese ferrite/reduced graphene oxide composites as energy storage electrode materials for supercapacitors," *Ionics (Kiel).*, 2024, doi: 10.1007/s11581-024-05477-6.

[99] S. P. Ghaemi, S. M. Masoudpanah, and P. Heidari, "Facile synthesis of Ni0.5Zn0.5Fe2O4/MXene composite powders for high-performance asymmetric supercapacitors," *J. Energy Storage*, vol. 72, no. PB, p. 108439, 2023, doi: 10.1016/j.est.2023.108439.

[100] P. Agale *et al.*, "Synthesis, characterization, and supercapacitor applications of Ni-doped CuMnFeO4 nano Ferrite," *Ceram. Int.*, vol. 49, no. 16, pp. 27003–27014, 2023, doi: 10.1016/j.ceramint.2023.05.240.

[101] M. Mayakkannan *et al.*, "One step microwave combustion synthesized spinel nano NiZnFe2O4 as an electrode material for supercapacitors with superior performance," *J. Mater. Sci. Mater. Electron.*, vol. 34, no. 18, pp. 1–13, 2023, doi: 10.1007/s10854-023-10796-x.

[102] B. Jeevanantham, M. K. Shobana, T. Pazhanivel, and H. Choe, "Pseudocapacitive behaviors of strontium-doped cobalt ferrite nanoparticles for supercapacitor applications," *J. Alloys Compd.*, vol. 960, p. 170651, 2023, doi: 10.1016/j.jallcom.2023.170651.

[103] A. Manohar, V. Vijayakanth, S. V. Prabhakar Vattikuti, and K. H. Kim, "Synthesis and characterization of Mg2+ substituted MnFe2O4 nanoparticles for supercapacitor applications," *Ceram. Int.*, vol. 48, no. 20, pp. 30695–30703, 2022, doi: 10.1016/j.ceramint.2022.07.018.

[104] S. A. Al Kiey, R. Ramadan, and M. M. El-Masry, “Synthesis and characterization of mixed ternary transition metal ferrite nanoparticles comprising cobalt, copper and binary cobalt–copper for high-performance supercapacitor applications,” *Appl. Phys. A Mater. Sci. Process.*, vol. 128, no. 6, pp. 1–13, 2022, doi: 10.1007/s00339-022-05590-1.

[105] T. Dippong, E. A. Levei, I. G. Deac, I. Petean, and O. Cadar, “Dependence of Structural, Morphological and Magnetic Properties of Manganese Ferrite on Ni-Mn Substitution,” *Int. J. Mol. Sci.*, vol. 23, no. 6, 2022, doi: 10.3390/ijms23063097.

[106] M. N. Akhtar *et al.*, “Physical, structural, conductive and magneto-optical properties of rare earths (Yb, Gd) doped Ni–Zn spinel nanoferrites for data and energy storage devices,” *Ceram. Int.*, vol. 47, no. 9, pp. 11878–11886, 2021, doi: 10.1016/j.ceramint.2021.01.028.

[107] T. Yaqoob *et al.*, “MXene/Ag2CrO4 nanocomposite as supercapacitors electrode,” *Materials (Basel).*, vol. 14, no. 20, 2021, doi: 10.3390/ma14206008.

[108] M. Safari and J. Mazloom, “Electrochemical performance of spindle-like Fe2Co-MOF and derived magnetic yolk-shell CoFe2O4 microspheres for supercapacitor applications,” *J. Solid State Electrochem.*, vol. 25, no. 8–9, pp. 2189–2200, 2021, doi: 10.1007/s10008-021-04989-9.

[109] S. Balideh, A. Aavazpour, G. Rezaei, and A. Nikzad, “Structural and magnetic properties of spinel nickel-cobalt ferrite nanoparticles substituted by dysprosium cation synthesized by hydrothermal method,” *Acta Phys. Pol. A*, vol. 140, no. 1, pp. 14–19, 2021, doi: 10.12693/APHYSPOLA.140.14.

[110] B. Nawaz, G. Ali, M. O. Ullah, S. Rehman, and F. Abbas, “Investigation of the electrochemical properties of ni0.5zn0.5fe2o4 as binder-based and binder-free electrodes of supercapacitors,” *Energies*, vol. 14, no. 11, 2021, doi: 10.3390/en14113297.

[111] W. Raza, G. Nabi, A. Shahzad, N. Malik, and N. Raza, “Electrochemical performance of lanthanum cerium ferrite nanoparticles for supercapacitor applications,” *J. Mater. Sci. Mater. Electron.*, vol. 32, no. 6, pp. 7443–7454, 2021, doi: 10.1007/s10854-021-05457-w.

[112] M. M. Baig, E. Pervaiz, M. Azad, Z. Jahan, M. B. Khan Niazi, and S. M. Baig,

"NiFe2O4/SiO2 nanostructures as a potential electrode material for high rated supercapacitors," *Ceram. Int.*, vol. 47, no. 9, pp. 12557–12566, 2021, doi: 10.1016/j.ceramint.2021.01.113.

[113] A. Anwar *et al.*, "Impact of rare earth Dy+3 cations on the various parameters of nanocrystalline nickel spinel ferrite," *J. Mater. Res. Technol.*, vol. 9, no. 3, pp. 5313–5325, 2020, doi: 10.1016/j.jmrt.2020.03.057.

[114] K. Tanbir, M. P. Ghosh, R. K. Singh, M. Kar, and S. Mukherjee, "Effect of doping different rare earth ions on microstructural, optical, and magnetic properties of nickel–cobalt ferrite nanoparticles," *J. Mater. Sci. Mater. Electron.*, vol. 31, no. 1, pp. 435–443, 2020, doi: 10.1007/s10854-019-02546-9.

[115] S. A. Mazen, H. M. Elsayed, and N. I. Abu-Elsaad, "Effect of divalent metal ions substitution on structural and magnetic properties of Li0.25Mn0.5-xMxFe2.25O4 (M = Co2+, Ni2+, Cu2+) spinel ferrites," *Mater. Chem. Phys.*, vol. 256, no. March, pp. 1–10, 2020, doi: 10.1016/j.matchemphys.2020.123676.

[116] G. Singh and S. Chandra, "Nano-flowered manganese doped ferrite@PANI composite as energy storage electrode material for supercapacitors," *J. Electroanal. Chem.*, vol. 874, p. 114491, 2020, doi: 10.1016/j.jelechem.2020.114491.

[117] J. P. Cheng, W. D. Wang, X. C. Wang, and F. Liu, "Recent research of core–shell structured composites with NiCo2O4 as scaffolds for electrochemical capacitors," *Chem. Eng. J.*, vol. 393, no. March, p. 124747, 2020, doi: 10.1016/j.cej.2020.124747.

[118] M. Barakzehi, M. Montazer, F. Sharif, T. Norby, and A. Chatzitakis, "MOF-modified polyester fabric coated with reduced graphene oxide/polypyrrole as electrode for flexible supercapacitors," *Electrochim. Acta*, vol. 336, p. 135743, 2020, doi: 10.1016/j.electacta.2020.135743.

[119] S. J. Uke, S. P. Mardikar, D. R. Bambole, Y. Kumar, and G. N. Chaudhari, "Sol-gel citrate synthesized Zn doped MgFe2O4 nanocrystals: A promising supercapacitor electrode material," *Mater. Sci. Energy Technol.*, vol. 3, pp. 446–455, 2020, doi: 10.1016/j.mset.2020.02.009.

[120] Y. Slimani *et al.*, "Investigation of structural and physical properties of Eu3+ ions substituted Ni0.4Cu0.2Zn0.4Fe2O4 spinel ferrite nanoparticles prepared via

sonochemical approach," *Results Phys.*, vol. 17, p. 103061, 2020, doi: 10.1016/j.rinp.2020.103061.

[121] M. A. Almessiere *et al.*, "Impact of Eu3+ ion substitution on structural, magnetic and microwave traits of Ni–Cu–Zn spinel ferrites," *Ceram. Int.*, vol. 46, no. 8, pp. 11124–11131, 2020, doi: 10.1016/j.ceramint.2020.01.132.

[122] J. Bhagwan, S. Khaja Hussain, and J. S. Yu, "Aqueous asymmetric supercapacitors based on ZnCo2O4 nanoparticles via facile combustion method," *J. Alloys Compd.*, vol. 815, p. 152456, 2020, doi: 10.1016/j.jallcom.2019.152456.

[123] H. Javed, F. Iqbal, P. O. Agboola, M. A. Khan, M. F. Warsi, and I. Shakir, "Structural, electrical and magnetic parameters evaluation of nanocrystalline rare earth Nd 3+ - substituted nickel-zinc spinel ferrite particles," *Ceram. Int.*, vol. 45, no. 8, pp. 11125–11130, 2019, doi: 10.1016/j.ceramint.2019.02.176.

[124] Y. Z. Cai, W. Q. Cao, Y. L. Zhang, P. He, J. C. Shu, and M. S. Cao, "Tailoring rGO-NiFe2O4 hybrids to tune transport of electrons and ions for supercapacitor electrodes," *J. Alloys Compd.*, vol. 811, p. 152011, 2019, doi: 10.1016/j.jallcom.2019.152011.

[125] R. R. Chilwar, A. R. Chavan, M. K. Babrekar, and K. M. Jadhav, "Impact of trivalent metal ion substitution on structural, optical, magnetic and dielectric properties of Li0.5Fe2.5O4 thin films," *Phys. B Condens. Matter*, vol. 566, pp. 43–49, 2019, doi: 10.1016/j.physb.2019.04.031.

[126] P. Bandyopadhyay, G. Saeed, N. H. Kim, and J. H. Lee, "Zinc-nickel-cobalt oxide@NiMoO4 core-shell nanowire/nanosheet arrays for solid state asymmetric supercapacitors," *Chem. Eng. J.*, vol. 384, p. 123357, 2020, doi: 10.1016/j.cej.2019.123357.

[127] A. Shokri, S. F. Shayesteh, and K. Boustani, "The role of Co ion substitution in SnFe2O4 spinel ferrite nanoparticles: Study of structural, vibrational, magnetic and optical properties," *Ceram. Int.*, vol. 44, no. 18, pp. 22092–22101, 2018, doi: 10.1016/j.ceramint.2018.08.319.

[128] M. Chandel, D. Moitra, P. Makkar, H. Sinha, H. S. Hora, and N. N. Ghosh, "Synthesis of multifunctional CuFe2O4-reduced graphene oxide nanocomposite: An efficient magnetically separable catalyst as well as high performance supercapacitor and first-

principles calculations of its electronic structures," *RSC Adv.*, vol. 8, no. 49, pp. 27725–27739, 2018, doi: 10.1039/c8ra05393f.

[129] F. M. Ismail, M. Ramadan, A. M. Abdellah, I. Ismail, and N. K. Allam, "Mesoporous spinel manganese zinc ferrite for high-performance supercapacitors," *J. Electroanal. Chem.*, vol. 817, pp. 111–117, 2018, doi: 10.1016/j.jelechem.2018.04.002.

[130] B. Bashir *et al.*, "Copper substituted nickel ferrite nanoparticles anchored onto the graphene sheets as electrode materials for supercapacitors fabrication," *Ceram. Int.*, vol. 45, no. 6, pp. 6759–6766, 2019, doi: 10.1016/j.ceramint.2018.12.167.

[131] S. R. Bhongale, H. R. Ingawale, T. J. Shinde, and P. N. Vasambekar, "Effect of Nd3+ substitution on structural and magnetic properties of Mg–Cd ferrites synthesized by microwave sintering technique," *J. Rare Earths*, vol. 36, no. 4, pp. 390–397, 2018, doi: 10.1016/j.jre.2017.11.003.

[132] V. Vignesh, K. Subramani, M. Sathish, and R. Navamathavan, "Electrochemical investigation of manganese ferrites prepared via a facile synthesis route for supercapacitor applications," *Colloids Surfaces A Physicochem. Eng. Asp.*, vol. 538, no. August 2017, pp. 668–677, 2018, doi: 10.1016/j.colsurfa.2017.11.045.

[133] M. L. Aparna, A. N. Grace, P. Sathyanarayanan, and N. K. Sahu, "A comparative study on the supercapacitive behaviour of solvothermally prepared metal ferrite (MFe2O4, M = Fe, Co, Ni, Mn, Cu, Zn) nanoassemblies," *J. Alloys Compd.*, vol. 745, pp. 385–395, 2018, doi: 10.1016/j.jallcom.2018.02.127.

[134] B. Bashir *et al.*, "Copper doped manganese ferrites nanoparticles anchored on graphene nano-sheets for high performance energy storage applications," *J. Alloys Compd.*, vol. 695, pp. 881–887, 2017, doi: 10.1016/j.jallcom.2016.10.183.

[135] F. Shahzad *et al.*, "Electromagnetic interference shielding with 2D transition metal carbides," *MXenes From Discov. to Appl. Two-Dimensional Met. Carbides Nitrides*, pp. 933–947, 2023, doi: 10.1201/9781003306511-47.

[136] P. Thakur, R. Sharma, V. Sharma, and P. Sharma, "Structural and optical properties of Mn0.5Zn0.5Fe2O4 nano ferrites: Effect of sintering temperature," *Mater. Chem. Phys.*, vol. 193, pp. 285–289, 2017, doi: 10.1016/j.matchemphys.2017.02.043.

[137] M. A. Mousa, M. Khairy, and M. Shehab, "Nanostructured ferrite/graphene/polyaniline

using for supercapacitor to enhance the capacitive behavior," *J. Solid State Electrochem.*, vol. 21, no. 4, pp. 995–1005, 2017, doi: 10.1007/s10008-016-3446-6.

[138] K. Praveena, K. Sadhana, S. Matteppanavar, and H. L. Liu, "Effect of sintering temperature on the structural, dielectric and magnetic properties of Ni0.4Zn0.2Mn0.4Fe2O4 potential for radar absorbing," *J. Magn. Magn. Mater.*, vol. 423, pp. 343–352, 2017, doi: 10.1016/j.jmmm.2016.09.129.

[139] P. Liu *et al.*, "Effect of Mn substitution on the promoted formaldehyde oxidation over spinel ferrite: Catalyst characterization, performance and reaction mechanism," *Appl. Catal. B Environ.*, vol. 182, pp. 476–484, 2016, doi: 10.1016/j.apcatb.2015.09.055.

[140] R. Tholkappiyan, A. N. Naveen, S. Sumithra, and K. Vishista, "Investigation on spinel MnCo2O4 electrode material prepared via controlled and uncontrolled synthesis route for supercapacitor application," *J. Mater. Sci.*, vol. 50, no. 17, pp. 5833–5843, 2015, doi: 10.1007/s10853-015-9132-8.

[141] H. Bahiraei, M. Z. Shoushtari, K. Gheisari, and C. K. Ong, "The effect of sintering temperature on the electromagnetic properties of nanocrystalline MgCuZn ferrite prepared by sol-gel auto combustion method," *Mater. Lett.*, vol. 122, pp. 129–132, 2014, doi: 10.1016/j.matlet.2014.02.027.

[142] F. Cai, Y. Kang, H. Chen, M. Chen, and Q. Li, "Hierarchical CNT@NiCo2O4 core-shell hybrid nanostructure for high-performance supercapacitors," *J. Mater. Chem. A*, vol. 2, no. 29, pp. 11509–11515, 2014, doi: 10.1039/c4ta01235f.

[143] R. P. Patil, S. D. Delekar, D. R. Mane, and P. P. Hankare, "Synthesis, structural and magnetic properties of different metal ion substituted nanocrystalline zinc ferrite," *Results Phys.*, vol. 3, no. 3, pp. 129–133, 2013, doi: 10.1016/j.rinp.2013.08.002.

[144] M. Rahimi, P. Kameli, M. Ranjbar, and H. Salamati, "The effect of sintering temperature on evolution of structural and magnetic properties of nanostructured Ni0.3Zn0.7Fe 2O4 ferrite," *J. Nanoparticle Res.*, vol. 15, no. 9, 2013, doi: 10.1007/s11051-013-1865-1.

[145] V. S. Kumbhar, A. D. Jagadale, N. M. Shinde, and C. D. Lokhande, "Chemical synthesis of spinel cobalt ferrite (CoFe 2 O 4) nano-flakes for supercapacitor application," *Appl. Surf. Sci.*, vol. 259, pp. 39–43, 2012, doi: 10.1016/j.apsusc.2012.06.034.

[146] M. F. Al-Hilli, S. Li, and K. S. Kassim, "Gadolinium substitution and sintering

temperature dependent electronic properties of Li-Ni ferrite," *Mater. Chem. Phys.*, vol. 128, no. 1–2, pp. 127–132, 2011, doi: 10.1016/j.matchemphys.2011.02.064.

[147] H. Su, H. Zhang, X. Tang, B. Liu, and Z. Zhong, "Study on low-temperature sintered NiCuZn and MgCuZn spinel ferrites," *J. Alloys Compd.*, vol. 475, no. 1–2, pp. 683–685, 2009, doi: 10.1016/j.jallcom.2008.07.112.

[148] S. D. Bhame and P. A. Joy, "Effect of sintering conditions and microstructure on the magnetostrictive properties of cobalt ferrite," *J. Am. Ceram. Soc.*, vol. 91, no. 6, pp. 1976–1980, 2008, doi: 10.1111/j.1551-2916.2008.02367.x.

[149] A. S. Gaikwad *et al.*, "Magneto-electric coupling and improved dielectric constant of BaTiO3 and Fe-rich (Co0.7Fe2.3O4) ferrite nano-composites," *J. Magn. Magn. Mater.*, vol. 465, no. March, pp. 508–514, 2018, doi: 10.1016/j.jmmm.2018.06.036.

[150] S. V. Bhandare *et al.*, "Effect of Mg-substitution in Co–Ni-Ferrites: Cation distribution and magnetic properties," *Mater. Chem. Phys.*, vol. 251, p. 123081, 2020, doi: 10.1016/j.matchemphys.2020.123081.

[151] J. Peng, M. Hojamberdiev, Y. Xu, B. Cao, J. Wang, and H. Wu, "Hydrothermal synthesis and magnetic properties of gadolinium-doped CoFe2O4 nanoparticles," *J. Magn. Magn. Mater.*, vol. 323, no. 1, pp. 133–137, 2011, doi: 10.1016/j.jmmm.2010.08.048.

[152] R. R. Kanna *et al.*, "Synthesis of dysprosium/Mn–Cu ferrite binary nanocomposite: Analysis of structural, morphological, dielectric, and optomagnetic properties," *Ceram. Int.*, vol. 46, no. 9, pp. 13695–13703, 2020, doi: 10.1016/j.ceramint.2020.02.157.

[153] S. Kavitha and M. Kurian, "Effect of zirconium doping in the microstructure, magnetic and dielectric properties of cobalt ferrite nanoparticles," *J. Alloys Compd.*, vol. 799, pp. 147–159, 2019, doi: 10.1016/j.jallcom.2019.05.183.

[154] U. G. Akpan and B. H. Hameed, "The advancements in sol-gel method of doped-TiO2 photocatalysts," *Appl. Catal. A Gen.*, vol. 375, no. 1, pp. 1–11, 2010, doi: 10.1016/j.apcata.2009.12.023.

[155] P. Nyamukamba, O. Okoh, H. Mungondori, R. Taziwa, and S. Zinya, "Synthetic Methods for Titanium Dioxide Nanoparticles: A Review," *Titan. Dioxide - Mater. a Sustain. Environ.*, no. June 2018, 2018, doi: 10.5772/intechopen.75425.

[156] I. Mohammed, J. Mohammed, and A. K. Srivastava, “Enhanced EMI shielding effectiveness of Ba1.8Sr0.2Zn2Fe11.9Dy0.1O22/CaTiO3/Ti3C2Tx-MXene composite,” *Phys. B Condens. Matter*, vol. 668, no. December 2022, p. 415240, 2023, doi: 10.1016/j.physb.2023.415240.

[157] S. V. Borisov and N. V. Podberezskaya, “X-ray diffraction analysis: A brief history and achievements of the first century,” *J. Struct. Chem.*, vol. 53, pp. 1–3, 2012, doi: 10.1134/S0022476612070013.

[158] A. A. Bunaciu, E. gabriela Udriştioiu, and H. Y. Aboul-Enein, “X-Ray Diffraction: Instrumentation and Applications,” *Crit. Rev. Anal. Chem.*, vol. 45, no. 4, pp. 289–299, 2015, doi: 10.1080/10408347.2014.949616.

[159] M. G. Lagally, “5. Diffraction Techniques,” *Methods Exp. Phys.*, vol. 22, no. C, pp. 237–298, 1985, doi: 10.1016/S0076-695X(08)60319-1.

[160] W. Harris and G. N. White, “X-ray diffraction techniques for soil mineral identification,” *Methods Soil Anal. Part 5 Mineral. Methods*, vol. 5, no. 5, pp. 81–115, 2015, doi: 10.2136/sssabookser5.5.c4.

[161] T. Ryan, “The development of instrumentation for thin-film X-ray diffraction,” *J. Chem. Educ.*, vol. 78, no. 5, pp. 613–616, 2001, doi: 10.1021/ed078p613.

[162] D. Cozzolino, “FTIR spectroscopy and water quality,” in *Spectroscopy and Machine Learning for Water Quality Analysis*, vol. 2002, no. June, IOP Publishing, 2021. doi: 10.1088/978-0-7503-3047-3ch1.

[163] M. Penchal Reddy, R. A. Shakoor, A. M. A. Mohamed, M. Gupta, and Q. Huang, “Effect of sintering temperature on the structural and magnetic properties of MgFe2O4 ceramics prepared by spark plasma sintering,” *Ceram. Int.*, vol. 42, no. 3, pp. 4221–4227, 2016, doi: 10.1016/j.ceramint.2015.11.097.

[164] S. Prati, E. Joseph, G. Sciutto, and R. Mazzeo, “New advances in the application of FTIR microscopy and spectroscopy for the characterization of artistic materials,” *Acc. Chem. Res.*, vol. 43, no. 6, pp. 792–801, 2010, doi: 10.1021/ar900274f.

[165] M. D. Ohi, “<scp>EM</scp> Analysis of Protein Structure,” in *Encyclopedia of Life Sciences*, no. 1958, Wiley, 2009, pp. 662–666. doi: 10.1002/9780470015902.a0021885.

[166] S. D. Sawant, A. A. Baravkar, and R. N. Kale, “FT-IR spectroscopy: Principle, technique

and mathematics," *Int. J. Pharma Bio Sci.*, vol. 2, no. 1, pp. 513–519, 2011.

[167] L. Armelao *et al.*, "Introduction to XPS Studies of Metal and Metal-oxide Nanosystems," *Surf. Sci. Spectra*, vol. 10, no. 1, pp. 137–142, 2003, doi: 10.1116/11.20050199.

[168] M. Aziz and A. F. Ismail, *X-Ray Photoelectron Spectroscopy (XPS)*. Elsevier B.V., 2017. doi: 10.1016/B978-0-444-63776-5.00005-X.

[169] L. Rosenberger, R. Baird, E. McCullen, G. Auner, and G. Shreve, "XPS analysis of aluminum nitride films deposited by plasma source molecular beam epitaxy," *Surf. Interface Anal.*, vol. 40, no. 9, pp. 1254–1261, 2008, doi: 10.1002/sia.2874.

[170] P. S. Bagus, E. S. Ilton, and C. J. Nelin, "The interpretation of XPS spectra: Insights into materials properties," *Surf. Sci. Rep.*, vol. 68, no. 2, pp. 273–304, 2013, doi: 10.1016/j.surfrep.2013.03.001.

[171] S. L. Erlandsen, C. Frethem, and Y. Chen, "Field emission scanning electron microscopy (FESEM) entering the 21st century: Nanometer resolution and molecular topography of cell structure," *J. Histotechnol.*, vol. 23, no. 3, pp. 249–259, 2000, doi: 10.1179/his.2000.23.3.249.

[172] T. Shiraiwa and N. Fujino, "Quantitative electron probe microanalysis of oxygen," *Jpn. J. Appl. Phys.*, vol. 9, no. 8, pp. 976–982, 1970, doi: 10.1143/JJAP.9.976.

[173] D. C. Wijeyesekera, M. H. Ho, X. Bai, and I. Bakar, "Strength and Stiffness Development in Soft Soils: A FESEM aided Soil Microstructure Viewpoint," *IOP Conf. Ser. Mater. Sci. Eng.*, vol. 136, no. 1, 2016, doi: 10.1088/1757-899X/136/1/012041.

[174] M. Abd Mutalib, M. A. Rahman, M. H. D. Othman, A. F. Ismail, and J. Jaafar, *Scanning Electron Microscopy (SEM) and Energy-Dispersive X-Ray (EDX) Spectroscopy*. Elsevier B.V., 2017. doi: 10.1016/B978-0-444-63776-5.00009-7.

[175] C. Cardell and I. Guerra, "An overview of emerging hyphenated SEM-EDX and Raman spectroscopy systems: Applications in life, environmental and materials sciences," *TrAC - Trends Anal. Chem.*, vol. 77, pp. 156–166, 2016, doi: 10.1016/j.trac.2015.12.001.

[176] M. Nuspl, W. Wegscheider, J. Angeli, W. Posch, and M. Mayr, "Qualitative and quantitative determination of micro-inclusions by automated SEM/EDX analysis," *Anal.*

Bioanal. Chem., vol. 379, no. 4, pp. 640–645, 2004, doi: 10.1007/s00216-004-2528-y.

[177] H. Takagi, H. Shima, T. Ui, and E. Asada, "A fundamental parameter method for measurement of the thickness of pure element films by an EDX technique with a proportional detector," *X-Ray Spectrom.*, vol. 13, no. 4, pp. 182–186, 1984, doi: 10.1002/xrs.1300130412.

[178] C. Angeles-Chavez, P. Salas, L. A. Daz-Torres, E. De La Rosa, R. Esparza, and R. Perez, "Structural and chemical characterization of Yb2O 3-ZrO2 system by HAADF-STEM and HRTEM," *Microsc. Microanal.*, vol. 15, no. 1, pp. 46–53, 2009, doi: 10.1017/S1431927609090047.

[179] R. L. Vander Wal, A. J. Tomasek, M. I. Pamphlet, C. D. Taylor, and W. K. Thompson, "Analysis of HRTEM images for carbon nanostructure quantification," *J. Nanoparticle Res.*, vol. 6, no. 6, pp. 555–568, 2004, doi: 10.1007/s11051-004-3724-6.

[180] H.-M. Kim, M. H. Lee, H.-S. Lee, J.-S. Wi, K. Lim, and K.-B. Kim, "Method of improving the quality of nanopatterning in atomic image projection electron-beam lithography," *J. Vac. Sci. Technol. B Microelectron. Nanom. Struct. Process. Meas. Phenom.*, vol. 27, no. 6, pp. 2553–2557, 2009, doi: 10.1116/1.3250262.

[181] W. Burgei, M. J. Pechan, and H. Jaeger, "A simple vibrating sample magnetometer for use in a materials physics course," *Am. J. Phys.*, vol. 71, no. 8, pp. 825–828, 2003, doi: 10.1119/1.1572149.

[182] A. Niazi, J. M. Islamia, P. Poddar, and A. K. Rastogi, "A precision, low-cost vibrating sample magnetometer," no. July, 2000.

[183] J. Lindemuth, J. Krause, and B. Dodrill, "Finite sample size effects on the calibration of vibrating sample magnetometer," *IEEE Trans. Magn.*, vol. 37, no. 4 I, pp. 2752–2754, 2001, doi: 10.1109/20.951296.

[184] L. Avilés-Felix, E. N. Monteblanco, and A. Gutarra, "Optimización de un magnetómetro de muestra vibrante para un curso de física de laboratorio," *Tecnia*, vol. 26, no. 2, p. 27, 2016, doi: 10.21754/tecnia.v26i2.55.

[185] D. Barrettino, "A low-cost, low-power, 10MHz multifrequency impedance analyzer," *I2MTC 2018 - 2018 IEEE Int. Instrum. Meas. Technol. Conf. Discov. New Horizons Instrum. Meas. Proc.*, pp. 1–6, 2018, doi: 10.1109/I2MTC.2018.8409789.

[186] Q. Meyer, S. Barass, O. Curnick, T. Reisch, and D. J. L. Brett, “A multichannel frequency response analyser for impedance spectroscopy on power sources,” *J. Electrochem. Sci. Eng.*, vol. 3, no. 3, pp. 107–114, 2013, doi: 10.5599/jese.2013.0033.

[187] J. McAlorum, C. Vlachakis, and M. Perry, “A low-cost electrical impedance analyser for interrogating self-sensing cement repairs,” *Conf. Rec. - IEEE Instrum. Meas. Technol. Conf.*, vol. 2021-May, pp. 1–6, 2021, doi: 10.1109/I2MTC50364.2021.9459871.

[188] B. W. C. Au, K. Y. Chan, W. L. Pang, C. L. Lee, S. K. Wong, and A. H. Mustafa, “Effect of bias voltage on the electrochromic properties of WO3 films,” *J. Phys. Conf. Ser.*, vol. 1349, no. 1, 2019, doi: 10.1088/1742-6596/1349/1/012040.

[189] M. H. F. Taha, H. Ashraf, and W. Caesarendra, “A brief description of cyclic voltammetry transducer-based non-enzymatic glucose biosensor using synthesized graphene electrodes,” *Appl. Syst. Innov.*, vol. 3, no. 3, pp. 1–33, 2020, doi: 10.3390/asi3030032.

[190] M. M. Vadiyar *et al.*, “Mechanochemical growth of a porous ZnFe2O4 nano-flake thin film as an electrode for supercapacitor application,” *RSC Adv.*, vol. 5, no. 57, pp. 45935–45942, 2015, doi: 10.1039/c5ra07588b.

[191] M. Mandal *et al.*, “Simple and Cost-Effective Synthesis of Activated Carbon Anchored by Functionalized Multiwalled Carbon Nanotubes for High-Performance Supercapacitor Electrodes with High Energy Density and Power Density,” *J. Electron. Mater.*, vol. 50, no. 5, pp. 2879–2889, 2021, doi: 10.1007/s11664-021-08796-w.

[192] M. D. Stoller and R. S. Ruoff, “Best practice methods for determining an electrode material’s performance for ultracapacitors,” *Energy Environ. Sci.*, vol. 3, no. 9, pp. 1294–1301, 2010, doi: 10.1039/c0ee00074d.

[193] L. M. Da Silva *et al.*, “Reviewing the fundamentals of supercapacitors and the difficulties involving the analysis of the electrochemical findings obtained for porous electrode materials,” *Energy Storage Mater.*, vol. 27, pp. 555–590, 2020, doi: 10.1016/j.ensm.2019.12.015.

[194] M. R. Islam, S. Afroj, K. S. Novoselov, and N. Karim, “Smart Electronic Textile-Based Wearable Supercapacitors,” *Adv. Sci.*, vol. 9, no. 31, 2022, doi:

10.1002/advs.202203856.

[195] P. S. Nnamchi and C. S. Obayi, *Electrochemical characterization of nanomaterials*. Elsevier Ltd., 2018. doi: 10.1016/B978-0-08-101973-3.00004-3.

[196] Y. Li, S. M. Chen, M. A. Ali, and F. M. A. AlHemaid, "Biosynthesis and electrochemical characterization of silver nanoparticles from leaf extract of adenium obesum and its application to antibacterial effect," *Int. J. Electrochem. Sci.*, vol. 8, no. 2, pp. 2691–2701, 2013, doi: 10.1016/s1452-3981(23)14341-0.

[197] V. Ganesh, S. Pitchumani, and V. Lakshminarayanan, "New symmetric and asymmetric supercapacitors based on high surface area porous nickel and activated carbon," *J. Power Sources*, vol. 158, no. 2 SPEC. ISS., pp. 1523–1532, 2006, doi: 10.1016/j.jpowsour.2005.10.090.

[198] J. Yang, Y. Liu, S. Liu, L. Li, C. Zhang, and T. Liu, "Conducting polymer composites: Material synthesis and applications in electrochemical capacitive energy storage," *Mater. Chem. Front.*, vol. 1, no. 2, pp. 251–268, 2017, doi: 10.1039/c6qm00150e.

[199] D. S. Mathew and R. S. Juang, "An overview of the structure and magnetism of spinel ferrite nanoparticles and their synthesis in microemulsions," *Chem. Eng. J.*, vol. 129, no. 1–3, pp. 51–65, 2007, doi: 10.1016/j.cej.2006.11.001.

[200] E. M. Masoud, "Improved initial discharge capacity of nanostructured Ni-Co spinel ferrite as anode material in lithium ion batteries," *Solid State Ionics*, vol. 253, pp. 247–252, 2013, doi: 10.1016/j.ssi.2013.10.017.

[201] F. J. Günter, J. B. Habedank, D. Schreiner, T. Neuwirth, R. Gilles, and G. Reinhart, "Introduction to Electrochemical Impedance Spectroscopy as a Measurement Method for the Wetting Degree of Lithium-Ion Cells," *J. Electrochem. Soc.*, vol. 165, no. 14, pp. A3249–A3256, 2018, doi: 10.1149/2.0081814jes.

[202] M. Arulepp *et al.*, "The advanced carbide-derived carbon based supercapacitor," *J. Power Sources*, vol. 162, no. 2 SPEC. ISS., pp. 1460–1466, 2006, doi: 10.1016/j.jpowsour.2006.08.014.

[203] F. Rafik, H. Gualous, R. Gallay, A. Crausaz, and A. Berthon, "Frequency, thermal and voltage supercapacitor characterization and modeling," *J. Power Sources*, vol. 165, no. 2, pp. 928–934, 2007, doi: 10.1016/j.jpowsour.2006.12.021.

[204] S. Balsure, V. More, S. Kadam, R. Kadam, and A. Kadam, “Synthesis, Structural, Magnetic, Dielectric and Optical Properties of Co Doped Cr-Zn Oxide Nanoparticles for Spintronic Devices,” *Eng. Sci.*, vol. 21, pp. 1–9, 2023, doi: 10.30919/es8d774.

[205] I. Sharifi and H. Shokrollahi, “Structural, magnetic and Mössbauer evaluation of Mn substituted Co-Zn ferrite nanoparticles synthesized by co-precipitation,” *J. Magn. Magn. Mater.*, vol. 334, pp. 36–40, 2013, doi: 10.1016/j.jmmm.2013.01.021.

[206] P. P. Hankare, S. D. Jadhav, U. B. Sankpal, S. S. Chavan, K. J. Waghmare, and B. K. Chougule, “Synthesis, characterization and effect of sintering temperature on magnetic properties of MgNi ferrite prepared by co-precipitation method,” *J. Alloys Compd.*, vol. 475, no. 1–2, pp. 926–929, 2009, doi: 10.1016/j.jallcom.2008.08.082.

[207] A. Sharma, S. K. Godara, and A. K. Srivastava, “Influence of composition variation on structural, magnetic and dielectric properties of Gd3Fe5O12(x)/MgFe2O4(1−x) composite,” *Indian J. Phys.*, vol. 12, no. x, 2022, doi: 10.1007/s12648-022-02365-5.

[208] R. P. Patil, P. P. Hankare, K. M. Garadkar, and R. Sasikala, “Effect of sintering temperature on structural, magnetic properties of lithium chromium ferrite,” *J. Alloys Compd.*, vol. 523, pp. 66–71, 2012, doi: 10.1016/j.jallcom.2012.01.025.

[209] A. A. Birajdar *et al.*, “Role of Cr3+ ions on the microstructure development, and magnetic phase evolution of Ni0.7Zn0.3Fe2O 4 ferrite nanoparticles,” *J. Alloys Compd.*, vol. 512, no. 1, pp. 316–322, 2012, doi: 10.1016/j.jallcom.2011.09.087.

[210] A. Ali *et al.*, “Effect of In on superparamagnetic CoInxFe2-xO4 (x = 0–0.15) synthesized through hydrothermal method,” *Results Phys.*, vol. 25, no. February, p. 104251, 2021, doi: 10.1016/j.rinp.2021.104251.

[211] T. Tekou *et al.*, “Crystal-structure analysis , Raman spectroscopy , dielectric measurements , magnetic and optical properties of Cr 3 + – Ni 2 + -substituted Co 2 Y-type barium hexaferrites,” *Mater. Res. Bull.*, vol. 145, p. 111564, 2022.

[212] S. S. Yattinahalli, S. B. Kapatkar, and S. N. Mathad, “Structural and Mechanical Properties of a Nano Ferrite,” *Adv. Sci. Focus*, vol. 2, no. 1, pp. 42–46, 2014, doi: 10.1166/asfo.2014.1079.

[213] D. V. Kurmude, R. S. Barkule, A. V. Raut, D. R. Shengule, and K. M. Jadhav, “X-ray diffraction and cation distribution studies in zinc-substituted nickel ferrite

nanoparticles," *J. Supercond. Nov. Magn.*, vol. 27, no. 2, pp. 547–553, 2014, doi: 10.1007/s10948-013-2305-2.

[214] R. Jabbar, S. H. Sabeeh, and A. M. Hameed, "Structural, dielectric and magnetic properties of Mn+2 doped cobalt ferrite nanoparticles," *J. Magn. Magn. Mater.*, vol. 494, no. August 2019, p. 165726, 2020, doi: 10.1016/j.jmmm.2019.165726.

[215] A. Amirabadizadeh and T. Amirabadi, "Effect of Substitution of Al for Fe on Magnetic Properties and Particle Size of Ni-Co Nanoferrite," *World J. Condens. Matter Phys.*, vol. 03, no. 03, pp. 131–135, 2013, doi: 10.4236/wjcmp.2013.33021.

[216] R. Sharma, P. Thakur, P. Sharma, and V. Sharma, "Ferrimagnetic Ni2+doped Mg-Zn spinel ferrite nanoparticles for high density information storage," *J. Alloys Compd.*, vol. 704, pp. 7–17, 2017, doi: 10.1016/j.jallcom.2017.02.021.

[217] M. Bhuvaneswari, S. Sendhilnathan, M. Kumar, R. Tamilarasan, and N. V. Giridharan, "Synthesis, investigation on structural and electrical properties of cobalt doped Mn-Zn ferrite nanocrystalline powders," *Mater. Sci. Pol.*, vol. 34, no. 2, pp. 344–353, 2016, doi: 10.1515/msp-2016-0046.

[218] S. V. Bhandare *et al.*, "Effect of Mg-substitution in Co–Ni-Ferrites: Cation distribution and magnetic properties," *Mater. Chem. Phys.*, vol. 251, no. March, p. 123081, 2020, doi: 10.1016/j.matchemphys.2020.123081.

[219] M. Augustin and T. Balu, "Estimation of Lattice Stress and Strain in Zinc and Manganese Ferrite Nanoparticles by Williamson-Hall and Size-Strain Plot Methods," *Int. J. Nanosci.*, vol. 16, no. 3, pp. 1–7, 2017, doi: 10.1142/S0219581X16500356.

[220] M. N. Akhtar and M. A. Khan, "Effect of rare earth doping on the structural and magnetic features of nanocrystalline spinel ferrites prepared via sol gel route," *J. Magn. Magn. Mater.*, vol. 460, pp. 268–277, 2018, doi: 10.1016/j.jmmm.2018.03.069.

[221] T. M. Hammad, S. Kuhn, A. A. Amsha, N. K. Hejazy, and R. Hempelmann, "Comprehensive Study of the Impact of Mg2+ Doping on Optical, Structural, and Magnetic Properties of Copper Nanoferrites," *J. Supercond. Nov. Magn.*, vol. 33, no. 10, pp. 3065–3075, 2020, doi: 10.1007/s10948-020-05559-2.

[222] A. V. Raut, R. S. Barkule, D. R. Shengule, and K. M. Jadhav, "Synthesis, structural investigation and magnetic properties of Zn 2+ substituted cobalt ferrite nanoparticles

prepared by the sol-gel auto-combustion technique," *J. Magn. Magn. Mater.*, vol. 358–359, pp. 87–92, 2014, doi: 10.1016/j.jmmm.2014.01.039.

[223] K. B. Modi, M. C. Chhantbar, and H. H. Joshi, "Study of elastic behaviour of magnesium ferri aluminates," *Ceram. Int.*, vol. 32, no. 2, pp. 111–114, 2006, doi: 10.1016/j.ceramint.2005.01.005.

[224] G. Dhillon, N. Kumar, M. Chitkara, and I. S. Sandhu, "Effect of A-site substitution and calcination temperature in Fe3O4 spinel ferrites," *J. Mater. Sci. Mater. Electron.*, vol. 31, no. 21, pp. 18903–18912, 2020, doi: 10.1007/s10854-020-04427-y.

[225] S. Hasan and B. Azhdar, "Synthesis of Nickel-Zinc Ferrite Nanoparticles by the Sol-Gel Auto-Combustion Method: Study of Crystal Structural, Cation Distribution, and Magnetic Properties," *Adv. Condens. Matter Phys.*, vol. 2022, 2022, doi: 10.1155/2022/4603855.

[226] S. Kavitha and M. Kurian, "Effect of zirconium doping in the microstructure, magnetic and dielectric properties of cobalt ferrite nanoparticles," *J. Alloys Compd.*, vol. 799, pp. 147–159, 2019, doi: 10.1016/j.jallcom.2019.05.183.

[227] R. Vishwarup and S. N. Mathad, "Facile Synthesis of Nano Mg-Co Ferrites (x=0.15, 0.20, 0.25, 0.30, 0.35, and 0.40) via Coprecipitation Route: Structural Characterization," *Mater. Int.*, vol. 2, no. 4, pp. 0471–0476, 2020, [Online]. Available: https://materials.international/wp-content/uploads/2020/10/2668572824.471476.pdf

[228] A. A. H. El-Bassuony and H. K. Abdelsalam, "Synthesis, characterization, magnetic and antimicrobial properties of silver chromite nanoparticles," *J. Mater. Sci. Mater. Electron.*, vol. 31, no. 4, pp. 3662–3673, 2020, doi: 10.1007/s10854-020-02924-8.

[229] H. Fakhr Nabavi, M. Aliofkhazraei, M. Hasanpoor, and A. Seyfoori, "Combustion and Coprecipitation Synthesis of Co–Zn Ferrite Nanoparticles: Comparison of Structure and Magnetic Properties," *Int. J. Appl. Ceram. Technol.*, vol. 13, no. 6, pp. 1112–1118, 2016, doi: 10.1111/ijac.12580.

[230] T. Tchouank Tekou Carol, J. Mohammed, H. Y. Hafeez, B. H. Bhat, S. K. Godara, and A. K. Srivastava, "Structural , Dielectric , and Magneto-Optical Properties of Al-Cr Substituted M-Type Barium Hexaferrite," *Phys. Status Solidi*, vol. 216, no. 16, p. 1800928, 2019, doi: 10.1002/pssa.201800928.

[231] S. Kumar Godara *et al.*, "Effect on Magnetic, morphological and structural properties of Zn2+-Zr4+ substituted SrM for permanent magnet based appliances," *J. Magn. Magn. Mater.*, vol. 560, no. May, p. 169626, 2022, doi: 10.1016/j.jmmm.2022.169626.

[232] K. Krieble, T. Schaeffer, J. A. Paulsen, A. P. Ring, C. C. H. Lo, and J. E. Snyder, "Mössbauer spectroscopy investigation of Mn-substituted Co-ferrite (Co Mn x Fe 2-x O 4)," *J. Appl. Phys.*, vol. 97, no. 10, pp. 2003–2006, 2005, doi: 10.1063/1.1846271.

[233] Hirthna and S. Sendhilnathan, "Enhancement in dielectric and magnetic properties of Mg2+ substituted highly porous super paramagnetic nickel ferrite nanoparticles with Williamson-Hall plots mechanistic view," *Ceram. Int.*, vol. 43, no. 17, pp. 15447–15453, 2017, doi: 10.1016/j.ceramint.2017.08.090.

[234] V. Verma, M. Kaur, and J. M. Greneche, "Tailored structural, optical and magnetic properties of ternary nanohybrid Mn 0.4 Co 0.6-x Cu x Fe 2 O 4 (x= 0, 0.2, 0.4, 0.6) spinel ferrites," *Ceram. Int.*, vol. 45, no. 8, pp. 10865–10875, 2019, doi: 10.1016/j.ceramint.2019.02.164.

[235] P. Chavan, L. R. Naik, P. B. Belavi, G. Chavan, C. K. Ramesha, and R. K. Kotnala, "Studies on Electrical and Magnetic Properties of Mg-Substituted Nickel Ferrites," *J. Electron. Mater.*, vol. 46, no. 1, pp. 188–198, 2017, doi: 10.1007/s11664-016-4886-6.

[236] R. S. Yadav *et al.*, "Structural, magnetic, dielectric, and electrical properties of NiFe2O4 spinel ferrite nanoparticles prepared by honey-mediated sol-gel combustion," *J. Phys. Chem. Solids*, vol. 107, pp. 150–161, 2017, doi: 10.1016/j.jpcs.2017.04.004.

[237] J. Sharma, N. Sharma, J. Parashar, V. K. Saxena, D. Bhatnagar, and K. B. Sharma, "Dielectric properties of nanocrystalline Co-Mg ferrites," *J. Alloys Compd.*, vol. 649, no. 108, pp. 362–367, 2015, doi: 10.1016/j.jallcom.2015.07.103.

[238] S. Aman, M. B. Tahir, and N. Ahmad, "The enhanced electrical and dielectric properties of cobalt-based spinel ferrites for high-frequency applications," *J. Mater. Sci. Mater. Electron.*, vol. 32, no. 17, pp. 22440–22449, 2021, doi: 10.1007/s10854-021-06730-8.

[239] C. V. Ramana, Y. D. Kolekar, K. Kamala Bharathi, B. Sinha, and K. Ghosh, "Correlation between structural, magnetic, and dielectric properties of manganese substituted cobalt ferrite," *J. Appl. Phys.*, vol. 114, no. 18, 2013, doi: 10.1063/1.4827416.

[240] A. Sharma, S. K. Godara, and A. K. Srivastava, “Influence of composition variation on structural, magnetic and dielectric properties of Gd3Fe5O12(x)/MgFe2O4(1−x) composite,” *Indian J. Phys.*, vol. 96, no. 14, pp. 4173–4184, Dec. 2022, doi: 10.1007/s12648-022-02365-5.

[241] K. P. Padmasree, D. K. Kanchan, and A. R. Kulkarni, “Impedance and Modulus studies of the solid electrolyte system 20CdI 2-80[xAg2O-y(0.7V2O5-0.3B 2O3)], where 1 ≤x/y ≤ 3,” *Solid State Ionics*, vol. 177, no. 5–6, pp. 475–482, 2006, doi: 10.1016/j.ssi.2005.12.019.

[242] N. Murali *et al.*, “Effect of Al substitution on the structural and magnetic properties of Co-Zn ferrites,” *Phys. B Condens. Matter*, vol. 522, no. July, pp. 1–6, 2017, doi: 10.1016/j.physb.2017.07.043.

[243] S. Kumar *et al.*, “Journal of Physics and Chemistry of Solids Optimization of structure-property relationships in nickel ferrite nanoparticles annealed at different temperature,” *J. Phys. Chem. Solids*, vol. 151, no. December 2020, p. 109928, 2021, doi: 10.1016/j.jpcs.2020.109928.

[244] K. V Zipare, S. S. Bandgar, and G. S. Shahane, “Effect of Dy-substitution on structural and magnetic properties of Mn e Zn ferrite nanoparticles *,” *J. Rare Earths*, vol. 36, no. 1, pp. 86–94, 2018, doi: 10.1016/j.jre.2017.06.011.

[245] S. Debnath, K. Deb, B. Saha, and R. Das, “Journal of Physics and Chemistry of Solids X-ray di ff raction analysis for the determination of elastic properties of zinc- with the determination of ionic radii , bond lengths , and hopping lengths,” *J. Phys. Chem. Solids*, vol. 134, no. July 2018, pp. 105–114, 2019, doi: 10.1016/j.jpcs.2019.05.047.

[246] J. L. Gunjakar, A. M. More, K. V. Gurav, and C. D. Lokhande, “Chemical synthesis of spinel nickel ferrite (NiFe 2 O 4) nano-sheets,” *Appl. Surf. Sci.*, vol. 254, no. 18, pp. 5844–5848, 2008, doi: 10.1016/j.apsusc.2008.03.065.

[247] A. Gadkari, T. Shinde, and P. Vasambekar, “Influence of rare-earth ions on structural and magnetic properties of CdFe2O4 ferrites,” *Rare Met.*, vol. 29, no. 2, pp. 168–173, 2010, doi: 10.1007/s12598-010-0029-z.

[248] M. Abdullah-Al-Mamun *et al.*, “Effect of Er substitution on the magnetic, Mössbauer spectroscopy and dielectric properties of CoFe2−xErxO4 (x = 0.00, 0.01, 0.03, 0.05)

nanoparticles," *Results Phys.*, vol. 29, 2021, doi: 10.1016/j.rinp.2021.104698.

[249] U. Naresh, R. J. Kumar, and K. C. B. Naidu, "Hydrothermal synthesis of barium copper ferrite nanoparticles: Nanofiber formation, optical, and magnetic properties," *Mater. Chem. Phys.*, vol. 236, p. 121807, 2019, doi: 10.1016/j.matchemphys.2019.121807.

[250] U. K. Wadne *et al.*, "Enhanced multiferroic effect in multi-phased Eu substituted Bi–Fe–Mn perovskite oxides," *Ceram. Int.*, vol. 49, no. 5, pp. 8132–8139, 2023, doi: 10.1016/j.ceramint.2022.10.336.

[251] R. H. Kadam *et al.*, "A thorough Investigation of Rare-Earth Dy3+ Substituted Cobalt-Chromium Ferrite and Its Magnetoelectric Nanocomposite," *Nanomaterials*, vol. 13, no. 7, 2023, doi: 10.3390/nano13071165.

[252] M. S. I. Sarker, M. Yeasmin, M. A. Al-Mamun, S. M. Hoque, and M. K. R. Khan, "Influence of Gd content on the structural, Raman spectroscopic and magnetic properties of CoFe2O4 nanoparticles synthesized by sol-gel route," *Ceram. Int.*, vol. 48, no. 22, pp. 33323–33331, 2022, doi: 10.1016/j.ceramint.2022.07.275.

[253] M. S. Shah, K. Ali, I. Ali, A. Mahmood, S. M. Ramay, and M. T. Farid, "Structural and magnetic properties of praseodymium substituted barium-based spinel ferrites," *Mater. Res. Bull.*, vol. 98, no. August 2017, pp. 77–82, 2018, doi: 10.1016/j.materresbull.2017.09.063.

[254] Y. Köseoğlu, F. Alan, M. Tan, R. Yilgin, and M. Öztürk, "Low temperature hydrothermal synthesis and characterization of Mn doped cobalt ferrite nanoparticles," *Ceram. Int.*, vol. 38, no. 5, pp. 3625–3634, 2012, doi: 10.1016/j.ceramint.2012.01.001.

[255] M. Arshad *et al.*, "Structural and magnetic properties variation of manganese ferrites via Co-Ni substitution," *J. Magn. Magn. Mater.*, vol. 474, pp. 98–103, 2019, doi: 10.1016/j.jmmm.2018.10.141.

[256] M. T. Farid, I. Ahmad, and S. Aman, "Characterization of nickel based spinel ferrites with small substitution of praseodymium," *J. Chem. Soc. Pakistan*, vol. 35, no. 3, pp. 793–799, 2013.

[257] L. Gama, A. P. Diniz, A. C. F. M. Costa, S. M. Rezende, A. Azevedo, and D. R. Cornejo, "Magnetic properties of nanocrystalline Ni-Zn ferrites doped with samarium," *Phys. B Condens. Matter*, vol. 384, no. 1–2, pp. 97–99, 2006, doi: 10.1016/j.physb.2006.05.161.

[258] K. Raju, G. Venkataiah, and D. H. Yoon, “Effect of Zn substitution on the structural and magnetic properties of Ni-Co ferrites,” *Ceram. Int.*, vol. 40, no. 7 PART A, pp. 9337–9344, 2014, doi: 10.1016/j.ceramint.2014.01.157.

[259] A. Munir, F. Ahmed, M. Saqib, and M. Anis-ur-Rehman, “Partial correlation of electrical and magnetic properties of Nd substituted Ni-Zn nanoferrites,” *J. Magn. Magn. Mater.*, vol. 397, no. August, pp. 188–197, 2016, doi: 10.1016/j.jmmm.2015.08.076.

[260] N. I. Shakir, “Carbon Coated MoO 3 Nanowires / Graphene oxide Ternary Nanocomposite for High-Performance Supercapacitors,” *Electrochim. Acta*, 2016, doi: 10.1016/j.electacta.2016.09.069.

[261] V. Bayram *et al.*, “MXene Tunable Lamellae Architectures for Supercapacitor Electrodes,” *ACS Appl. Energy Mater.*, vol. 3, no. 1, pp. 411–422, Jan. 2020, doi: 10.1021/acsaem.9b01654.

[262] G. Cui, L. Wang, L. Li, W. Xie, and G. Gu, “Synthesis of CuS nanoparticles decorated Ti3C2Tx MXene with enhanced microwave absorption performance,” *Prog. Nat. Sci. Mater. Int.*, vol. 30, no. 3, pp. 343–351, 2020, doi: 10.1016/j.pnsc.2020.06.001.

[263] P. Ramadevi, A. Sangeetha, F. Kousi, and R. Shanmugavadivu, “Structural and electrochemical investigation on pure and aluminium doped nickel ferrite nanoparticles for supercapacitor application,” *Mater. Today Proc.*, vol. 33, no. 3, pp. 2116–2121, 2019, doi: 10.1016/j.matpr.2020.02.888.

[264] R. Tiwari, M. De, H. S. Tewari, and S. K. Ghoshal, “Structural and magnetic properties of tailored NiFe2O4 nanostructures synthesized using auto-combustion method,” *Results Phys.*, vol. 16, p. 102916, 2020, doi: 10.1016/j.rinp.2019.102916.

[265] A. V. Humbe, J. S. Kounsalye, M. V. Shisode, and K. M. Jadhav, “Rietveld refinement, morphology and superparamagnetism of nanocrystalline Ni0.70−xCuxZn0.30Fe2O4 spinel ferrite,” *Ceram. Int.*, vol. 44, no. 5, pp. 5466–5472, 2018, doi: 10.1016/j.ceramint.2017.12.180.

[266] L. Shao, A. Sun, Y. Zhang, L. Yu, N. Suo, and Z. Zuo, “Microstructure, XPS and magnetic analysis of Al-doped nickel–manganese–cobalt ferrite,” *J. Mater. Sci. Mater. Electron.*, vol. 32, no. 15, pp. 20474–20488, 2021, doi: 10.1007/s10854-021-06557-3.

[267] X. D. Jing, Z. G. Li, Z. T. Chen, Z. Y. Li, C. Y. Qin, and H. Y. Gong, "Effect of praseodymium valence change on the structure, magnetic, and microwave absorbing properties of M-type strontium ferrite: the mechanism of influence of citric acid dosage and calcination temperature," *Mater. Today Chem.*, vol. 30, 2023, doi: 10.1016/j.mtchem.2023.101537.

[268] S. Goel, A. Garg, H. B. Baskey, M. K. Pandey, and S. Tyagi, "Studies on dielectric and magnetic properties of barium hexaferrite and bio-waste derived activated carbon composites for X-band microwave absorption," *J. Alloys Compd.*, vol. 875, p. 160028, 2021, doi: 10.1016/j.jallcom.2021.160028.

[269] Y. Li *et al.*, "Facile preparation of: In situ coated Ti3C2Tx/Ni0.5Zn0.5Fe2O4 composites and their electromagnetic performance," *RSC Adv.*, vol. 7, no. 40, pp. 24698–24708, 2017, doi: 10.1039/c7ra03402d.

[270] P. Liu, Z. Yao, J. Zhou, Z. Yang, and L. B. Kong, "Small magnetic Co-doped NiZn ferrite/graphene nanocomposites and their dual-region microwave absorption performance," *J. Mater. Chem. C*, vol. 4, no. 41, pp. 9738–9749, 2016, doi: 10.1039/c6tc03518c.

[271] J. He *et al.*, "Tunable electromagnetic and enhanced microwave absorption properties in CoFe2O4 decorated Ti3C2 MXene composites," *Appl. Surf. Sci.*, vol. 504, p. 144210, 2020, doi: 10.1016/j.apsusc.2019.144210.

[272] B. J. Rani *et al.*, "Ferrimagnetism in cobalt ferrite (CoFe2O4) nanoparticles," *Nano-Structures and Nano-Objects*, vol. 14, pp. 84–91, 2018, doi: 10.1016/j.nanoso.2018.01.012.

[273] T. P. Gujar, W. Y. Kim, I. Puspitasari, K. D. Jung, and O. S. Joo, "Electrochemically deposited nanograin ruthenium oxide as a pseudocapacitive electrode," *Int. J. Electrochem. Sci.*, vol. 2, no. 9, pp. 666–673, 2007.

[274] B. Bhujun, M. T. T. Tan, and A. S. Shanmugam, "Study of mixed ternary transition metal ferrites as potential electrodes for supercapacitor applications," *Results Phys.*, vol. 7, no. May, pp. 345–353, 2017, doi: 10.1016/j.rinp.2016.04.010.

[275] B. Bhujun, M. T. T. Tan, and A. S. Shanmugam, "Evaluation of aluminium doped spinel ferrite electrodes for supercapacitors," *Ceram. Int.*, vol. 42, no. 5, pp. 6457–6466, 2016,

doi: 10.1016/j.ceramint.2015.12.118.

[276] K. Kannan, K. K. Sadasivuni, A. M. Abdullah, and B. Kumar, “Current trends in MXene-based nanomaterials for energy storage and conversion system: A mini review,” *Catalysts*, vol. 10, no. 5, May 2020, doi: 10.3390/CATAL10050495.

[277] A. Ali *et al.*, “3D NiO nanowires@NiO nanosheets core-shell structures grown on nickel foam for high performance supercapacitor electrode,” *J. Electroanal. Chem.*, vol. 857, p. 113710, 2020, doi: 10.1016/j.jelechem.2019.113710.

[278] A. Z. AL Shaqsi, K. Sopian, and A. Al-Hinai, “Review of energy storage services, applications, limitations, and benefits,” *Energy Reports*, vol. 6, pp. 288–306, 2020, doi: 10.1016/j.egyr.2020.07.028.

[279] W. Wang, Q. Hao, W. Lei, X. Xia, and X. Wang, “Ternary nitrogen-doped graphene/nickel ferrite/polyaniline nanocomposites for high-performance supercapacitors,” *J. Power Sources*, vol. 269, pp. 250–259, 2014, doi: 10.1016/j.jpowsour.2014.07.010.

List of Publication

1. Publication

Sintering Temperature Impact on the Structural-Magnetic Properties of the $Zn_{0.2}Mg_{0.8}Fe_2O_4$ Spinel Ferrite

Kiranjot Kaur[a], Hamnesh Mahajan[b], A.K. Srivastava[c], Deepak Basandrai[d]

Department of Physics, School of Chemical Engineering & Physical Sciences, Lovely Professional University, Phagwara, Punjab-144411, India

[a]Kiranjot.kaur.3388@gmail.com
[b] Mahajanhamnesh@gmail.com
[c]Corresponding author: ak.srivastava@lpu.co.in
[d] deepak.basandrai@lpu.co.in

Abstract. This research work investigated the influence of sintering temperature on the structural and magnetic properties of $Zn_{0.2}Mg_{0.8}Fe_2O_4$ ferrite synthesized by the sol-gel auto combustion process at different sintering temperatures (400 °C, 600 °C, 800 °C). XRD study confirmed the $Zn_{0.2}Mg_{0.8}Fe_2O_4$ ferrite exhibits cubic symmetry. The crystallite size and unit cell volume are increasing as the sintering temperature increases. FTIR spectrum shows the vibrational band near 600 cm^{-1} to 400 cm^{-1} which are corresponding to the tetrahedral and octahedral sites respectively. FESEM micrographs show the inhomogenous microstructure and agglomeration due to the existence of magnetic interactions. EDX study indicates the presence of all the elements in the sample.VSM reveals that the saturation magnetization increases as the temperature increases. The soft ferromagnetic nature was exhibited by all the prepared samples owing to its low coercivity value and found its application in power and electromagnetic devices.
Keywords: Spinel ferrites, Coercivity, Saturation magnetization, Ferromagnetic, Sintering

INTRODUCTION

Spinel ferrites, MFe_2O_4 where M (M=Cu, Mn, Mg, Ni, etc) is a divalent metal cation, which exhibits extraordinary magnetic and structural properties. Ferrites have a broad range of applications used in microwaves, energy storage devices, computer memories, heat transfer, information technology, etc [1]. Spinel structure is made up of a cubic close packing arrangement of oxygen atoms containing metal cations in tetrahedral (Td) and octahedral (Oh) sites [2]. The physical properties can be tailored by sintering the metal ions or using the different synthesis methods. Metal ion variation impacts their optical, electrical, magnetic, and structural properties due to various metal ions' site preferences [3]. Numerous methodology techniques can be used to synthesize the spinel ferrites such as the sol-gel method, solid-state method, hydrothermal method, and Co-precipitation method [4][5]. The influence of sintering ferrite can be analyzed by its optical, magnetic, and microstructural properties. Sintering temperature can also affect the chemical composition or synthesis method, and adding divalent or trivalent metal ions. Pedzich et al examined the impact of sintering temperature (900–1400 °C) of Mg-Zn ferrites [5]. The morphology was varied by sintering temperature (Ts), examined the impact on the various properties such as magnetic, and electrical conductivity [6]. Haque et al have studied Cu-doped Mg-Zn ferrite at various Ts (1050–1200 °C) and the particle size, permeability, and density are increased with an increases Ts. Chauhan et al have analyzed the effect of different sintering temperatures of $NiFe_2O_4$ ferrite [7].

A significant amount of research work has been done on the Ni–Zn ferrites. Ni–Zn ferrites also exhibit high saturation magnetization and resistivity [8]. Co–Zn ferrites were also investigated for their magnetic properties. Co–Zn ferrites exhibit high cubic magnetocrystalline anisotropy [5]. But no information is available on the $Zn_{0.2}Mg_{0.8}Fe_2O_4$ ferrites. $ZnFe_2O_4$ and $MgFe_2O_4$ exhibit the normal ferrites where Zn and Mg is occupying the tetrahedral sites and Fe occupies the octahedral sites. It is soft spinel ferrites.

The sol-gel auto combustion methodology is adopted in this work to synthesize the $Zn_{0.2}Mg_{0.8}Fe_2O_4$ ferrites at different sintering temperatures (400°C,600°C, 800°C). Several techniques are used viz. FTIR, FESEM, XRD, and VSM to study the magnetic, structural, and morphology properties.

3rd International Conference on Functional Materials, Manufacturing, and Performances
AIP Conf. Proc. 2986, 030150-1–030150-7; https://doi.org/10.1063/5.0193013
Published by AIP Publishing. 978-0-7354-4840-7/$30.00

2. Publication

Journal of MATERIALS RESEARCH

Article
DOI:10.1557/s43578-023-01119-1

Manganese doped cobalt–nickel spinel ferrite via. sol–gel approach: Insight into structural, morphological, magnetic, and dielectric properties

Kiranjot Kaur[1], Hamnesh Mahajan[1], Anjori Sharma[1], Ibrahim Mohammaed[1], Ajeet Kumar Srivastava[1,a)], Deepak Basandrai[1,a)]

[1] *Department of Physics, Lovely Professional University, Phagwara, Punjab 144411, India*

[a)] Address all correspondence to these authors. e-mails: srivastava_phy@yahoo.co.in; deepakbasandrai@gmail.com

Received: 1 December 2022; accepted: 21 June 2023

The structural, morphological, magnetic, and dielectric properties of $Mn_xCo_{0.5-x}Ni_{0.5}Fe_2O_4$ (x = 0.0, 0.2, and 0.4) synthesized by sol–gel auto-combustion are reported in this paper. X-ray diffraction pattern of the samples confirms the formation of a single-phase spinel ferrite and the crystallite size (*D*) is in the range of 32.60–33.62 nm. Fourier transform infrared spectra have a vibrational band at 534.20 cm^{-1} and 420.13 cm^{-1} which corresponds to the tetrahedral and octahedral sites of the $Mn_xCo_{0.5-x}Ni_{0.5}Fe_2O_4$ respectively. Field emission scanning electron microscope reveals the cubic morphology of the synthesized spinel ferrite with inhomogeneous grain size. Vibrating sample magnetometer analysis showed the ferromagnetic nature of all samples. All the samples exhibit a multi-domain because the value of M_r/M_s lies in the range of 0.153–0.336. Dielectric properties reveal the hopping of the charge carrier which has improved the conduction mechanism of the $Mn_xCo_{0.5-x}Ni_{0.5}Fe_2O_4$.

Introduction

For the past few decades, ferrites have gained a lot of fascination due to their peculiar properties such as saturation magnetization, structural properties, chemical, thermal stabilities, high coercivity, and mechanical hardness [1]. Due to these properties, ferrites materials have been widely used in catalysts [2], drug delivery systems [3], sensors [4], data storage systems [5], energy storage devices [6], and magnetic resonance imaging (MRI) [7]. Spinel ferrite exhibits a cubic structure and the molecular representation of spinel ferrite is MFe_2O_4 in which M is a divalent metallic cation (e.g., Mn, Zn, Ni, Co, Cu, Mg, etc.) [8]. The structure of spinel ferrite is complex having a face-centered cubic (fcc) core. It can be formed by combining a trivalent cation (Fe^{3+}) with another divalent metallic cation (M^{2+}). The spinel ferrites (MFe_2O_4) unit consists of 64 divalent tetrahedral sites and 8 of which are involved and 32 trivalent octahedral sites and 16 of which are involved. Ferrites can be doped with one or more metal cations, and due to this doping their chemical structure, morphology, and grain size can be changed [9]. Owing to the excellent magnetic and dielectric characteristics, the spinel ferrites are the subject of extensive research. Out of the several spinel ferrites, nickel ferrite ($NiFe_2O_4$) and cobalt ferrite ($CoFe_2O_4$) have gained attention due to their magnetic properties such as high coercivity, moderate saturation, and magnetic anisotropy [10]. $CoFe_2O_4$ is a magnetically hard ferrite and researcher showed interest due to its interesting properties such as high Curie temperature, chemical, and thermal stability, mechanical hardness, high electrical resistance, high resistance to corrosion, and low eddy current losses [11]. These properties make them compatible with a variety of technological applications, including high-density digital recording disks, photocatalysis, gas sensors, recording devices, medical diagnostics such as magnetic resonance imaging (MRI), hyperthermia, magnetically guided drug delivery, etc. [11, 12]. $NiFe_2O_4$ is a soft ferrite due to its commendable ferromagnetic properties, low eddy current losses, abundance in nature, electrochemical stability, catalytic behaviour, etc. [13]. However, Manganese is said to be an appropriate dopant due to its alluring properties such as high magnetic permeability, good chemical stability, low electrical losses, and also soft ferrite [8]. Nickel and Cobalt spinel ferrites have an inverse structure, whose formula can be represented as $(Fe^{3+}_j)_A[Ni_{1-j}Fe_{2-j}]_BO_4$ and $(Fe^{3+}_j)_A[Co_{1-j}Fe_{2-j}]_BO_4$. The divalent

3. Publication

Inorganic Chemistry Communications 159 (2024) 111717

Contents lists available at ScienceDirect

Inorganic Chemistry Communications

journal homepage: www.elsevier.com/locate/inoche

Short communication

Crystal structure refinement, morphological, and magnetic properties of ternary nanohybrid $Pr_xMn_{0.5}Co_{0.5}Fe_{2-x}O_4$ $(0.00 < x < 0.04)$ spinel ferrite

Kiranjot Kaur, Tchouank Tekou Carol Trudel, Kamlash Rani, A.K. Srivastava, Deepak Basandrai *

Department of Physics, Lovely Professional University, Punjab 144411, India

ARTICLE INFO

Keywords:
Spinel ferrites
Structural Properties
Magnetic Properties
Morphology

ABSTRACT

Rare earth Pr^{3+} ion substituted in the Mn - Co spinel ferrite was prepared via. sol–gel route. The phase composition of the prepared samples was analyzed by X-ray diffraction (XRD). Rietveld refinement confirms the single phase for the samples (x = 0.0, 0.01, 0.02) and shows a secondary phase for the samples with higher concentrations of Pr^{3+} (x = 0.03 and 0.04). The absorption band occurs within 400–600 cm^{-1} which affirms the formation of spinel ferrite by the Fourier transform infrared (FTIR) spectra. Field emission scanning electron microscopy (FESEM) micrograph reveals the presence of porous morphology and non-uniform grain growth inhomogeneous in size and shape due to the agglomeration present in the prepared sample. A vibrating sample magnetometer (VSM) study reveals all the samples exhibit a ferromagnetic nature. The coercivity (H_c) increases from 441.78 to 557.32 Oe and then decreases to 503.48 Oe. Owing to the basis of large surface area, presence of pore size, and soft magnetic nature synthesized spinel ferrites are best suitable for supercapacitor electrode material.

1. Introduction

Based on their structures, ferrites can be classified into spinel, garnet, and hexagonal ferrites. Spinel ferrite has gained much attention owing to its remarkable magnetic and electrical properties and is widely used for the fabrication of energy storage devices (i.e., batteries, sensors, and supercapacitors). Spinel ferrite has potential applications in electronic devices, bio-processing, magnetic recording [1], microelectronics [2], magnetic resonance imaging (MRI) [3], sensors [4], microelectronics [5], data storage systems [6], pollution control [7], anticorrosive paint ferrofluids [8], and magnetic recording [9]. Ferrite nanoparticles exhibit unique chemical, electrical, mechanical, structural, and magnetic properties and have a variety of promising technological applications in high-density recording devices, color imaging, ferrofluids, high-frequency devices, and magnetic refrigerators [10]. The spinel ferrite molecular representation is MFe_2O_4 where, 'M' is transition metal (Zn, Mn, Mg, Ni, Co, and Cu) tetrahedral and 'Fe' octahedral sites with oxygen ions (O^{2-}). The crystal structure of spinel ferrite is face-centered cubic (fcc) with the space group Fd-3 m and has two crystallographic sublattice sites namely tetrahedral (A) and octahedral (B). The cation occupancies at A and B crystallographic sites strongly influence magnetization in spinel ferrites.The magnetic moments of the resulting spinel ferrites, M_B and M_A, are related to the magnetic moments of the octahedral B and tetrahedral A sites, respectively [11]. The spinel structure consists of a closely packed oxygen anion, with 32 oxygen anions forming a complete structure unit cell. These oxygen anions form a face-centered cubic arrangement, leaving two types of spaces between them: tetrahedral or A-site spaces surrounded by four oxygen particles, and octahedral or B-site spaces surrounded by six oxygen particles. Every spinel ferrite unit cell contains sixty-four tetrahedral sites, eight of which are involved, and thirty-two octahedral sites, 16 of which are involved. However, the formula $(A_{1-\delta}\ B_{\delta})[A_{\delta}B_{2-\delta}]O_4$ represents many possible intermediary distributions that denote considerable cation disorder, indicating that this structure requires special attention in terms of magnetic characterization [12]. δ indicates the degree of the inversion factor, when $\delta = 0$, the spinels are normal, for $\delta = 1$, spinels are termed as inverse and for $0 \ll \delta \ll 1$, spinels are mixed [13]. The variations in the magnetization of these lattice sites provide the net magnetization of the spinel structure. The presence of metal (divalent or trivalent) cations at lattice sites has been investigated using crystal field theory [14,15]. Furthermore, the occupancy of metal cation (divalent or trivalent) to these tetrahedral and octahedral sites depends on a few key factors viz.

* Corresponding author.
E-mail address: deepakbasandrai@gmail.com (D. Basandrai).

https://doi.org/10.1016/j.inoche.2023.111717
Received 8 August 2023; Received in revised form 22 October 2023; Accepted 8 November 2023
Available online 15 November 2023

4. Publication

J Mater Sci: Mater Electron (2024) 35:229

PrMnCo-Ti_3C_2 MXene nanocomposite-based supercapacitor for the optimization of electrochemical performance

Kiranjot Kaur[1], Hamnesh Mahajan[1], Sachin Kumar Godara[2], Pragati Kumar[3], Nupur Saxena[4], Ajeet Kumar Srivastava[1], and Deepak Basandrai[1,*]

[1] *Department of Physics, Lovely Professional University, Punjab 144411, India*
[2] *Department of Chemistry, Guru Nanak Dev University, Punjab 143005, India*
[3] *Deparatment of Nano Sciences and Materials, Central University of Jammu, Jammu 181143, India*
[4] *Deparatment of Physics, Indian Institute of Technology, Jammu 181121, India*

Received: 5 April 2023
Accepted: 5 January 2024
Published online: 25 January 2024

ABSTRACT

The popularity of MXene has increased amongst researchers owing to its marvelous electrochemical properties. The current research work explores the synthesis of nanocomposites $Pr_{0.02}Mn_{0.5}Co_{0.5}Fe_{1.98}O_4$–$Ti_3C_2$) which is most suitable for supercapacitor applications. The sol–gel method was used to synthesize the spinel ferrite ($Pr_{0.02}Mn_{0.5}Co_{0.5}Fe_{1.98}O_4$) and the etching method for Ti_3C_2 MXene's. The final ($Pr_{0.02}Mn_{0.5}Co_{0.5}Fe_{1.98}O_4$–$Ti_3C_2$) nanocomposite was prepared using mechanical blending. The X-ray diffraction (XRD) analysis revealed the enhancement of the crystallite size of the $Pr_{0.02}Mn_{0.5}Co_{0.5}Fe_{1.98}O_4$–$Ti_3C_2$ nanocomposite compared to the $Pr_{0.02}Mn_{0.5}Co_{0.5}Fe_{1.98}O_4$, and Ti_3C_2. Field emission electron microscopy (FESEM) affirms the porous morphology that helps to enhance the electrochemical activity. The average crystallite size (D) $Pr_{0.02}Mn_{0.5}Co_{0.5}Fe_{1.98}O_4$, Ti_3C_2, and $Pr_{0.02}Mn_{0.5}Co_{0.5}Fe_{1.98}O_4$–$Ti_3C_2$ samples which are found to be 38 nm, 15 nm, and 31 nm respectively. The XPS results $Pr_{0.02}Mn_{0.5}Co_{0.5}Fe_{1.98}O_4$–$Ti_3C_2$ composite affirms the presence of peaks viz. Ti 2p, Pr 3d, Mn 2p, Co 2p, Fe 2p, C 1s, O 1s. The electrochemical properties of the $Pr_{0.02}Mn_{0.5}Co_{0.5}Fe_{1.98}O_4$–$Ti_3C_2$ nanocomposite were found to be superior to those of $Pr_{0.02}Mn_{0.5}Co_{0.5}Fe_{1.98}O_4$ and Ti_3C_2. The specific capacitances of the $Pr_{0.02}Mn_{0.5}Co_{0.5}Fe_{1.98}O_4$–$Ti_3C_2$, Ti_3C_2, and $Pr_{0.02}Mn_{0.5}Co_{0.5}Fe_2O_4$ electrodes 1310.54 F g^{-1}, 1181.95 F g^{-1}, and 947.81 F g^{-1} at a current density of 2 A g^{-1}. The nanocomposite showed good electrochemical performance and hence it is a promising material for supercapacitors.

Address correspondence to E-mail: deepakbasandrai@gmail.com

https://doi.org/10.1007/s10854-024-11972-3